Combining asteroseismic and s-process nucleosynthesis observations to constrain the evolution of rotating low-mass stars

Jacoba Wilhelmina den Hartogh

A thesis submitted to Keele University
for the Degree of Doctor of Philosophy

School of chemical and physical sciences, Keele University.

October, 2020

Abstract

In this thesis, I study the evolution of low-mass (around 2 $M_\odot$) solar-metallicity stars including the effect of rotation and magnetic fields. These stars produce a significant amount of elements heavier than iron via the so-called s process and thus have a large impact on galactic chemical evolution. In the last decade, researchers have been able to obtain rotational properties from asteroseismic observations of stars. These observations cannot be reproduced by current stellar evolution models. It is now generally accepted that a process of transport of angular momentum is missing from the current implementations of rotation in stellar evolution models. The aim of the thesis is to explore the impact of rotation on the evolution and nucleosynthesis of low-mass stars, and to use the asteroseismic and s-process nucleosynthesis observations as constraints. To do so, I calculated rotating and non-rotating models, with and without the Tayler-Spruit dynamo. To constrain the missing process of angular momentum, I included an additional, artificial viscosity to models. The main findings are the following. I determined the amount of additional viscosity needed for the cores within my stellar evolution models to rotate within the asteroseismically constrained rotation rates of core helium burning stars and white dwarfs. The value I had to use for such viscosity is ν_{add} $=10^6$-10^7 cm^2 s^{-1}, several orders of magnitude higher than the value found to match observations for lower mass stars. I then calculated for the first time the s-process nucleosynthesis of stellar evolution models that match these constraints on rotation rates. I concluded that the effect of rotation on the s-process production of low mass AGB stars is negligible, which is in agreement with s-process observations. I also placed constraints on the mixing of chemical elements by the missing process of angular momentum, and I have listed future work involving magnetic dynamos.

Acknowledgements

All MESA and MPPNP models in this thesis are calculated by me, but little would have been possible without my collaborators, friends, and relatives.

First and foremost my thanks goes to my supervisor Raphael Hirschi. Thanks for the PhD position, the guidance and support, all the cheese, and for the freedom to let me decide what I do in my evenings and weekends. Quite often friends and family back home asked me how I was dealing with the PhD stress, usually accompanied with an article filled with horror stories about PhD students and their mental health issues. I have read all those stories and every time I concluded that the reason I couldn't imagine me and my PhD to end up in one of those articles was because of you and your style of supervising. Thank you.

My collaborators in the NuGrid collaboration team deserve a special thanks, as they allowed me to use the post-processing code MPPNP, as well as their analysis tools for MESA and MPPNP models. Patrick Eggenberger (and all his coffee) was a great source of knowledge when I was getting familiar with the models presented in Chapter 4 and with the asteroseismic community more generally. Maria Lugaro and Carolyn Doherty were generous with their time and advice when I was working through the corrections. More general support and inspiration came from my friends in 'Raphael's corner', but more importantly from three intelligent young women: Emmal is ridiculously optimistic and dramatic, Luna always shows me how valuable it is to have a free spirit, and Franka

keeps reminding me that we can do whatever we want to do, including making a change when it is time to move on. You're on top of the world and the world knows it.

My brothers Marinus, Petran, and Corneel, deserve a thanks for listening to my complaining about being tired and 'having to travel again'. My parents Jan and Marijn are almost as responsible for me submitting this thesis as I am. They have always encouraged us to form our own opinions and communicate them. They made sure we were at place at our school and university, so that we could relax and focus. But most importantly they showed us that sometimes, no matter how hard you work, it takes a while until you see results.

Het verlies van mijn tante Nel tijdens mijn PhD heb ik als heftig ervaren. Zij hielp mij op mijn gemak rond te lopen in de medische wereld, omdat dat nu eenmaal moest. Zij zou het beste hebben begrepen hoe lang de weg van toen naar het inleveren van mijn proefschrift is geweest.

Jacqueline den Hartogh

Contents

List of Figures

List of Tables

1 Introduction

Stars are important to us for several reasons. For instance, stars create the elements necessary for life. Our Sun is a star, which keeps us warm and provides the light we need. Understanding how stars are born and die is important to understand what will happen to us and our solar system. Stellar interiors are physical laboratories with extreme conditions that test many different areas of physics: nuclear physics, particle physics, thermodynamics, hydrodynamics, and (classical) mechanics. As a result, the study of stars is fascinating yet complicated, because the conditions of stellar interiors cannot usually be reproduced in a laboratory on Earth and different processes interact and feedback on each other in a complex way.

This thesis focusses on the lives and nucleosynthesis low mass stars. A few of the reasons of why these stars are important in relation to the work presented in this thesis are listed here. First, because of their large number compared to massive stars, as the initial mass function of stars strongly decreases with increasing stellar mass (see e.g. Salpeter 1955). Second, because of their interesting nucleosynthesis (the s process in particular) which makes them important for the chemical evolution of our Universe (see e.g. Travaglio et al. 2004; Kobayashi, Karakas & Umeda 2011; Kobayashi et al. 2011; Bisterzo 2017; Prantzos et al. 2018). Third, because recent asteroseismic surveys allow astronomers to probe the interior low-mass stars (Aerts, Christensen-Dalsgaard & Kurtz 2010; Beck et al. 2012).

1.1 Evolution of low mass stars

In this section the evolution of low-mass stars will be presented, starting by defining what a low mass star is before moving to detailed stellar evolution theory, which is loosely based on the stellar evolution lecture notes of Pols (2009) and Pettini (2014), and on the book by Kippenhahn & Thomas (1970). The main focus of this section will be on the asymptotic giant branch (AGB) phase, as this is where the s process takes place, providing an important observational constraint for the stellar evolution models

presented in this work.

Binary interaction has also been shown to play an important role in the evolution of stars (see e.g. De Marco & Izzard 2017, for a recent overview). There are however many problems to solve concerning single star evolution and the effects of rotation, including the missing process of angular momentum transport and the effect of rotation on the s-process production in AGB stars. Therefore in this thesis I solely focus on single stars.

1.1.1 General considerations

Fig. 1.1 and the accompanying text in Karakas & Lattanzio (2014) presents a schematic overview of the different evolutionary paths of single stars, covering the whole spectrum of initial masses. The least massive stars with an initial mass of about 0.08-0.5 $M_\odot$ are shown on the left, these stars only burn hydrogen (H) into helium (He) in their cores and form He white dwarfs. The most massive stars with an initial mass of about 25 $M_\odot$ and higher are depicted on the far right. These stars undergo all nuclear burning phases (H, He, carbon (C), neon (Ne), oxygen (O), and silicon (Si)) and most are expected to form black holes. In between these extremes, the distinction for the different initial masses is made based on the following:

- Low-mass stars: stars with an initial mass of about 0.5-2.2 $M_\odot$. These stars start the core He burning phase with He flashes under degenerate conditions, proceed through the AGB phase and end their lives as CO white dwarfs (Herwig 2005; Karakas & Lattanzio 2014).

- Intermediate-mass stars: stars with an initial mass of about 2.2-10 $M_\odot$. Unlike low-mass stars, these stars start the core He burning phase gently without the He flashes under degenerate conditions. In Fig. 1.1 intermediate-mass stars are split in three groups: the lower intermediate-mass stars (2.2-7 $M_\odot$) which do not ignite C in their core, the middle intermediate-mass stars (7-9.5 $M_\odot$) which ignite C via C flashes, and end their lives as O-Ne white dwarfs, and the massive intermediate-mass stars (9.5-10 $M_\odot$) which ignite C in C flashes and end their
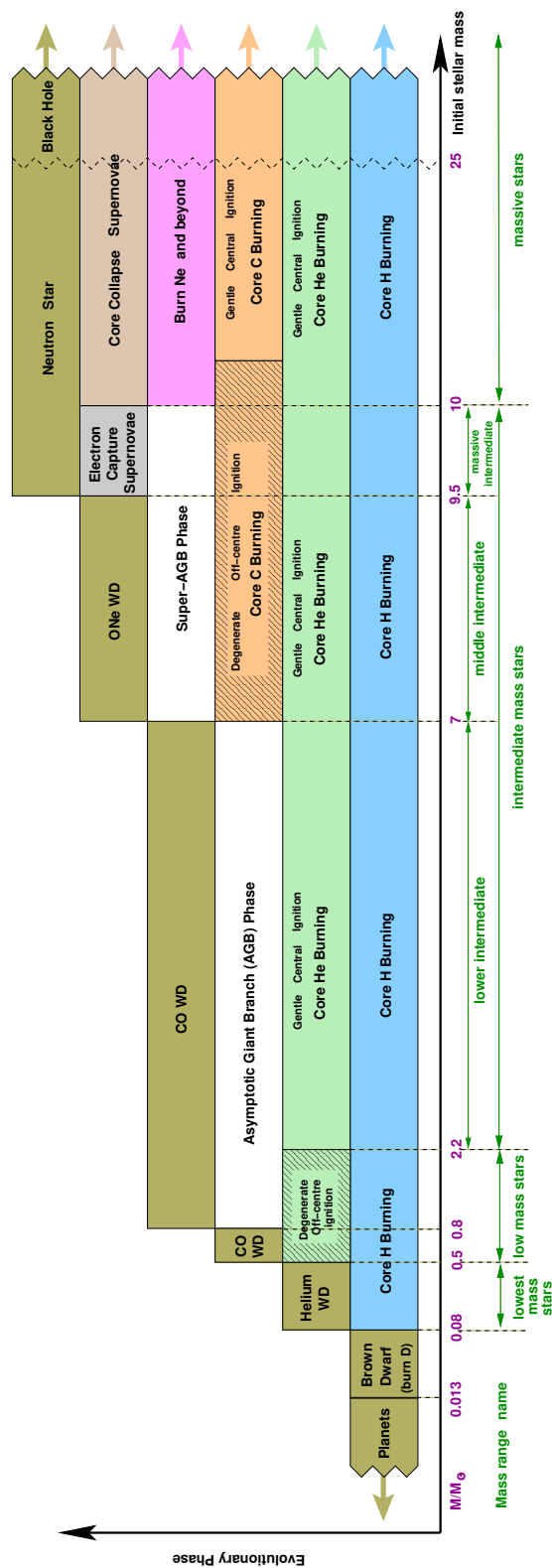
Figure 1.1: Schematic overview of how stars with different initial masses have different evolutionary paths. The initial masses on the horizontal axis differ for different metallicities (the models included in this figure are calculated at solar metallicity) and stellar evolution codes and are thus rough estimates. Figure from Karakas & Lattanzio (2014).

lives as neutron stars. Before their final fate, these stars all experience the AGB phase (see Section 1.1.3 and Herwig 2005; Karakas & Lattanzio 2014).

- Massive stars: stars with an initial mass $\gtrsim 10$ M$_\odot$. These stars start the core C burning phase gently without C flashes, and proceed further through core Ne, O, Si burning phases. These stars end their lives as neutron stars or black holes, see Heger et al. (2003).

These initial masses are all rough estimates taken from Karakas & Lattanzio (2014), which vary with initial metallicity and composition, and when different physical processes (like rotation) are included in the stellar evolution calculations.

The stellar evolution models presented in this thesis have an initial mass that positions them around the border between low-mass and (lower) intermediate-mass stars. For convenience, I refer to them as 'low-mass' even if they do not experience He flashes at the start of the core He burning phase.

The majority of stars are in very long-lived phases, such that no change can be observed during our lifetime. All the forces acting on the gas elements inside stars are in balance with each other, creating a mechanical equilibrium. This equilibrium is commonly referred to as the hydrostatic equilibrium (or HE) and states that gravity and pressure forces are balanced inside the star. So the equation of motion for a gas particle is in balance, and there is no acceleration for each gas particle:

$$\ddot{r} = 0 = -\frac{Gm}{r^2} - \frac{1}{\rho}\frac{dP}{dr} \tag{1.1}$$

with $\ddot{r}$ being the acceleration of the gas particle, G the gravitational constant, m the mass coordinate of the particle within the star, ρ the density and P the pressure of the surrounding of the gas particle. When using $dm/dr = 4\pi r^2 \rho$, Eq. 1.1 can be rewritten as:

$$\frac{dP}{dm} = -\frac{Gm}{4\pi r^4} \tag{1.2}$$

which is the commonly known expression for the hydrostatic equilibrium, with dm being the thickness in mass coordinates of the shell in the star.

Estimates of what happens when this equilibrium is perturbed can be given by assuming

that the pressure forces are suddenly not present any more, so only inwards gravity is present. Then, the star collapses under its own gravity on a 'dynamical time scale', τ_{dyn}, or 'free fall time scale', calculated by approximating the inward acceleration:

$$\ddot{r} = \frac{R}{\tau_{\mathrm{dyn}}^2} \tag{1.3}$$

as this acceleration is the gravitational acceleration $g = \frac{GM}{R^2}$, with R and M being the total radius and mass of the star, the expression for τ_{dyn} becomes:

$$\tau_{\mathrm{dyn}} \sim \left(\frac{R^3}{Gm}\right)^{1/2} \tag{1.4}$$

For the Sun, τ_{dyn} is about half an hour, much shorter than its evolutionary time scale. This means that stars have very fast responses to changes in their mechanical equilibrium. Stars can reach HE again after a perturbation, but small scale oscillations around HE may occur (see Section 1.3).

A consequence of the HE is a relation called the virial theorem, which connects the two main energy sources within a star. The virial theorem is derived from the HE (Eq. 1.2) by integrating over the whole star:

$$\int_0^M \frac{4}{3}\pi r^3 \frac{\mathrm{d}P}{\mathrm{d}m}\mathrm{d}m = -\frac{1}{3}\int_0^M \frac{Gm}{r}\mathrm{d}m \tag{1.5}$$

assuming spherical symmetry and with P being the pressure, and m and r the mass and radius coordinates respectively within the star. The integral on the right results in the gravitational potential energy, while the integral on the left can be integrated by parts so that Eq. 1.5 becomes:

$$[VP]_{r=0}^{r=R} - \int_{V_{\mathrm{r}=0}}^{V_{\mathrm{r}=R}} P\mathrm{d}V = -\frac{1}{3}E_{\mathrm{gr}} \tag{1.6}$$

where V is the volume of the star within radial coordinate r. The first term on the left side is zero at both integration limits (the volume is zero at $r=0$, the pressure is zero at $r = R$), whereas the second term on the left side can be rewritten as $\int_{V_{\mathrm{r}=0}}^{V_{\mathrm{r}=R}} \frac{P}{\rho}\mathrm{d}m$. Assuming the star is made up of mono-atomic ideal gas, then the pressure is given by:

$$P = \frac{\rho}{\mu m_{\mathrm{u}}}\mathrm{k_B}T \tag{1.7}$$

where μ is the mass of the gas in atomic mass units, k_B the Boltzman constant, and m_u the atomic mass unit. The internal energy u of each ideal gas particle $\frac{3}{2}k_bT$, which becomes $\frac{3}{2}\frac{k_bT}{\mu m_u}$ per mass unit. This can be simplified to $u = \frac{3}{2}\frac{P}{\rho}$. Substituting this relation into the remaining terms in Eq. 1.6 leads to $\int \frac{P}{\rho}dm = \frac{3}{2}\int u\,dm$ which is $\frac{3}{2}$ times the internal energy E_{int}. The virial theorem for an ideal gas is therefore:

$$E_{\text{int}} = -\frac{1}{2}E_{\text{gr}} \tag{1.8}$$

which provides a strong relation between internal and gravitational energy of the star: when the star contracts, it becomes more strongly bound and thus increases the gravitational pull inwards, the internal energy has to increase as well, which can be achieved by increasing the temperature of the star.

When nuclear reactions take place within the star, the energy generated can compensate for the energy that is radiated away at the surface. When the energy generation is actually balancing the energy losses at the surface, the star is in thermal equilibrium (TE) and the total energy of the star is conserved. Like with the HE, it is important to consider what would happen when the thermal equilibrium is violated. This can be done by assuming that the energy generation within the star is larger than the amount of energy radiated away at the surface ($L_{\text{nuc}} > L$). The total energy of the star would then increase, making the star expand and cool due to the virial theorem. As the nuclear reactions are temperature dependent, the temperature decrease leads to a decrease in energy generation, until the energy generation again matches the energy loss. Like the HE, the TE is thus a stable equilibrium.

The time scale over which the star reacts to changes to the TE is called the *thermal* time scale, or the Kelvin-Helmholtz time scale. It is characterised as the time a star needs to radiate away all gravitational binding energy, assuming a constant luminosity and no energy generation in the star:

$$\tau_{\text{KH}} \sim \frac{E_{\text{int}}}{L} = \frac{E_{\text{grav}}}{2L} \tag{1.9}$$

$$\tau_{\text{KH}} \sim \frac{GM^2}{2RL} \tag{1.10}$$

with the Sun's current values, this corresponds to 1.5×10^7 years, much longer than the dynamical time scale but still much shorter than its lifetime.

A star can remain in TE as long as nuclear fuel is available. The nuclear time scale is the time scale on which the star will exhaust the current burning phase if it continues at a constant rate:

$$\tau_{nuc} \sim \frac{qXMr}{L/Q} \tag{1.11}$$

where q is the fraction of fuel available for the burning phase, X the mass fraction of the fuel in the star, M the total mass of the star, r the burning rate, L the total luminosity of the star, and Q is the energy released per mass of the fuel. For the Sun, this is corresponds to 10^{10} years, a few orders of magnitude larger than the thermal time scale.

To conclude:

$$\tau_{\text{nuc}} \gg \tau_{\text{KH}} \gg \tau_{\text{dyn}} \tag{1.12}$$

and thus the nuclear time scale determines the stellar evolution pace, and stars can be assumed to be in HE and TE for most of their lives.

In the previous paragraphs the ideal gas law was used as equation of state. However, this equation of state is not always applicable. The other frequently mentioned equation of state is the degenerate one.

A gas can become degenerate when its free particles (in AGB stars usually electrons, i.e. fermions) are limited to a finite volume at a high density. If the density increases, the electrons are more limited in their movement and the Pauli exclusion principle becomes important (Pauli 1925). This principle states that two or more electrons are not able to occupy the same momentum state. The Heisenberg uncertainty principle (Heisenberg 1927), applicable to all particles, states that:

$$\Delta x \Delta p \geq \frac{h}{4\pi} \tag{1.13}$$

where Δx is the uncertainty (standard deviation) of the position of the particles, Δp the uncertainty in momentum, and h the Planck constant. When the density increases, the

Δx will decrease as well. Thus Δp has to increase as stated in the Heisenberg principle, meaning the spread of electron velocities will go up independent of the temperature. When the pressure due to these increased velocities exceeds the pressure from the thermal motion of the electrons, the gas is referred to as degenerate matter. The degeneracy pressure, only dependent on density, is: $P = C \times \frac{\rho}{\mu_e}$ where C is a constant of about 1×10^{13} (cgs units), and μ_e is the mean molecular weight of an electron. The transition from an ideal gas to a strongly degenerate gas happens smoothly, and is called *partial degeneracy*.

As the temperature and pressure are disconnected in fully degenerate gases, perturbations of TE (like the $L_{nuc} > L$ example discussed when defining the thermal time scale) have a different effects on the star than in ideal gas conditions described in the previous section. In a degenerate gas, the extra energy generation will not lead to an expansion and thus cooling of the star. Instead, the extra energy will lead to heating of the region, followed by even more enhanced energy generation, leading to more heating, followed by more enhanced energy generation. This unstable process is called *thermonuclear runaway* and will continue until the gas is hot enough to start acting like an ideal gas again. An example of thermonuclear runaways is the core He flash in low-mass stars, see Section 1.1.2.

These unstable nuclear burning conditions can also occur in shell burning phases, if the burning shell is sufficiently thin (the *thin shell instability*). This can be shown by considering a shell with mass δm, with r_0 as inner boundary and r as outer boundary in radius, and with thickness $D = r - r_0 \ll r_0$. If the shell is in TE, the energy generated inside the shell is equal to the energy flowing out of the shell. When there is more energy generated than flowing out, the shell will expand by δr. When r_0 remains roughly constant, then $dr = dD$. The expansion of the shell leads to a decrease in pressure according to HE:

$$\frac{\delta P}{P} = -4\frac{\delta r}{r} \tag{1.14}$$

as $m \sim r^2 \rho D$ and $dm = 0$:

$$\frac{\delta \rho}{\rho} = -\frac{\delta D}{D} = -\frac{\delta r}{r}\frac{r}{D} \tag{1.15}$$

$$\text{and } \frac{\delta P}{P} = 4\frac{\delta \rho}{\rho}\frac{D}{r}. \tag{1.16}$$

When using a generic equation of state: $P = C\rho^a T^b$, the pressure term can be eliminated:

$$b\frac{\delta T}{T} = (4\frac{D}{r} - a)\frac{\delta \rho}{\rho}, \tag{1.17}$$

then the shell is thermally stable when the expansion results in a decrease in temperature, resulting in the following expression for stability:

$$4\frac{D}{r} > a. \tag{1.18}$$

From Eq. 1.18 it follows that if the shell is sufficiently thin, a thermal instability will develop as the expansion will not lead to a significant temperature drop. Therefore, a runaway reaction in the case of degeneracy described above can occur (Kippenhahn & Thomas 1970; Yoon, Langer & van der Sluys 2004). Runaway reactions within the AGB phase leading to the recurrent thermal pulses, see Section 1.1.3.

1.1.2 Main-sequence (MS) to the asymptotic giant branch (AGB) phase

As a representative example of the evolution of a low-mass star investigated in this thesis, Fig. 1.2 shows a Hertzsprung-Russell diagram (HRD) and a Kippenhahn diagram (or structure evolution diagram), in the top and bottom panels of the figure, respectively. The HRD shows the evolution of surface properties of a star. Two versions of the HRD exist: an observational one showing the relationship between stellar magnitude and its colour or temperature derived from observations, and a theoretical one showing the star's luminosity and its effective temperature from a stellar evolution model. Fig. 1.2 shows the theoretical one, from the start of the MS to the white dwarf phase. The Kippenhahn diagram shows the internal structure of the star as a function of time. Again several
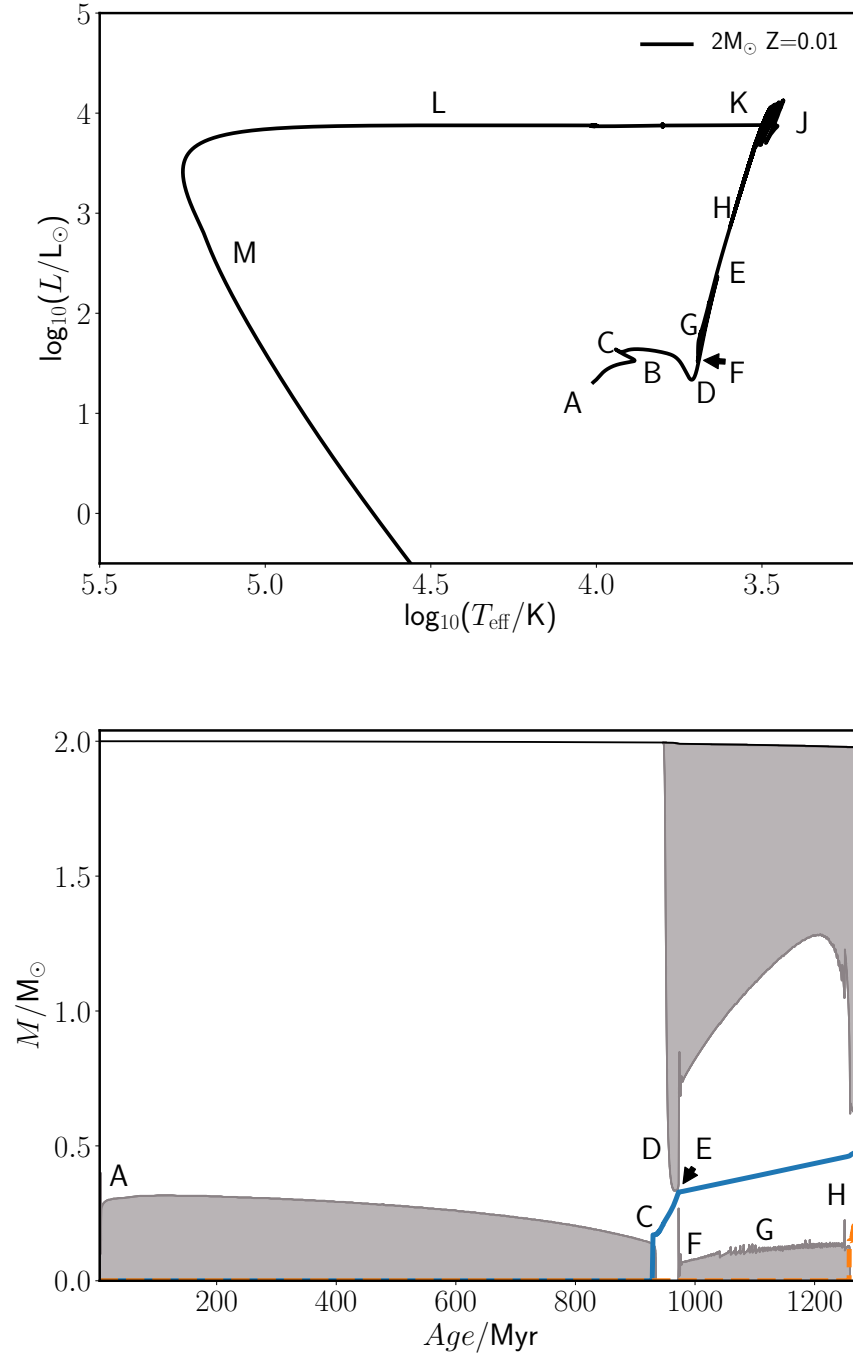
Figure 1.2: The HRD and Kippenhahn diagram of a 2 M$_\odot$, Z=0.01, non-rotating model presented in the Chapter 5. The HRD shows the entire evolution, the Kippenhahn diagram is cut off at the start of the AGB phase. In the Kippenhahn diagram the grey regions represent convective regions, while the lines indicate the H free (solid line) and the He free (dashed line) boundaries. The letters indicate beginnings and ends of evolutionary phases and event during the evolution, see text for details.

versions of this diagram exist, but all have a measure of time on the horizontal axis and a spatial or mass coordinate of the star from centre to surface on the vertical axis. The version in Fig. 1.2 shows the age of the star and the mass coordinate in solar mass unit. During the main sequence (points A-C in Fig. 1.2) H is converted into He, or more precisely protons (p) into ^{4}He (also known as α-particles), as the temperature in the core is so high that the electrons are no longer bound to the hydrogen atoms. The conversion can happen via two pathways, named the pp-chains and the CNO cycles. There are three pp-chains: the ppI-chain follows the path:

$$p + p \rightarrow D + e^+ + \nu_e \tag{1.19}$$

$$p + D \rightarrow {}^3\text{He} + \gamma \tag{1.20}$$

$$^3\text{He} + {}^3\text{He} \rightarrow {}^4\text{He} + 2p. \tag{1.21}$$

with D being ^{2}H, e^+ a positron, ν_e an electron neutrino, and γ gamma radiation. The ppII-chain branches out at ^{3}He:

$$^3\text{He} + {}^4\text{He} \rightarrow {}^7\text{Be} + \gamma \tag{1.22}$$

$$^7\text{Be} + e^- \rightarrow {}^7\text{Li} + \nu_e \tag{1.23}$$

$$^7\text{Li} + p \rightarrow 2\,{}^4\text{He}. \tag{1.24}$$
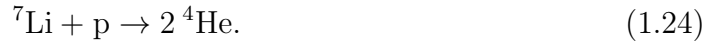
while the ppIII chain branches out at ^{7}Be:

$$^7\text{Be} + p \rightarrow {}^8\text{B} \tag{1.25}$$

$$^8\text{B} \rightarrow {}^8\text{Be} + e^+ + \nu_e \tag{1.26}$$

$$^8\text{Be} \rightarrow 2\,{}^4\text{He}. \tag{1.27}$$

When temperatures of 2×10^7 K are reached and C, N, and O are present, the CNO cycle dominates over the pp-chains. This temperature is reached in stars with an initial

mass of about 1.3 $M_\odot$ and higher. The reaction sequence of the CN-cycle (or CNO I) is:

$$^{12}\text{C} + \text{p} \rightarrow {}^{13}\text{N} + \gamma \tag{1.28}$$

$$^{13}\text{N} \rightarrow {}^{13}\text{C} + \text{e}^+ + \nu_e \tag{1.29}$$

$$^{13}\text{C} + \text{p} \rightarrow {}^{14}\text{N} + \gamma \tag{1.30}$$

$$^{14}\text{N} + \text{p} \rightarrow {}^{15}\text{O} + \gamma \tag{1.31}$$

$$^{15}\text{O} \rightarrow {}^{15}\text{N} + \text{e}^+ + \nu_e \tag{1.32}$$

$$^{15}\text{N} + \text{p} \rightarrow {}^{12}\text{C} + {}^4\text{He}. \tag{1.33}$$

At higher temperature the NO-cycle becomes active in addition to the CN-cycle (CNO II):

$$^{15}\text{N} + \text{p} \rightarrow {}^{16}\text{O} + \gamma \tag{1.34}$$

$$^{16}\text{O} + \text{p} \rightarrow {}^{17}\text{F} + \gamma \tag{1.35}$$

$$^{17}\text{F} \rightarrow {}^{17}\text{O} + \text{e}^+ + \nu_e \tag{1.36}$$

$$^{17}\text{O} + \text{p} \rightarrow {}^{14}\text{N} + {}^4\text{He}. \tag{1.37}$$

Due to the energy production, the core is now convective[1] while burning through the H present in the core. At point B in Fig. 1.2, the H abundance in the core is significantly reduced, and the core of the star starts contracting as the energy production due to nuclear burning reduces. As the whole star contracts, the effective temperature and the luminosity both increase. The time between point B and C is too short to be visible in the Kippenhahn diagram. Point C is where there is no H left in the core, which has now become radiative.

The sharp hook at point C in the HRD of Fig. 1.2 is when the H-shell burning starts, this is the phase where the evolutionary paths of low-mass and intermediate-mass stars diverge. The difference is due to the Schönberg-Chandrasekhar (SC) limit (see Schönberg & Chandrasekhar 1942), which states that there is a limit to the fraction of core mass

---

[1]Convection and radiation are the two main processes for energy transport in stars and will be described in detail in Chapter 2

over stellar mass that can be supported by an isothermal (= constant temperature) core:

$$\left(\frac{M_{ic}}{M_T}\right)_{SC} \simeq 0.37 \left(\frac{\mu_{env}}{\mu_{ic}}\right)^2 \simeq 0.1 \tag{1.38}$$

where M_{ic} is the mass of the isothermal core (isothermal at this moment to be able to stay in thermal equilibrium), M_T is the total stellar mass, and μ_{env} and μ_{ic} are the mean molecular weights of the envelope and core respectively. If the mass of the He core exceeds this limit at the end of the main sequence, then the pressure within the core is not high enough to sustain the weight of the envelope. This leads to rapid core contraction until the core temperature is high enough to ignite He. If the core mass is smaller than this limit at the end of the main-sequence, then the hydrogen burning shell will increase the core mass until the limit is reached. At this moment, the rapid core contraction starts on the thermal timescale, while the star is no longer in hydrostatic and thermal equilibrium. Stars with an initial mass up to about 1.5 M$_\odot$ never reach the SC limit, as their cores become degenerate before the limit is reached. The degeneracy pressure (explained in Section 1.1.1) allows the core to sustain the weight of the envelope. The core of the 2 M$_\odot$ star shown in Fig. 1.2 is just below the SC limit when it leaves the main sequence. Therefore, it starts H-shell burning (thick solid blue line in the Kippenhahn diagram of Fig. 1.2) in equilibrium until the SC limit is reached. The central part of the core has become degenerate by this time, and the H-shell burning phase can continue without rapid contraction.

The core continues to contract after point C while the envelope expands and cools. This is called the 'mirror principle': when a region within a burning shell contracts, then the region outside the shell expands, and vice versa. This is not a physical law and a convincing explanation of this behaviour has not been found (see Aerts, Christensen-Dalsgaard & Kurtz 2010, page 176 and references therein). A simplified explanation is as follows: a basic relation between gravity and internal pressure is called the virial theorem, as introduced in Section 1.1.1. Furthermore, the total energy is the sum of gravitational potential energy, internal energy, and kinetic energy due to bulk motion in the gas. However, during HE the kinetic energy is zero by definition. Therefore, the total internal energy of a star is equal to minus 1/2 times the total gravitational potential energy. If

the total energy remains constant and the virial theorem remains constant, which is correct on thermal time scales, than both internal and gravitational energy are conserved. Therefore, if the star contracts in a region, it has to expand in another region. And when the temperature in the core increases, the envelope has to cool for the internal energy to remain conserved. At lower temperatures opacities are large, which leads to convection being the preferred energy transport instead of radiation, thus the expanding and cooling envelope now becomes convective. The star has now reached point D in Fig. 1.2, which is the start of the red giant branch (RGB). From point C to point D also the luminosity of the star decreases, as the energy generation from the H-shell is absorbed by the envelope expansion instead of being radiated from the surface.

From point D to E the core continues to contract, the envelope continues to expand and convection continues to reach further down in the star. The expansion of the envelope would result in a decrease of effective temperature, but the convective motions reaches now deeper into the star, where the temperature is higher. The mixing of the cooler surface layers and the deeper and hotter layers balances out the cooling due to expansion and the effective temperature remains nearly constant between point D and E. The expansion of the envelope does not absorb the full amount of energy generated by the H-shell anymore, as convection is a more efficient method of energy transportation than radiation. The excess energy causes the luminosity to increase. When point E is reached, the convective region has reached into the region where H-shell burning ashes are located. This material is now mixed by convection and reaches the surface of the star. This process, transporting material from central regions of the star to the surface, is called *dredge-up* and this event is the *first dredge-up*. The material that is mixed up to the surface by the first dredge-up is enriched with products from partial H burning including ^{4}He, ^{13}C, and ^{14}N (Boothroyd & Sackmann 1999; Karakas & Lattanzio 2014).

The start of the core He burning phase is different for low- and intermediate-mass stars, as the low-mass stars have a degenerate He core and the intermediate-mass stars do not, with partial degeneracy linking the two mass regimes. The intermediate-mass stars ignite He in the core, when the core temperature is high enough. The low-mass stars have to lift the degeneracy first. The temperature and density in degenerate regions are

decoupled, which means that when the ignition of He starts, the energy released does not lead to expansion of the region, but instead stays as thermal energy, raising the temperature locally. This temperature increase speeds up the He burning rate, leading to a runaway reaction (He flash, introduced Section 1.1.1) until the degeneracy is lifted and a more quiescent He burning phase starts. The degree of degeneracy dictates the strength of the He flashes needed to lift the degeneracy of the whole core (Deupree 1984; Deupree & Wallace 1987). The core of the 2-$M_\odot$ star in Fig. 1.2 becomes partially degenerate. There is no off-centre He flash at the start of the core He burning phase, but instead the ignition starts in the centre. Due to the partial degeneracy of the core, the burning zone is as large as the whole He-rich core before settling on a more quiescent burning in the inner 0.15 $M_\odot$. The degeneracy in the core is completely lifted about halfway through the core He burning phase.

Since the H shell is still burning, the ashes make the He core grow with time. Therefore, the envelope contracts, heats up, which decreases the opacity and as a result the convective envelope recedes. This leads to the star moving back down to the base of the RGB phase in the HRD at point F. When the envelope is mostly radiative again, the star heats up more and starts burning He in its core, a moment known as the zero-age horizontal-branch (ZAHB) at point G in the HRD (the evolution of E-G is fast and therefore impossible to label correctly in the Kippenhahn diagram, therefore in this figure point G reflect the steady core He burning phase, and point F the start of it). There are no stable isotopes with a mass twice that of ^{4}He, hence another path has to be followed to produce heavier nuclei. At temperatures around 1.5 10^8 K, the triple-α reaction takes place:

$$^4\text{He} + {}^4\text{He} \rightarrow {}^8\text{Be} \tag{1.39}$$

$$^4\text{He} + {}^8\text{Be} \rightarrow {}^{12}\text{C} + 2\gamma \tag{1.40}$$

$$\tag{1.41}$$
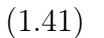
At a much lower rate than the triple-α reaction, this α process also takes place:

$$^{12}\text{C} + {}^4\text{He} \rightarrow {}^{16}\text{O} \tag{1.42}$$

making ^{12}C and ^{16}O the main components of the stellar core at the end of the core helium burning phase. For the next core burning phase higher core temperatures are needed, which are only reached in stars with a higher initial mass than those considered in this thesis.

In order to be able to transport the energy generated by core He burning, the core becomes convective again. Most of the energy needed to remain (close to) TE, comes from the H-shell allowing the He-core to slowly burn through the He. Hence the core He burning phase lasts about 250 Myr, which is 25 % of the main sequence lifetime (950 Myr) in this 2 M$_\odot$ star, as is shown in Fig. 1.2.

When the He in the core is depleted, the core contracts again and the envelope starts expanding again, therefore the stars moves to the right in the HRD (point H).

1.1.3   The AGB phase

At point H, the stellar structure is similar to the structure during the H-shell burning phase: the CO core is contracting and becoming degenerate again, while the envelope is expanding (due to the mirror principle) and becoming convective again. This is the early asymptotic giant branch (E-AGB) phase. The He-shell is now active and moving to higher mass coordinates, doubling the size of the core. The H-shell is barely active (and therefore the mirror principle is applicable and not the double mirror principle), and the He-shell approaches the mass coordinate of the H-shell. Here the He-shell is running out of fuel, as it is burning through He faster than the H-shell is creating it. This is the start of the thermally pulsing asymptotic giant branch (TP-AGB) phase at point J in Fig. 1.2. In Fig. 1.3 an overview of this region of an AGB star is shown. The He-rich region between the two shells (the intershell) is where recurrent He flashes (thermal pulses or TPs) take place, as thin-shell instabilities (as introduced in Section 1.1.1). The runaway reaction first leads to enhanced (partial) He burning, creating mainly ^{12}C via triple-α, then to the expansion and cooling of the region, which subsequently becomes convective (pulse-driven convective zone PDCZ) and mixes all chemical elements within the intershell region. The thermal pulses are visible in the HRD in Fig. 1.2 around point
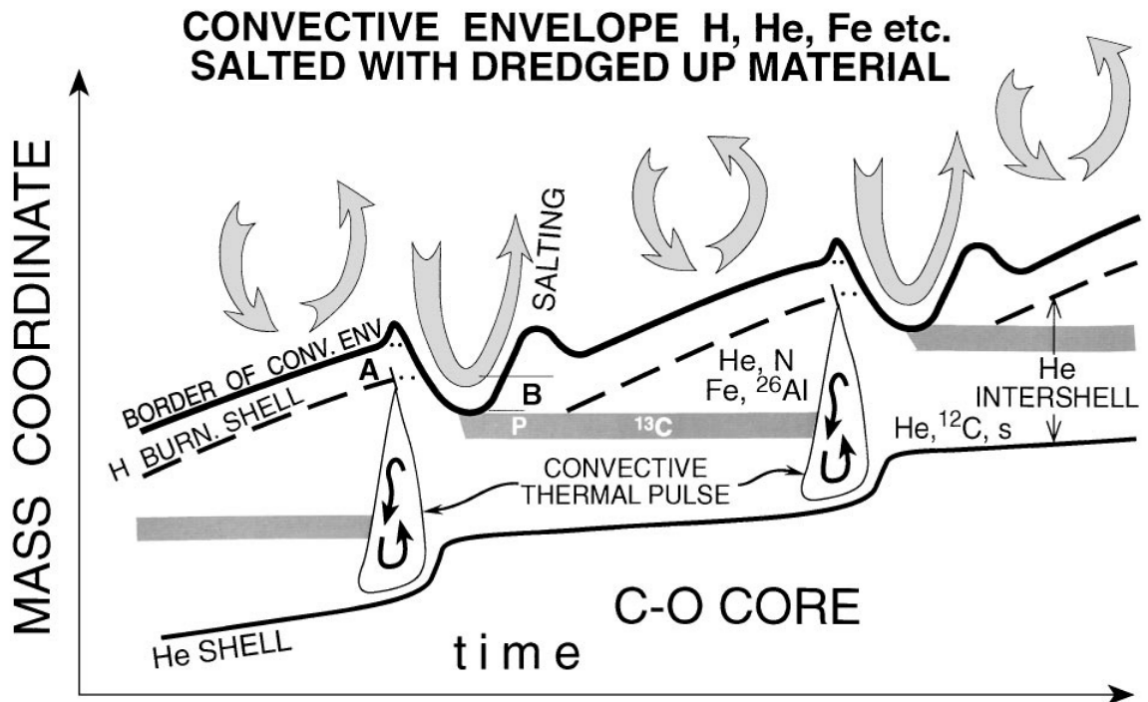
Figure 1.3: Schematic overview of the region between the CO core and the convective envelope in a TP-AGB. Please note that the time evolution is not to scale. The term 'salting' refers to the enrichment of the envelope by TDU events. From Busso, Gallino & Wasserburg (1999).

J, as the repetitive increased luminosity and reduced effective temperature features. After the runaway reaction, He shell burning is no longer unstable, and soon dies down which makes the pulse-driven convective zone disappear. The intershell has expanded due to the large energy production, and has become partly convective, connecting to the convective envelope. This merged convective region allows for intershell material to be dredged up (third dredge-up or TDU[2]) to the surface. An important consequence of the TDUs is the creation of carbon rich stars. At the start of the AGB phase, the surface C/O ratio is well below unity, but with each TDU event C from the C-rich intershell is mixed to the surface. When the surface C/O ratio exceeds unity, the star is called a C star (discovered by Fr. Angelo Secchi in the 1860, see McCarthy 1994). Observations of these C stars and in particular the carbon star luminosity function can be used to constrain the TP-AGB stellar evolutionary models and their TDUs (see e.g. Marigo, Bressan & Chiosi 1996; Marigo, Girardi & Bressan 1999; Stancliffe, Tout & Pols 2005, and others).

Within the H burning shell, proton capture reactions take place as before, but now also includes TDU material. ^{12}C is converted into ^{14}N which acts as the seed for many other elements. For instance, α-capture on ^{14}N leads to the production of the unstable ^{18}F. This isotope decays to ^{18}O, which captures another α-particle to create ^{22}Ne (Iben 1975). Within the intershell, through He burning, also ^{19}F can be created via ^{14}N$(\alpha,\gamma)^{18}$F$(\beta^+)^{18}$O$(p,\alpha)^{22}$Ne$(\alpha,\gamma)^{19}$F. Fluorine is an interesting element as its creation and destruction in stars are sensitive to physical conditions (see, e.g. Lucatello et al. 2011) thus providing strong constraints on stellar evolution models. Various astrophysical sites for the production of fluorine have been suggested (see, e.g. Goriely, Jorissen & Arnould 1989; Jorissen, Smith & Lambert 1992), but a discrepancy between observed and predicted abundances remained. Recently it was shown that the technique to derive the ^{19}F abundances from observation was prone to inconsistencies in the line data of the HF molecule, leading to differences in the F abundance of up to ~ 0.3 dex (see Jönsson et al. 2014a,b, 2017). AGB stars are assumed to be a significant production site, but also

---

[2]The second dredge-up does not occur in stars in the initial mass range discussed here and is therefore not included in this chapter

Wolf-Rayet stars (H-poor, hot massive stars) are mentioned as a possible contributor (see e.g. Stancliffe et al. 2005). This recent development concerning the observational values has inspired the AGB community to re-examine the fluorine production and trends in stellar evolution models (Abia et al. 2019). More light element nucleosynthesis takes places in AGB stars with a higher initial mass. For instance, proton capture chains lead to the creation of ^{23}Na from ^{20}Ne via consecutive proton captures and beta decays. A similar chain exists for the production of ^{27}Al from ^{24}Mg, via ^{27}Si. To produce ^{23}Na a temperature of about 20×10^6 K is needed, while the creation of ^{27}Al requires a temperature of 30×10^6 K (Arnould, Goriely & Jorissen 1999).

The TDU may also allow for H to be mixed into the intershell via convective boundary mixing (CBM), where it can be used to create ^{13}C. The ^{12}C present in the intershell and the H produces ^{13}C via ^{12}C(p,γ)^{13}N($\beta^+\nu$)^{13}C (see Iben & Renzini 1982b). As a consequence a ^{13}C-rich layer or '^{13}C pocket' (see Iben 1976; Iben & Renzini 1982a) forms, where neutrons are released via radiative burning ^{13}C(α,n)^{16}O (Straniero et al. 1995) that can be used via the slow neutron capture process (s process) to create elements heavier than Fe (Gallino et al. 1998).

The details of how the ^{13}C-pocket is formed are still not fully understood. It is clear however that the amount of ^{13}C formed in the ashes of the H-shell is too low and another process must be active to produce enough ^{13}C for a significant s process to occur (Gallino et al. 1998). Several mechanisms have been proposed, but there is no consensus on which process is the dominant one. In this thesis convective boundary mixing (CBM or convective overshoot) is used as a depth dependent diffusion coefficient (Herwig 2000; Cristallo et al. 2009, 2011). This process is able to transport H from the envelope to the intershell (Freytag, Ludwig & Steffen 1996). This treatment was recently extended to include the effect of mixing H into the intershell by gravity waves (see Denissenkov & Tout 2003; Battino et al. 2016, and Section 1.3 for more information on gravity waves). Convection and semi-convection have also been suggested to allow for H to be mixed into the intershell (Hollowell & Icko 1988). The differences in the numerics concerning the implementation the convective criterion explains why some codes need CBM to create TDU events and others do not (Mowlavi 1999; Pols & Tout 2001; Stancliffe, Izzard & Tout

2004). Rotationally induced mixing has also been suggested to mix H into the intershell by Langer et al. (1999). Their rotating models were analysed in more detail by Herwig, Langer & Lugaro (2003), who found that the ^{13}C-pocket created via rotationally induced mixing did not have enough mass to achieve the s-process abundances as observed in AGB stars. Herwig, Langer & Lugaro (2003) also found that in a 3-$M_\odot$ star of solar metallicity rotating with an initial rotational velocity of 250 km s^{-1}, the rotational mixing reduces the number of neutrons available for the s process (as confirmed by Siess, Goriely & Langer 2004). The reduction is caused by the extra mixing of the neutron poison ^{14}N produced by ^{13}C(p,γ)^{14}N (Wallner et al. 2016) into the ^{13}C pocket. This mixing takes place during the interpulse phase and after an initial ^{13}C had formed from the assumed convective boundary mixing expressed in the exponential diffusion model. Consequently, rotation alone did not lead to significant s-process production in AGB models.

The possibility of creating a ^{13}C-pocket by magnetic buoyancy was proposed by Nucci & Busso (2014). These authors derive, based on 2D and 3D simulations, an expression for magneto-hydrodynamical mixing processes at the base of the convective envelope in evolved stars. The ensuing mixing of H into the intershell during the TDU, allows the creation of a significant ^{13}C-pocket (Trippella et al. 2016).

Due to the many uncertainties around the formation of the ^{13}C-pocket and the lack of consensus on which process is responsible for the formation of the pocket, another commonly used option to create the ^{13}C is to simply add the H during the post-processing calculation. This artificial method includes parameters that alter the shape and mass extent of the ^{13}C-pocket, which results in reasonable fits to the observed s-process abundances (Gallino et al. 1998; Bisterzo et al. 2010; Goriely & Mowlavi 2000; Lugaro et al. 2012; Buntain et al. 2017).

The s process refers to the slow neutron capture process on iron-group elements (Burbidge et al. 1957; Cameron 1957; Wallerstein et al. 1997; Käppeler et al. 2011). Successive neutron captures and β-decays lead to the creation of heavier elements. The s process can produce elements from iron seeds (Fe, Z=26) via strontium (Sr, Z=38), barium (Ba, Z=56) all the way up to lead (Pb, Z=82) (Gallino et al. 1998). Fig. 1.4 shows the solar abundances broken down into different components. Peaks are visible around Sr
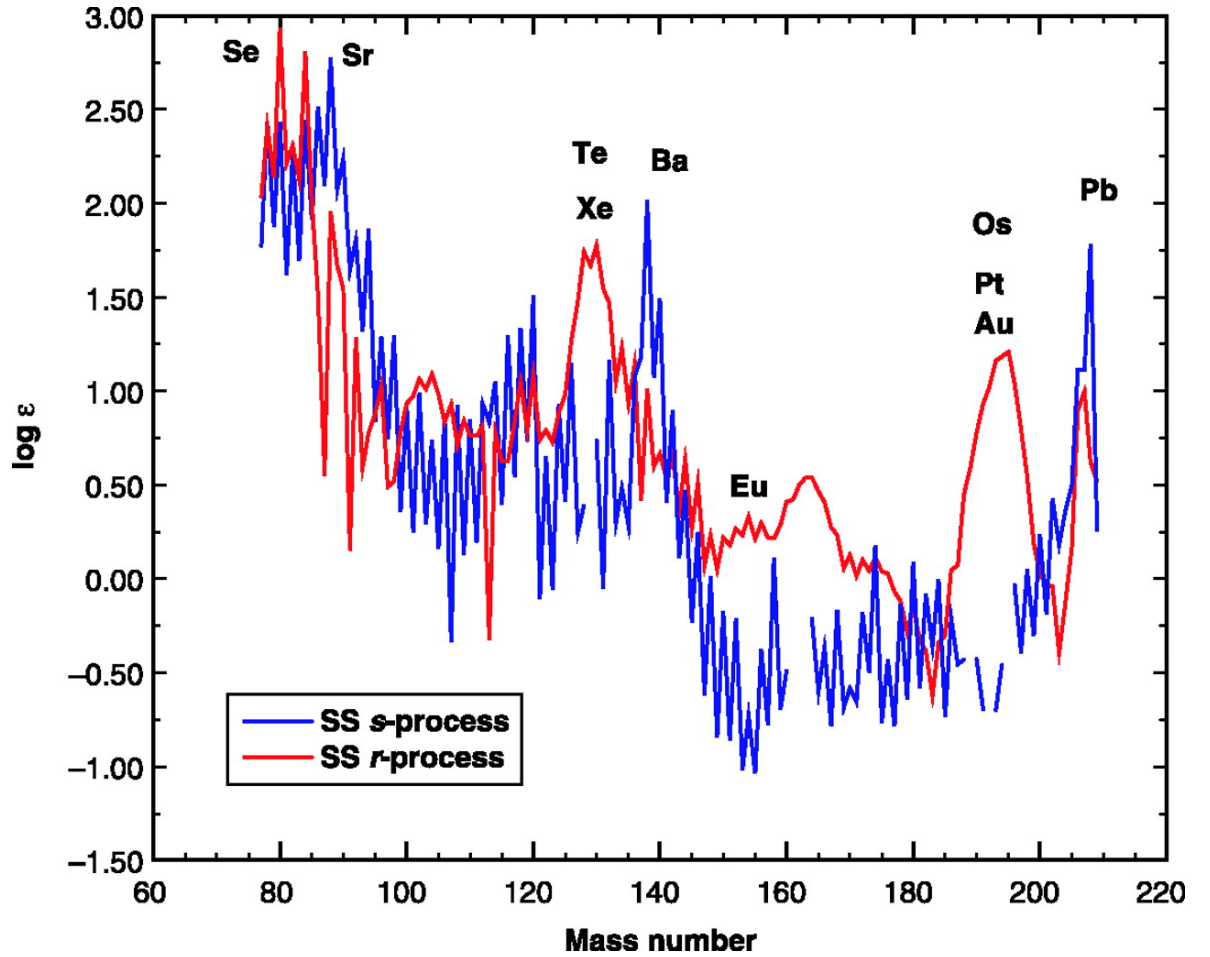
Figure 1.4: The solar system abundances broken down into s- and r-process components. The peaks in strontium, barium, and lead correspond to the three s-process peaks. Figure from Sneden (2003).

(including rubidium, yttrium and zirconium, generally referred to as the first s-process peak or light s-process (ls) elements), Ba (including lanthanum, cerium, neodymium, and samarium, generally referred to as the second s-process peak or heavy s-process (hs) elements), and Pb (the third s-process peak at Z=82). These isotopes have in common that they have a magic number of neutrons (n=50, 82, 126), meaning the neutrons within the atomic nucleus fill a complete shell at those numbers. These nuclei have very low neutron capture cross sections compared to the other elements, and therefore act as bottlenecks along the s-process path. The isotopes are thus visible as peaks in the composition shown in Fig. 1.4, as the s-process peaks.

The reaction path of the s process remains close to the valley of β stability in the nuclear chart as the neutron-capture time scales of the involved isotopes are long compared to β-decay time scales, hence the name 'slow' neutron capture[3]. The s process follows this general sequence of reactions:

$$(Z, A) + n \rightarrow (Z, A+1) + \gamma \tag{1.43}$$

$$(Z, A+1) \rightarrow (Z+1, A+1) + e^- + \nu_e \tag{1.44}$$
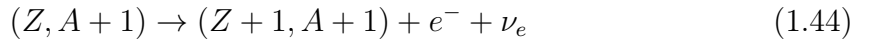
where Z is the number of protons and A the atomic weight, the sum of all protons and neutrons. The first reaction is the neutron capture reaction, the second is the β-decay reaction, see Fig. 1.5 for a section of the s-process path.

For some isotopes both reactions can take place with comparable probability. These isotopes are called branching points, where both neutron capture and β-decay are possible depending on the exact conditions. Branching points are an important feature of the s-process, visible in Fig. 1.5, as these points allow for the creation of different isotopes that are not on the main path of the s-process. These branching points are characterized by the neutron capture time scale and the β-decay time scale of an isotope having the same order of magnitude. The local neutron density then defines which path on the branching point is preferred. The analysis of observed branching point abundances thus

---

[3]The other main neutron capture process is called the rapid neutron capture process, or r process,
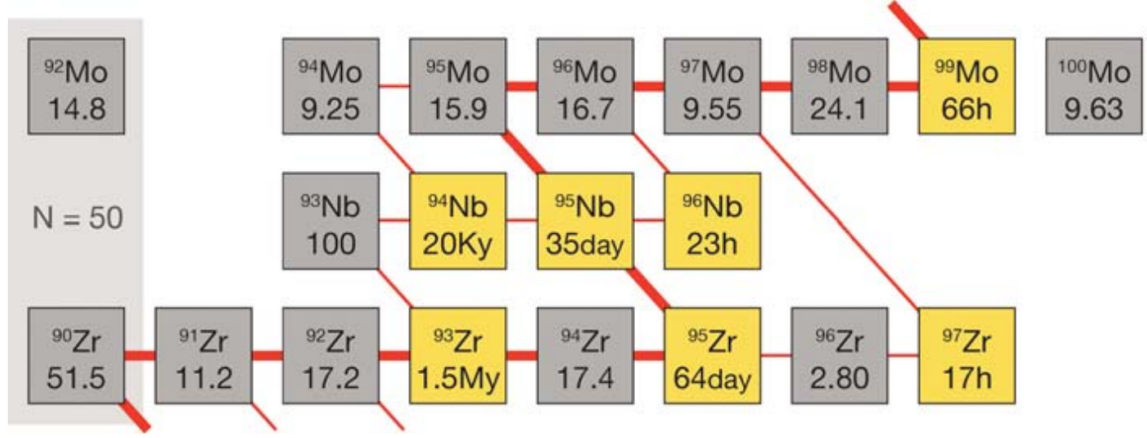
Figure 1.5: Detail of the chart of nuclide, showing the s-process path (thick red line), with extra paths going through the branching points (thin red line). The neutron number increases along the horizontal axis, and the proton number along the vertical axis. The unstable nuclides are in yellow, with their half-life as additional number in the box. The stable nuclides are in grey, with their isotopic abundance fraction. From Herwig (2005).

allows for the determination of the conditions during s-process nucleosynthesis. The quantity that determines the relative abundances of the first, second, and third s-process peaks during the s-process is the neutron exposure, i.e. the integrated neutron flux:

$$\tau = \int v_\mathrm{T} N_\mathrm{n} dt \tag{1.45}$$

where v_T is the thermal neutron velocity and N_n the neutron density. The neutron exposure and density depend on the conditions of the production site in which the neutron source is activated.

Two distinct astrophysical production sites for s-process nucleosynthesis have been identified: massive stars during core He and C shell burning, which typically produce the so-called *weak* component (up to Sr), and low/intermediate mass stars during the AGB phase, which typically produce the so-called *main* and *strong* component of the s process

(up to Pb). The s-process isotopes between Fe and Sr are created in massive stars with the reaction:

$$^{22}\text{Ne} + \alpha \rightarrow {}^{25}\text{Mg} + n \tag{1.46}$$

as neutron source, activated at temperatures around 3×10^8 during the core He burning phase and around 10^9 K during the C shell burning. Neutron densities of 10^6-10^7 cm^{-3} in the core He burning phase and 10^{12} cm^{-3} in the C shell are reached (Pignatari et al. 2010; Käppeler et al. 2011), and neutron exposures of 0.2 and 0.01 mbarn^{-1} respectively. This process is unable to produce nuclides further up the s-process path than Sr, as there are many neutron poisons (elements with large neutron absorption cross-sections) available that act like neutron sinks. Only a fraction of the neutrons released are captured by iron-group elements (see e.g. Pignatari et al. 2010). At lower metallicities, and when including fast rotation, the s process in massive stars is able to reach further along the s-process path, however there is no consensus on whether Pb can be produced (Frischknecht et al. 2016; Chieffi & Limongi 2017; Choplin et al. 2018).

During the TP-AGB phase, the main and strong components of the s process create elements up to Pb (Gallino et al. 1998; Arlandini et al. 1999). There are two location within an AGB star where s process can take place, the convective PDCZ and the radiative intershell. The second is the main location for s-process production in the majority of AGB stars. The neutron source

$$^{13}\text{C} + \alpha \rightarrow {}^{16}\text{O} + n \tag{1.47}$$

is activated at a temperature around 10^8K, releasing neutrons at a neutron density of around 10^7 cm^{-3} with neutron exposures of around 0.1-2 mbarn^{-1} on a timescale of around 10^4 years.

The PDCZ, however, only lasts a few years. Here neutron densities up to 10^{11} cm^{-3} are reached, with neutron exposures around 10^{-2} mbarn^{-1}. The effect of this neutron source is thus small on the overall s-process production, but at branching points different paths

---

and captures neutron in shorter time scales than the β-decay time. This process thus follows a different path through the chart of nuclei, see Thielemann et al. (2011) for an overview.

are activated than in the ^{13}C-pocket, thus affecting the isotopic abundances involved in the branching points (Busso, Gallino & Wasserburg 1999; Lugaro et al. 2003).

Tthe products of the nucleosynthesis (most importantly C and the s-process products) are brought to the stellar surface by third dredge-up events (TDUs). TDUs occur when the envelope expands and thus cools following the runaway reaction and the TP, allowing for the region that is unstable against convection to reach further down into the star. During the TP-AGB phase, TDUs can occur after each TP. The TDU efficiency has been defined as:

$$\lambda_{\mathrm{TDU}} = \frac{\Delta M_{\mathrm{TDU}}}{\Delta M_{\mathrm{H}}} \tag{1.48}$$

where ΔM_{TDU} is the decrease in mass of the hydrogen exhausted core due to the TDU mixing H into the intershell and ΔM_{H} is the increase of mass in the H exhausted core by H burning during the whole previous interpulse period (see, e.g. Frost & Lattanzio 1996; Mowlavi 1999). Different stellar evolution codes give different values and trends for this TP-AGB parameter. In Fig. 1.6 the λ_{TDU} evolution versus core mass in 3 $M_{\odot}$, Z=0.02 models is shown, comparing the results of five different AGB studies (Straniero et al. 1997; Herwig 2000; Stancliffe, Tout & Pols 2005; Karakas & Lattanzio 2007; Cristallo et al. 2011). For these studies different codes or different versions of the same codes were used, which means the input physics between the models differ and the comparison is not straightforward. However, differences in key quantities that influence the TDU events can still be compared. For instance, the results by Cristallo et al. (2011, labelled as 'FRUITY') and Straniero et al. (1997, labelled as 'Stra97') are calculated with the same code, but using different settings for the mixing through the convective boundary of the envelope into the radiative zone below it. The inclusion of this extra mixing in the model by Cristallo et al. (2011) has led to the TDU events to occur at an earlier point in the AGB evolution (as the first TDU happened at a lower core mass) than in the model of Straniero et al. (1997). Also, the maximum value for the dredge up efficiency is higher in the model by Cristallo et al. (2011) due to this extra mixing. Further differences between these models are due to differences in the mass loss rates, as

the TDU efficiency depends on the envelope mass: λ_{TDU} decreases or remains constant when the envelope mass substantially decreases. The differences between the mass loss rates are also the main reasons for the differences between the models of Cristallo et al. (2011) and Stancliffe, Tout & Pols (2005, labelled as 'Sta04'), as the latter is calculated without mass loss. The envelope mass thus does not substantially decrease, and the λ_{TDU} can continue to increase unlike in the model by Cristallo et al. (2011). The model by Karakas & Lattanzio (2007, labelled as 'K07') is calculated with a milder mass loss rate than the model by Straniero et al. (1997), hence reaching higher λ_{TDU} values than the model by Straniero et al. (1997). The most efficient TDUs occur in the model by Herwig (2000, labelled as 'He00'), while their mass loss rate is moderate compared to Karakas & Lattanzio (2007). However, Herwig (2000) uses the strongest mixing through the convective boundary below the envelope and thus enhancing the λ_{TDU} (see Herwig 2000, for a detailed discussion on this effect).

In general, λ_{TDU} increases with core and envelope mass, and decreases with metallicity (Karakas, Lattanzio & Pols 2002; Cristallo et al. 2011). Convection prescriptions influence the TDUs, with a larger mixing length predicting larger λ_{TDU} (Boothroyd & Sackmann 1988). The choice of the criterion for convection and its implementation also influence the occurrence and the efficiency of TDUs (Mowlavi 1999; Pols & Tout 2001).

1.1.4 Evolutionary phases after the AGB phase

The TP-AGB phase is also characterized by mass-loss, which leads to the enrichment of the interstellar medium in s-process elements. This mass loss is thought to be driven by large stellar pulsations, which in turn create the right conditions for dust formation in the outer layers of the atmosphere of the star. The dust particles can easily be accelerated leading to a large outflow (Höfner & Olofsson 2018), and lead to the removal of the envelope. During the final phase of the TP-AGB, the mass loss rate can reach values of 10^{-7}-10^{-4} M$_\odot$ year^{-1}. Afterwards, in the post-AGB phase (first observed by Westbrook et al. 1975, and point K in the HRD of Fig. 1.2) the envelope moves away from the
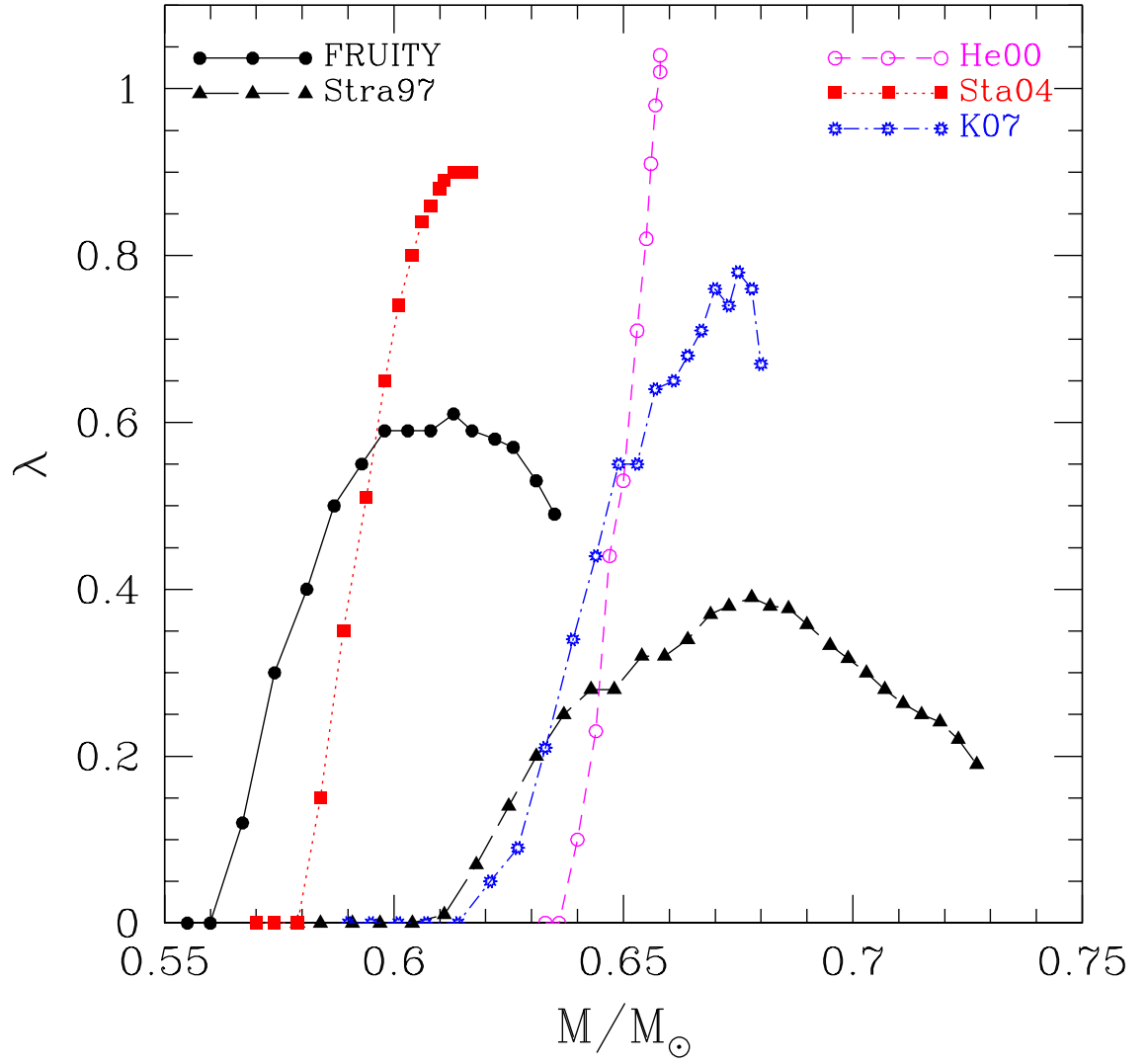
Figure 1.6: Comparison of the λ_{TDU} evolution versus core mass for 3 M$_\odot$, Z=0.02 AGB models from Cristallo et al. (2011); Straniero et al. (1997); Herwig (2000); Stancliffe, Tout & Pols (2005); Karakas & Lattanzio (2007), labelled as FRUITY, Sta97, He00, Sta04, K07 respectively. Figure from Cristallo et al. (2011).

central star and the central star ionizes the ejecta and forms a planetary nebula (first discovered by Charles Messier in 1764, see Chapter 1 of Kwok 2000, for a full historical overview, and point L in the HRD of Fig. 1.2). During the post-AGB phase, the star consists of a CO degenerate core, the intershell, and the small remaining H-rich envelope. The material removed by winds is moving further away from the star, exposing the remaining object, while the H- and He-shells can still be active and keep the luminosity constant. When the H and He shells become extinct, the remaining carbon oxygen white dwarf evolves along the cooling track (point M in the HRD of Fig. 1.2).

1.2   Observational evidence of the s process in low-mass AGB stars

The s-process production in rotating AGB stellar evolution models is presented in this thesis, and therefore in this section the focus is on the observational evidence that the s-process takes place during the TP-AGB phase. I present the various observational sites for s-process elements, and the newest results on the understanding of the spread in s-process observations.

Most determinations of s-process abundances come from spectroscopic observations, as absorption and emission lines at specific wavelengths hold information on the chemical composition of the star. Technetium (^{99}Tc) can be found in AGB stellar spectra and can be used as a tracer for the s process taking place, because it is formed by the s process and it is unstable. The half-life of ^{99}Tc is 2×10^5 years, which makes it a very sensitive indicator of s-process and third dredge-ups (Merrill 1952; Cosner & Truran 1981; Little, Little-Marenin & Bauer 1987). Its discovery in AGB spectra was a major breakthrough as it is a sign of ongoing s-process nucleosynthesis. The presence of Tc thus indicates that the star is an 'intrinsic' s-process star, meaning s-process elements are produced in the star. 'Extrinsic' s-process stars have instead received the s-process elements by mass transfer within a binary system.

S-process elements around the first and second s-process peaks have been observed for a

large sample of AGB stars, at different metallicities, see e.g. Lambert (1985); Smith & Lambert (1990); Plez, Smith & Lambert (1993); Abia et al. (2002). The s-process production of an AGB star can also be observed in later evolutionary phases, such as post-AGB stars (see e.g. Reddy et al. 2002; Reyniers et al. 2004, 2007; van Aarle et al. 2013; De Smedt et al. 2014), and planetary nebulae (see e.g. Sterling, Dinerstein & Bowers 2002; Sharpee et al. 2007; Sterling et al. 2009; Otsuka & Tajitsu 2013). Furthermore, the intershell abundances of light elements like He, C and O can be observed directly in post-AGB H-deficient stars, and in planetary nebulae (see e.g. Werner & Herwig 2006; Werner, Rauch & Kepler 2014; Péquignot et al. 2000; Rodríguez & Delgado-Inglada 2011; Delgado-Inglada et al. 2015).

The above-mentioned observations are all from intrinsic s-process sites, while extrinsic s-process stars have been observed too, see e.g. Busso et al. (2001), and Sneden, Cowan & Gallino (2008). Also CEMP-s stars (carbon-enhanced metal-poor stars, see e.g. Aoki et al. 2000; Izzard et al. 2009; Abate et al. 2015; Hansen et al. 2016), which are the binary companions of metal poor AGB stars, show s-process nucleosynthesis in their spectra. Another example is Ba stars, (first defined by Bidelman & Keenan 1951), which are the binary companions of evolved AGB stars, and the metal-rich analogue of CEMP stars. The first major attempt at constraining s-process models to such a wealth of information was by Busso et al. (1995); Lambert et al. (1995); Busso et al. (2001). In these papers a spread of s-process nucleosynthesis was found in both the intrinsic and extrinsic s-process observations, and this spread remains one of the major questions concerning s-process nucleosynthesis in AGB stars. The observed spread could not be matched with predicted s-process nucleosynthesis, unless in stellar models the ^{13}C abundance in their standard ^{13}C-pocket was multiplied by a factor between $1/24$ and 2. This procedure is justified by the uncertainties surrounding the formation of the ^{13}C-pocket, and no further physical justification was given. Since then, the AGB community has worked towards understanding the physical origin behind this spread in s-process observations. The next step was to separate the large sample of observations and try to match each subset with theoretical predictions using population synthesis (Bonačić Marinović et al. 2007). In this paper, the observed spread per stellar type could be matched by using

multiplication factors for their ^{13}C-pocket in single digits instead of double digits as in Busso et al. (2001), however, a physical motivation for this multiplication factor was still missing. Therefore Cristallo et al. (2011) showed the comparison between the s-process nucleosynthesis resulting from their stellar evolution models without using the multiplication factor. Their results presented in Fig. 1.7 show the spread of predicted and the observed s-process [hs/ls], calculated in Cristallo et al. (2011) via (spectroscopic notation):

$$[ls/Fe] = ([Sr/Fe] + [Y/Fe] + [Zr/Fe])/3 \tag{1.49}$$

$$[hs/Fe] = ([Ba/Fe] + [La/Fe] + [Nd/Fe] + [Sm/Fe])/4 \tag{1.50}$$

$$\text{using } [a/b] = \log_{10}(a/b) - \log_{10}(a/b)_\odot \tag{1.51}$$

$$\text{and } [hs/ls] = [hs/Fe] - [ls/Fe] \tag{1.52}$$

The recent studies on understanding the observed s-process spread are focussed on the large data sets of one type of s-process observation with small error bars. I discuss here a study on Ba stars, and on stardust grains. de Castro et al. (2016) presented a spectroscopic study of 169 Ba stars. Cseh et al. (2018) improved the analysis of the error bars on s-process enrichment of these Ba stars and compared them to the s-process nucleosynthesis in AGB stellar evolution models, as shown in Fig. 1.8. The figure shows that the main trends in the spectroscopic data are matched by the non-rotating models, although outliers are present. Rotating AGB star models bu Piersanti, Cristallo & Straniero (2013) were also included in the comparison, but found to provide a worse match to the observed data set than the non-rotating models.

Another way to investigate s-process production in stars is analysing star dust. Meteorites carry individual stardust grains, believed to be formed directly from stellar material around stars and supernovae. A variety of grains have been discovered, among which carbon-rich grains including silicon carbide (SiC, see e.g. Bernatowicz et al. 1987) that can only be formed when C/O > 1[4]. These SiC grains have also been found to have

---

[4]From C/O > 0.7 onwards C-rich grains are formed, but only in small quantities until C/O=1 is reached. Then onward the environment favours the formation of C-rich grains over O-rich grains.
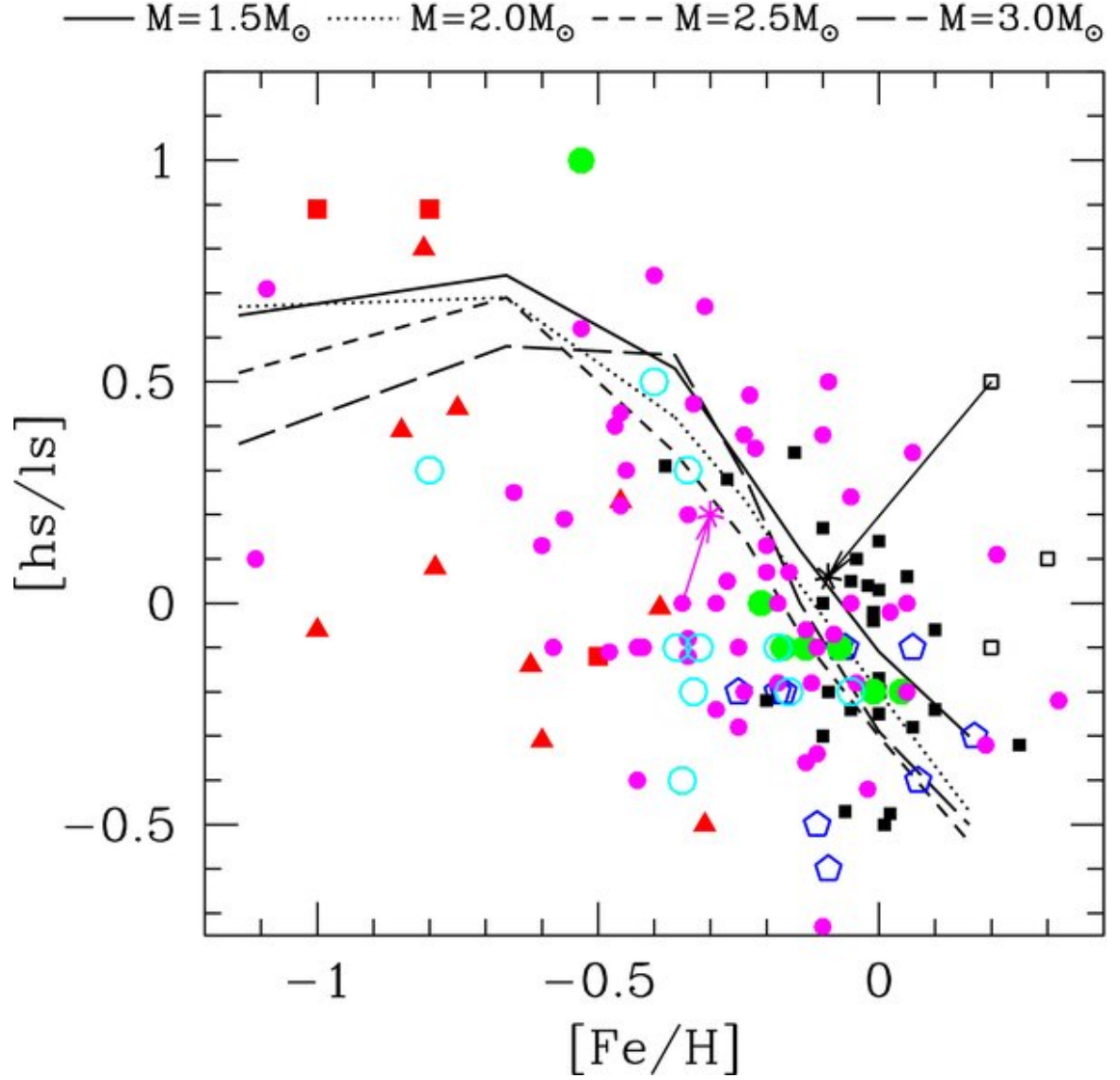
Figure 1.7: Comparison between observed and predicted spread in s-process nucleosynthesis, showing the spread over a range of metallicities. Different colour and symbol combinations are used to distinguish between different types of intrinsic and extrinsic s-process enriched stars, see Cristallo et al. (2011) for more details on the observations. An average spread of 1 dex is found in the observed values, while the predicted values show a spread of maximum 0.3 dex. Typical error bars are of the order of ±0.1 dex, while conservative evaluations suggest ±0.3 dex. Corrections to two observed values are also given. Figure from Cristallo et al. (2011).
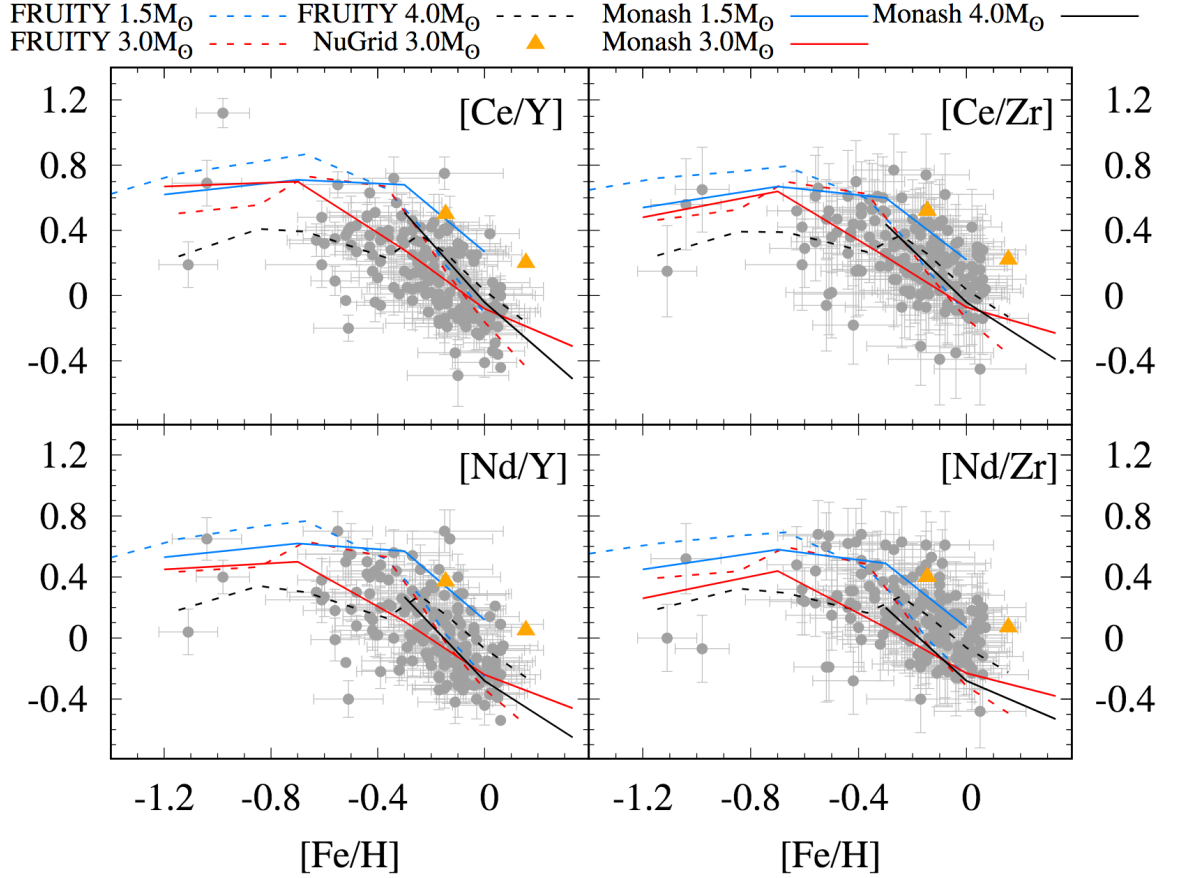
Figure 1.8: Comparison between Ba star observations of de Castro et al. (2016) with updated error bars from Cseh et al. (2018) and the predicted final surface composition for a selection of FRUITY (Cristallo et al. 2009, 2011; Cristallo et al. 2015) and Monash models (Lugaro et al. 2012; Fishlock, Karakas & Stancliffe 2014; Karakas & Lugaro 2016; Karakas et al. 2018), and the 3 $M_\odot$ models from Battino et al. (2016). The predictions match the main features of the element ratios from the observations, however, there are outliers outside of the range covered by the models. Figure from Cseh et al. (2018).

enhanced levels of the s-process only[5] isotopes ^{128}Xe and ^{130}Xe, provide strong evidence that low-mass, C-rich TP-AGB stars undergoing TDUs are the source of these grains (Hoppe & Ott 1997; Lugaro et al. 1999; Lewis, Amari & Anders 1990; Ott & Begemann 1990; Zinner, Amari & Lewis 1991). The isotopic ratios in these grains can be used to constrain AGB models.

Mass spectroscopy is the main tool that is used to analyse these grains, where the sample is ionized into ions, which are extracted from the sample. These ions are then sorted by their mass and charge via an electric and/or magnetic field, as ions of different masses will follow different trajectories in an electromagnetic field. Once the ions are sorted, they can be counted via an ion detector. The isotopic ratios of elements within the stardust grains can then be obtained and compared to stellar evolution models. These isotopic ratios are usually presented in parts per thousand (‰) with respect to solar values. For example, the ^{29}Si/^{28}Si ratio is expressed as:

$$\delta(^{29}\text{Si}/^{28}\text{Si}) = \left(\frac{(^{29}\text{Si}/^{28}\text{Si})_{\text{measured}}}{(^{29}\text{Si}/^{28}\text{Si})_{\text{solar}}} - 1 \right) \times 1000 \qquad (1.53)$$

Interesting comparisons can be made between models and grains, as some isotopic ratios are sensitive to the neutron exposure, like ^{88}Sr/^{86}Sr, while others are sensitive to the neutron density, like ^{96}Zr/^{94}Zr as discussed in Lugaro et al. (2014); Battino et al. (2016); Lugaro et al. (2018). The latter authors compare also super-solar metallicity AGB models to the pre-solar grain data, showing a better agreement than the solar metallicity models (Fig. 1.9). As for the Ba star comparison discussed before, the main features in the isotopic ratios are well matched by the models, proving that indeed the AGB stars are the likely source of the grains. However, there are again outliers present.

Therefore, both the Ba stars and the grain data show that the spread in s-process observations can be explained almost completely by s-process predictions. Outliers are visible in both comparisons though. To explain these outliers, extra mixing processes like rotation and magnetic fields have been mentioned (Herwig, Langer & Lugaro 2003; Battino et al. 2016; Cseh et al. 2018). A still highly debated question is what the effect

---

[5]These isotopes can only be formed by the s process due to their location on the nuclear chart.
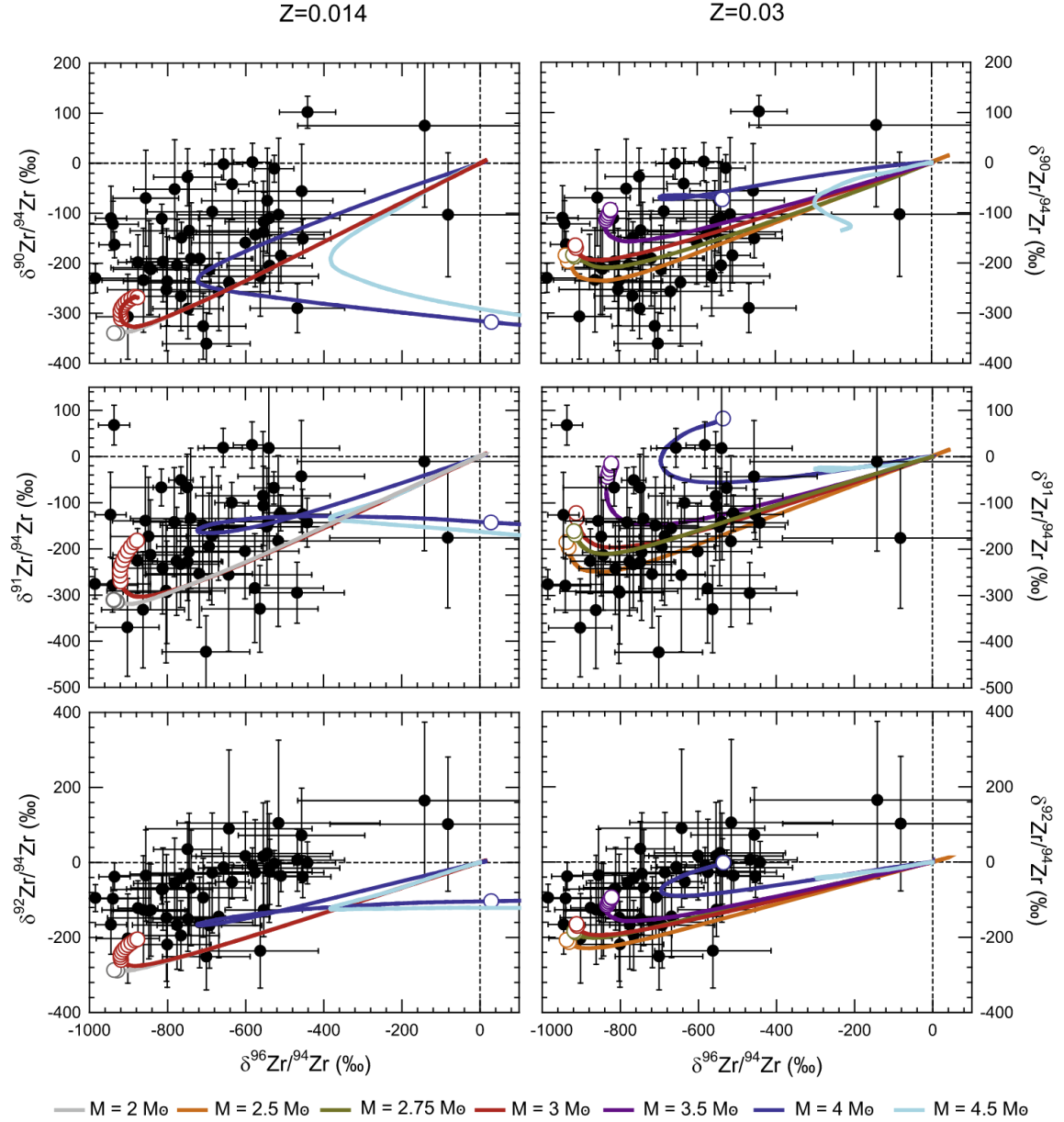
Figure 1.9: Comparison of Zr grain data (Liu et al. 2014) and the surface evolution of AGB models of solar metallicity (left panels) and twice-solar metallicity (right panels) of Monash models (Lugaro et al. 2018). The coloured lines represent the models with each open circle indicating a TDU when the envelope is C-rich. From Lugaro et al. (2018).

of rotation is on the s-process in AGB stars. This is a question I am addressing in this thesis.

1.3   Stellar rotation

This thesis focusses on rotating stellar evolution models and their comparison to observations of rotating stars. The fact that stars rotate can be explained by two principles: turbulence in the interstellar medium and conservation of angular momentum. Stars form from clouds of gas that collapse under their own gravity. The large-scale turbulence in these rotating clouds adds up to a non-zero total angular momentum, and the cloud thus rotates. The amount of angular momentum in each cloud varies greatly, but during its collapse the rotation rate of the cloud increases due to the conservation of angular momentum (Toomre 1964; Black & Bodenheimer 1975; Terebey, Shu & Cassen 1984; Yorke & Bodenheimer 1999). Since stars rotate, its effects on stellar evolution needs to be investigated.

A common way to measure surface rotation rates is via spectroscopy. The faster the star rotates, the wider the lines in the spectra due to the Doppler effect. Spectra of stellar populations have provided us with large data sets of surface rotation rates, see e.g. Huang, Gies & McSwain (2010). These authors show the results of using this method on the spectra of hundreds of very young stars (Fig. 1.10), and their results can be used to set the initial rotation rates in stellar evolution calculations. Fig. 1.10 shows the derived projected rotational velocity $V \sin(i)$ normalised by the derived critical rotational velocity V_{crit}. This critical velocity is the break-up velocity of a star, which is reached when the absolute values of the centrifugal and gravitational forces are equal. The histogram shows the derived values, with a polynomial fit through the data as a thin line. The deconvolution technique of Lucy (1974) is used to then derive the $V_{\mathrm{eq}}/V_{\mathrm{crit}}$ distribution, without the $\sin(i)$ dependence. This deconvoluted distribution is shown by the thick line in the panels of Fig. 1.10. The different panels show the rotational velocity distribution for three subcategories of very young B stars based on their mass, with the top panel

showing the least massive subcategory and the bottom panel the most massive ones. The statistics show that the least massive stars rotate faster (have an higher $V_{\mathrm{eq}}/V_{\mathrm{crit}}$ value), with the fraction of slow rotators (defined as $V_{\mathrm{crit}}/V_{\mathrm{crit}}$ smaller than 0.5) in the panels being 37%, 53%, and 84% from top to bottom panel respectively. Possible reasons given in Huang, Gies & McSwain (2010) for the slower rotational velocities in the more massive stars are mass loss and binary interaction.

Recently, information about the internal structure of stars has been determined via asteroseismic observations (Beck et al. 2011; Beck et al. 2012). Asteroseismology is the study of stellar oscillations. Internal vibrations caused by mechanisms described below can be measured as they cause subtle, rhythmic changes in the luminosity of the star (Cowen 2012). Due to their subtleness, these features can only be analysed if uninterrupted high-precision photometric (using the whole stellar spectrum without differentiating by wavelength) time-series data sets are available. The periods of the different rhythms can be converted into frequencies using Fourier transforms. These frequencies can be compared to predicted frequencies, calculated by assuming perturbations in the stellar evolutionary equations. Seismic modelling therefore is the study of finding a stellar evolutionary model whose frequency spectrum matches the observed spectrum (see Aerts, Christensen-Dalsgaard & Kurtz 2010, for more details).

Oscillating stars can be found all over the HRD, see Fig. 1.11. The Sun is the most studied pulsating star, see Leighton, Noyes & Simon (1962); Balmforth (1992) for the first discovery of the pulsations and Gizon, Birch & Spruit (2010) for a recent review on helioseismology. The mechanism that drives the pulsations in the Sun, is also present in other Solar-like stars (Fig. 1.11). These stars have a surface convective zones, and the speeds of the convective motion near the surface reaches values close to the speed of sound. This configuration is an efficient source of acoustic radiation, and thus creates oscillations caused by sound waves (see Houdek 2006; Chaplin & Miglio 2013, for overviews of this pulsation mechanism). Another pulsation mechanism is the κ-mechanism (first proposed by Eddington 1917), where κ stands for opacity. This pulsation mechanism takes place below the photosphere layer of the star, where He is ionised. When this layer is heated, the He atoms become doubly ionised (He atoms with no electrons left) which makes the
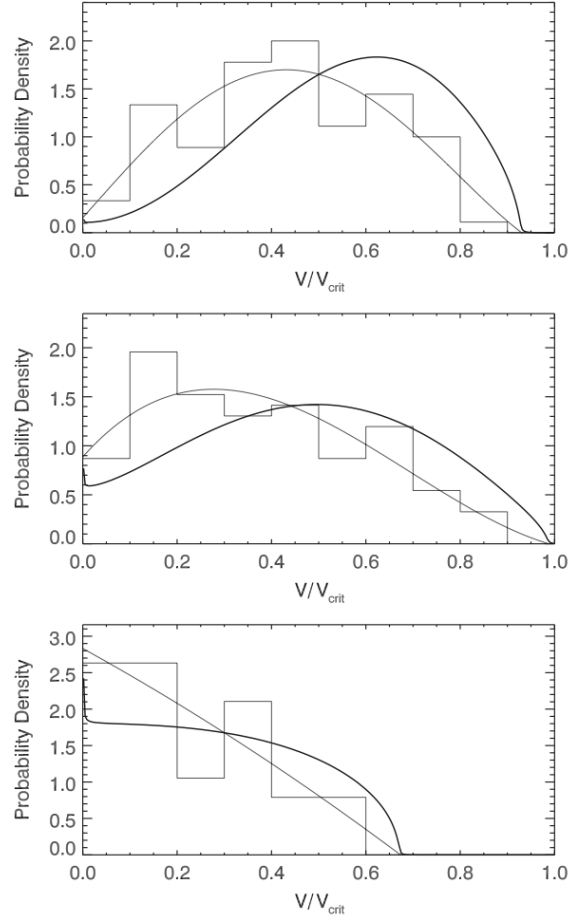
Figure 1.10: Rotational velocity distribution of three subcategories of the very young B star data set presented by Huang, Gies & McSwain (2010). From top to bottom are shown stars with $2 < M/M_\odot < 4$, $4 < M/M_\odot < 8$, and $8 < M/M_\odot$. The histograms are the $V\sin(i)/V_{\mathrm{crit}}$ values as obtained from observations, the thin solid line is the polynomial fit through the data. The $V_{\mathrm{eq}}/V_{\mathrm{crit}}$ distribution is plotted as thick solid line. See text for more details.

layer more opaque. The more He is doubly ionized, the less radiation escapes the layer. This will cause the star to expand, leading to the cooling of the doubly ionized He, and turn it into a once ionised He. This cools the star, and in turn this results in contraction of the outer layers, leading to the heating and thus ionization of the He layers again. The process will repeat itself periodically. For overviews on stars pulsating according to this mechanism, see Sandage & Tammann (2006) and Winget & Kepler (2008).

 Pulsations created by the κ-mechanism and the solar-like excitation mechanism resonate throughout the star. Depending on the location within the star, these pulsations drive pressure modes (p-modes) or gravity modes (g-modes). P-modes hold information about the envelope, while g-modes probe the inner part of the star. The detection of mixed modes (Beck et al. 2011; Beck et al. 2012) in data from the Kepler spacecraft (Borucki et al. 2010) as predicted by Dupret et al. (2009) has been a breakthrough, as mixed modes have p-mode characteristics in the envelope and g-mode characteristics in the core. The mixed modes are created when the frequencies of the p-modes and the g-modes overlap, due to the core contraction and envelope expansion during the red giant phase. As the frequencies of the modes are similar, the two modes couple and form a mixed mode. They carry information on the centre of the star (g-mode characteristic), and are observable at the surface (p-mode characteristic). These modes have allowed researchers to determine the rotation rate from the surface to the core. Internal rotation rates have now been obtained for stars on the main sequence, red giants (Solar-like oscillators), and DAV white dwarfs. Fig. 1.12 shows a recent overview of all 1210 known (on 01-08-2018) core rotation rates obtained from Kepler observations (see Mosser et al. 2012; Deheuvels et al. 2012, 2014, 2015; Kurtz et al. 2014; Beck et al. 2014; Beck et al. 2018; Aerts, Reeth & Tkachenko 2017; Hermes et al. 2017; Gehan et al. 2018, and references therein). The initial masses of these stars are between 0.72 and 7.9 $M_\odot$, with about half of the more massive stars in the sample being main sequence stars. For a small subsample of 45 stars both the core and envelope rotation rates are known. These stars are shown in the bottom panel of Fig. 1.12. The main sequence stars in this panel rotate uniformly, and stars belonging to the second clump (core He burning stars that did not undergo core He flashes) show small differential rotation. The H shell burning stars however do show
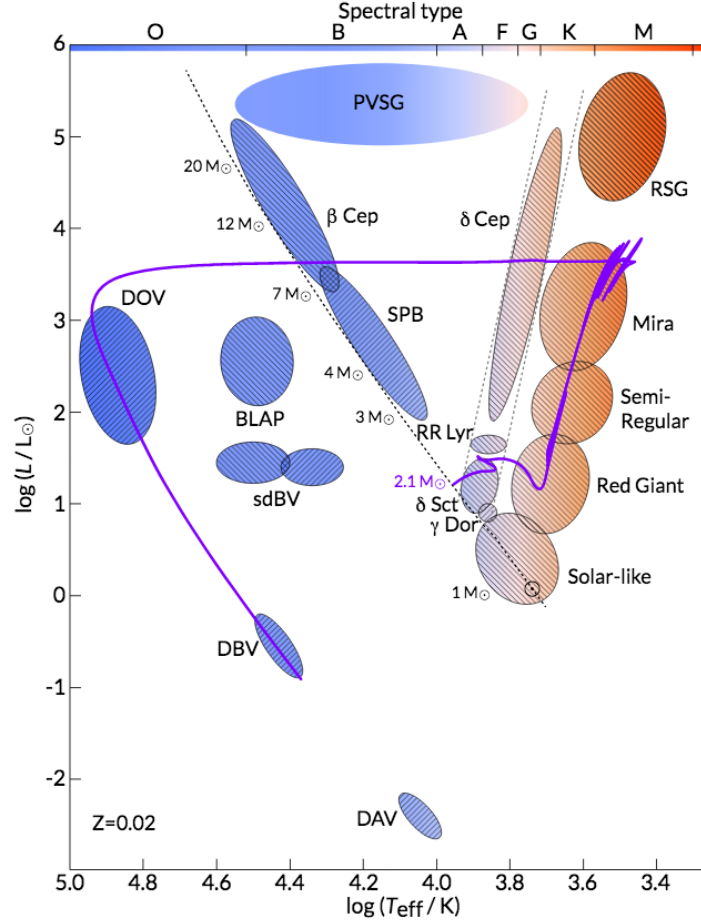
Figure 1.11: HRD showing the different types of pulsating stars. Along the main sequence (dashed line) pulsating stellar types are identified (for details see Aerts, Christensen-Dalsgaard & Kurtz 2010, and references therein) from low to high mass are listed Gamma Doradus variables ('γ Dor'), rapidly oscillating Ap stars ('roAo'), Delta Scuti variables ('δ Sct'), slowly pulsating B-type stars ('SPB') and Beta Canis Majoris stars ('β Cep'). Evolved pulsating stars can also be characterized in various types: along the 'instability strip' the region between the two long-dashed lines, almost completely filled with Cepheid variables ('Ceph') and RR Lyrae variables ('RR Lyr'). Next to these, the Red Giants, Semiregular variable stars ('SR') and the Mira variables ('Mira') can be found. During final evolutionary phases, stars pulsate as subdwarf or subluminous variable B stars ('sdBV') or along the white dwarf cooling track as variable dwarf with having only hydrogen in its spectrum ('DAV'), only helium ('DBV'), and a mixture of carbon, helium and oxygen ('DOV'). The solid line shows the evolutionary track for a 2.1 $M_\odot$ star. From Paxton et al. (2019).

stronger differential rotation.

One crucial topic in the study of stellar rotation is the fact that there is a discrepancy between the observed rotation rates and the ones from stellar evolution theory. This discrepancy suggests that there is a process missing from the models that is efficient in the transport of angular momentum from the core to the outer layers. Key evidence for this missing process is provided by the internal rotation of the Sun. Indeed, models that include only hydrodynamic transport processes predict a high degree of radial differential rotation in the solar radiative zone between 0.3-0.7 $R_{\odot}$ in disagreement with helioseismic measurements (e.g. Pinsonneault et al. 1989; Chaboyer, Demarque & Pinsonneault 1995; Eggenberger, Maeder & Meynet 2005). Further evidence for missing angular momentum transport in stars was provided by Suijs et al. (2008) who showed that stellar evolution codes predict core rotation rates at least an order of magnitude faster than white dwarf rotation rates. Then, Denissenkov et al. (2010) demonstrated the need for additional angular momentum transport when investigating the spin-down of solar-type open-cluster stars. These various lines of evidence for missing angular momentum transport have now been confirmed. Since 2012 crucial new information on the internal rotation profile of low-mass stars resulted from asteroseismology studies of observations provided by the Kepler spacecraft (Borucki et al. 2010; Aerts, Mathis & Rogers 2019). Stellar evolution codes have again been unable to match the observed low core rotation rates (see Fig. 1.13 and Eggenberger, Montalbán & Miglio 2012; Marques et al. 2013; Tayar & Pinsonneault 2013; Cantiello et al. 2014). In view of this mounting evidence that has accumulated over more than a decade, there is now consensus that a process of angular momentum transport is missing in the theory of rotating stellar evolution models.

There is no consensus yet however on the physical origin of this missing process. Broadly speaking there are three possibilities: hydrodynamical, wave-driven, or magnetic (Pinsonneault et al. 1989). The hydrodynamical processes are included in the implementation of rotation in stellar evolutionary codes, and consist of shear and large scale circulation processes. The magnetic process commonly used to study transport of angular momentum is the Tayler-Spruit (TS) dynamo (Spruit 1999, 2002), which has proven to be effective in coupling the core and envelope to increase the transport of angular momentum (see
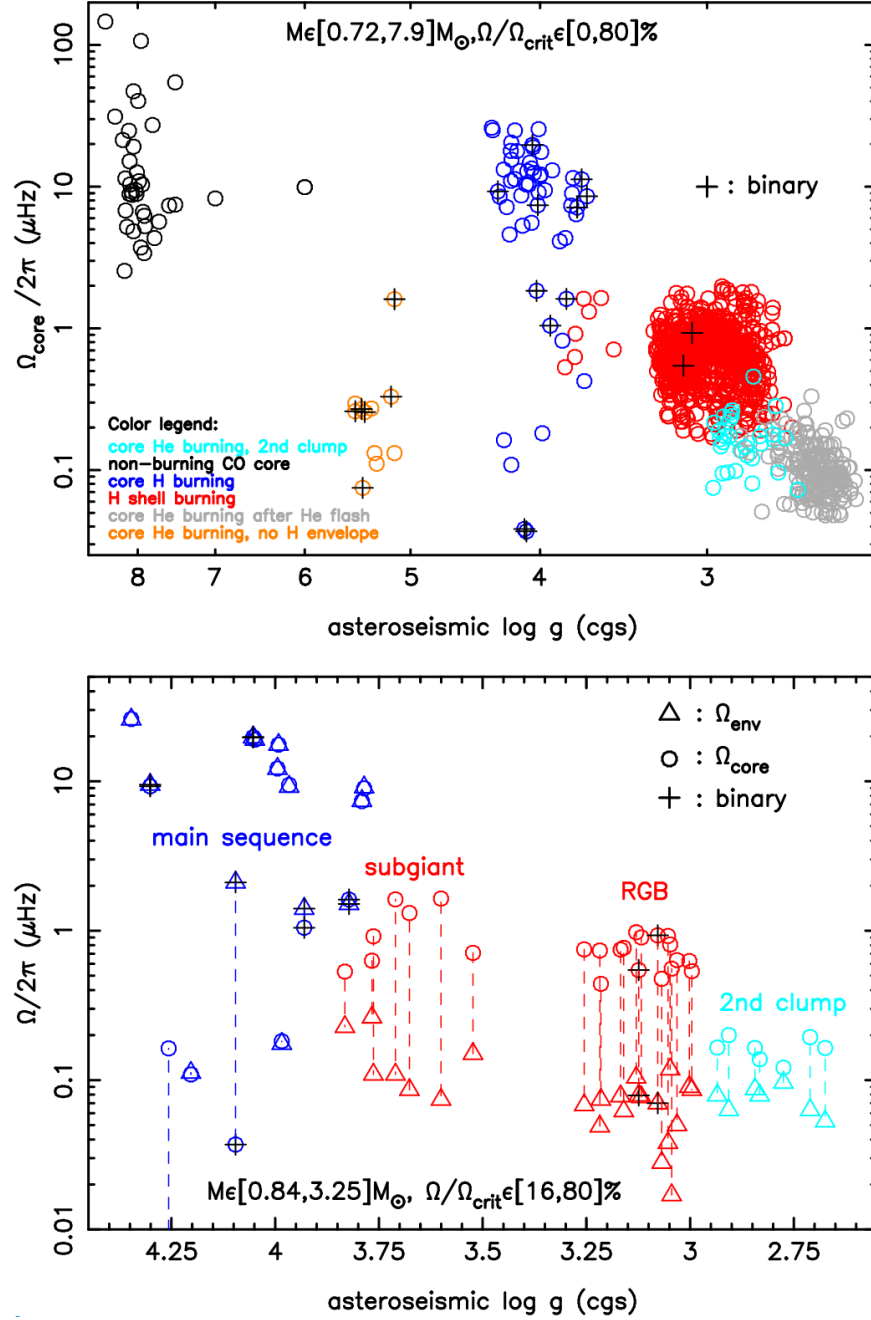
Figure 1.12: Overview of all known core rotation rates from the Kepler observations, colours indicate the stellar evolutionary phase. The top panel shows the 1210 stars for which only the core rotation rate has been determined, the bottom panel shows the 45 stars for which both rotation rates are known. From Aerts, Mathis & Rogers (2019).
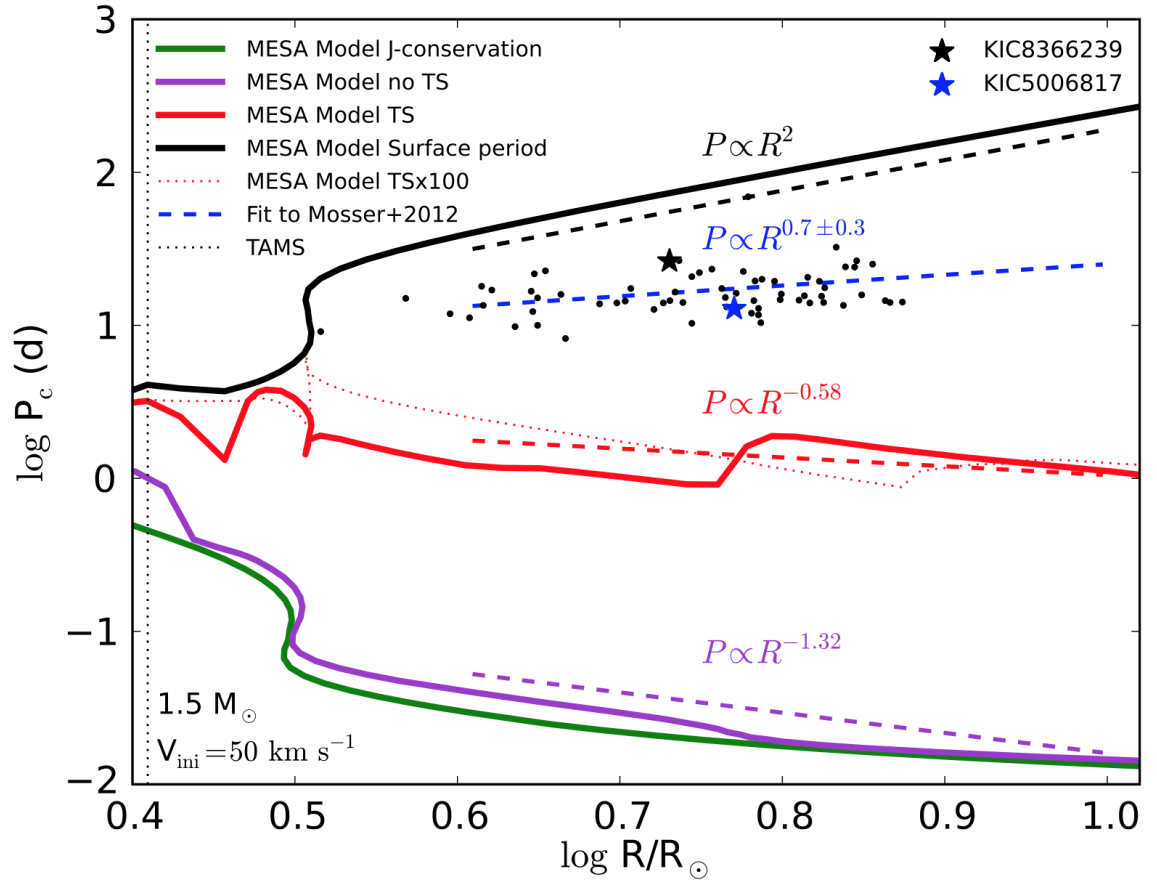
Figure 1.13: Log_{10} of period versus log_{10} of radius comparison between stellar evolution models with different assumptions of angular momentum transport and asteroseismic observations of the core rotation of red giants by Mosser et al. (2012). The calculated core rotation rates are too high compared to the observed values. Figure from Cantiello et al. (2014).

Eggenberger, Maeder & Meynet 2005; Suijs et al. 2008; Cantiello et al. 2014). However, the increased transport by this process alone is still not enough to match observed rotation rates (apart from the Sun). A recent study using different prescriptions for magnetized stellar winds reached the same conclusion, that more transport of angular momentum is needed (Tayar & Pinsonneault 2018). Recently a new derivation of the dynamo has been presented (Fuller, Piro & Jermyn 2019).

Angular momentum transport by internal gravity waves has been studied mainly in multi-D simulations (Fuller et al. 2014; Rogers 2015; Rogers & McElwaine 2017). While their results are promising, they struggle with translating its behaviour to a 1D parametrisation that can be included in 1D stellar evolutionary codes. Also, first efforts of estimating the effect of this mechanism show that also this process alone is insufficient (Pinçon et al. 2017).

For both magnetism and wave-driven processes much work needs to be done to understand and implement the related mechanisms. Therefore, constraints are required on its efficiency, so that its physical character can be revealed. This can be done by adding a constant called additional viscosity, ν_{add}, to the equation that described transport of angular momentum in stellar evolutionary codes (see Eggenberger, Montalbán & Miglio 2012; Eggenberger 2015; Eggenberger et al. 2017, 2019). While this additional viscosity has no physical meaning, its values can help us reveal information on the missing process. For instance, a result coming from those publications is that the efficiency of the missing process increases with increasing initial mass. The main goal of including ν_{add} in stellar evolution models is to collect enough information to find the physical origin of the missing process via reverse engineering.

1.4   Stellar evolution models

Our understanding of rotation and its impact on stellar evolution is still a major challenge in the study of stars. Pioneering work has been done by Kippenhahn & Thomas (1970), Endal & Sofia (1978) and Pinsonneault et al. (1989). For many years though, rotation

was not included in stellar evolution models, because including rotation means that the assumption of spherical symmetry in stars is no longer valid, resulting in more complicated equations to be solved. Stars, however, do rotate and a number of discrepancies between observations and models exist. Most of these discrepancies point towards the need for extra mixing in the models and adding rotation to the models would do exactly that. In Meynet & Maeder (1997), a list of these discrepancies is given, which can be summarized into abundance issues and issues with number ratios of stars with different spectral types or temperatures. Maeder & Meynet (2012) note that recent progress in astrophysical observations in high resolution spectroscopy and asteroseismology, among others, resulted in larger deviations from non-rotating models.

Interestingly, rotation is predicted to have an impact on the s-process in AGB stars as already mentioned in Section 1.1.3. In Herwig, Langer & Lugaro (2003) and Siess, Goriely & Langer (2004), rotation was found to prevent the s-process from taking place in AGB stars. Then, Piersanti, Cristallo & Straniero (2013, the FRUITY models) presented the first set of yields for rotating AGB stars. As in Herwig, Langer & Lugaro (2003), these authors found that adding rotation leads to extra mixing within the ^{13}C pocket. However, they found that rotation did not prevent the occurrence of the s process. Their models could produce a spread of s-process production patterns in AGB stars. An important difference between the FRUITY study and the earlier publications is that Piersanti, Cristallo & Straniero (2013) used lower initial rotation rates of 10, 30, 60, and 120 km s^{-1} and also varied efficiency parameters of rotationally induced mixing, hence reducing the amount of extra mixing due to rotation, and its consequences for the s-process production.

The effect of rotation on the s-process production in low-mass AGB stars has recently been inferred using observations of 169 Ba stars, which are binary stars that have experienced mass transfer during the AGB phase of the primary and therefore show s-process enrichment in their envelope (de Castro et al. 2016). Cseh et al. (2018) compared them to non-rotating and rotating models (see their Fig. 7), showing that the s-process production by non-rotating models provides a better match to the observed s-process enrichment than the rotating models by Piersanti, Cristallo & Straniero (2013). This

result provides another observational constraint on the s-process production in rotating low-mass stars.

1.5 Aims and motivations of this thesis

The unique aspect of this thesis is to combine both asteroseismic and nucleosynthesis observations to constrain stellar evolution in the 1.5-3 $M_\odot$ mass range. The aim of this work is to calculate rotating stellar evolution models, and to reproduce simultaneously the asteroseismic and nucleosynthesis observations.

The contents of this thesis are as follows: the stellar evolution theory of low-mass stars is presented in Chapter 2. In Chapter 3, I describe the methodology of the models presented in the result chapters. Chapter 4 is the first result chapter, in which I present the calibration of the artificial, additional viscosity for 2.5-$M_\odot$ stars, which is then used as input in Chapter 5. In this chapter I present the nucleosynthesis of rotating AGB models that have core rotation rates matching asteroseismic observations. Chapter 6 is a collection of exploratory studies. This thesis ends with a chapter on final remarks, including a summary, discussion, future work section. My publication record is listed after my conclusions. Appendices are added to show the derivations of some important equations, and the input files of my stellar evolution calculations.

2   Stellar evolution theory

This chapter gives an overview of stellar evolution theory. The various physical ingredients as well as the implementation of rotation are presented in detail.

2.1   Non-rotating stellar structure

Non-rotating, single stars without strong magnetic fields will only experience pressure and gravity forces, which are isotropic. Therefore, these stars are spherically symmetric and the equations describing them can therefore assume spherical symmetry. All quantities in stellar evolution are then constant on spheres, which means only one spatial variable is needed to describe them and only one dimension needs to be considered. The radius would be the obvious independent variable, but the mass, m, is chosen because compositional changes are easier to follow in the Lagrangian (mass) coordinates than in the Eulerian (radius) coordinates.

The full set of stellar structure equations is:

$$\text{mass conservation: } \frac{\partial r}{\partial m} = \frac{1}{4\pi r^2 \rho} \tag{2.1}$$

$$\text{hydrostatic equilibrium: } \frac{\partial P}{\partial m} = -\frac{Gm}{4\pi r^4} \tag{2.2}$$

$$\text{energy generation: } \frac{\partial l}{\partial m} = \epsilon_n - \epsilon_\nu - \frac{\partial u}{\partial t} + \frac{\delta}{\rho}\frac{\partial P}{\partial t} \tag{2.3}$$

$$\text{energy transport: } \frac{\partial \ln T}{\partial m} = -\frac{Gm}{4\pi r^4 P}\min\left[\nabla_{\text{MLT}}, \nabla_{\text{rad}}\right] \tag{2.4}$$

$$\text{with: } \nabla_{\text{MLT}} \text{ (see Section 2.2.3, in convective zones)} \tag{2.5}$$

$$\nabla_{\text{rad}} = \frac{3}{16\pi acG}\frac{\kappa l P}{mT^4} \text{ (in radiative zones)} \tag{2.6}$$

$$\delta = \frac{\chi_T}{\chi_P} = \frac{T(\partial P/\partial T)_{\rho,X_i}}{\rho(\partial P/\partial \rho)_{T,X_i}} \tag{2.7}$$

$$\text{chemical composition: } \frac{\partial X_i}{\partial t} = \left(\frac{\partial}{\partial m}\right)_t\left[(4\pi r^2\rho)^2 D_{\text{mix}}\left(\frac{\partial X_n}{\partial m}\right)_t\right] \tag{2.8}$$

$$+\frac{m_i}{\rho}\left(\Sigma_j r_{ji} - \Sigma_k r_{ik}\right)$$

with r being the radius, m the mass, ρ the density, P the pressure, G the gravitational constant, l the local luminosity, ϵ_n the nuclear energy produced per unit mass and per second, ϵ_ν the energy carried away by neutrinos per unit mass and per second, u the internal energy per unit mass, t the time, T the temperature, ∇ the temperature gradient with respect to pressure $\frac{d\ln T}{d\ln P}$, m_i the mass of element i, X_i the mass fraction of a certain nuclide i, the subscript t in some derivatives means time is kept constant while calculating the derivative, D_{mix} the diffusion coefficient of all mixing processes included in the calculation, and r_{ji} and r_{ik} the reaction rates creating and destroying element i, respectively (Kippenhahn & Thomas 1970).

The final equation needed to complete this set is the equation of state, which describes the microscopic properties of stellar matter, for a given density ρ, temperature T and composition X_i. This thermodynamic description of matter is usually expressed as the relation between the pressure and these quantities

$$P = P(\rho, T, X_i). \tag{2.9}$$

as introduced in Section 1.1.1. This expression is simple for a perfect gas which is totally ionised. When the gas becomes partially degenerate or ionised, the equation of state becomes much more complicated. As this computation is expensive and will therefore slow down stellar evolution codes, it is common in stellar evolution codes to get the thermodynamic properties of the matter from pre-calculated tables. The 2005 update of the OPAL EOS tables are used in this thesis, see Rogers, Swenson & Iglesias (1996) and Rogers & Nayfonov (2002), and can be found on `https://opalopacity.llnl.gov/EOS_2005/`. The same OPAL group has created opacity tables. These tables also have a CO enhanced option, which are needed for core He burning and further phases. These CO enhanced tables are used in calculations performed in this thesis. The OPAL tables are used within the temperature range of $\log_{10} T = 3.75$ to 8.7. Below this temperature range, the opacity tables of Ferguson et al. (2005) are used. These tables include the effect of molecules and grains on the opacity. Updates on these molecular opacities are already available in Marigo & Aringer (2009), who included updates on atomic and molecular absorption coefficients. The update also include full freedom in defining the chemical composition of the gas. However, comparison studies have shown that both molecular opacity tables are comparable in the stellar evolutionary calculations performed for this thesis (close to solar metallicity, 2 to 3 $M_\odot$), differences only occur at lower metallicities (see Ventura & Marigo 2010; Constantino et al. 2014; Fishlock, Karakas & Stancliffe 2014).

2.2 Convection and convective boundaries

The set of equations for stellar structure, see Eqs. 2.2-2.8, includes the equation for energy transport. As shown in this equation, there are two options for transport of energy: radiation and convection. Radiation always takes place, convection sets in when it is more efficient to transport energy than radiation. Transport of energy by radiation is done by repetitive absorption and emission of photons, creating a random motion of the photons. When a zone is convective, the material itself is unstable to vertical motion and patterns of rising and falling parcels develop.

2.2.1 Brunt-Väisälä frequency

The Brunt-Väisälä frequency is used in the criteria for convective instability and can be derived by considering a fluid element in a star at some level r_0, which is in pressure equilibrium with the surrounding medium. If this element is displaced vertically, in an adiabatic motion without viscous effects, its equation of motion is:

$$\varrho_{\text{int}} \frac{d^2 r}{dt^2} + g(\varrho_{\text{int}} - \varrho_{\text{ext}}) = 0 \tag{2.10}$$

with g being the gravity, and ϱ_{int} and ϱ_{ext} the interior and exterior density relative to the element. For a small displacement, $(r - r_0)$ a first order solution can be derived, being the equation of harmonic motions without damping. The solution is of the form:

$$(r - r_0) = A e^{iNt} \tag{2.11}$$

which yields:

$$-\varrho_{\text{int}} N^2 A e^{iNt} + g \left(\frac{d\varrho_{\text{int}}}{dr} - \frac{d\varrho_{\text{ext}}}{dr} \right) A e^{iNt} = 0 \tag{2.12}$$

with A being a constant. The oscillation frequency N, called the Brunt-Väisälä frequency, of a fluid element out of equilibrium position is given by:

$$N^2 = \frac{g}{\varrho_{\text{int}}} \left(\frac{d\varrho_{\text{int}}}{dr} - \frac{d\varrho_{\text{ext}}}{dr} \right) \tag{2.13}$$

$$\text{or, if } \Delta\varrho = \varrho_{\text{int}} - \varrho_{\text{ext}} \text{ then:} \tag{2.14}$$

$$N^2 = \frac{g}{\varrho} \frac{d(\Delta\varrho)}{dr} \tag{2.15}$$

These oscillations are also known as gravity waves since gravity is the restoring force. When N^2 is positive, the medium is stable against convection, while when N^2 is negative, it is unstable against convection.

Equation 2.15 can be expressed in terms of temperature gradients, as the density gradient can be written as:

$$\frac{1}{\rho} \frac{d(\Delta\rho)}{dr} = \delta \left(\frac{d\ln T_{\text{ext}}}{dr} - \frac{d\ln T_{\text{int}}}{dr} - \psi \frac{d\ln \mu_{\text{ext}}}{dr} \right) \tag{2.16}$$

where pressure terms are neglected as pressure equilibrium is assumed. Then, while using the definition for pressure scale height $H_P^{-1} \equiv -\frac{\text{dlnP}}{\text{dr}}$, which is the distance over which the pressure is changing by a factor e, the oscillation frequency N becomes:

$$N^2 = \frac{g\delta}{H_P}(\nabla_{int} - \nabla + \frac{\varphi}{\delta}\nabla_\mu) \tag{2.17}$$

with $\delta = -(\frac{\partial \ln \varrho}{\partial \ln T})_{P,\mu}$, $\varphi = (\frac{\partial \ln \varrho}{\partial \ln \mu})_{P,T}$, $\nabla_{int} = \frac{dlnT_{\text{int}}}{dlnP}$, $\nabla = \frac{dlnT_{\text{ext}}}{dlnP}$, and $\nabla_\mu = \frac{dln\mu_{\text{ext}}}{dlnP}$. The stability criterion then becomes:

$$\nabla < \nabla_{\text{int}} + \frac{\varphi}{\delta}\nabla_\mu \tag{2.18}$$

$$\text{or: } \nabla_{\text{rad}} < \nabla_{\text{ad}} + \frac{\varphi}{\delta}\nabla_\mu \tag{2.19}$$

which is known as the Ledoux criterion, with ∇_{ad} the adiabatic temperature gradient defined as $\frac{P}{T\rho c_p}$. By assuming a star is a chemically homogeneous medium, the last term is zero. The criterion is then known as the Schwarzschild criterion. According to this latter criterion, the dominant source for energy transportation becomes convection when the envelope is cool (leading to a higher opacity and thus higher ∇_{rad}), or when the ratio of l/m is high, for instance, in regions with a high energy flux (again leading to a higher ∇_{rad}). In Section 1.1 examples of both regions have been mentioned in the evolution of low-mass stars.

Deciding on which criterion should be used has been discussed extensively, mainly for massive stars (see Salaris & Cassisi 2017, for a recent review). The different criteria for convection create HRD tracks of massive stars that are either on the cool (red) side or the hot (blue) side at the point of core He ignition, which is unfortunately not enough to provide strong constraints on which criterion to use (Langer & Maeder 1995). For lower masses the effects are smaller. The main difference is that the core mass growth during the main-sequence and core He burning phase and thus its life time during these phases is smaller when the Ledoux criterion is used (Robertson & Faulkner 1972; Aguirre et al. 2011; Paxton et al. 2013; Salaris & Cassisi 2017).

Recently published results of 3D hydro studies indicate that the Schwarzschild criterion should be preferred over Ledoux (Arnett et al. 2019; Arnett et al. 2019).

2.2.2   Semiconvection and thermohaline mixing

Two other mixing processes are linked to convection: semiconvection and thermohaline mixing. Semiconvection is the name for the region that is stable according to the Ledoux criterion, but unstable according to the Schwarzschild criterion. Several descriptions to calculate the diffusion coefficient for semiconvection exist in modern stellar evolution codes (Langer, Fricker & Sugimoto 1983; Weaver, Zimmerman & Woosley 1978), however, semiconvection is only included when the Ledoux criterion is used.

Semiconvection occurs when an upwards displaced convective parcel is denser than the surrounding medium (follows from the Ledoux criterion), it is thus moved downwards by gravity (Kato 1966; Kippenhahn, Weigert & Weiss 2013). The parcel is also hotter than the surrounding medium (as it is unstable against Schwarzschild), thus it radiates into the surrounding medium, increasing the pressure of the medium and therefore increasing the density within the parcel. As a result, the parcel will move downwards faster, and its oscillation around the equilibrium become larger and larger. These oscillations are semiconvection. It is used in low-mass models, to account for mixing due to breathing pulses that occur at the end of the core He burning phase. These pulses are present when a small amount of He is added to the core that is mostly He-depleted. This He will enhance the energy production rate, and thus luminosity, resulting in an increase of ∇_{rad}. This increase leads to a short-lived growth of the core boundary, which is called a 'breathing pulse' (Eggleton 1972; Robertson & Faulkner 1972). Its existence is controversial as its unclear if it is a physical or numerical effect. Stellar evolution models that do not experience these pulses and thus the semiconvective mixing afterwards seem to better match observational data (Caputo et al. 1989; Cassisi, Salaris & Irwin 2003). A recent overview on the difficulties found when modelling the core He burning phase can be found in Salaris & Cassisi (2017).

∇_{μ} can be negative in some cases and thus increases outwards, due to binary interaction (Marks & Sarna 1998; Bitzaraki et al. 2004; Stancliffe & Glebbeek 2008; Wellstein, Langer & Braun 2001), accretion during the planetary formation (Vauclair 2004), or off-centre ignition of nuclear burning like the core He or C flashes (Thomas 1967; Siess 2009).

When ∇_μ is negative, the configuration of a parcel with higher μ in a layer with a lower μ is stable if the parcel is hot enough to have lower density. However, due to radiative losses, the temperature of the parcel reduces, the pressure inwards increases and thus the density increases. As a result, the parcel will sink resulting in efficient mixing. This is thermohaline convection[1]. It can be included in low mass stellar evolution models (up to an initial mass of 2 $M_\odot$), as it is assumed to operate during core He burning flashes, and at the base of the convective envelope at the start of the RGB phase (Eggleton, Dearborn & Lattanzio 2006; Charbonnel & Lagarde 2010; Angelou et al. 2012). Its influence is mainly on the surface abundances of, for instance, ^{3}He and lithium (see Charbonnel & Lagarde 2010; Lagarde et al. 2011, 2012). As this mixing process does not influence the structure of the star (Lagarde et al. 2012), it is expected to have no influence on the s-process production.

2.2.3   Mixing-length theory (MLT)

The mixing length theory (see e.g. Biermann 1932; Böhm-Vitense 1958) describes transport of energy by convection. To determine how far a fluid parcel travels (l_{MLT}) before it dissolves in the background, a free parameter $\alpha = l_{\mathrm{MLT}}/H_P$ is defined. In other words this parameter shows how efficient convection is, as a large α indicates that a fluid parcel travelled a larger distance before dissolving. In my calculations I use the standard MLT prescription (Cox & Giuli 1968), which assumes no radiative losses of the fluid parcels. It is therefore only applicable for regions of high opacity, but despite this restriction, it is the default version of MLT.

The MLT equations for convective speed v_{c}, convective flux F_{c}, and convective efficiency

---

[1]The derivation of this mixing process is not unlike the rotating instability GSF (see Section 2.4.5), as this instability requires a negative gradient of specific angular momentum. See Angelou (2014) for a extensive discussion on this similarity.

Γ_{c} are:

$$v_{\mathrm{c}}^2 = \frac{l^2 g Q (\nabla_{\mathrm{conv}} - \nabla')}{8 H_P} \tag{2.20}$$

$$F_{\mathrm{c}} = \frac{\rho v_{\mathrm{c}} c_{\mathrm{p}} T l (\nabla_{\mathrm{conv}} - \nabla')}{2 H_P} \tag{2.21}$$

$$\Gamma_{\mathrm{c}} = \frac{\nabla_{\mathrm{conv}} - \nabla'}{\nabla' - \nabla_{\mathrm{ad}}} = \frac{c_{\mathrm{p}} \rho^2 l v_{\mathrm{c}} \kappa}{24 \sigma T^3} \tag{2.22}$$

with ∇' being the temperature gradient of the fluid parcel, ∇_{conv} the average temperature gradient within the convective region that is present in Eq. 2.4, and $Q = -\frac{\mathrm{dln}\rho}{\mathrm{dln}T}\big|_P$. From these three expressions a simple algebraic equation can be obtained to provide a value for ∇. The equation is (Cox & Giuli 1968):

$$\xi^{1/3} + B\xi + a_0 B^2 \xi - a_0 B^2 = 0 \tag{2.23}$$

where ξ is:

$$\xi = \frac{\nabla_{\mathrm{r}} - \nabla}{\nabla_{\mathrm{r}} - \nabla_{\mathrm{ad}}} \tag{2.24}$$

and the values for A, B, and a_0 can be obtained via:

$$\Gamma = A(\nabla - \nabla'^{1/2}) \tag{2.25}$$

$$\nabla_{\mathrm{r}} - \nabla = a_0 A(\nabla - \nabla')^{3/2} \tag{2.26}$$

$$B = \left[(A^2/a_0)(\nabla_{\mathrm{r}} - \nabla_{\mathrm{ad}})\right]^{1/3} \tag{2.27}$$

The convective diffusion coefficient is then calculated by $D_{\mathrm{conv}} = \frac{1}{3}\alpha_{\mathrm{MLT}} v_{\mathrm{c}} H_P$, which is used in Eq. 2.8.

2.3   Rotating stellar structure

In rotating stars, centrifugal forces lead to deviations from the spherical symmetry used in the derivation of equations 2.2 - 2.8. This deformation is axisymmetric, until the rotational energy becomes a notable fraction of the binding energy leading to triaxial

deformations. This stage, where the rotational velocity is of the order of or higher than the critical velocity (where the gravitational pull inwards is in balance with the centrifugal motion outwards), can be reached both in the central regions and in the envelope, see Hirschi, Meynet & Maeder (2005) and Georgy, Meynet & Maeder (2011). This stage is only reached in the final phases of massive star evolution, and therefore not considered in this work.

Even when the star is slowly rotating, the shapes of constant pressure, density and temperature surfaces will be affected by centrifugal forces and deviate from spherical symmetry. As a result, several of the stellar evolution equations have to be altered. In total, there are four ways in which rotation may affect the equations of stellar structure (Endal & Sofia 1976):

1. Centrifugal forces reduce the effective gravity at any point not on the axis of rotation;

2. Centrifugal forces are generally not parallel to the force of gravity, the equipotential surfaces are no longer spheres and thus the spherical symmetry used in the derivation of the stellar evolution equations is no longer valid;

3. Radiative flux varies with local effective gravity which has a latitude dependence, described by the von Zeipel theorem (see Zeipel 1924; Maeder 2009);

4. Rotational instabilities transport chemical elements and angular momentum.

The first three effects are directly incorporated in the stellar evolution equations (Kippenhahn & Thomas 1970). In that paper, the spherical surfaces normally used are replaced by isobars. This method is corrected, completed and also simplified by assuming anisotropic turbulence acts much faster on the isobars than in the perpendicular vertical direction (Chaboyer & Zahn 1992; Zahn 1992). This enforces rotation that is constant as a function of radius at a given latitude in radiative regions. This type of rotation is called *shellular* rotation (Meynet & Maeder 1997). As a result of the strong horizontal turbulence, matter on isobars is approximately chemically homogeneous and therefore a
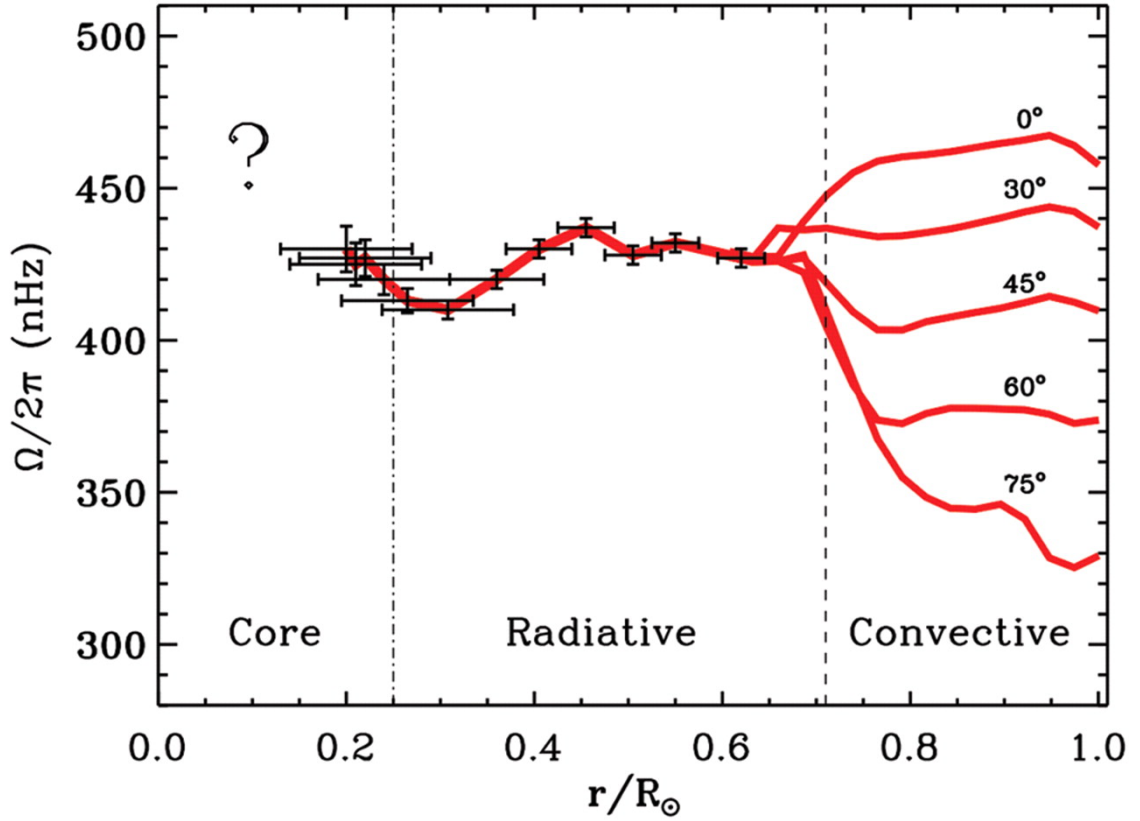
Figure 2.1: Internal rotation rate of the Sun, using long time series of 2088 days (García et al. 2004; Korzennik 2005). These time series allow for the determination of the Solar rotation profile with small error bars, down to 0.3 R/R$_\odot$. This analysis shows that the Sun is rotating rigidly in the radiative zone independent of the latitude, and differentially rotating at different colatitudes in the convective region (see also Section 2.3.2). Figure from García et al. (2007).

one-dimensional description is still appropriate.

The radiative zone of the Sun is in agreement with shellular rotation as it rotates at a uniform rate, see Fig. 2.1 and Kosovichev (1988), Brown et al. (1989), Elsworth et al. (1995), Thompson et al. (1996), and García et al. (2007). The rotation profile within the radiative Solar core is still unknown, although a recent publication suggests that the core is rotating faster than the surrounding radiative zone (Fossat et al. 2017).

2.3.1   Equations for stellar structure including rotation

New equations for the stellar structure can now be derived, using isobars. On an isobar, pressure is constant by definition. Let V_P be the volume enclosed by a surface S_P of constant pressure P. Its radius r_P, defined as the radius of the sphere of the same volume V_P, is such that $V_P=4\pi r_P^3/3$. Then the equation of mass conservation, conservation of momentum and energy transport are altered in the following way:

$$\left(\frac{\partial m_P}{\partial r_P}\right)_t = 4\pi r_P^2 \bar{\rho} \tag{2.28}$$

$$\left(\frac{\partial P}{\partial m_P}\right)_t = -\frac{Gm_P}{4\pi r_P^4 f_P} \tag{2.29}$$

$$\left(\frac{\partial ln\bar{T}}{\partial m_P}\right)_t = \frac{Gm_P}{4\pi r_P^4 P} f_P \min\left[\nabla_{\mathrm{MLT}}, \nabla_{\mathrm{rad}}\frac{f_T}{f_P}\right] \tag{2.30}$$

with m_P being the mass interior to the equipotential surface and the f-factors:

$$f_P = \frac{4\pi r_P^4}{Gm_P S_P}\left\langle g^{-1}\right\rangle^{-1} \tag{2.31}$$

$$f_T = \left(\frac{4\pi r_P^2}{S_P}\right)^2 \left(\langle g\rangle \left\langle g^{-1}\right\rangle\right)^{-1} \tag{2.32}$$

where $\langle g\rangle$ is g averaged over the isobaric surface, the subscript 'P' refers to the isobar with a pressure equal to P, and $\bar{x}$ is the average of quantity x in a volume separating two isobars. The first three of the ways rotation affects the stellar evolution equations are now accounted for: the first one by including f_P, the second by using isobaric surfaces, and the third one by including f_T. Including the fourth one involves adding new terms to the equation for the transport of chemical elements.

The transport of angular momentum ($j \propto \Omega r^2$) is treated in the diffusive approximation with an equation for the angular velocity, as the radius is assumed locally constant (Endal & Sofia 1976; Pinsonneault et al. 1989; Heger, Langer & Woosley 2000):

$$\left(\frac{\partial \Omega}{\partial t}\right)_m = \frac{1}{i}\left(\frac{\partial}{\partial m}\right)_t\left[(4\pi r^2\rho)^2 i D_{\mathrm{am}}\left(\frac{\partial\Omega}{\partial m}\right)_t\right] - \frac{2\Omega}{r}\left(\frac{\partial r}{\partial t}\right)_m\left(\frac{1}{2}\frac{d\ln i}{d\ln r}\right) \tag{2.33}$$

where Ω is the angular velocity, $i = \frac{2}{3}r^2$ is the specific angular momentum for a spherical shell at mass coordinate m, D_{am} is also known as the *turbulent viscosity* (Heger, Langer & Woosley 2000). The various contributions to D_{am} are derived in Section 2.4, and the diffusion equation Eq. 2.33 is derived in Appendix 7, as well as the diffusion equation for the mixing of chemical elements (Eq. 2.8).

2.3.2 Rotation in convective regions

Shellular rotation is assumed for the radiative zones, as the horizontal turbulence smooths out differential rotation along the isobars. However, this is not true for convective zones. Currently there are two treatments for rotation in a convective region:

- Treatment A: Convective regions are treated as solid body rotators. The argument behind this option is that the convective motions create strong turbulent viscosity which homogenises the distribution of angular velocity. As a result the convective region will have a uniform distribution of angular velocity.

- Treatment B: Convective regions have a constant distribution of angular momentum. The argument for this treatment is that the large-scale convective motions dominate the region, and that they conserve their angular momentum. As a result, the convective region has a uniform distribution of angular momentum.

Treatment A is the standard treatment in stellar evolution models. Only a few studies consider treatment B (i.e., see Kawaler & Hostler 2005; Cantiello et al. 2014; Tayar & Pinsonneault 2018). In Cantiello et al. (2014) both options were tested, as both are included in the implementation of rotation in MESA. The choice for option A or B did not influence their conclusions on the evolution of core rotation rates, as the mixing process that are responsible for the transport of angular momentum are still identical. Their dependence on the molecular weight gradients remains the limiting factor for the transport of angular momentum. As shown in Fig. 2.1, the solar rotation profile is nearly constant in its convective region, with no dependence on radius. Therefore, treatment A

is currently the preferred option in 1D stellar evolution models.

3D simulations of rotating convective regions indicate that the situation is more compli-
cated than the two treatments presented above. For instance, Toomre & Brun (2004)
shows 3D simulations of solar convection, and concludes that the angular velocity distri-
bution is not at all constant throughout the region. Browning, Brun & Toomre (2004)
presents 3D simulations of core convection in a 2-$M_\odot$ star, rotating at different rotation
rates. They also find differential rotation in the convective region, as well as elongation
of the core along the rotation axis. The overview of Deupree (2004) indicates that indeed
the two treatment of rotation in convective regions are unrealistic. Nevertheless, these
options are currently the standard in 1D stellar evolution codes. Brun & Palacios (2009)
show that the convective motion itself depends on the rotation rate of the star, which
impacts the convective boundary mixing (Brun et al. 2017).

2.4 Rotational induced instabilities

When rotation is included in stellar evolution models, the number of instabilities increases
(Heger, Langer & Woosley 2000; Maeder & Meynet 2012). All these instabilities have
a common effect: they redistribute angular momentum and chemical elements. In the
next subsections, these processes and prescriptions used in stellar evolution codes are
presented.

2.4.1 Solberg-Høiland (SH) instability

The Brunt-Väisälä frequency, see Section 2.2.1, was derived for a non-rotating medium.
Displaced elements in a rotating medium, however, are also subject to the centrifugal
force which modifies the oscillation frequency and thus the criterion for convective

stability (Wasiutynski 1946). The Solberg-Høiland criterion for convective stability is:

$$N^2 = \mathrm{N}_T^2 + N_\mu^2 + N_\Omega^2 \sin\theta \geq 0 \tag{2.34}$$

$$\text{or}: N^2 = R_{SH} = \frac{g\delta}{H_P}\left(\nabla_{\mathrm{ad}} - \nabla + \frac{\varphi}{\delta}\nabla_\mu\right) + \frac{1}{r^3}\frac{d}{dr}(r^2\Omega)^2 \geq 0 \tag{2.35}$$

Like convection, this instability takes place on the dynamical time scale. It can occur in regions where the specific angular velocity strongly decreases outwards, and is calculated in a similar way to the dynamical shear instability. The diffusion coefficient for this instability can be calculated by the square of the extent of the unstable region d_{inst} divided by the dynamical time scale, as this instability works on the dynamical time scale. The d_{inst} is limited to the pressure scale height, and in an attempt to smooth the transition between stable and unstable regions, this length scale is multiplied by a factor close to unity of rR_{SH}/g:

$$D_{\mathrm{SH}} = \left[\min\left\{d_{\mathrm{inst}}, H_{\mathrm{P}}\right\}\left(\frac{rR_{\mathrm{SH}}}{g}\right)\right]^2 / \tau_{\mathrm{dyn}} \tag{2.36}$$

Some authors exclude this instability (i.e. Hirschi, Meynet & Maeder 2004) assuming the dynamical shear instability (defined in the next section) is always dominant over the SH instability.

2.4.2 Dynamical shear instability (DSI)

Stars have both rotational velocity and density gradients, due to their stratified internal structure. The instability created by two regions moving with a denser region on top of a less dense region is known as the Rayleigh-Taylor instability, while the instability created when two regions move at different velocities is called the Kelvin-Helmholtz instability. This instability can be seen in nature, for instance by wind blowing over the sea creating waves, or in the shape of clouds. The interplay of the two instabilities needs to be studied in detail, and is expressed by the Richardson criterion (Zahn 1974; Endal & Sofia 1978). The Richardson criterion was derived by Chandrasekhar (1961), who considered two cells at levels z and $z + \partial z$, moving with velocities v and $v + \partial v$. respectively. The instability

takes place when the work done against gravity due to the displacement is smaller than the kinetic energy available. The work done against gravity can be expressed as:

$$\partial W = g \partial \rho \partial z^2 \tag{2.37}$$

and the kinetic energy available is:

$$\partial K = \frac{1}{2}\rho \left[(v^2 + (v + \partial v)^2) - 2\left(v + \frac{\partial v}{2}\right)\right] \tag{2.38}$$

$$= \frac{1}{4}\rho(\partial V)^2 \tag{2.39}$$

As the instability occurs when $\partial K > \partial W$, we get:

$$\frac{1}{4}\rho(\partial v^2) > g\partial\rho\partial z^2 \tag{2.40}$$

$$Ri \equiv \frac{g}{\rho}\frac{\partial\rho/\partial z}{(\partial v/\partial z)^2} < \frac{1}{4} = Ri_{\mathrm{c}} \tag{2.41}$$

where the critical Richardson number is $1/4$. Then, by using Eqs. 2.15-2.17, the Richardson criterion can be rewritten as:

$$Ri \equiv \frac{N^2}{(\partial v/\partial z)^2} < Ri_{\mathrm{c}} \tag{2.42}$$

$$\text{or}: N^2 < Ri_{\mathrm{c}}\left(\sin\theta r\frac{\partial\Omega}{\partial r}\right)^2 \tag{2.43}$$

as in shellular rotation $\partial v/\partial z = r\sin\theta(\partial\Omega/\partial r)$ where θ is the latitude.

This instability occurs on the dynamical time scale, and therefore effects working on longer time scale can be neglected (i.e. thermal effects). The corresponding diffusion coefficient is calculated by first multiplying the spatial extent of the unstable region, d_{inst} (limited to the pressure scale height H_{P}), with the extent of the deviation of Ri from Ri_{c}. The square of this multiplication is then divided by the local dynamical time scale:

$$D_{\mathrm{DSI}} = \left[\min\{d_{\mathrm{inst}}, H_{\mathrm{P}}\}\left(1 - \max\left\{\frac{R_{\mathrm{i}}}{R_{\mathrm{i,c}}}, 0\right\}\right)\right]^2 / \tau_{\mathrm{dyn}} \tag{2.44}$$

where the term between the round brackets is included to allow for a smooth transition between stable and unstable regions. The instability is assumed to be weaker when the

deviation from the Richardson criterion is smaller. When $R_\mathrm{i} > R_\mathrm{i,c}$ the flow is assumed to be stable against the dynamical shear instability, however it might be unstable against the secular shear instability (explained in the next section).

2.4.3   Secular shear instability (SSI)

Thermal effects, working on thermal time scales, can reduce the density gradient and thus their stabilizing effects. These effects can thus allow for shear instabilities to occur on thermal time scales, even in regions that are stable according to the Richardson criterion. Molecular weight gradients, however, inhibit the secular shear. Both aspects have to be included in the stability criterion (Endal & Sofia 1978). The first condition, concerning the thermal effects, includes the Prandtl number, P_r. The Prandtl number is calculated by dividing the kinematic viscosity by the thermal diffusivity. The stronger the thermal diffusion, the weaker the density gradient and thus the stronger the secular shear. The first criterion for stability against secular shear is:

$$Ri_{\mathrm{SSI},1} = \frac{R_\mathrm{crit}}{8} P_\mathrm{r} Ri > \frac{1}{4} \tag{2.45}$$

with R_crit being the critical Reynolds number which is $\simeq 10^3$ (Zahn 1974; Richard 1999). This condition implies that in the inviscid limit of $P_\mathrm{r} \to 0$, any differentially rotating region is unstable against secular shear independent of molecular weight gradients. This is not correct. To account for this, the second condition only considers the dependence of N^2 on the molecular weight gradient when including N^2 in the Richardson criterion as in Eq. 2.43 (Heger, Langer & Woosley 2000):

$$Ri_{\mathrm{SSI},2} = \frac{\rho \psi \nabla_\mu}{P} \left(g \frac{d\ln r}{d\Omega} \right)^2 > \frac{1}{4} \tag{2.46}$$

Only when both criteria are violated, the secular shear instability will occur. Its strength is determined by calculating its velocity. This velocity is calculated by dividing the size scale of the turbulent element l by the time scale $\tau \backsim R_\mathrm{crit}/(d\Omega/d\ln r)$ (a thermal time

scale):

$$l^2 \sim \nu R_{\text{crit}}/(d\Omega/d\ln r) \tag{2.47}$$

$$v_{\text{SSI}} = l/\tau = [\nu(d\Omega/d\ln r)/R_{\text{crit}}]^{1/2} \tag{2.48}$$

$$\text{and } H_{\text{v,SSI}} = \left| \frac{dr}{d\ln v_{\text{SSI}}} \right| \tag{2.49}$$

where $H_{\text{v,SSI}}$ is the typical velocity scale height of the flow, used here as the typical length scale of the instability. Then, the equation for the diffusion coefficient is the following:

$$D_{\text{SSI}} = \min\{v_{\text{SSI}}, c_s\} \min\{H_{\text{v,SSI}}, H_P\} \left(1 - \frac{\max\{R_{\text{i,SSI,1}}, R_{\text{i,SSI,2}}\}}{R_{\text{i,c}}}\right)^2 \tag{2.50}$$

2.4.4 Eddington-Sweet (ES) circulation

This large-scale circulation arises as the centrifugal forces make the isobars oblate, instead of spherical. As a consequence, the isobars are less close to each other at the equator than at the polar regions. Since the radiative flux is proportional to the effective gravity, there is a deficiency of this flux at the equator and an excess at the poles. This imbalance causes the circulation (Zeipel 1924; Eddington 1925; Sweet 1950; Kippenhahn 1974), known as the Eddington-Sweet circulation or meridional circulation. Also the Earth is oblate and experiences meridional (north-south direction) and zonal (west-east) air flows. Meridional flows are responsible for strong storms and extreme weather (heat and cold waves)[2].

The derivation of the Eddington-Sweet circulation velocity starts with the first law of thermodynamics:

$$\nabla \cdot \mathbf{F} = \rho\epsilon - c_{\text{P}}\rho\frac{dT}{dt} + \delta\frac{dP}{dt} \tag{2.51}$$

$$\text{or } \nabla \cdot \mathbf{F} = -\delta\frac{\nabla_{\text{ad}} - \nabla}{\nabla_{\text{ad}}} g\rho v_{\text{r}} \tag{2.52}$$

---

[2]`www.scientificamerican.com/article/why-do-we-have-a-hurricane-season/`

where $\mathbf{F}$ is the radiative flux, and all other symbols have been defined before. The meridional velocity v_r then becomes:

$$v_r = \frac{1}{\rho g} \frac{\nabla_{ad}}{\delta \nabla_{ad} - \nabla} \left[\rho \epsilon - c_P \rho \frac{dT}{dt} + \delta \frac{dP}{dt} \right] \tag{2.53}$$

$$\text{and } v_r = \frac{\nabla_{ad}}{\delta \nabla_{ad} - \nabla} \frac{\Omega^2 r^3 l}{(Gm)^2} \left[\frac{2(\epsilon_n + \epsilon_v) r^2}{l} - \frac{2r^2}{m} - \frac{3}{4\pi \rho r} \right] \tag{2.54}$$

For all derivation steps in between the above equation, see Kippenhahn (1974). The μ-gradient suppresses or even inhibits the meridional circulation, and this effect can be written as a 'stabilizing' circulation velocity v_μ (Kippenhahn 1974; Pinsonneault et al. 1989):

$$v_\mu = \frac{H_P}{\tau_{KH}^*} \frac{\varphi \nabla_\mu}{\partial(\nabla - \nabla_{ad})} \tag{2.55}$$

where τ_{KH}^* is the local Kelvin-Helmholtz time scale. The difference between v_r and v_μ is the effective velocity v_{ES}. The resulting diffusion coefficient is then (Endal & Sofia 1978):

$$D_{ES} = \min \left\{ d_{inst}, H_{v,ES} \right\} v_{ES} \tag{2.56}$$

with $H_{v,ES}$ the typical length scale of the instability:

$$H_{v,ES} = \left| \frac{dr}{d\ln v_{ES}} \right| \tag{2.57}$$

The strong effect of the μ-gradient is due to gravity: the μ-gradient always decreases outwards, meaning that the gravitational forces have to be overcome for the ES circulation to proceed. When the ES-circulation is not strong enough to do so, the circulation is deflected horizontally, see Mestel (1953) for more details.

The ES circulation is the only instability described in this section that is active in regions of constant Ω, while all others are active when Ω is changing. Therefore, the ES circulation mixes chemical elements and transports angular momentum in large (radiative) regions within stars, while the other instabilities are active in smaller regions.

2.4.5 Goldreich-Schubert-Fricke (GSF) instability

The GSF instability is formed when the surfaces of constant specific angular momentum make an angle relative to the rotation axis, see Goldreich & Schubert (1967); Fricke

(1968). Like the Eddington-Sweet circulation, the GSF instability is suppressed when μ-gradients are present, and v_μ is therefore used here again. However, the GSF instability is excluded from most of the stellar evolution models presented in this thesis, based on the independent studies of Hirschi & Maeder (2010) and Caleo, Balbus & Tognelli (2016). Both papers show that viscosity, assumed to be negligible in the original derivation of the instability (James & Kahn 1970, 1971), either turbulent as in Hirschi & Maeder (2010) or molecular and radiative as in Caleo, Balbus & Tognelli (2016), suppresses the GSF instability. Hirschi & Maeder (2010) shows that for several evolutionary phases of a 20-$M_\odot$ star, the GSF instability is always weaker than the dynamical shear. The implementation of the GSF instability in MESA currently follows Heger, Langer & Woosley (2000) and does not include the stabilising effect of the viscosity. Therefore, I exclude GSF from my stellar evolution calculations.

2.4.6   Other implementations and instabilities

Other rotational induced, hydrodynamical instabilities are the ABCD-instability (Spruit, Knobloch & Roxburgh 1983) and the triple diffusive instability (Knobloch & Spruit 1983). Due to a lack of reliable estimates of their efficiency is their inclusion in stellar evolution calculations currently unjustified (Heger, Langer & Woosley 2000; Maeder 2009).

2.5   Magnetic dynamos

Magnetic fields exist in stars in two different configurations: long-lived and stable or short-lived and dynamical. The stable or fossil fields are remnant fields present since the formation of the star and are generally associated with strong, static, large-scale fields (Cowling 1945; Braithwaite & Spruit 2004; Braithwaite 2006). These fossil fields might be a relic of a field present in the star forming region, and somehow locked into the star. Dynamical fields are dynamo-driven fields relying on instabilities, and are commonly
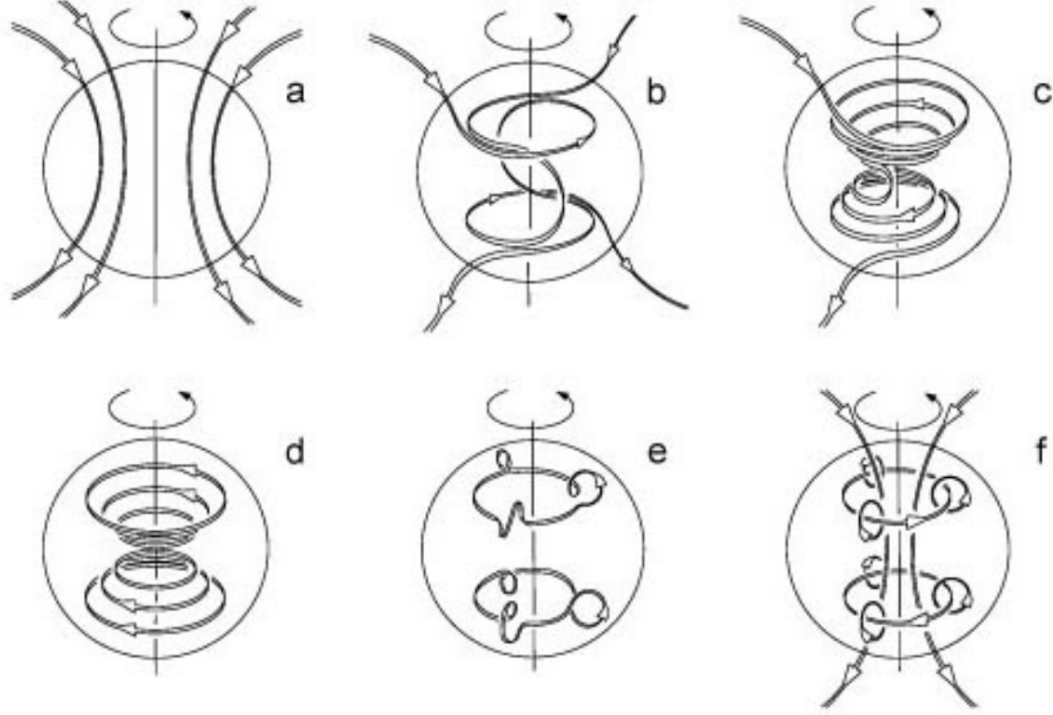
Figure 2.2: Schematic overview of the process of winding up magnetic field lines. Figures a-c show the omega effect, while figures d-f show the alpha effect, explained in the text. Figure from Fletcher (2006).

found in slowly rotating stars. These fields are weak, and are assumed to be created in rotating stars (Tayler 1973; Markey & Tayler 1973; Wright 1973). The development of the understanding of both types of fields is ongoing, see e.g. Walder, Folini & Meynet (2012) for a recent overview.

 Some of the stellar evolution models presented in this thesis include dynamical fields, because of their link to angular momentum transport. These fields can be created in differentially rotating stars. The theory of the formation of dynamical fields starts with assuming shellular rotation (differentially rotating) and a weak initial or seed magnetic field. Due to the differential rotation, the magnetic field lines are wound up and the non-axisymmetrical components are expelled. This process of making the field axisymmetric is fast, of the order of hundreds of years (estimated with values reasonable

for the Sun). The azimuthal field formed by the winding up of the weak initial field increases in strength until instabilities start to form, with the Tayler-Spruit instability being the most important one (Tayler 1973). This instability, present in radiative zones, generates a new field component in the radial direction and this field is also wound up by differential rotation, see Fig. 2.2a-c. Applied to stellar interiors, this dynamo field leads to an effective viscosity influencing the transport of angular momentum and additional mixing of the chemical elements (Spruit 1999, 2002).

The inclusion of these effects in the stellar evolution codes used to calculate the models shown in this thesis are both based on the Tayler-Spruit instability, derived by Spruit (2002). The effective diffusivity generated by the Tayler-Spruit instability is:

$$D_{e,TS} = \frac{D_{e0}D_{e1}}{D_{e0} + D_{e1}} f_q \tag{2.58}$$

$$\text{with: } f(q) = 1 - \frac{q_{min}}{q} \text{ (if } q > q_{min}) \tag{2.59}$$

$$= 0 \text{ (if } q < q_{min}) \tag{2.60}$$

$$q = \frac{r}{\Omega} \frac{\partial \Omega}{\partial r} \tag{2.61}$$

$$q_{min} = q_0 + q_1 \tag{2.62}$$

$$= \left(\frac{N_\mu}{\Omega}\right)^{7/4} \left(\frac{\eta}{r^2 N_\mu}\right)^{1/4} + \left(\frac{N_T}{\Omega}\right)^{7/4} \left(\frac{\eta}{r^2 N_T}\right)^{1/4} \left(\frac{\eta}{\kappa}\right)^{3/4} \tag{2.63}$$

$$D_{e0} = r^2 \Omega q^4 \left(\frac{\Omega}{N_\mu}\right)^6 \tag{2.64}$$

$$D_{e1} = r^2 \Omega \max\left[q\left(\frac{\Omega}{N_T}\right)^{3/4}\left(\frac{\kappa}{r^2 N_T}\right)^{3/4}, q^4\left(\frac{\Omega}{N_T}\right)^6\right] \tag{2.65}$$

with f being a factor added to the stress so that it vanishes smoothly as the gradient q approaches the minimum value required, q_{min}, for dynamo action to take place (Spruit 2002). D_{e0} represents the case where the effects of stratification are dominated by the compositional gradient and D_{e1} represents the case where thermal diffusion (the stabilizing stratification is due entirely to the entropy gradient) dominates. The right term in the maximum operator in Eq. 2.65 dominates over the left term when the thermal diffusion has no effect. The value of q_{min} takes into account that the dynamo action is only possible when the rotational gradient is strong enough to overcome the stabilising

effects of both the compositional gradient (q_0) and of the thermal buoyancy (q_1). It is important to note that in Spruit (2002) it is written that the algebraic complexity of the expressions included in the derivation are not equal to the level of sophistication of their analysis. Therefore, the two cases (domination by the compositional gradient and the thermal diffusion) are combined by using a 'patching formula' as shown in Eq. 2.58. The effective diffusivity $\nu_{e,ST}$ generated by the Tayler-Spruit instability is included in the equation for mixing of chemical elements (Eq. 2.8). The effective viscosity that is included in the transport of angular momentum in Eq. 2.33 is derived similarly as to the effective diffusivity:

$$\nu_{e,TS} = \frac{\nu_{e0}\nu_{e1}}{\nu_{e0} + \nu_{e1}} f_q \tag{2.66}$$

$$\nu_{e0} = r^2 \Omega q^2 \left(\frac{\Omega}{N_\mu}\right)^4 \tag{2.67}$$

$$\nu_{e1} = r^2 \Omega \max \left[q \left(\frac{\Omega}{N_T}\right)^{1/2} \left(\frac{\kappa}{r^2 N_T}\right)^{1/2}, q^2 \left(\frac{\Omega}{N_T}\right)^4 \right] \tag{2.68}$$

Ω will only approach N when the rotation rate is close to the critical rotation, which is not reached in the models presented in this thesis. Therefore, $\Omega \ll N$ is true in general (Spruit 2002), a difference in value of several orders of magnitude. Therefore, $D_{e,TS}$ is much smaller than $\nu_{e,TS}$ which means that the TS-dynamo is much more effective at transporting angular momentum than mixing chemical elements.

2.6   Uncertainties concerning rotation

Now that all rotationally induced mixing processes have been defined, I can present the sums that make up the total diffusion coefficients as included in the transport of angular momentum (Eq. 2.33) and the mixing of chemical elements (Eq. 2.8):

$$D_{am} = D_{DSI} + D_{SH} + D_{SSI} + D_{GSF} + D_{ES} + \nu_{TS} \tag{2.69}$$

$$D_{mix} = D_{DSI} + D_{SH} + D_{SSI} + D_{GSF} + D_{ES} + D_{TS} \tag{2.70}$$

where the only difference is the inclusion of the dynamo effects. Several uncertainties are however present.

The first is the treatment of mixing processes like the dynamical shear instability in stellar modelling, due to the need to parametrize and approximate aspects of hydrodynamics in hydrostatics. Multidimensional studies of the processes and the comparison between 1D and multi-D simulations are needed to improve the treatments. A comparison between the 1D hydrostatic model and 2D hydrodynamical simulation of the DSI is published in Edelmann et al. (2017). They conclude that most of the differences between 1D and 2D come from the fact that in stellar evolution models the evolutionary time step is larger than the time scale of the dynamical shear instability. Details on how to deal with this were beyond the scope of that paper, but it does mention possible options, like combining the dynamical and secular shear in one prescription.

The difference between the evolutionary time step and the dynamical time scale has led to some research groups excluding all rotationally induced dynamical processes from their calculations[3]. As most of these processes only occur in late stellar evolutionary phases (Hirschi, Meynet & Maeder 2004, see e.g.), this exclusion has very minor effects on the outcome of stellar evolution models.

Furthermore, the interaction between the instabilities included Eqs. 2.69 and 2.70 is not included in the theory. Studies on this problem have been published (see e.g Chaboyer & Zahn 1992; Zahn 1992; Urpin, Shalybkov & Spruit 1996; Meynet & Maeder 1997; Maeder 1997; Talon & Zahn 1997; Talon et al. 1997; Maeder et al. 2013), however, the effect in stellar model of these interactions are not large and are therefore not included. Another uncertainty is that there are different variants of the equation for the transport of angular momentum and also how it is included in stellar evolution models differs. Two options are available, and the first is given in Eq. 2.33. The second option is to follow Zahn (1992), as done in the GENEC code (Maeder & Zahn 1998; Eggenberger et al.

---

[3]Private communication with Prof. S.C. Yoon

2008) and use:

$$\rho \frac{\partial}{\partial t}(r^2\Omega)|_{M_r} = \frac{1}{5r^2}\frac{\partial}{\partial r}(\rho r^4 \Omega U(r)) + \frac{1}{r^2}\frac{\partial}{\partial r}(\rho D r^4 \frac{\partial\Omega}{\partial r}) \qquad (2.71)$$

with $\Omega(r)$ being the mean angular velocity at level r, $U(r)$ the vertical component of the meridional circulation velocity and D the sum of the different diffusion processes. As a consequence of keeping M_r constant, angular momentum is conserved during contraction or expansion. The first term on the right side is an advective term describing the meridional circulation, while the second is a diffusive term describing the diffusive processes like shear. Treating meridional circulation as advection is more physical than treating it as diffusion and is thus considered to be more correct (Paxton et al. 2013), but it is also numerically more expensive. The differential equation in MESA therefore treats the meridional circulation as a diffusive process, following Heger, Langer & Woosley (2000).

The differential equation for the mixing of chemical elements can also be written as an advective-diffusive equation as eq. 2.71. Chaboyer & Zahn (1992) found that when the horizontal component of the diffusion is large, the vertical advection of the elements can be expressed as a diffusion process:

$$D_{\mathrm{eff}} = \frac{|rU(r)|^2}{30D_{\mathrm{h}}} \qquad (2.72)$$

$$\text{with: } D_{\mathrm{h}} = |rU(r)| \qquad (2.73)$$

where the latter expression is derived by Zahn (1992).

Tests have been performed (Potter, Tout & Eldridge 2012; Potter, Tout & Brott 2012) to investigate whether one implementation of transport of angular momentum should be preferred over the others. These tests are done for both individual stars (intermediate-mass and massive stars) and stellar populations, and included Heger, Langer & Woosley (2000) and two versions of the above-described GENEC implementation. While there were differences between the resulting three sets of main-sequence models, the authors of Potter, Tout & Eldridge (2012); Potter, Tout & Brott (2012) and were unable to identify a preferred implementation. Instead, they state that the different options generate significant differences in results based on mass, metallicity, and rotation rate, but that

the different models lead to similar qualitative conclusions. Finally, the TS-dynamo is controversial. There are several papers challenging the derivation of the TS-dynamo. One of the papers on the TS-dynamo is Denissenkov & Pinsonneault (2007), where a disagreement with an extrapolation in the original derivation leads to lower viscosities and a stronger dependence on the μ-gradients. As a result, the coupling between core and envelope is weaker and the gap between model outcomes and observations is bigger in this version than in the original the TS-dynamo. In Zahn, Brun & Mathis (2007) the TS-dynamo is criticised too, for being too simple to be applied in stellar evolution codes, when compared to their 3D simulations. Another revision can be found in Maeder & Meynet (2004), where the derivation of the diffusion coefficients of the TS-dynamo differs from the one in Spruit (2002). In Spruit (2002) the solution was limited to two cases, one where the μ-gradient dominates and one where the thermal gradients dominate. In Maeder & Meynet (2004) a more general solution is derived, that still matches the limiting cases of Spruit (2002). As a result of the new equations, the diffusion coefficient for the transport of angular moment is larger and the coupling between core and envelope is stronger.

Fig. 2.2 also shows the alpha effect (Steenbeck, Krause & Rädler 1966; Brandenburg 2001), which in turn transforms the toroidal magnetic field back into a poloidal one. This transformation is due to the Coriolis effect[4], creating twists in the magnetic field lines (Fig. 2.2e), which then become small loops. Both the toroidol field and the Coriolis force have opposite signs on the northern and southern hemisphere, making the small loops rotate in the same direction. Due to magnetic diffusivity, these loops create a poloidal field. This dynamo is included in Potter, Chitre & Tout (2012), who found that this dynamo improved their comparison to observed surface nitrogen enrichment of massive stars.

Recently a new derivation of the TS-dynamo was published (Fuller, Piro & Jermyn 2019). The details of this derivation and some initial results will be discussed in Chapter 6 and

---

[4]The Coriolis Effect is the apparent deflection of a moving object when viewed from a rotating frame of reference.

7.

2.7 Effect of rotation on stellar evolution

The consequences of including rotation in stellar evolution models will be noticeable at both large and small scales, as some instabilities occur on the dynamical time scale and some on slower time scales. In this section I discuss the studies that include rotating stellar evolution models in the mass range considered in this thesis.

To investigate the effect of rotation on the HRD of stellar evolution models, I created Fig. 2.3. This figure shows a comparison between non-rotating and rotating (with an initial rotation rate of $\Omega/\Omega_{crit}=0.4$) models with an initial mass of 2 and 3 $M_\odot$, at solar metallicity, calculated with MESA by the MIST group (Choi et al. 2016) and with GENEC (Ekström et al. 2012). As described in Section 2.4.6, these two codes use two different implementations of rotation and there is therefore no added benefit from including more models (i.e. Charbonnel & Lagarde 2010; Brott et al. 2011; Potter, Chitre & Tout 2012). Fig. 2.3 consists of two panels, the top one showing the evolution of the eight included models up to the AGB phase, while the lower panel shows only the main sequence and the star of the RGB phase. At first glance these figures show that the same general trends are present in these models, both non-rotating and rotating, as described in Section 1.1 with Fig. 1.2. There are minor differences visible though. For instance, all rotating models start the main sequence at a lower effective temperature than their non-rotating counterparts due to the centrifugal forces making the rotating stars slightly more 'puffy' at their surfaces. Also, all rotating models shown in Fig. 2.3 have a wider main sequence than the non-rotating models. This is because of the extra mixing due to rotation, which mixes H into the core during the main sequence, thus lengthening this evolutionary phase. The effect is more profound in the GENEC models than in the MIST models, possibly due to the differences in the implementation of rotation. The main sequence of the rotating GENEC models ends at a luminosity 5-10 % higher than the non-rotating GENEC models, due to their more massive rotating cores caused by the

lengthened main sequence. This effect is not visible in the MESA models as the main sequence width in the rotating MESA models is more similar to the non-rotating MESA models, and thus their masses (and thus luminosities) are similar as well.

The MESA models converge early on the RGB, while the GENEC models converge at the start of the vertical part of the RGB. At this point the MESA models are hotter than the GENEC models. The differences between the MESA and GENEC models might be explained by differences in the treatment of convection, convective boundary mixing, and opacities. A similar comparison of GENEC and MESA models has recently been presented by Gossage et al. (2018), who also included models with initial masses of 4 and 7 $M_\odot$. The trends in these models are the same as in the lower initial masses.

There is another point to discuss when explaining Fig. 2.3, which is that the cores of these rotating models rotate too fast when compared to asteroseismically determined core rotation rates. Therefore, the differences will probably be even smaller between non-rotating MESA models and the rotating MESA models with cores that rotate at rates matching the asteroseismic observed ones.

Due to the convergence of the HRD tracks, the rotating and non-rotating stellar evolution models will have core masses that are similar at the start of the TP-AGB phase. Piersanti, Cristallo & Straniero (2013) report in their Table 1 a difference in core mass at the first TP of < 5 % between a 2-$M_\odot$ non-rotating model and a 2-$M_\odot$ model with an initial rotation rate of 120 km s^{-1}. Also these models have core rotation rates that are too high when compared to asteroseismic observations, which means this trend is expected to hold as well in models that have cores that do match the asteroseismic rotation rates. Their s-process production in the AGB phase is however strongly dependent on the rotation rate, and those yields will likely be different in the models match the asteroseismic rotation rates.

The above mentioned studies discuss the effect of rotation on the stellar structure, but not on the chemical composition. The changes due to rotation in surface abundances pre-AGB in stars with an initial mass of 1-4 $M_\odot$ were performed by Charbonnel & Lagarde (2010) and Lagarde et al. (2011). They also include thermohaline mixing (see Section 2.2.2) in their models. They find that the thermohaline mixing accounts for the
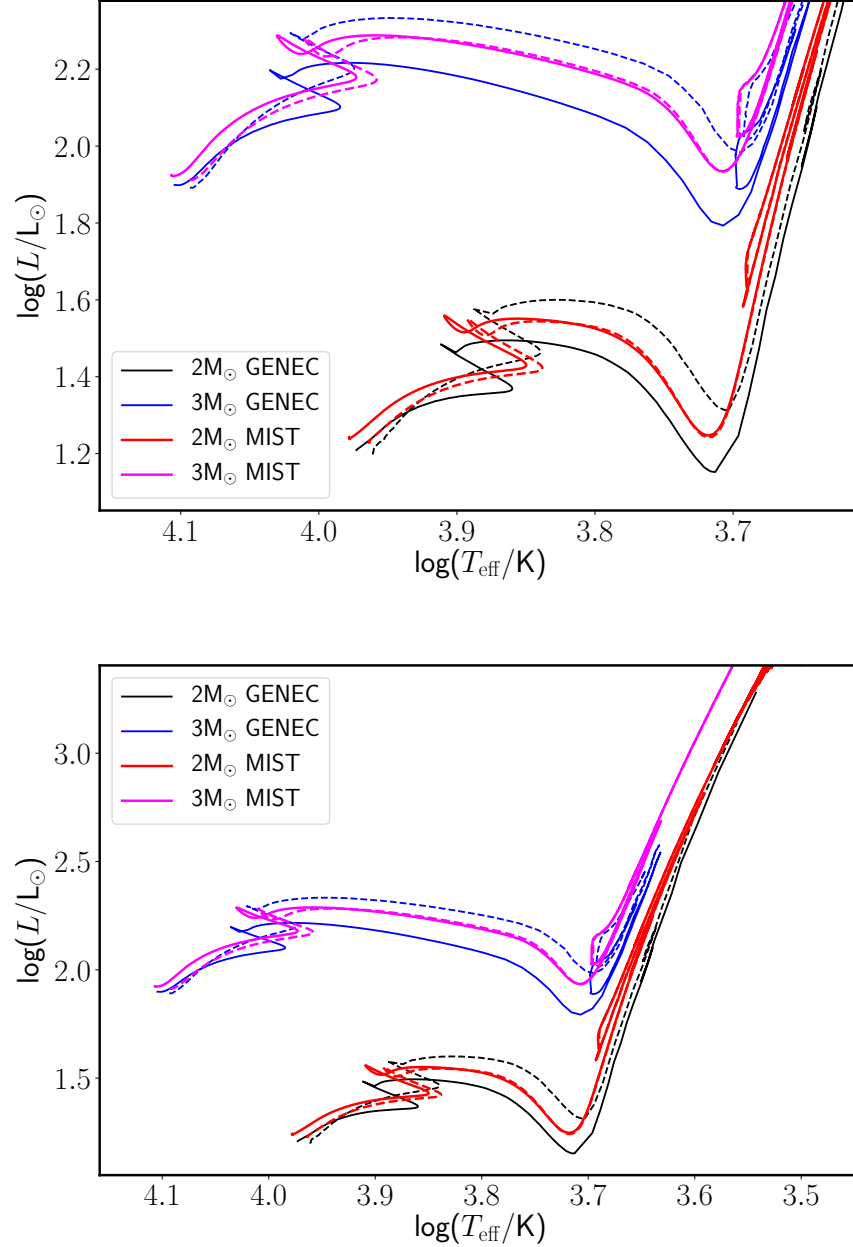
Figure 2.3: HRDs of non-rotating and rotating stellar evolution models at solar metallicity of two initial masses (2 and 3 $M_\odot$) and two codes: MESA models by the MIST group (Choi et al. 2016) and GENEC models by the Geneva group (Ekström et al. 2012). The non-rotating models are plotted in solid lines, the rotating models (initial rotation rate of $\frac{\Omega}{\Omega_{\mathrm{crit}}}$=0.4) in dashed lines, but in the same colour as the corresponding non-rotating model. The bottom panel shows the evolution up to the AGB phase, while the top panel is a zoomed in on the main sequence and the start of the RGB. Similar trends are visible in all models, with minor changes between the non-rotating and rotating models (see text for more details).

observed ratios of light elements in Galactic open glusters, field stars, and planetary nebulae. Rotationally induced mixing is able to add the star-to-star variations in those ratios, as well as structural changes leading to the thermohaline instability to occur at lower initial masses than in non-rotating models. Again, these models rotate at rates that do not match the asteroseismically obtained ones and the effect based on rotation in their models are therefore likely overestimated.

Currently there are only a few publications on stellar evolution models that do match the asteroseismically obtained core rotation rates. These publications all focus on how these core rotation rates are reached, and not on the effect of rotation on the chemical composition of the stars (see, e.g. Spada et al. 2016; Eggenberger et al. 2017; Tayar & Pinsonneault 2018). The goal of my thesis is to fill this gap. In the next Chapter I will introduce the initial parameters of models that will do this.

3   Methodology

The stellar evolution models presented in this thesis have been calculated with modules for experiments in stellar astrophysics (MESA, see Paxton et al. 2011, 2013; Paxton et al. 2015, 2018, 2019). MESA is open source, has independent modules for physics and numerical algorithms that can be used as stand-alones and runs well on desktops, laptops, and multi-core architectures. The code includes comprehensive microphysics and is being maintained and developed since its first release on 23 January 2007 by a dedicated code development team[1]. This combination makes MESA widely applicable in astrophysics. Extra physics is added and users are encouraged to share all information needed for others to recreate their results. The broad applicability to astrophysics of MESA is visible in the list of published results, which can be found at `http://mesastar.org/results`. It includes publications across the entire initial stellar mass-range, metallicity studies, studies on progenitors of supernovae and studies on processes like mass loss, tidal heating and gravity modes. The MESA revision used to calculate the models in this thesis is 8845, released on June 19 2016.

In this chapter I will present all input parameters for my MESA calculations, followed by sections on the details of the resolution and rotation settings of my MESA models. Then, I will present the second code I have used, a post-processing code called MPPNP, see Section 3.4. I used MPPNP to calculate the s-process nucleosynthesis. This chapter continues with an overview of the running times of each code and the machines used. The chapter ends with an introduction to each result chapter.

3.1   Input parameters MESA

Many of the input parameters for non-rotating processes have been chosen to match the ones in Nugrid papers (Pignatari et al. 2016; Battino et al. 2016; Ritter et al. 2018), so

---

[1]`mesa.sourceforge.net/index.html`

that my models can be used in conjunction with those papers. An overview is given in Table 3.1, which includes the settings to physics discussed in Chapter 2 and in the following subsections.

Table 3.1: Table with a summary of the MESA settings.

Parameter	Setting
Convection:	
Criterion	Schwarzschild
Semiconvection	Excluded
Thermohaline	Excluded
MLT mixing length α	1.73 (see Herwig 2005)
CBM:	
Treatment	Exp. decaying diffusion (Herwig et al. 1997)
During AGB	Double exp. decaying diffusion (Battino et al. 2016)
Mass loss:	
Starting at RGB	Reimers (1975): η_R=0.5
Starting at AGB	Blöcker (1995): η_B=0.01, 0.04, 0.5
Opacities:	
Log_{10}T=3.75 to 8.7	OPAL CO enhanced
Log_{10}T<3.75	Ferguson et al. (2005)
Chemical composition:	
Initial composition	Grevesse & Noels (1993)
Network	agb.net, 19 isotopes
Reaction rates	NACRE Angulo et al. (1999), with exceptions
Rotation:	
Angular momentum transport	Diffusive as in Heger, Langer & Woosley (2000)
f parameters	f_c=1/30, f_μ=0.05
Convective regions	Solid body

3.1.1   Initial composition and network

The reference solar abundance used in this thesis is taken from Grevesse & Noels (1993). The composition is followed in the MESA models by a network named agb.net which includes 19 isotopes: neutrons, ^{1}H, ^{2}H, ^{3}He, ^{4}He, ^{7}Li, ^{7}Be, ^{8}B, ^{12,13}C, ^{13,14,15}N,

^{16,17,18}O, ^{19}F, ^{22}Ne, and ^{56}Fe. A set of 27 reactions are used to calculate the changes in the composition. These 27 reactions include all the pp-chain reactions and the CN- and NO-cycles as listed in Section 1.1.2, as well as the triple-α reaction and several α-capture reactions: ^{12}C(α,γ)^{16}O, ^{14}N(α,γ)^{18}F(e^{+},ν)^{18}O, ^{18}O(α,γ)^{22}Ne, ^{13}C(α,γ)^{16}O, and ^{19}F(α,p)^{22}Ne. Together, the isotopes and reactions included are sufficient to track the energy generation of a low-mass AGB star with an initial mass of 2 M$_\odot$.

The NACRE reaction rate compilation (Angulo et al. 1999), is used for most reaction rates in the MESA calculations, with a few exceptions: the rate for ^{12}C(α,n)^{16}O is from Kunz et al. (2002), the rate for the ^{14}N(p,γ)^{15}O is from Imbriani et al. (2004) and the rate for triple-α is from Fynbo et al. (2005).

3.1.2 Mass loss

The Reimers formula for mass loss (Reimers 1975) is used during the RGB phase:

$$\dot{M} = 4 \times 10^{-13} \eta_{\mathrm{R}} \frac{(L/\mathrm{L}_\odot)(R/\mathrm{R}_\odot)}{M/\mathrm{M}_\odot} \mathrm{M}_\odot/[yr^{-1}] \tag{3.1}$$

with η_{R} being an efficiency factor. This formula was determined by analysing the line profiles in spectroscopic observations of cool giant stars, and is widely used in the stellar evolution community when modelling giants. During the AGB phase however, mass loss is observed to be higher than the Reimers formula predicts (Blöcker 1995; Höfner & Olofsson 2018). For this phase we change to the Blöckers mass loss formula (Blöcker 1995) in the AGB phase:

$$\dot{M} = 4.83 \times 10^{-9} \eta_{\mathrm{B}} \frac{(L/\mathrm{L}_\odot)^{2.7}}{(M/\mathrm{M}_\odot)^{2.1}} \frac{\dot{M}_R}{\eta_{\mathrm{R}}} \mathrm{M}_\odot [yr^{-1}] \tag{3.2}$$

with η_B being an efficiency factor for this mass loss formula. This formula was built on the results of Reimers (1975) and atmosphere modelling of Mira-like stars by Bowen (1988). The Blöcker mass loss formula was constructed with three goals in mind: the formula had to reflect the strong mass loss in AGB stars, had to be applicable to stellar evolution equations, and had to agree with the observed initial-final mass relationships. Several mass loss formulae exist for the AGB phase and were compared in Stancliffe & Jeffery

(2007). This paper compares the mass loss formulae of Reimers (1975); Blöcker (1995); Vassiliadis & Wood (1993) for a 1.5-$M_\odot$ star at Z=0.008 and reports large differences in the yields of the models. All yields, however, are mostly consistent with the observations and therefore a ranking of mass loss formulae was not provided.

The efficiency factors of the Reimers and Blöcker mass loss formulae have been set to values used in previous publications of collaborators (see Nugrid papers Pignatari et al. 2016; Battino et al. 2016): η_R=0.5, and η_B=0.01 during the O-rich phase and η_B=0.04 during the C-rich phase. This change in η_B is motivated by observational constraints, like the maximum level of C enhancement seen in C-rich stars and planetary nebulae (Herwig 2005; Marigo & Girardi 2007; Mattsson, Wahlin & Höfner 2010; Nanni et al. 2017), as well as in hydrodynamical studies of mass loss rates in C-rich stars, see Mattsson & Höfner (2011).

It is common for convergence issues to arise during the final TPs of stellar evolution calculations and these issues also occur in the models presented in this thesis. While these issues are common, it is unclear if their nature is physical or numerical as discussed in detail in Lau et al. (2012). Observational constraints are needed to settle this issue. There are however two options formulated on how to proceed, the first being the continuation of the AGB phase with a higher mass loss rate and the second the ejection of the whole remaining envelope (see Wood & Faulkner 1986; Herwig, Bloecker & Schoenberner 1999; Sweigart 1999; Lau et al. 2012). We proceed with the models by increasing the mass loss parameter to η_B=0.5, which allows for a smooth continuation of the models into the white dwarf phase.

The effect of rotation on mass loss in my models is discussed in Section 3.3.

3.1.3   Convective boundary mixing

The Schwarschild and Ledoux criteria for convection do not give a description of the boundaries of the convective zones. Their derivations predict that displaced fluid elements have zero acceleration at the boundary, but their velocity is not equal to zero. This means that they should be able to continue travelling into the non-convective neighbouring

region. One way of predicting the extent of convective boundary mixing (CBM) is using the exponentially decaying diffusion coefficient by Herwig et al. (1997). This coefficient is based on the convective boundaries found in the work of Freytag, Ludwig & Steffen (1996) that could best be described by:

$$D_{\text{CBM}} = D_0 \exp\left[\frac{-2z}{f_1 H_{P0}}\right] \tag{3.3}$$

where D_0 and H_{P0} are the diffusion coefficient and pressure scale height at the convective boundary respectively, and z is the distance calculated from the formal convective boundary into the radiative zone. This CBM treatment starts inside the convective zone, at distance $f_1 H_{P0}$ from the edge and that is the location where D_0 is set. By doing so, the problem of D=0 at the exact edge of the zone is avoided. Denissenkov & Tout (2003) and Herwig et al. (2007), have shown the diffusion coefficient for certain convective boundaries in the AGB phase, and their effect on the AGB phase has been investigated in Battino et al. (2016). This CBM treatment for the AGB phase is based on matching the slope of the diffusion coefficients found in Denissenkov & Tout (2003) and Herwig et al. (2007). They found that this could best be done by adding a second exponential:

$$D_2 = D_0 \exp\left[-2z_2/(f_2 H_{P0})\right] \tag{3.4}$$

which is adopted for distances of $z > z_2$. The diffusion coefficient for CBM at distances $z > z_2$ is:

$$D_{\text{CBM}} = D_2 \exp\left[-2(z - z_2)/f_2 H_{P0}\right] \tag{3.5}$$

As in Pignatari et al. (2016); Battino et al. (2016); Ritter et al. (2018), I use $f_1 = 0.014$ for all convective boundaries expect for the one below the TP and below the TDU, for which I use the double exponential method as described above. The values of f_2 and D_2 for the two regions it is used are summarised in Table 3.2, and match the values in Battino et al. (2016).

Table 3.2: Table with the f_2 and D_2 values used in the MESA calculations.

Parameter	TP	TDU
f_2	0.14	0.25
D_2 (cm^{2}s^{-1})	10^5	10^{11}

3.1.4   Minor code alterations

Sometimes the mixing length of a convective zone is larger than the zone itself. I found that it is standard treatment in MESA since revision 3713 onwards to limit the mixing length to the size of the zone, a procedure named 'clipping'. The inclusion or exclusion of this treatment leads to similar nucleosynthesis results as it only affects very small convective regions (see Battino et al. 2016). However, as 'clipping' is a numerical fix to a problem created by implementing the poorly understood physical process that is convection, it is not used in this work.

I also altered the implementation of the CBM to ensure the double exponential CBM only becomes active during the TPs and TDUs. Finally, I made a modification related to the implementation of opacities in MESA. As in Pignatari et al. (2016) and Battino et al. (2016). I only use the OPAL Type 2 opacities throughout the evolution. To do this in revision 8845, I needed to adjust the MESA source code to cancel the blending of the two types of OPAL opacity tables as this blending created an opacity jump in the region of interest.

3.2   Resolution settings

In this Section I present all resolution settings used in my MESA calculations. The same settings are used for non-rotating and rotating models. Most settings are either the same as in Pignatari et al. (2016); Battino et al. (2016), or stricter.

Two files in MESA working directories allow the user to change the settings for all parameters either before the calculation starts, or during the calculation. The first is

called `inlist`, the second `run_star_extra.f` (located in the `src`-folder in the working directory). I use both files, which allows me to calculate the main sequence to the end of the AGB phase without human intervention. My `inlist` only contains the settings needed to start the model, like initial mass, metallicity, general output settings, and the settings needed for the main sequence calculation. Settings for later phases, like CBM settings for the AGB phase, are included in the `run_star_extra.f` file. The change in mass loss during the AGB phase is also done via the `run_star_extra.f` file, as well as minor changes in resolution settings. Examples of both files can be found Appendix B. The general resolution setting in MESA is called `varcontrol_target`, which is the target value for relative variation in the structure of the star from one models to the next. The variables included in varcontrol are density, temperature, radius, luminosity, energy, velocity, and gas pressure. This target is set to 5×10^{-5} in my `inlist`, while the MESA default is 10^{-4}. This default time step adjustment is based on the comparison of the actual variation and this value. If the actual variation is smaller than the target, the time step will increase. Thus the higher this target value, the bigger the average time step and the shorter the running time will be. However, many other settings for the time resolution exist which will influence the time step, which will be discussed below.

Several extra settings for the time resolution are limits on the magnitude of change in $\log_{10}$ central density, effective temperature, central temperature, and luminosity:

```
delta_lgRho_cntr_limit = 0.05
delta_lgRho_cntr_hard_limit = 0.1

delta_lgT_cntr_limit = 0.01
delta_lgT_cntr_hard_limit = 0.02

delta_lgTeff_limit = 0.01
delta_lgTeff_hard_limit = 0.02

delta_lgL_limit = 0.1
```

```
delta_lgL_hard_limit = 0.2
```

when the 'limit' is reached the next time step will be reduced, while when the 'hard limit' is reached the current time step will be recalculated with a smaller time step. These four 'limit' values are the default values, the four 'hard limit' values are set to be twice the correspoding 'limit'. No default exists for these 'hard limits'. Extra luminosity limits are activated to increase the time resolution during PDCZ:

```
delta_lgL_He_limit = 0.01
lgL_He_drop_factor = 0.5
lgL_He_burn_min = 2.0
```

The first line is another limit on the magnitude of the change in He burning luminosity, the second line is the factor by which the limit is multiplied when the He burning luminosity is reducing, and the third line limits the activation of the limits He burning luminosity to values higher than $\log_{10}L_{He}=2$. The last condition thus ensures the other two limits are only active during the PDCZ. Default values for these three settings are 0.025, 1, and 2.5. Limits to changes in abundances are also included for the time resolution:

```
dH_limit_min_H = 1.e-2
dH_limit = 0.1

dH_div_H_limit_min_H = 1d-5
dH_div_H_limit = 0.5

dHe_limit_min_He = 1.e-2
dHe_limit = 0.1

dHe_div_He_limit_min_He = 1d-5
dHe_div_He_limit = 0.5
```

The second line means that when the change in H abundance is larger 0.1, the next time step is reduced. The first line gives a limit on when this limit on the change of H is activated: only when the H abundance is larger than 0.01. The lines 3-4 repeat this procedure for the relative change of the H abundance, again this limit is only activated when the H abundance is larger than 10^{-5}. The lines 5-8 repeat these limits for the absolute and relative change of the He abundance. The default settings for these limits are 10^{99} for the absolute change of both elements. The default values for limits on the relative change of both elements are respectively 10^{-3} and 0.9, so all eight limits are set to stricter values in my calculations than the defaults. All eight limits are only activated when the abundance decreases.

Resolution settings for the spatial/mass zoning have also been included to allow for extra mesh points at regions of interest, for instance the ^{13}C-pocket. The resolution settings are:

```
xa_function_species(1) = 'h1'
xa_function_weight(1) = 10
xa_function_param(1) = 1d-9

xa_function_species(2) = 'he4'
xa_function_weight(2) = 10
xa_function_param(2)  = 1d-4

xa_function_species(3) = 'c13'
xa_function_weight(3) = 25
xa_function_param(3) = 3d-10

xa_function_species(4) = 'n14'
xa_function_weight(4) = 25
xa_function_param(4) = 5d-9
```

```
omega_function_weight = 50
```

These different settings are included in the following equation:

```
xa_function = xa_function_weight*log10(xa + xa_function_param)
```

where the 'weight' and 'param' are set for the four elements defined in the 'species' line, and 'xa' is the abundance of the element in the mesh point for which the function is calculated. Default settings only exist for ^{4}He, and are 30 for weight and 10^{-2} for the param, which are the threshold settings for a split of a mesh point into two mesh point. Using these stricter mesh resolution settings allows for extra mesh points in the intershell during AGB phase, as shown in Table 3.4.

Another reason why these settings are much stricter than the defaults is that there are barely any resolution settings dedicated to rotation. The only one is the above included `omega_function_weight`, which allows for extra mesh points in regions of high Ω values and not gradients. The regions with Ω gradients are however more important for the resolution, as this is where most rotationally induced instabilities are active. These instabilities lead to changes in abundances though, as these instabilities are calculated on the interface between two mesh points, with gradients and derivatives being calculated for the change in a variable from one zone to the next. Changes in abundance are dealt with in the mesh resolution settings.

As can be expected, there are more mesh points in the rotating models than in the non-rotating ones as shown in Tables 3.3 and 3.4. Table 3.3 list the total number of time steps per evolutionary phase, the duration of the phase in years, and then the ratio showing the typical length of the time steps in each phase. The same information is given about the total number of mass zones and the typical mass per mass zone in each phase. These values are given for both the non-rotating 2-M$_\odot$ model and a rotating 2-M$_\odot$ model, the latter includes an additional, artificial viscosity to enforce core rotation rates comparable to the asteroseismically obtained values. The main differences between these two models can be found in the number of mass zones, especially in the TP-AGB phase,

confirming that the changes in abundances due to rotationally induced mixing and the changes in Ω are included in the above presented mesh resolution settings.

Table 3.4 shows the same quantities as in Table 3.3, but for three important AGB phases: the pulse driven convective zone, the third dredge-up, and the ^{13}C-pocket. Again the rotating model has more mesh points, but only in the ^{13}C-pocket. The convective regions are not affected by the rotationally induced mixing, as convection works on the dynamical time scale and dominant rotationally induced instabilities work on the secular one.

It is not common in the stellar evolution community to publish detailed resolution settings and detailed information on the time steps and mass zones used. Three papers do mention those details for non-rotating studies, either for the AGB phase (Straniero et al. 1997; Pols & Tout 2001), or for the general evolution (Fields et al. 2016, a study performed with MESA as well). The number of time steps and mass zones as presented in Table 3.4 are larger than the values presented by Straniero et al. (1997); Pols & Tout (2001), and the typical length per time step and the typical mass per mass zone are smaller than in both two papers. The focus of Fields et al. (2016) is on the effect of the experimental uncertainties in H and He burning reaction rates, and the number of mass zones in their models is therefore larger than mine during the main sequence. Similar values for the number of time steps and mass zones are obtained in the AGB phase.

The only study I found on resolution settings in rotating models is Lau, Izzard & Schneider (2014), who study the effect of resolution on the surface enrichment of ^{14}N in massive stars during the main sequence. The authors of this paper find that the nitrogen enrichment in their models is similar when using between 100 and 10000 time steps for the main sequence, when using a fixed mass per zone of 0.05 M$_\odot$. My models have around 400 time steps during the main sequence, with a typical mass per zone of 0.002 M$_\odot$.

In the following result chapters I present abundance profiles and time evolution plots that show well resolved features.

Table 3.3: Table with the typical numbers of time steps and mass zones of the MESA calculations, showing a non-rotating and rotating model ('250 6') from Chapter 5. The non-rotating model experiences one extra TP in its TP-AGB phase than the rotating model, hence the difference in number of time steps for the TP-AGB phase. Concerning the 'final' white dwarf points: the default MESA stopping criterion for WD tracks is used. This criterion is based on the equations of state currently implemented in MESA. This stopping criterion is reached at $\log_{10}L/L_\odot \simeq$ -5.25 and $\log_{10}T_{\rm eff}/{\rm K} \simeq$ 3.41.

Phase	Time steps	Duration(yr)	yr/step	Mesh zones	$M_\odot$/zone
		Non rotating			
MS	428	9.2×10^8	2.1×10^6	1000	2.0×10^{-3}
H shell burning	1537	4.3×10^7	2.8×10^4	2200	1.3×10^{-3}
Core He burning	1250	2.9×10^8	2.3×10^5	2300	1.6×10^{-3}
E-AGB	1881	2.0×10^7	1.1×10^4	3200	2.7×10^{-4}
TP-AGB	103867	3.5×10^6	33	up to 5500	2.7×10^{-4}
Post AGB - PN	5354	3.7×10^4	6.9	4500	1.3×10^{-4}
WD	1027	1.4×10^{10}	1.4×10^7	down to 1600	3.9×10^{-4}
		Rotating			
MS	393	9.6×10^8	2.4×10^6	1200	1.7×10^{-3}
H shell burning	1652	4.5×10^7	2.7×10^4	2200	9.1×10^{-4}
Core He burning	1311	2.9×10^8	2.2×10^5	2300	8.6×10^{-4}
E-AGB	1472	1.8×10^7	1.2×10^4	3200	1.6×10^{-3}
TP-AGB	96016	3.5×10^6	36	up to 8000	1.9×10^{-4}
Post AGB - PN	17545	2.0×10^4	1.1	6500	9.5×10^{-5}
WD	1020	1.4×10^10	1.3×10^7	down to 1700	3.6×10^{-4}

Table 3.4: Table with the typical numbers of time steps and mass zones of the AGB phase in the MESA calculations, showing a non-rotating and rotating model ('250 6') from Chapter 5.

Phase	Time steps	Duration (yr)	yr/step	Mesh zones	Mass ($M_\odot$)	$M_\odot$/zone
		Non rotating				
PDCZ	650	40	0.06	4200	0.025	6.0×10^{-6}
TDU	400	200	0.5	2900	0.0035	1.2×10^{-6}
^{13}C-pocket	2000	5.0×10^5	250	5300	1.0×10^{-4}	1.9×10^{-8}
		Rotating				
PDCZ	650	40	0.06	4200	0.025	6.0×10^{-6}
TDU	350	200	0.5	3100	0.0035	1.1×10^{-6}
^{13}C-pocket	2000	5.0×10^5	250	7600	1.0×10^{-4}	1.3×10^{-8}

3.3   Rotation settings

Most calculations presented in the result chapters include rotation, for which a large number of extra input parameter have to be included. Here I present all these parameters, as well as the effect of the inclusion of rotation on various physical processes already discussed in Section 3.1. This section ends with the code modification made to enhance transport of the angular momentum, which is needed to match the core rotation rates derived from asteroseismic observations, as discussed in Section 1.3.

3.3.1   Input parameters

There are two free parameters in the implementation of rotation in MESA: the first is f_c (`am_D_mix_factor`) in Eq. 2.70, which allows the user to vary the contribution of the rotationally induces instabilities to the mixing of chemical elements (first introduced by Pinsonneault et al. 1989). The second is f_μ (`am_gradmu_factor`), which is added in front of the molecular weight gradient ∇_μ that appears in the derivation of the SH instability, secular shear, and ES circulation see Section 2.4. The parameter f_μ determines the dependence of the individual instability on the molecular weight gradient. Both f parameters are introduced to compensate for various simplifications in the derivation of the instabilities, and are limited to values between 0 and 1.

The values of f_c and f_μ are set to 1/30 and 0.05 respectively in Heger, Langer & Woosley (2000). The value of the first f parameter is based on theoretical work by Chaboyer & Zahn (1992), who found a value of 1/30 for the combination of shear and meridional circulation. The value of the second f parameter is calibrated by Heger, Langer & Woosley (2000) to match the surface enrichment of nitrogen in massive stars at the end of the main sequence. Other values have been used for both parameters and are summarized in Table 3.5. For instance, Pinsonneault et al. (1989) calibrated f_c and f_μ to the Sun. They found that the f_μ value has little effect on their solar model, and is therefore set to the 'standard' value of 1. Their f_c value is set to 0.046, similar to the

value of Chaboyer & Zahn (1992), to match the lithium depletion in the Sun. Based on VLT Flames data on rotational velocities and nitrogen surface abundances from Hunter et al. (2009), Brott et al. (2011) found that a value of f_c=0.0228 best fits the data. This is only half the value of Pinsonneault et al. (1989). Brott et al. (2011) set the f_μ value to 0.1, following the calibration of Yoon & Langer (2005) of their models including the TS-dynamo to He surface abundances at the end of the main-sequence. Finally I mention that also Chieffi & Limongi (2013) calibrated these f parameters, and set the f_c value to 1 (referred to as 'conservative approach'), and fitted f_μ to match the nitrogen surface enrichment at the end of the main-sequence. What makes the calibration complicated, is that the two parameters are dependent on each other and convective boundary mixing. The dependence on these two f parameters of the s-process production in low-mass AGB stars has been investigated by Siess, Goriely & Langer (2004) and Piersanti, Cristallo & Straniero (2013). Siess, Goriely & Langer (2004) varied f_μ between $0-0.05$ and found that f_μ=0 leads to no s-process production even for very slow rotators, while slow rotators with f_μ=0.05 results in s-process production. Piersanti, Cristallo & Straniero (2013) found that varying f_μ between $0.05-1$ and f_c between $0.04-1$ results in variation in s-process production similar to the spread of s-process production obtained by changing the initial rotation rate between 10 and 120 km s^{-1}.

In this thesis I used the same values as Heger, Langer & Woosley (2000). The main reason for this choice is that it is now know from asteroseismology observations that a process of angular momentum transport is missing from the implementation of rotation in stellar evolutionary codes. This knowledge currently eliminates the possibility of a meaningful calibration. Furthermore, the calibrations of these parameters in codes comparable to MESA, being Heger, Langer & Woosley (2000) and Brott et al. (2011), give similar values (see Table 3.5) so possibly the range of values to be used for the f parameters is small. The values from Pinsonneault et al. (1989) and Chieffi & Limongi (2013) are different, but less reliable as the models presented in Pinsonneault et al. (1989) show little effect to changes in f_μ, and the models presented in the result section in Chieffi & Limongi (2013) are calculated with another implementation of rotation that does not include f parameters.

Table 3.5: Calibration of f parameters in stellar evolution codes.

f_c	f_μ	reference
0.046	1	Pinsonneault et al. (1989)
1/30	0.05	Heger, Langer & Woosley (2000)
0.0228	0.1	Brott et al. (2011)
1	0.03	Chieffi & Limongi (2013)

Instead of varying the f parameters, the strategy in this thesis is to use observations to constrain the missing process of angular momentum transport.

For each of the rotationally induced instabilities there are several input parameters available in MESA. These include a factor to multiply the strength with (`D_ES_factor` etc., 0 means the instability is not used, 1 is the standard value), and the possibility to smooth the diffusion coefficient over time and mass zones. None of the smoothing methods are used in my models, with the only exception being in the models including the TS-dynamo in Section 4.3. The possible effects and the disadvantages of the smoothing methods are discussed in Section 5.A.3.

The models presented in the result chapters include different sets of rotationally induced instabilities, to test the effect of the current implementation of the instabilities on both the transport of angular momentum and the mixing of chemical elements. A typical `inlist` can be found in Appendix B.

3.3.2 Code alterations for the enhanced transport of angular momentum

As introduced in Chapter 1, asteroseismic observations have shown that an efficient mechanism for the transport of angular momentum is missing from the current stellar evolution theory. While the missing mechanism is now a well known, code-independent conclusion, the physical nature of this mechanism is still unknown. The impact of the Tayler-Spruit dynamo on the internal rotation was investigated by Cantiello et al. (2014),

who found that this mechanism does not provide sufficient coupling between the core and the envelope in the post main-sequence evolution to reproduce the low values of core rotation for red giants. A preliminary study of the effect of internal gravity waves by Fuller et al. (2014) has reached the same conclusion. Mixed oscillation modes were investigated by Belkacem et al. (2015), who found that this transport mechanism seem to play only a negligible role during the subgiant and early red-giant phase, but it could be important later on for more evolved red giants. In the following subsections, a set of code modifications to investigate this missing mechanism are introduced.

To reveal the physical nature of the missing process of transport of angular momentum, I start by characterizing its efficiency by including an additional, artifcial viscosity ν_{add} (as introduced in Section 1.3). The implementation of this ν_{add} is straightforward, as it is a constant value, which is added to the total diffusion coefficient used in the transport of angular momentum equation:

$$\left(\frac{\partial \Omega}{\partial t}\right)_m = \frac{1}{j}\left(\frac{\partial}{\partial m}\right)_t \left[(4\pi r^2 \rho)^2 j D_{\text{am}}\left(\frac{\partial \Omega}{\partial m}\right)\right] - \frac{2\Omega}{r}\left(\frac{\partial r}{\partial t}\right)_m \left(\frac{1}{2}\frac{d\ln j}{d\ln r}\right) \tag{3.6}$$

and:

$$D_{\text{am}} = \sum D_{\text{rot,i}} + \nu_{\text{add}} \tag{3.7}$$

where $D_{\text{rot,i}}$ is the sum over all rotationally induced instabilities.

Spada et al. (2016) tested the dependency on the angular momentum transport efficiency on internal rotation and published results using a two-zone model. Their approach was to explore a simple power law dependence of the internal rotation by setting the angular momentum diffusion coefficient to:

$$D = D_0 \left(\frac{\Omega_{\text{core}}}{\Omega_{\text{env}}}\right)^\alpha \tag{3.8}$$

Where D_0 and α are parameters to be determined. Note that the implementation results in a diffusion coefficient that is dependent on time via the ratio of Ω's, but independent of spatial coordinate. Their values scale with and are sensitive to the internal rotational profile. In Spada et al. (2016), solid body rotation is enforced until the TAMS, or until 1Gyr after the TAMS. The latter settings are needed for them to match asteroseismically

obtained core rotation rates of both subgiants and giants.

The extra viscosity ν_{add} and the approach by Spada et al. (2016) are only included in the transport of angular momentum and not in the equation for mixing of chemical elements. The reason for this is that there is ample observational evidence that a strong process of transport of angular momentum is missing, while there is no observational evidence that mixing of chemical elements needs to be strongly increased in low- and intermediate-mass stars. I did investigate the inclusion of ν_{add} in the mixing of chemical elements, the results are presented in Section 6.2.

3.3.3   Rotation and mass loss

The angular momentum removed via winds corresponds to the angular momentum contained by the removed mass. Rotationally enhanced mass loss is generally not included in low-mass evolutionary models, as there is only observational proof of rotationally enhanced mass loss in massive stars (i.e, see Gathier, Lamers & Snow 1981; Vardya 1985; Nieuwenhuijzen & de Jager 1988). Choi et al. (2016) therefore only uses the rotationally enhanced mass loss for stars with an initial mass above 10 $M_\odot$, Ekström et al. (2012) however includes it for all their rotating models.

I performed a test to investigate how sensitive the core rotation rate is to this loss in angular momentum due to the mass loss caused by winds. The test is as follows: I ran three rotating models (initial mass of 2 $M_\odot$, metallicity of Z=0.01, initial rotation rate of 125 km/s) with as only difference the mass loss. In model 1 I set this to my standard settings: Reimers mass loss efficiency of 0.5, no rotationally enhanced mass loss. In model 2 the only change from model 1 is that I set the Reimers mass loss efficiency to 1.0, which results in a doubled mass loss rate, see eq. 3.1. Model 3 includes the rotationally enhanced mass loss factor as in Langer (1998):

$$\dot{M}(\Omega) = \dot{M}(0) \left(\frac{1}{1 - \Omega/\Omega_{\text{crit}}} \right)^{\xi} M_\odot/[yr^{-1}] \tag{3.9}$$

$$\text{with: } \Omega_{\text{crit}}^2 = \left(1 - \frac{L}{L_{\text{Edd}}} \right) \frac{GM}{R^3} \tag{3.10}$$

Table 3.6: Table of the model characteristics of the three models included in the mass-loss parameter study. Listed are the total mass of the star, core rotation rate, and surface angular momentum at the moment of the first thermal pulse. Relative differences to the standard model are given between brackets.

		$M_{*,\mathrm{TP1}}$ $(M_\odot)$	Ω_core (s^{-1})	j_surface $()\mathrm{cm}^2\ \mathrm{s}^{-1})$
Model 1	standard	1.98	5.87E-02	3.91E17
Model 2	higher η	1.95 (-1.5%)	5.69E-02 (-3.0%)	3.70E17 (-5.5%)
Model 3	rot.enhanced	1.98 (0%)	6.08E-02 (+3.6%)	3.94E17 (0.77%)

where $\dot{M}(0)$ is the non-rotating mass-loss rate, ξ is assumed to be 0.43, Ω_crit is the critical angular velocity at the surface and the Eddington luminosity L_Edd is a mass-weighted averaged luminosity.

The results of tests are shown in Table 3.6. For all three models, the total mass, the core rotation rate, and the specific angular momentum at the surface are shown at the moment of the first TP. All parameters in Model $2-3$ are within 6 % of the Model 1 parameters. This means that the changes in the mass loss routine do not influence the core angular momentum, which justifies using the Model 1 parameters. The reason for this is that the mass loss during the pre-AGB evolution is small, and the surface rotation rate throughout the evolution of low-mass stars is a small fraction of the critical velocity. Therefore the rotationally enhanced mass loss is negligible. During the AGB phase the mass loss is significant and will result in removing the whole envelope. During this evolutionary phase however, the molecular weight and angular velocity gradients built up at the edge of the core are strong enough to eliminate diffusion over this edge. Extra coupling between core and envelope is needed to overcome these gradients and allow for angular momentum to be transported from the inner to the outer regions of the star, in order to match the asteroseismically obtained rotation rates (see Chapter 4).

3.4   Post-processing code MPPNP

Calculating a stellar evolution model with MESA, or with any stellar evolution code, with a full s-process nuclear reaction network is costly due to the large number of isotopes and reactions that have to be included. The memory needed for calculations within stellar evolution codes is proportional to the amount of isotopes and mesh points included in the model. As memory is finite, this means that one can either include a large network or a large number of mesh points. This is one of the reasons why stellar evolution calculations and detailed nucleosynthesis are often decoupled and performed separately. The only requirement for this is that the network included in the stellar evolution calculations is able to calculate the energy generation at any point in the star in sufficient detail. This is done as well for the models presented in this thesis. In Section 3.1.1 I describe the network included in my MESA calculations, which indeed includes all energy generating reactions and isotopes. I have performed the detailed s-process nucleosynthesis calculations with MPPNP, which is described next. Following this are presented a composition comparison between MESA and MPPNP.

3.4.1   Nuclear reaction network in MPPNP

Using the MESA output files, the detailed nucleosynthesis can be calculated with MPPNP (Multi-zone, Post-Processing Nucleosynthesis Parallel), described in Pignatari et al. (2016). This code is able to calculate the nucleosynthesis over the whole star (=multi-zone), and is parallelised with MPI (see `https://www.mpi-forum.org/docs/`). I use the same reaction network as in Pignatari et al. (2016), and other NuGrid papers like Battino et al. (2016) and Ritter et al. (2018). This network includes about 10^3 isotopes between H and Bi, and about 50000 nuclear reactions. The network is dynamic, isotopes are added to and removed from the network depending on stellar conditions. By allowing for these changes to the network, the calculation can be made more efficient as nuclear reactions that do not lead to a change in abundance are not calculated (see Bennett et al. 2012; Pignatari et al. 2016, for details).

The reaction rates are taken from different data sets: the NACRE compilation (Angulo et al. 1999) is used for the charged particle reactions from H to Z<14 (^{28}Si(p,γ)^{29}P is the final reaction included in this dataset), Iliadis et al. (2001) is used for the proton-induced reaction for A=20-40 (starting with ^{20}Ne(p, γ)^{21}Na and ending with ^{40}Ca(p, γ)^{41}Sc), updating some of the reactions in Angulo et al. (1999). When more recent updates are available, then these are included: Fynbo et al. (2005) for triple-α, Kunz et al. (2002) for ^{12}C(α, γ)^{16}O, and Imbriani et al. (2004) for ^{14}N(p,γ)^{15}O. These settings correspond to the MESA network settings. Concerning the important neutron sources, Heil et al. (2014) is used for ^{13}C(α,n)^{16}O and Jaeger et al. (2001) for ^{22}Ne(α,n)^{25}Mg.

Neutron capture reaction rates are taken from the Kadonis compilation (Dillmann et al. 2014). Some exceptions are the neutron-capture cross sections for the Zr isotopes, for which the recommended rates of Lugaro et al. (2014) are used. The β-decay and electron-capture rates are taken from Fuller, Fowler & Newman (1985), Oda et al. (1994), Langanke & Martínez-Pinedo (2000), and Aikawa et al. (2005), completed with the JINA reaclib library Cyburt et al. (2010).

For every stellar evolution time step, the temperature, the density, and the total diffusion coefficient are used to calculate the abundances of a 10^3-isotope nuclear reaction network. This is followed by a time implicit diffusion solver, meaning that the solver uses information of both the current and the next time step to calculate the composition of the next time step. This is computationally expensive, but numerically more stable than using only the current time step in the calculation (as in explicit solvers). The reaction flux of each isotope at current state is used to adapt the problem size every time step and in every computational grid cell. The combination of multi-zone calculations and the inclusion of the diffusion coefficient in the calculations, means that MPPMP can be used for rotating models as well.

3.4.2   Comparison MPPNP-MESA

When using two separate codes for stellar evolution and detailed nucleosynthesis instead of one, the accuracy of the chain of codes has to be checked. In Fig. 3.1 I compare the

abundances of four main isotopes calculated by MESA and MPPNP. The profiles of MESA are drawn in colour, with the MPPNP profiles in a dashed black line. In the top panel, the region from the core up to the start of the convective envelope is shown for a non-rotating 2.5-$M_\odot$ model at the start of the AGB phase. In the bottom panel, the profiles are shown at the end of the AGB phase, zoomed into the ^{13}C-pocket region. The main isotopes within the intershell are shown, and the abundance profiles mostly overlap. Differences come from the fact that in MESA the mixing and nucleosynthesis are calculated at the same time, while in MPPNP these calculations are performed separately.

To quantity this comparison I performed a χ^2-test (Pearson 1900), which is a statistical hypothesis test for observed and predicted distributions. The purpose of the test is to find out how likely the observed distribution is, assuming the null hypothesis is true. This is done by calculating the χ^2-value:

$$\chi^2 = \sum_{i=1}^{nz} \frac{(x_{i,\text{MPPNP}} - x_{i,\text{MESA}})^2}{x_{i,\text{MESA}}} \tag{3.11}$$

with i being the number of zones, and nz the total number of zones. This χ^2 value is then transformed in a probability. The χ^2 values are shown in Table 3.7 for all four mass fractions at the start and end of the AGB phase. The whole mass range shown in Fig. 3.1 is included in the analysis, but mass fractions below 10^{-6} are excluded. The null hypothesis is defined as that the two distribution are the same. A value for χ^2 close to zero means the probability of the null hypothesis to be rejected is small. The exact value for these probabilities per χ^2 values is given in Table 3.7 between brackets. The ^{1}H mass fractions of both codes at the start of the TP-AGB phase are identical, and no χ^2 values is given.

Commonly chosen values for the significance level of the probabilities are 0.05 and 0.1, which means that there is a 5% or 10% (respectively) chance of concluding that a difference exists, while the distributions are the same. All eight probabilities presented in Table 3.7 are above both values, and thus the null hypothesis is statistically significant. Unfortunately, χ^2 values of other post-processing codes are not published, so I cannot provide a comparison of my values.
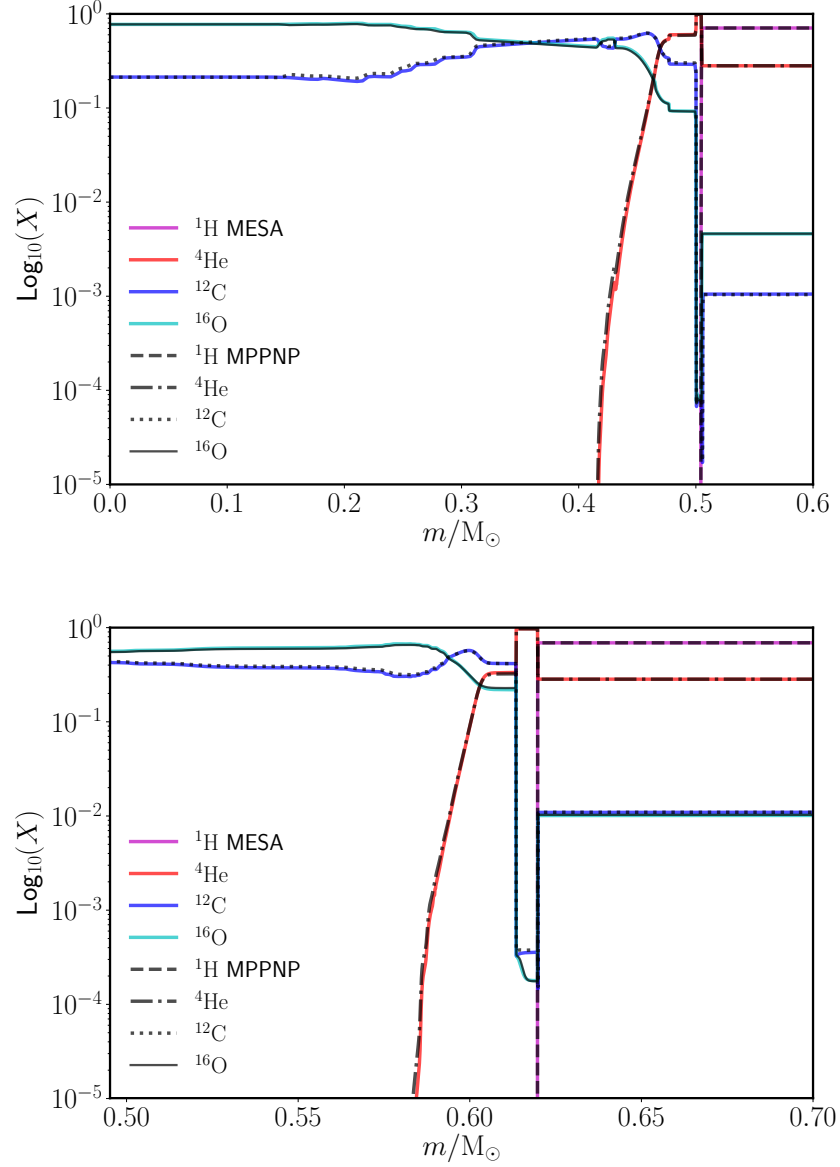
Figure 3.1: Comparison between chemical composition of MESA and MPPNP. Top panel shows the abundances of the main isotopes at the start of the AGB phase. The bottom panel the same isotopes at the end of the AGB phase, zoomed into the ^{13}C-pocket region. Mass fractions of MPPNP is shown in black lines plotted over the MESA abundance profiles which are drawn in colour. The χ^2 values for these eight comparisons are shown in Table 3.7. The profiles are taken from the non-rotating model presented in Chapter 5.

Table 3.7: Table with the χ^2 values of the comparison between MESA and MPPNP. The value between the brackets is the probability corresponding to the χ^2-value. The null hypothesis is that the mass fraction profiles from both codes are the same at the start and and of the TP-AGB, corresponding to a probability of 1.

isotope	χ^2 (p) start TP-AGB	χ^2 (p) end TP-AGB
^{1}H	-	0.0455 (0.83)
^{4}He	0.0826 (0.77)	0.854 (0.36)
^{12}C	0.178 (0.67)	1.42 (0.23)
^{16}O	0.00525 (0.94)	1.78 (0.18)

3.5 Computational cost and architectures

In this Section I will explain details of the running times of the different codes used and which machines were used for the calculations. Both codes are parallelised (MESA with OpenMP and MPPNP with MPI), so I will also discuss how many cores I used for each calculation.

How well the codes scale, meaning the extra speed-up in computational time when extra cores are made available, is important to check when deciding on the number of cores used for each calculation. To examine the speed-up $S(p)$ I use Amdahl's law (Amdahl 1967):

$$S(p) = \frac{t_{\rm s}}{t_{\rm p}} = \frac{1}{1 - f + f/p} \tag{3.12}$$

which gives the maximum speed-up $S(p)$ for a fixed amount of work. In this equation, $t_{\rm s}$ and $t_{\rm p}$ are the time the calculation takes on one and on several (p) processors, respectively. p is the number of cores involved in the calculation, and f the fraction of the calculation that benefits from parallelisation. I performed a test to find out what MESA's f-fraction is and up to how well MESA scales with the maximum speed-up calculated by Amdahl's law with the given f fraction. I used the non-rotating model of Chapter 5 for this test, and I varied the number of cores included from 1 to 24. The results are shown in Fig. 3.2, the top panel. This figure shows the MESA scaling for a typical set-up as used in Chapter 5, up to the end of the AGB phase. The comparison to the speed-ups calculated

via Amdahl's law and with different f values shows that about 70% of the MESA code benefits from parallelisation. When the serial fraction is known, theoretical speed-up is limited to:

$$\text{Maximum speed up} = \frac{1}{1 - f} \tag{3.13}$$

a relation found when taking the limit of Amdahl's law for an unlimited number of processors. For MESA, $f=0.7$, and thus the maximum speed-up is 3. When using 16 cores, this value is almost reached. However, when including four cores, the speed-up is already above 2. Therefore, I typically use eight cores, compromising between speed-up and efficiency.

The scaling of MPPNP is shown in the bottom panel of Fig. 3.2, for a typical set-up as used in Chapter 5, for calculations up to the end of the AGB phase. As comparison Amdahl's scaling for different f values are again included, which show that about 99% of MPPNP benefits from parallelisation. This f values means the total speed-up of MPPNP is 100. The small maximum speed-up of MESA compared to MPPNP is the second main reason why I use MPPNP for the detailed stellar evolution calculations (similar results on scaling factors for stellar evolution and nucleosynthesis codes are presented here: Martin, José & Longland 2018). The number of cores I can use for my MPPNP calculations are currently limited to 450 cores (computer cluster restrictions). I typically used around 400 cores for each run. A full AGB post-processing run lasts about 48 hours on Viper, which is the computer cluster of 5500 cores at the University of Hull[2]. An average total cpu core hours per run is thus 20 000.

---

[2]http://hpc.wordpress.hull.ac.uk/what-is-viper/
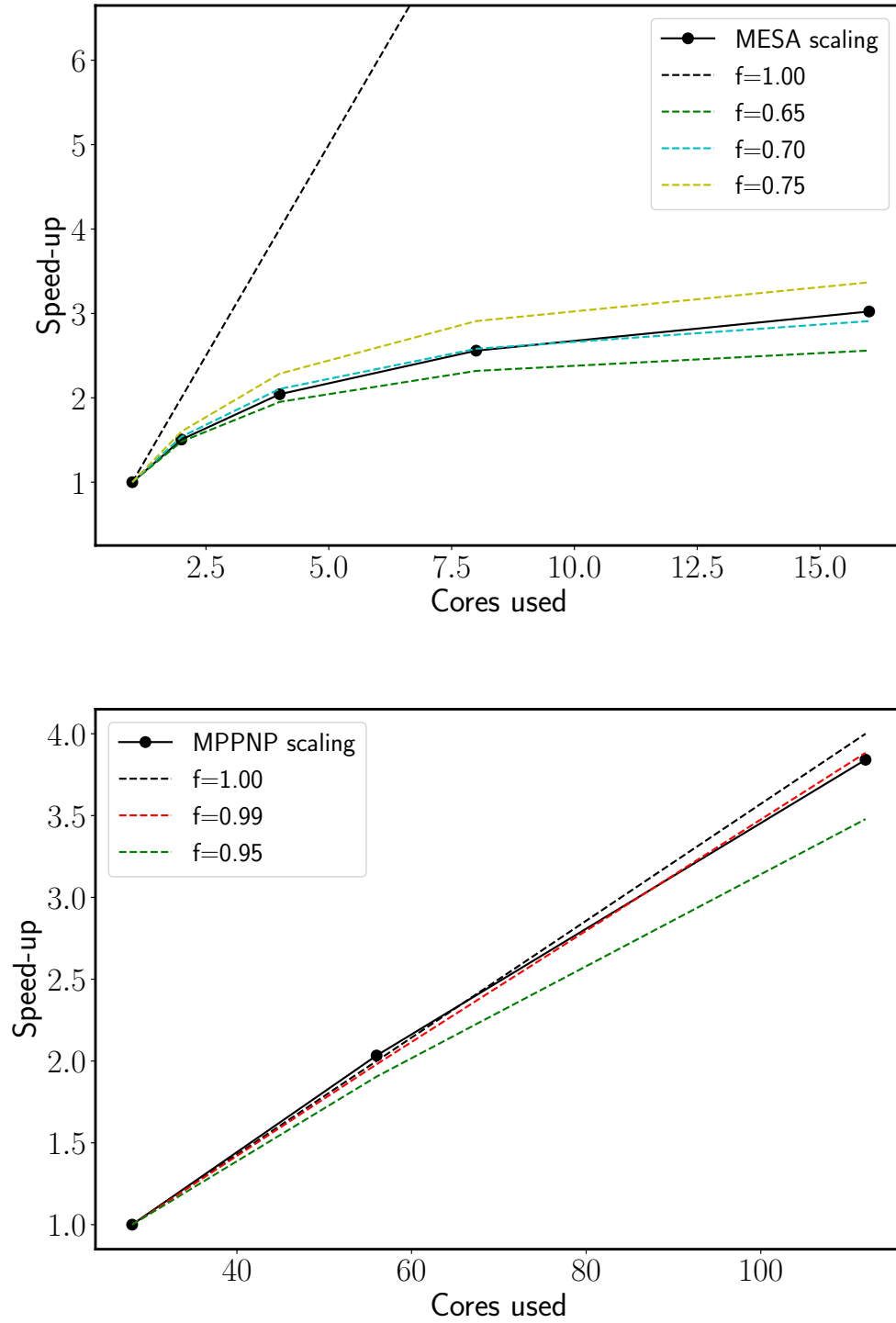
Figure 3.2: Speed up figures of MESA and MPPNP (top and bottom panel respectively), compared with different tracks of the Amdahl's law, using several parallelised fractions. The horizontal axis shows the amount of core included in the calculation, and the vertical axis the speed-up factor.

3.6   Overview of results chapters

Here I give an overview of the following third result chapters. All MESA and MPPNP calculations presented in these chapters are performed by me.

3.6.1   First result chapter

First-author publication in A&A, 2019, 622

The transport of angular momentum has been a challenging topic within the stellar evolution community, even more so since the recent asteroseismic surveys. All published studies on rotation using asteroseismic observations show a discrepancy between the observed and calculated rotation rates, indicating there is an undetermined process of angular momentum transport active in these stars.

In this chapter I am particularly interested in being able to reproduce with 2.5-$M_\odot$ stellar evolution models the asteroseismically observed rotation rates of the seven core He burning stars in Deheuvels et al. (2015). This observational set was chosen since these seven stars have both the core and surface rotation rates determined, a combination that is rare. I also use the known white dwarf rotation rates, as a second observational set. I investigate the effects on the core rotation rates by including the TS-dynamo and the artificial, additional viscosity. I present the set of parameters that allowed me to enforce the core rotation rates of my models to match the above mentioned observed rotation rates.

3.6.2   Second result chapter

First-author publication in A&A,2019, 629

In this chapter I extend the results of the first result chapter by investigating the s-process nucleosynthesis in both non-rotating and rotating models. The aim of this chapter is to find out if rotation, when the core rotation rates match asteroseismically obtained values, is able to influence the s-process production in low-mass AGB stars. A set of

2-M$_\odot$ MESA and MPPNP calculations are presented.

In this chapter I try to enforce the core rotation rates of my models to match the general trends in the observed values, which now include all core rotation rates of stars with a mass between 1.4 and 3 M$_\odot$ derived from Kepler observations. I enforce models to match these values as an upper limit using the results of the first paper. I also use those results to enforce the models to match the observed white dwarf rotation rates.

The aim of these models is to obtain an estimate of the s-process production in rotating AGB stars, that rotate at rates matching the asteroseismically obtained values. I also include a model that rotates an order of magnitude faster than the observational values, which can be seen as a conservative limit on the s-process production.

I end the chapter with a discussion on all uncertainties of the models, both the increased transport of angular momentum and the implementation of rotation in general.

3.6.3 Exploratory studies chapter

In this chapter I present exploratory studies that did not make it into either of my papers. The following research questions are considered:

- Only one surface rotation rate of an AGB star (R Doradus) has been determined, but stellar evolution models for single stars have been unable to match this value. Can the surface rotation rates of my stellar evolution models that include an additional, artificial visocsity match the surface rotation rate of R Doradus?

- What is the effect of including this additional, artificial viscosity in the mixing of chemical elements?

- What happens to the efficiency of the transport of angular momentum in the TS-dynamo, when the dependency on the molecular weight profile is removed?

- A new derivation for the TS-dynamo has been presented in Fuller, Piro & Jermyn (2019). Does this process indeed transport enough angular momentum out of the stellar core? The results of this study has been included in A&A, 2019, 631 (I

am second author).

4 Constraining transport of angular momentum in stars: combining asteroseismic observations of core helium burning stars and white dwarfs

J. W. den Hartogh, P. Eggenberger, and R. Hirschi

4.1 Overview

Context: Transport of angular momentum has been a challenging topic within the stellar evolution community, even more since the recent asteroseismic surveys. All published studies on rotation using asteroseismic observations show a discrepancy between the observed and calculated rotation rates, indicating there is an undetermined process of angular momentum transport active in these stars.

Aims: We aim to constrain the efficiency of this process by investigating rotation rates of 2.5-$M_\odot$ stars.

Methods: First, we investigated whether the Tayler-Spruit dynamo could be responsible for the extra transport of angular momentum for stars with an initial mass of 2.5 $M_\odot$. Then, by computing rotating models including a constant additional artificial viscosity, we determined the efficiency of the missing process of angular momentum transport by comparing the models to the asteroseismic observations of core helium burning stars. Parameter studies were performed to investigate the effect of the stellar evolution code used, initial mass, and evolutionary stage. We evolved our models into the white dwarf phase, and provide a comparison to white dwarf rotation rates.

Results: The Tayler-Spruit dynamo is unable to provide enough transport of angular momentum to reach the observed values of the core helium burning stars investigated in this chapter. We find that a value for the additional artificial viscosity ν_{add} around

10^7 cm^2 s^{-1} provides enough transport of angular momentum. However, the rotational period of these models is too high in the white dwarf phase to match the white dwarf observations. From this comparison we infer that the efficiency of the missing process must decrease during the core helium burning phase. When excluding the ν_{add} during core helium burning phase, we can match the rotational periods of both the core helium burning stars and white dwarfs.

4.2   The seven KIC stars

In Table 4.1 we summarise the important parameters of the seven KIC stars used as comparison sample, which are taken from Deheuvels et al. (2015). We include the core and surface rotation rates, the ratio between them, and the surface gravity (log g), all with their error margins. The metallicities of the seven stars are around solar, according to the APOGEE Data Release 14 (Abolfathi et al. 2018), which includes all seven stars. We used a metallicity of Z = 0.014 and the metal abundance mixture of Grevesse & Noels (1993), and therefore focus on matching the global trends of the seven stars as a group instead of trying to find best-fit models for each star individually. This allows us to constrain the missing process of angular momentum for core helium burning stars. The initial mass of our models is chosen to be 2.5 M$_\odot$ because this is very close to the mean observed mass of the seven KICs. In Appendix 4.B we will see that the influence of the stellar evolution code used on the rotational properties is negligible.

Other observations of rotation rates in evolved stars in the same mass range have been published in Massarotti et al. (2007), Mosser et al. (2012), Tayar et al. (2015), and Ceillier et al. (2017) and analysed in Tayar & Pinsonneault (2018). These data sets, however, only include either the surface or the core rotation rates. To date, the data set of Deheuvels et al. (2015) is the only data set in the 2 to 3 M$_\odot$ mass range that provides both rotation rates. This allows us to constrain our models better than when we only have one of the rates, so we only use the data set of Deheuvels et al. (2015) in this study.

Table 4.1: Properties of the seven KIC stars from Deheuvels et al. (2015). From left to right we list the Kepler Input Catalog ID, the obtained mass, surface gravity and rotation rates of core and envelope. The last column shows the ratio of the rotation rates.

KIC-id	$M/M_\odot$	$\log_{10}(g/\mathrm{cm\ s^{-2}})$	$\Omega_c/(2\pi\ \mathrm{nHz})$	$\Omega_s/(2\pi\ \mathrm{nHz})$	Ω_c/Ω_s
KIC5184199	2.18 ± 0.23	2.907 ± 0.012	200 ± 13	63 ± 20	3.2 ± 1.0
KIC4659821	2.21 ± 0.18	2.935 ± 0.013	165 ± 14	79 ± 15	2.1 ± 0.4
KIC8962923	2.23 ± 0.26	2.832 ± 0.013	138 ± 8	79 ± 10	1.8 ± 0.3
KIC3744681	2.45 ± 0.35	2.712 ± 0.015	194 ± 20	63 ± 36	3.1 ± 1.8
KIC9346602	2.51 ± 0.36	2.675 ± 0.013	164 ± 6	53 ± 15	3.1 ± 0.9
KIC7467630	2.57 ± 0.27	2.776 ± 0.015	121 ± 18	96 ± 28	1.3 ± 0.4
KIC7581399	2.90 ± 0.34	2.843 ± 0.013	164 ± 12	87 ± 14	1.9 ± 0.3

It is important to note that the rotation rates labelled as 'core' rotation rates are actually 'near core' values, as shown in Fig. 5 of Deheuvels et al. (2015). The comparison of the calculations to the region where the observations of the core rotation originate from is explained in Appendix C.

4.3 Can the TS dynamo provide enough coupling to explain asteroseismic derived rotation properties of core helium burning stars?

The first goal of this chapter is to investigate whether the TS dynamo provides enough coupling between core and envelope to match the observations of the core helium burning stars analysed by Deheuvels et al. (2015). Cantiello et al. (2014) show for stars with an initial mass of 1.5 $M_\odot$ that during the early RGB, inclusion of the TS dynamo provides more coupling between core and envelope but not enough to match the RGB rotation rates provided by Mosser et al. (2012). Thus, they concluded that the RGB phase is the evolutionary phase where more coupling is needed. However, the evolution of 1.5-$M_\odot$ and 2.5-$M_\odot$ stars are very different, in particular during the RGB phase. Stars with an initial mass below about 2 $M_\odot$ undergo helium flashes in the core after they have become

degenerate, and cores of stars with a higher initial mass ignite core helium burning before becoming degenerate. As a consequence, the times between the end of core hydrogen and the start of core helium burning are different; our calculations show a difference of one order of magnitude. For this reason, testing the conclusions of Cantiello et al. (2014) for 2.5-$M_\odot$ stars is a valuable task, especially when comparing them with observations of stars that are already past the RGB phase.

Figure 4.1 shows the core (solid line) and envelope (dashed line) rotation rates of our 2.5-$M_\odot$ models as a function of the surface gravity with different initial rotational velocities: 25, 50, and 150 km s^{-1}. The start of the main sequence (MS) is where the core and envelope rotation rates are equal (top left) and the end of the core helium burning phase is where core and surface rotation rates are the furthest apart (middle and bottom right). The core H and core He burning phases are both shown in thick line widths, while the RGB phase is shown in thinner line width. Starting with the comparison of the surface rotation rates (dashed lines), we see that the 50 km s^{-1} models, with the TS dynamo (wTS) and without (nTS), reach five of the seven data points, while the 25 km s^{-1} model reaches one of the seven and the 150 km s^{-1} model reaches none. We therefore set the initial rotation rate of all the models to 50 km s^{-1}. The two other data points can be reached by reducing the initial mass of the models, see Appendix 4.B.

When focussing on core rotation rates during the core helium burning phase, we see that all models including the TS dynamo ($\Omega_c \simeq 10^4$ nHz) are two orders of magnitude away from the data points. Including the TS dynamo improves the match to the observations as the difference between observations and the model without the TS dynamo ($\Omega_c \simeq 10^{6-7}$ nHz) is more than 3 orders of magnitude worse. We thus conclude that also for the 2.5-$M_\odot$ stars, the TS dynamo does not provide enough coupling between core and envelope to reduce the core rotation rates enough to match asteroseismic observations of the core helium burning stars.
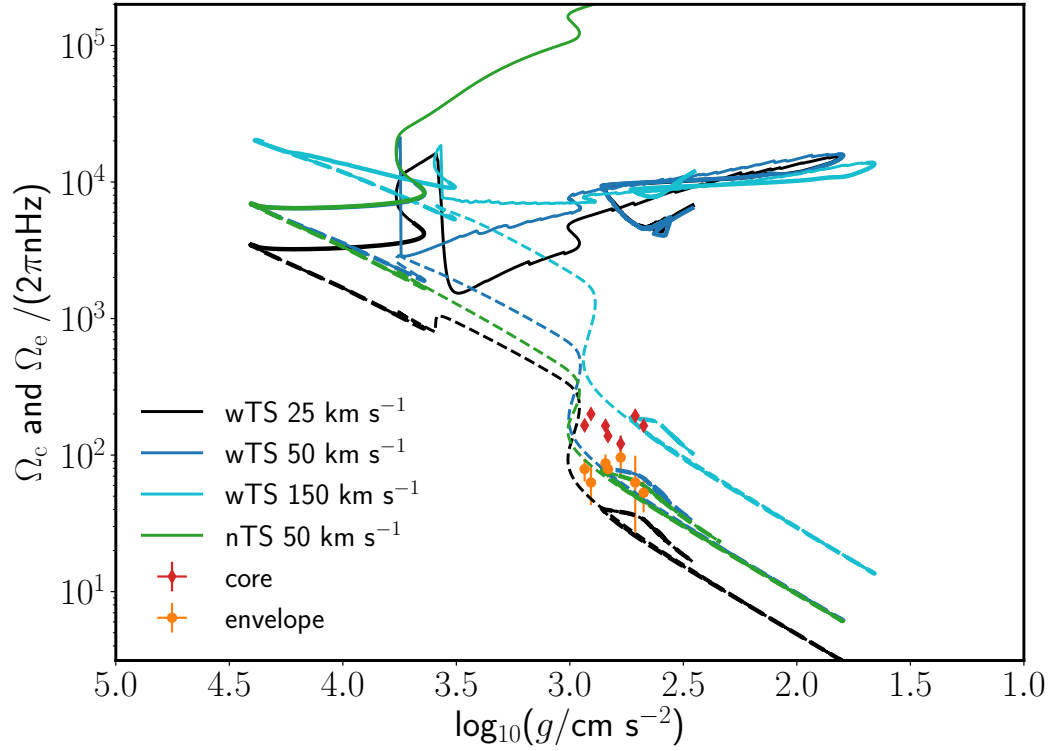
Figure 4.1: Effect of inclusion of the TS dynamo. Rotation rates of the core (solid line) and envelope (dashed line) of the models with the TS dynamo (wTS) and without (nTS). The initial rotation rates of the models are included in the legend. Data points are from Deheuvels et al. (2015).

4.4 Additional viscosity needed to reproduce observations of helium burning stars

Now that we have shown that the models with and without the TS dynamo cannot reproduce the asteroseismic observations of the seven secondary clump stars from Deheuvels et al. (2015), we continue by determining the strength of the missing process of angular momentum transport as a first step to revealing its physical nature. To do so, a constant ν_{add} is added to the transport of angular momentum. We stress, however, that we do not believe the missing process of angular momentum transport is constant.

4.4.1 Determination of the additional viscosity needed to reproduce the Deheuvels et al. (2015) data

From Eggenberger et al. (2017) we know that the efficiency of the unknown transport process for angular momentum increases with stellar mass. Therefore, in this study a stronger process is expected than employed by Eggenberger, Montalbán & Miglio (2012), studying a 1.5-$M_\odot$ star, and Eggenberger et al. (2017), studying a 0.84-$M_\odot$ star. As mentioned before, we did not attempt to fit all stars separately, but we look for global trends instead. Using Fig. 4.2, we determined the global efficiency of the missing process of angular momentum in the seven KIC stars. Figure 4.2 shows the ratio of core to envelope rotation rate, which, as mentioned by Eggenberger et al. (2017), allows us to determine ν_{add} independently of the initial rotation rate. The best match in Fig. 4.2 is $\nu_{\mathrm{add}}=10^7$ cm^2 s^{-1}, which matches five of the seven data points. The other two models included reach none ($\nu_{\mathrm{add}}=10^6$ cm^2 s^{-1}) or two ($\nu_{\mathrm{add}}=10^8$ cm^2 s^{-1}) of the data points. More importantly, the general trend shown by the data points is best matched by the model that includes a ν_{add} of 10^7 cm^2 s^{-1}. Again, the two data points with the highest surface gravities cannot be reached (see Appendix 4.B for how to reach these points). When comparing the lines in Fig. 4.3 to the lines in Figs. 4.7 and 4.8, we can determine the start of the core He burning phase in Fig. 4.3. This is at the lowest surface gravity, in the bottom right corner of the figure. Then, both surface gravity g and the core rotation

rate Ω_c increase in a short amount of time until steady core He burning sets in and a slow decrease in both surface gravity and the core rotation rate characterises the rest of this phase. All data points are positioned around the turning point of the trend in surface gravity. From Fig. 4.8 it follows that these seven stars are thus in the early phases of core He burning.

In Fig. 4.3 the core and surface rotation rates are shown for the same three models as in Fig. 4.2. This figure confirms the choice for the initial rotation rate because the data points for surface rotation are matched. Also in this comparison, the general trend shown by the data points is best matched by the model with a ν_{add} of 10^7 cm^2 s^{-1}.

4.4.2 Time dependence of the additional viscosity

In Sect. 4.4.1 we showed that the mean efficiency of the missing transport mechanism in the seven stars of Deheuvels et al. (2015) is around 10^7 cm^2 s^{-1} when adding the ν_{add} at the start of the main sequence. In this section we investigate whether this is dependent on the evolutionary phase during which ν_{add} is added to the calculation. By doing this we are able to determine whether there is a phase in which the transport of angular momentum dominates the rest of the evolution. In this section we focus on the evolution up to the core helium burning phase and in Sect. 4.5.2 we focus on the later phases to investigate the influence of the inclusion of ν_{add} on the final white dwarf spin.

We calculated models that include the ν_{add} only from the end of the main sequence and from the start of the core helium burning phase. For the first, we find that adding the same ν_{add} is sufficient to reach the data points, see Fig. 4.4, and that this model is comparable to the model in which we included ν_{add} from the start of the main sequence. Therefore, we conclude that the main sequence is not a dominant phase for angular momentum transport in our models, but we have no arguments to exclude ν_{add} during the main sequence either.

The inclusion of ν_{add} only at the start of the core helium burning phase changes the evolution of the rotation rates, see again Fig. 4.4. Without the ν_{add} earlier in the calculation, the core rotation rate is higher at the start of the core helium burning phase
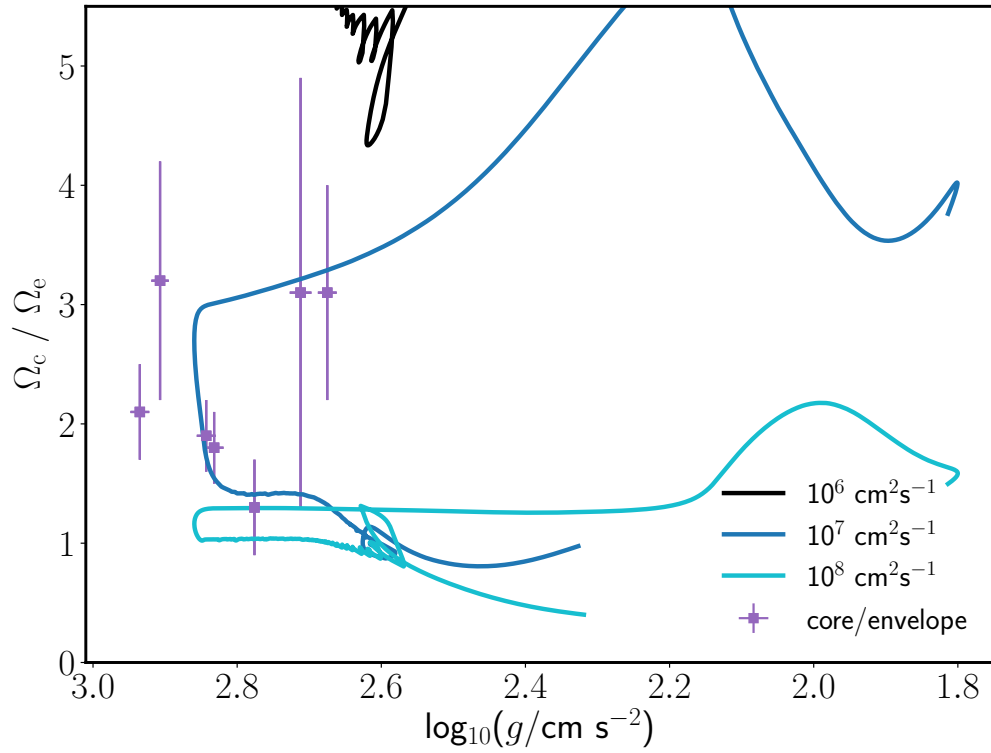
Figure 4.2: Effect of varying ν_{add} on the ratio of core and surface rotation rate. The ratio of core to surface rotation rate as a function of surface gravity for three models calculated with an initial rotational velocity of 50 km s^{-1}, while the ν_{add} is varied. The data points are from Deheuvels et al. (2015).
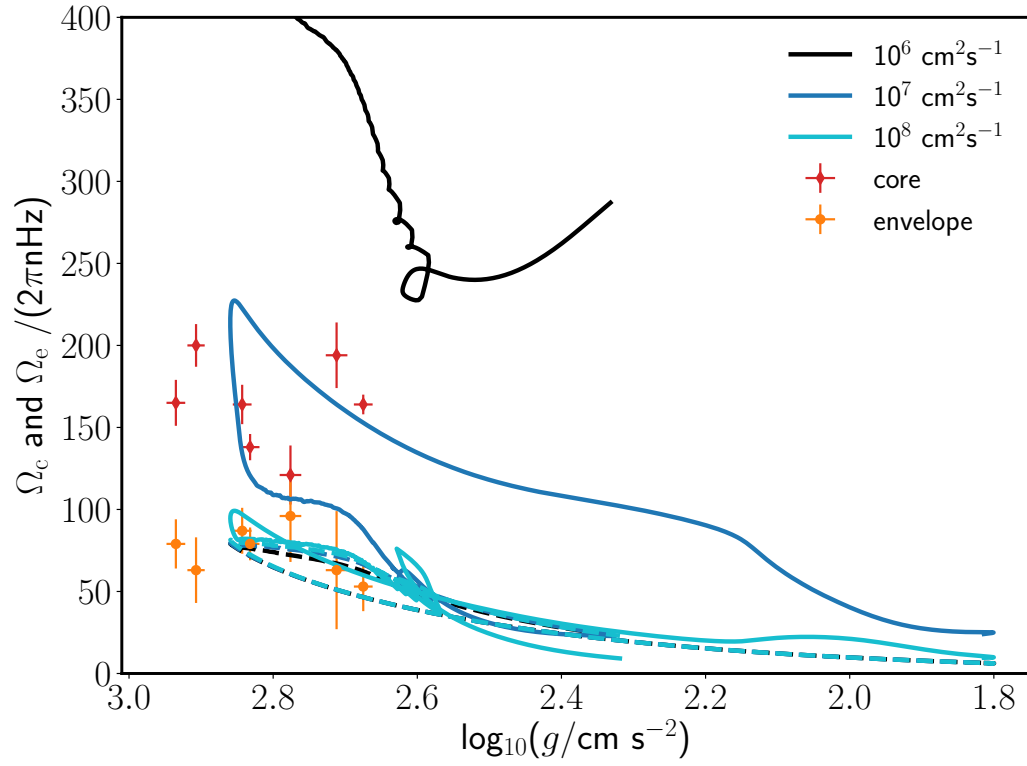
Figure 4.3: Effect of varying ν_{add} on the ratio of core and surface rotation rate. Core and surface (solid and dashed line, respectively) rotation rates as a function of surface gravity for three models in Fig. 4.2. The data points are from Deheuvels et al. (2015).

in this model than in the models that do include ν_{add} earlier in the evolution. This is why the line of this model starts at a different point (top-left corner) in the figure. However, this difference has disappeared around $\log_{10}(g/\text{cm s}^{-2}) \simeq 2.8$. The location of the curve in this model is dependent on ν_{add}, shown by the model labelled '2.5 10^6 cm^2 s^{-1}', this number being the ν_{add} added at the start of the core helium burning phase. Thus, when we add the ν_{add} at the start of the core helium burning phase, we are still able to reach all data points. However, we then have to use a value in the range of 2.5 $10^6 < \nu_{\text{add}}$ cm^2 s$^{-1} < 10^7$. While the data cannot rule out the models that include ν_{add} at the start of the core helium burning phase, the data does favour earlier inclusion of ν_{add} because no data points are found with an angular velocity of the core above 200 nHz.

When we suppress the ν_{add} from the start of the core helium burning phase onwards, we are unable to reach any data points. The reason for this is that the molecular weight gradient is too strong and without any ν_{add} there is no transport of angular moment over this gradient. Therefore, we conclude that the crucial phase for the transport of angular momentum is the start of the core helium burning phase.
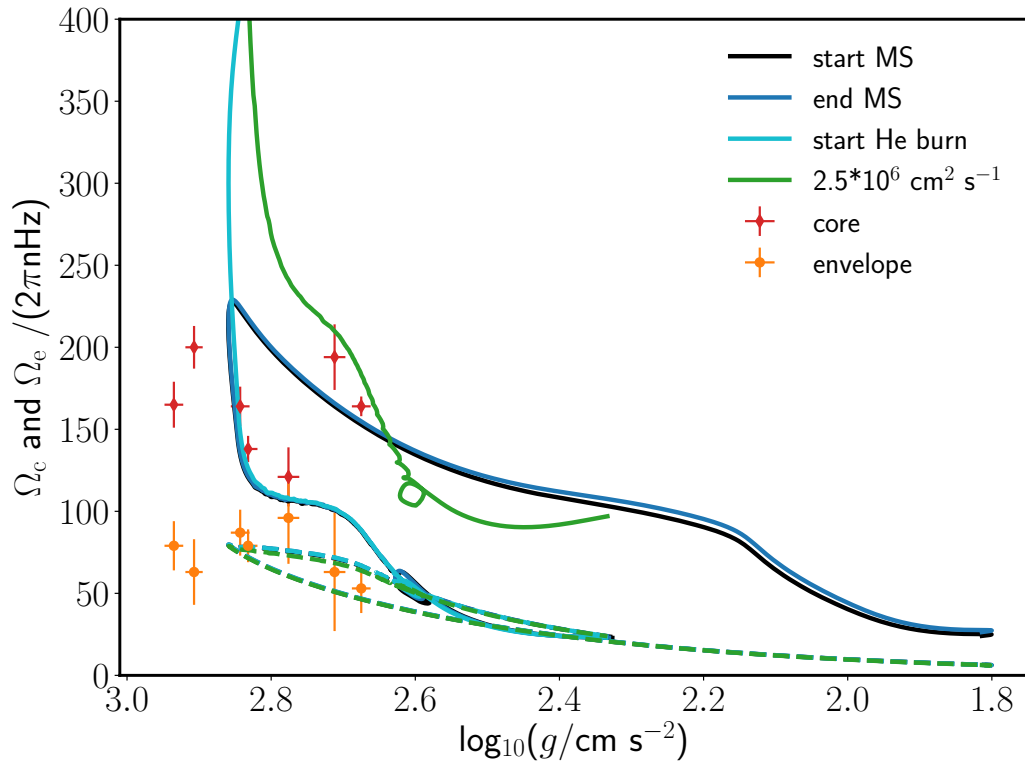
Figure 4.4: Effect of varying the inclusion time of ν_{add} on the core and surface rotation rate. The models presented here have been calculated with the best fit parameters (50 km s^{-1}, 10^7 cm^2 s^{-1}), apart from the model labelled '2.5*10^6 cm^2 s^{-1}', while varying the moment of including the ν_{add}. The labels reflect the phase when the ν_{add} is included. For the 2.5 10^6 cm^2 s^{-1} model, the moment of inclusion is at the start of the core helium burning phase.

4.5 White dwarf rotation rates

After the core helium burning phase, we continued the models until they reached the white dwarf phase. In between these two phases, the stars pass through the asymptotic giant branch phase (AGB). During this phase, the energy production comes from the hydrogen and helium burning shell, located between the core and envelope. The helium shell becomes unstable, resulting in thermal pulses (TP-AGB phase). Around 25 to 30 thermal pulses take place in this phase in our models, and between each TP a third dredge-up (TDU) can occur. During the TP-AGB phase mass loss is enhanced, leading to removal of the envelope. Via the planetary nebulae phase, the star moves to the white dwarf track.

4.5.1 Calculation of the AGB phase

We calculated the full AGB phase as we would have done when studying the s-process nucleosynthesis (see Pignatari et al. 2016; Battino et al. 2016, for details). For instance, for the mass-loss treatment during the AGB phase we used Blöcker (1995) with an efficiency of 0.01 at the start of the AGB phase, 0.04 from when the envelope is carbon rich, and to 0.5 when the convergence issues appear (see below). We also used calibrated parameters for convective boundary mixing specifically for the AGB phase.

This is an improvement compared to the works of Suijs et al. (2008, no AGB specific mass loss, manually stopped models somewhere in AGB phase), Tayar & Pinsonneault (2013, no details given apart from initial mass and rotational velocity), and Cantiello et al. (2014, unphysical large mass loss efficiencies in the AGB phase which shorten this phase). By calculating the whole AGB phase, we can investigate the effects of the ν_{add} on the thermal pulse cycle by investigating both the transport of angular momentum and the s-process nucleosynthesis, and compare them to the standards models without ν_{add}. We report that the models with ν_{add} included during the TP-AGB phase are able to transport angular momentum during the TDUs. This is due to the TDU reducing the molecular weight gradient and therefore the (local) barrier that has to be overcome to

transport angular momentum.

It is common for convergence issues to arise during the final TPs in calculations like these and we report that these issues also occur in all models presented in this chapter. There are two options for how to proceed, the first being the continuation of the AGB phase with a higher mass loss rate and the second the ejection of the whole remaining envelope (see Wood & Faulkner 1986; Herwig, Bloecker & Schoenberner 1999; Sweigart 1999; Lau et al. 2012). We proceed with the models by increasing the mass loss parameter from 0.04 to 0.5, which allows for a smooth continuation of the models into the white dwarf phase.

4.5.2   Final spins of best fit models

In this section we show the comparison between the calculated rates and the observed white dwarf rotation rates by Hermes et al. (2017) and the compilation by Kawaler (2015). Most pulsating white dwarfs (WDs) in these two papers are DAVs, variable WDs with spectral type DA having only hydrogen absorption lines in their spectra. These pulsating WDs can be found in a specific temperature regime where their surface hydrogen has to become partially ionised. This regime for white dwarfs with masses around 0.6 M$_\odot$ is between 12 600 and 10 600 K, so we show the rotational periods of our models when passing through that same temperature regime in Fig. 4.5. The observational points from other pulsating white dwarfs are depicted as black crosses, while the DAVs are shown as black diamonds. The number of observed white dwarf periods is still low (36, we removed EPIC 201730811 because it is in a post-common envelope close binary according to Hermes et al. 2015), so no statistical comparison is provided. White dwarf spins are also available for magnetic white dwarfs (see Kawaler 2015, for a summary). All of our models are non-magnetic, with only one exception, so we do not include these data points in our comparison.

All coloured symbols in Fig. 4.5 are WDs from our models. The two blue symbols correspond to the models introduced in Sect. 4.3, where we tested the impact of the TS dynamo. These models are the only ones without ν_{add} in Fig. 4.5. As already shown by Suijs et al. (2008) and Cantiello et al. (2014), the model without the TS dynamo (nTS,

dark blue circle) is orders of magnitude lower than the observed white dwarf periods. The model that does include the TS dynamo (wTS, light blue hexagon) reaches the lower limit of observed white dwarf periods, but as we saw before this model does not reach the observed periods of core He burning stars.

All models that include ν_{add} in Fig. 4.5, have a spin period that is larger than all observed white dwarf rotation rates. There are three models with ν_{add} of 10^6, 10^7, and 10^8 cm^2 s^{-1} included during the whole calculation (three triangles), and one model where we excluded the ν_{add} of 10^7 cm^2 s^{-1} from the end of the core He burning phase (square). All these models are introduced in Sect. 4.4.1, except for the last one. From the previous section, we know that only the models labelled '10^7 cm^2 s^{-1}' and 'end core He b' match the core He burning observations. However, they all transport too much angular momentum in the later phases of the evolution to match the white dwarf observations. Even the model that does not include ν_{add} after the core He burning phase is finished does not reach the observed white dwarfs periods. Therefore, the efficiency of the missing process of angular momentum is negligible after the end of the core He burning phase according to our models, and the efficiency of the missing process also has to change during the core helium burning phase itself.

To investigate this last conclusion in more detail, we calculated models where we include ν_{add} at the ZAMS and exclude it at different moments during the core helium burning phase. The whole core helium burning phase lasts for 183 Myr in these models and ν_{add} has been excluded from times that correspond to 1/4, 2/4, and 3/4 of that time span. After excluding ν_{add} we continue the calculation into the white dwarf phase. These three new models have also been included in Fig. 4.5. Again the rotational period within the DAV temperature range is used[1]. All three models are located within the range of observed white dwarf periods, and all three therefore match both the core helium burning and white dwarf observed rotation rates.

---

[1]Apart from model '1/4' because this model undergoes a very late thermal pulse (VLTP) during the WD phase and is rebrightened before the DAV temperature range is reached. Convergence issues prevent the model from returning to the WD phase. We therefore calculated the rotational period of this WD just before the VLTP.
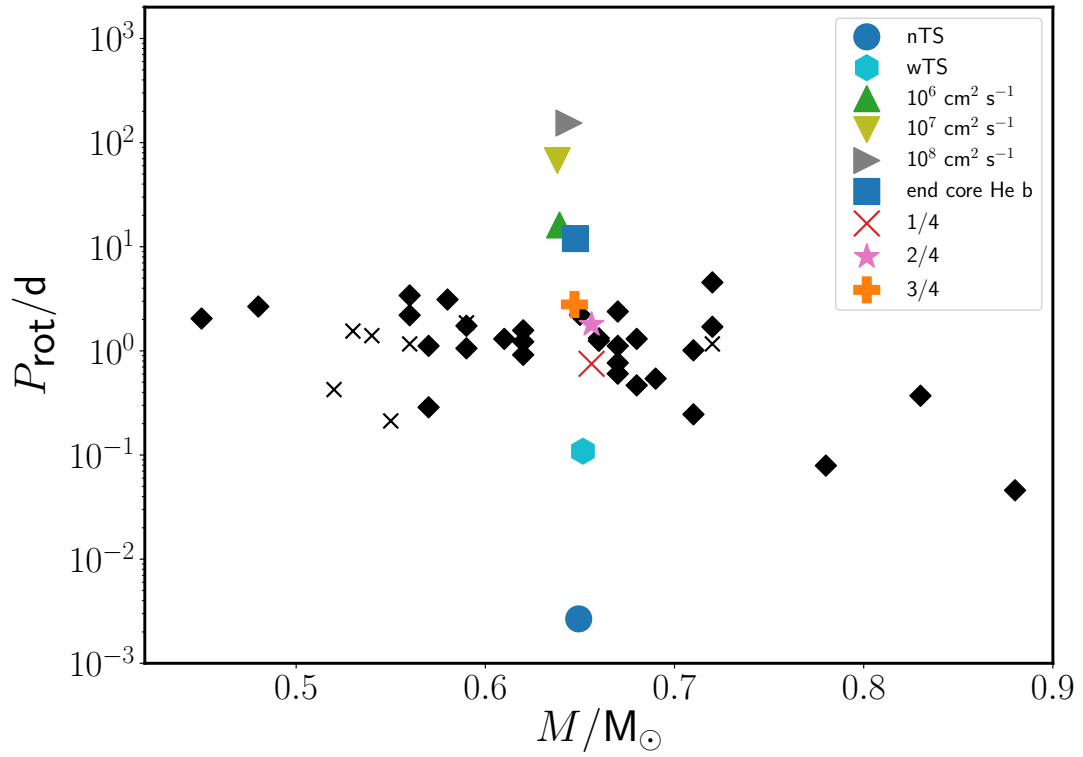
Figure 4.5: WD periods as a function of WD mass. The data points are from Kawaler (2015) and Hermes et al. (2017). The black diamonds are the DAVs, the black crosses are other pulsating white dwarfs. All coloured symbols are our predicted WD periods: the sphere and hexagon are the models without ν_{add}; the triangles are the models with different values of ν_{add}; the square is the model that excludes ν_{add} at the end of core helium burning; and the star, cross, and plus signs are the models that exclude ν_{add} at different times during the core helium burning phase.

4.6   Conclusions

In this chapter, we investigated the efficiency of the missing process of angular momentum by calculating 1D stellar evolution models with an initial mass of 2.5 $M_\odot$. As observational tests, we used the observed core and surface rotation rates of core helium burning stars as published by Deheuvels et al. (2015) and white dwarf rotational periods published by Kawaler (2015) and Hermes et al. (2017). The main conclusions of this chapter are the following:

- As for the 1.5-$M_\odot$ of Cantiello et al. (2014), the 2.5-$M_\odot$ models including the TS dynamo do not provide enough coupling between core and envelope to match asteroseismic observations of core rotation rates.

- We have added a constant additional viscosity to our model as a first step towards revealing the physical nature of the missing process of angular momentum transport.

- We are able to match the core rotation rates published by Deheuvels et al. (2015) by adding $\nu_{\mathrm{add}} = 10^7$ cm^{2}s^{-1} and using an initial rotational velocity of 50 km s^{-1}. This order of magnitude for ν_{add} is independent of stellar evolution code, and initial mass (see Appendix 4.B).

- The trends identified by Eggenberger et al. (2017) concerning the increase in ν_{add} with both initial mass and evolutionary phase are confirmed here. See Table 4.2 for an overview of all published studies on ν_{add}. The strong increase in ν_{add} from the two lower mass studies to this 2.5-$M_\odot$ study suggests that when increasing the initial mass of the star, the change from radiative to convective core has less effect on the efficiency of the missing process of angular momentum than the absence of helium flashes in the more massive stars.

- We show that the dynamical instabilities (DSI and SH) are not attributed to the transport of angular momentum from ZAMS to the end of core helium burning in our models (see Appendix 4.B).

Table 4.2: Summary of all published values for ν_{add} to date

Initial mass ($M_\odot$)	ν_{add} (cm^2 s^{-1})	Phase	reference
0.84	1×10^3-1.3×10^4	early red giant	Eggenberger et al. (2017)
1.5	3×10^4	red giant	Eggenberger et al. (2012)
2.5	10^7	core He burning	this work

- We show that the extra transport of angular momentum that fits the observations of the core helium burning phase leads to rotation periods in the WD phase that are too high. Our results show that the efficiency of the missing process needs to change during the core helium burning phase, and must be strongly decreased before the end of the core helium burning phase.

- When excluding ν_{add} at 1/4, 2/4, or 3/4 of the whole duration of the core helium burning phase, our models match the observed rotation rates of both the set of core helium burning stars and the set of white dwarfs.

- This implies that transport processes for which the efficiency only depends on the amount of differential rotation (such as the diffusive mixing introduced in Spada et al. 2016, based on the AMRI by Rüdiger et al. 2007) are incompatible with the result that the missing process has to be strongly decreased by the end of the core helium burning phase, unless an inhibiting effect is included to facilitate the decrease. A consequence of this work is that we have all initial parameters for the follow-up study, which will focus on the s-process production in rotating AGB stars. For this study, having a core rotation rate in the AGB phase that is consistent with asteroseismic observations of earlier and later evolutionary phases is crucial.

4.A   Evolution of rotation from ZAMS to core helium burning

Here we discuss the rotational evolution of the models up to the core helium burning phase. The Hertzsprung-Russell diagram (HRD) of two models, one without a ν_{add} (labelled nTS) and one with a ν_{add} (labelled 10^7 cm^2 s^{-1}) is shown in Fig. 4.6. The two models do not include the TS dynamo. This figure shows that the two models are comparable. The same is true for the evolution of the surface gravity g shown in Fig. 4.7, where log g is shown versus $\log_{10}(t^*)\simeq\log(t_{\mathrm{WD}}$-$t)$. In this figure, the horizontal segments of the lines are the core hydrogen (MS) and helium (Core He b) burning phases. The hydrogen shell burning phase takes place in a short amount of time at $\log_{10}(t^*/\mathrm{yr})\simeq10.160$, the hydrogen/helium shell burning phase after the core helium burning phase at $\log_{10}(t^*/\mathrm{yr})\simeq10.154$. In this chapter we focus on the core helium burning phase, which starts at $\log_{10}(g/\mathrm{cm\ s}^{-2})\simeq1.8$ and a $\log_{10}(t^*/\mathrm{yr})\simeq10.160$. Then, in a relatively short amount of time, $\log_{10}(g/\mathrm{cm\ s}^{-2})\simeq2.9$ is reached. From there, during the remaining core helium burning phase log g evolves with a constant slope until $\log_{10}(g/\mathrm{cm\ s}^{-2})\simeq2.4$ is reached. This loop is visible in the $\log_{10} g$ vs Ω figures, where the lower halve of the curves is the long-lasting phase.

Figure 4.8 shows the time evolution of the angular velocity of core Ω_{c} (solid lines) and envelope Ω_{e} (dashed lines) from the start of the main sequence to the start of the AGB phase. During the core burning phases, the rotation rates of core and envelope are close to constant in both models, with the model including ν_{add} showing a near solid body rotation trend during the main sequence. The nTS model, however, shows large differences between core and envelope rotation rates during the shell burning phases. These phases are characterised with core contraction and envelope expansion (also known as the mirror principle, see Kippenhahn, Weigert & Weiss 2013), resulting in a steeply increasing core rotation rate and steeply decreasing envelope rotation rate.

The model including ν_{add} shows different trends during the shell burning phases. The coupling provided by ν_{add} allows for transport of angular momentum even when the core is contracting. As a result, the core rotation rate follows the trends of the envelope

rotation rate and decreases during the shell burning phases (orange lines in Fig. 4.8). This trend is as observed by Aerts, Reeth & Tkachenko (2017), who compare a compilation of rotation rates of main sequence stars to the rotation rates of more evolved stars by Mosser et al. (2012). They find that there must be a drop in core rotation before or during the end of hydrogen and the start of helium core burning phases.

The details of the angular velocity Ω and corresponding angular momentum j profiles from core to surface are given in Figs. 4.9 and 4.10. Both figures show this profile at four moments in the evolution: the start and end of the main sequence and the start and end of the core helium burning phase. The solid body start of the models is visible in both figures, and from there the differences appear. As mentioned before, the angular velocity of the core and envelope in the model without ν_{add} (left panel of Fig. 4.9) evolve separately and oppositely due to the mirror principle. This effect is already visible at the end of the main sequence, and results in a difference between core and envelope rotation rate of several orders of magnitude at the end of the core helium burning phase. In the right panel the j profiles are shown. A decrease in j in a region during a certain phase indicates transport of angular momentum. A sharp feature is usually the outer edge of a convective zone, which creates a barrier for transport of angular momentum. The general lack of transport of angular momentum in the nTS model is visible in the j profiles of Fig. 4.9, because they largely overlap.

When an additional viscosity of $\nu_{\mathrm{add}}{=}10^7$ cm^2 s^{-1} is added, the differences between core and envelope angular velocity are smaller than in the nTS model (left panel of Fig. 4.10). The whole star is close to solid body rotation up to the end of the core helium burning phase, as also shown in Fig. 4.8. In this model a large amount of angular momentum is transported out of the core between the end of the main sequence and the start of the core helium burning phase (right panel of Fig. 4.10). This efficient transport is also able to overcome the edge of convective regions, resulting in a lack of sharp features in the j-profiles. The transport continues during the core helium burning phase, creating a short moment at the end of the core helium burning phase when the convective envelope rotates at a higher angular velocity than the rest of the star.
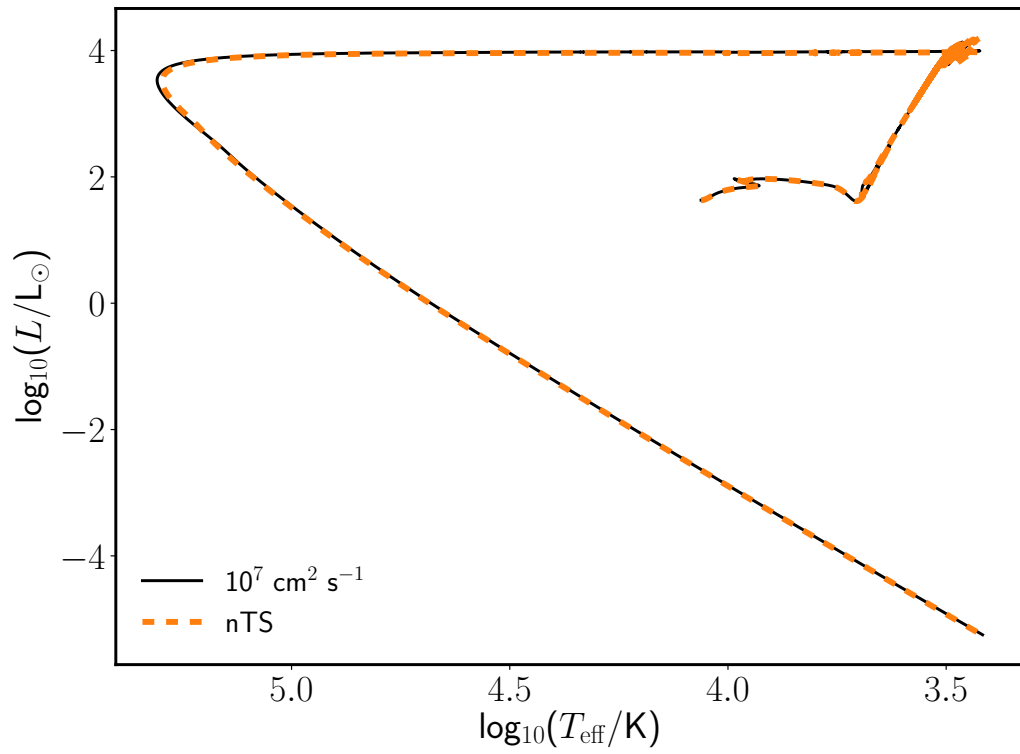
Figure 4.6: Hertzsprung-Russell diagram of 2.5 $M_\odot$ models, one without a $\nu_{\rm add}$ of 10^7 (dashed line) and one with a $\nu_{\rm add}$ of 10^7 (solid line). Neither model includes the TS dynamo.
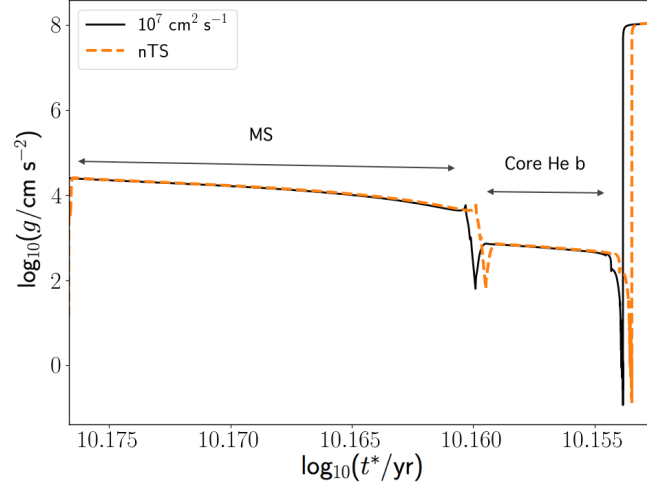
Figure 4.7: Time evolution of surface gravity g. Timescale is $t^*=t_{\mathrm{WD}}-t$), with t_{WD} being the age of the star at the end of the calculations. The offset in time comes from a slightly longer white dwarf phase for the 10^7 cm^2 s^{-1} model compared to the nTS model.
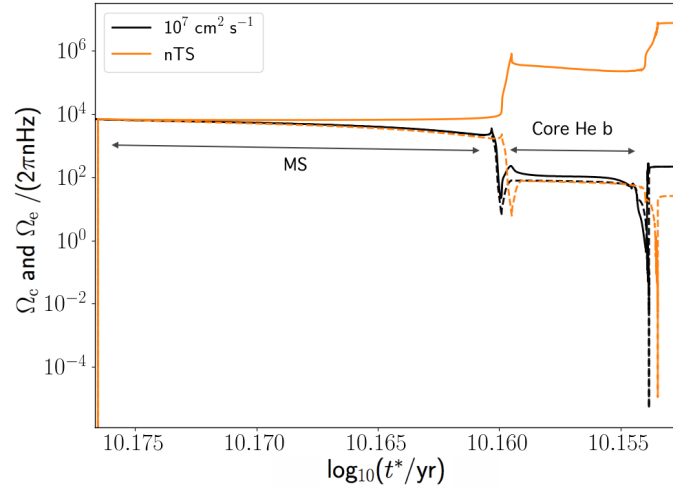
Figure 4.8: Coupling made visible: the evolution of core (solid line) and envelope (dashed) rotation rates from the ZAMS to the start of the AGB phase. Differences between the two models become visible at the start of the hydrogen shell burning phase, where the model without TS dynamo and ν_{add} shows that the core and envelope rotation rates move apart, while the model including a ν_{add} of 10^7 cm^2 s^{-1} shows the rotation rates are coupled.
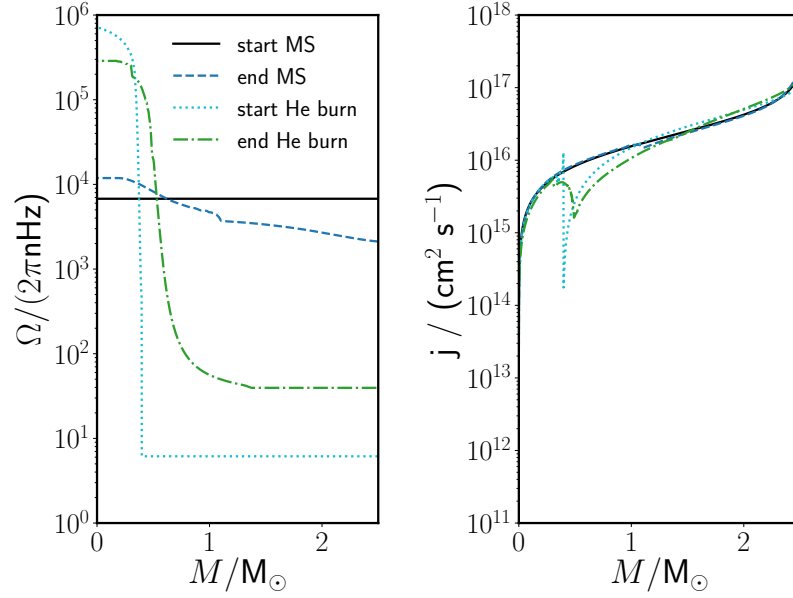
Figure 4.9: Angular velocity and angular momentum profiles of the nTS model for four moments as described in the label.
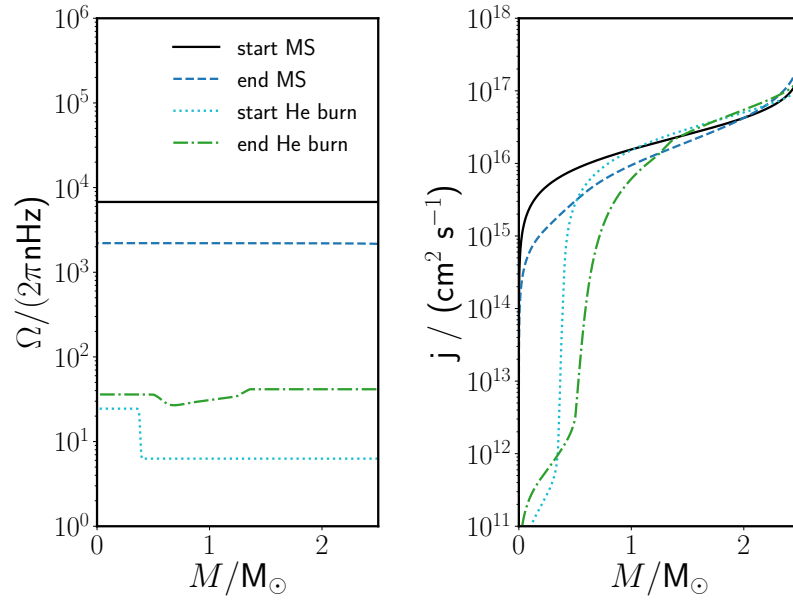
Figure 4.10: Same as Fig. 4.9, but for the model that includes a ν_{add} of 10^7 cm^2 s^{-1}.

4.B Model uncertainties

In Sect. 4.4 we were not able to match the data points at the highest surface gravities corresponding to KIC5184199 and KIC4659821. Here, we show that this is a consequence of setting the initial mass to 2.5 $M_\odot$. When matching the initial mass to the masses listed in Table 4.1, we can indeed match the highest surface gravities, as shown in Fig. 4.11. For all models in this comparison, we use $\nu_{add} = 10^7$ cm^2 s^{-1}. The model with the lowest initial mass (2.2 $M_\odot$) reaches the higher surface gravities of the two data points earlier unreached. These two data points correspond to the observations of stars with initial masses of 2.18 ± 0.23 and 2.21 ± 0.18 $M_\odot$, indeed matching the lower initial mass of 2.2 $M_\odot$. When comparing the model with the highest initial mass (2.9 $M_\odot$) to the data points, we find that the star with the highest mass, KIC7581399, of 2.90 ± 0.34 $M_\odot$, has a $\log_{10}(g/\text{cm s}^{-2}) = 2.843 \pm 0.013$ and is located on the 2.5-$M_\odot$ model. This might imply that the actual mass of KIC7581399 is located near the lower end of the error margin. The implementation of rotation in MESA allows for the inclusion and exclusion of individual rotationally induced instabilities. The dynamical instabilities (DSI and SH) are not part of the GENEC models as published by Eggenberger et al. (2012, 2017). Here we investigate their effects on the transport of angular momentum in the MESA models presented in this chapter. To test this, we calculated an extra model with an initial mass of 2.5 $M_\odot$ and $\nu_{add} = 10^7$ cm^2 s^{-1} with only the ES and SSI included, and added this model to Fig. 4.3 with the label 'ES+SSI'. The overlap of this model and the 2.5-$M_\odot$ model, which also includes the dynamical instabilities, shows that the SH and DSI do not contribute to the transport of angular momentum. Edelmann et al. (2017) have already shown issues with the 1D implementation of the DSI in stellar evolutionary codes, and therefore being able to exclude this instability in studies on angular momentum transport reduces the uncertainties of our results. They also confirm that the settings of the GENEC models are satisfactory. We show a comparison between MESA and GENEC models (see Eggenberger et al. 2008, for a description of this code and their implementation of rotation) in Fig. 4.12, with their ν_{add} and initial mass, as labelled. The same trends can be identified in these models as in the MESA models of earlier
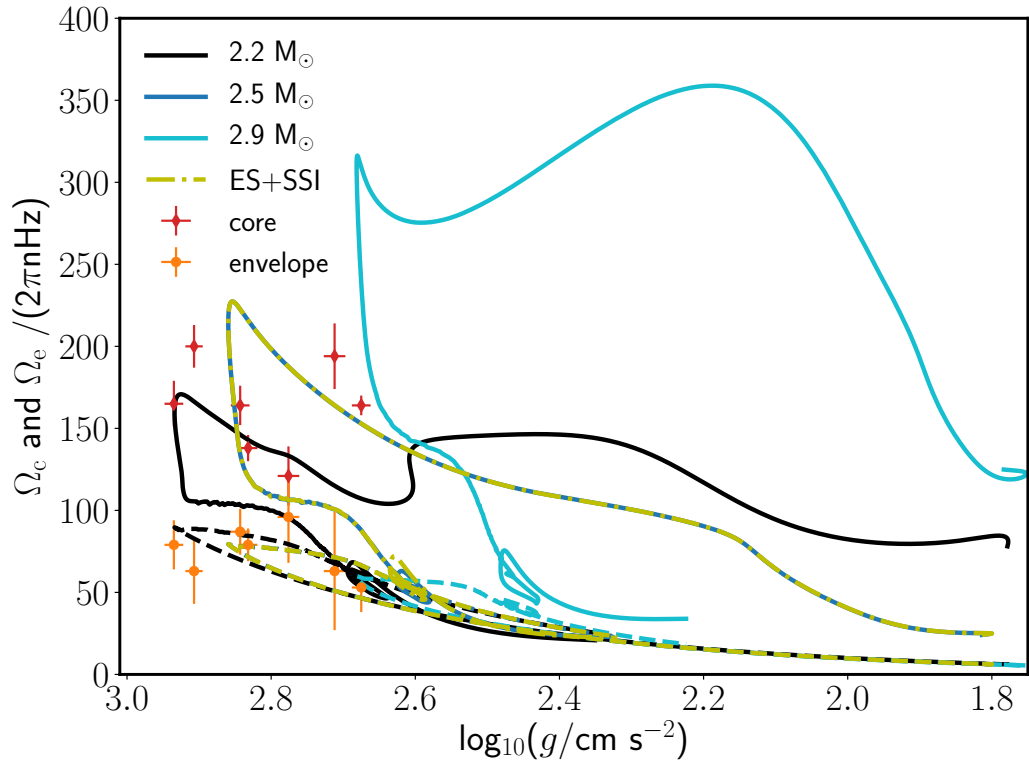
Figure 4.11: The effect of model uncertainties on the core and surface rotation rates. The first three models presented here have been calculated with the best fit parameters (50 km s^{-1}, 10^7 cm^2 s^{-1}), while the initial mass is varied. The fourth model includes only the ES and SSI instability. The models labelled '2.5 M$_\odot$' and 'ES+SSI' overlap.
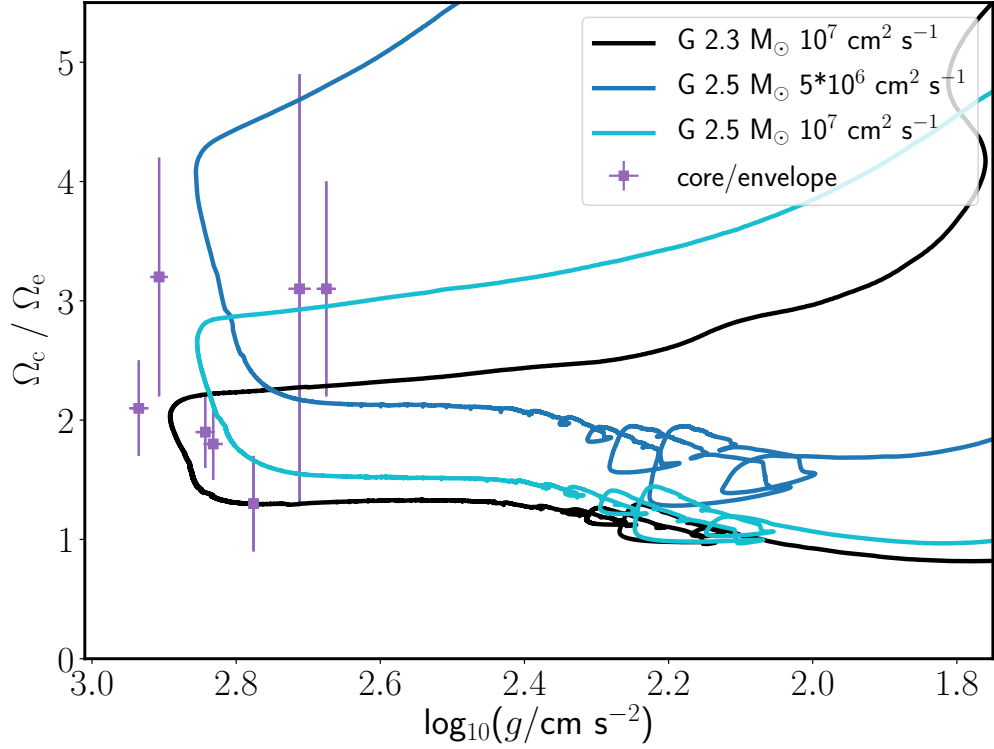
Figure 4.12: Code comparison: the models presented here are calculated with GENEC to show our conclusions are independent from evolutionary code.

sections: when the initial mass is reduced, the data points at high surface gravities can be reached. A ν_{add} of 10^7 cm^2 s^{-1} provides a better fit than 5×10^6 cm^2 s^{-1}. Therefore, our conclusions are code independent.

4.C Rotation near the core

As mentioned in Sect. 4.2, the numbers in the core rotation rates column in Table 4.1 are actually 'near core' rotation rates. Their location is 0.1–1% of the normalised radius away from the most central point, see Fig. 5 in Deheuvels et al. (2015). In this region the obtained rotation rate is constant despite the noise in this figure. In Fig. 4.13 we show a
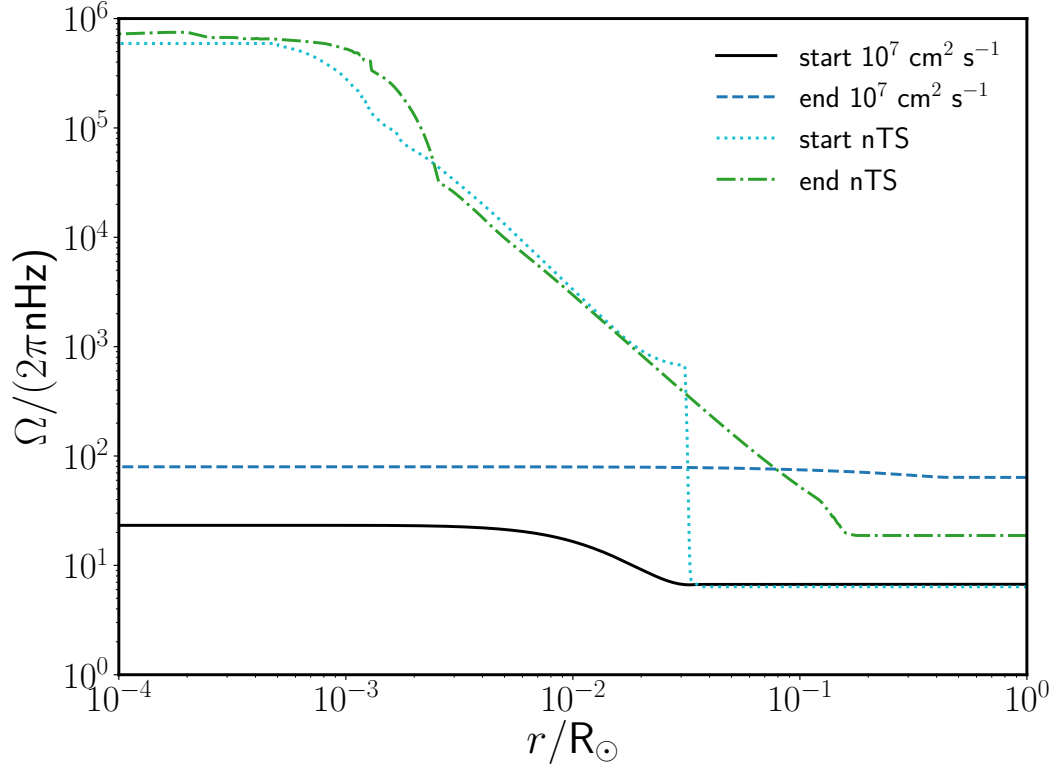
Figure 4.13: For comparison with Fig. 5 of Deheuvels et al. (2015). The region of interest is between $r/\mathrm{R}_\odot$ of 10^{-3} and 10^{-2}.

similar figure for the nTS and 10^7 cm^2 s^{-1} models, where the rotation rate at the start and end of the core helium burning phase is shown. We see that the model including the extra ν_{add} shows a constant trend in the region of interest at both times, as needed for the comparison to the data of Deheuvels et al. (2015). However, the nTS model shows a strong decrease in this region, providing another argument against these standard models.

5 The s process in rotating low-mass AGB stars: Nucleosynthesis calculations in models matching asteroseismic constraints

J.W. den Hartogh, R. Hirschi, M. Lugaro, C.L. Doherty, U. Battino, F. Herwig, M. Pignatari, and P. Eggenberger

5.1 Overview

Aims: In this chapter I investigate the s-process during the AGB phase of stellar models whose cores are forced to rotate at rates consistent with asteroseismology observations of their progenitors and successors.

Methods: I calculated new $2M_\odot$, Z=0.01 models, rotating at 0, 125, and 250 km s^{-1} at the start of main sequence. An artificial, additional viscosity was added to enhance the transport of angular momentum in order to reduce the core rotation rates to be in agreement with asteroseismology observations. I compared rotation rates of my models with observed rotation rates during the MS up to the end of core He burning, and the white dwarf phase.

Results: I present nucleosynthesis calculations for these rotating AGB models that were forced to match the asteroseismic constraints on rotation rates of MS, RGB, He-burning, and WD stars. In particular, I calculated one model that matches the upper limit of observed rotation rates of core He-burning stars and I also included a model that rotates one order of magnitude faster than the upper limit of the observations. The s-process production in both of these models is comparable to that of non-rotating models.

Conclusions: Slowing down the core rotation rate in stars to match the above mentioned asteroseismic constraints reduces the rotationally induced mixing processes to the point that they have no effect on the s-process nucleosynthesis. This result is independent of

the initial rotation rate of the stellar evolution model. However, there are uncertainties remaining in the treatment of rotation in stellar evolution, which need to be reduced in order to confirm my conclusions, including the physical nature of my approach to reduce the core rotation rates of my models, and magnetic processes.

5.2   Set of models

Table 5.1: Properties of stellar evolution models. Names of the models are a combination of initial rotation rate (first number) and the order of magnitude of ν_{add} (second number). The H-free core mass and the core rotation rate are given at the time the first TP (TP1) occurs. The white dwarf mass (M_{DAV}) is taken when the star proceeds through the DAV phase (see text for details) on the white dwarf cooling track.

Model	$v_{\mathrm{rot,i}}$ km s^{-1}	ν_{add} cm^2 s^{-1}	$M_{\mathrm{c,TP1}}$ M$_\odot$	$\Omega_{\mathrm{c,TP1}}$ 2πnHz	M_{DAV} M$_\odot$
noR	-	-	0.501		0.622
125 0	125	0	0.501	4.98×10^6	0.620
125 6	125	10^6	0.500	3.52×10^3	0.621
250 0	250	0	0.504	6.68×10^6	0.621
250 5	250	10^5	0.502	5.00×10^4	0.620
250 6	250	10^6	0.502	5.20×10^3	0.613

Our set of models is listed in Table 5.1. I calculated 2-M$_\odot$ models at metallicity Z=0.01. I chose two initial rotation rates set at the ZAMS: 125 and 250 km s^{-1} corresponding to a v/v$_{\mathrm{crit}}$ of 0.27 and 0.57 respectively. These initial values match the range found for very young B stars (log g$_{\mathrm{polar}}$ > 4.15) by Huang, Gies & McSwain (2010) and are similar to those used in previous publications of rotating AGB stars: Langer et al. (1999); Herwig, Langer & Lugaro (2003); Siess, Goriely & Langer (2004) used 250 km/s for their 3-M$_\odot$ model, while Piersanti, Cristallo & Straniero (2013) used up to 120 km s^{-1} for their 2-M$_\odot$ star.
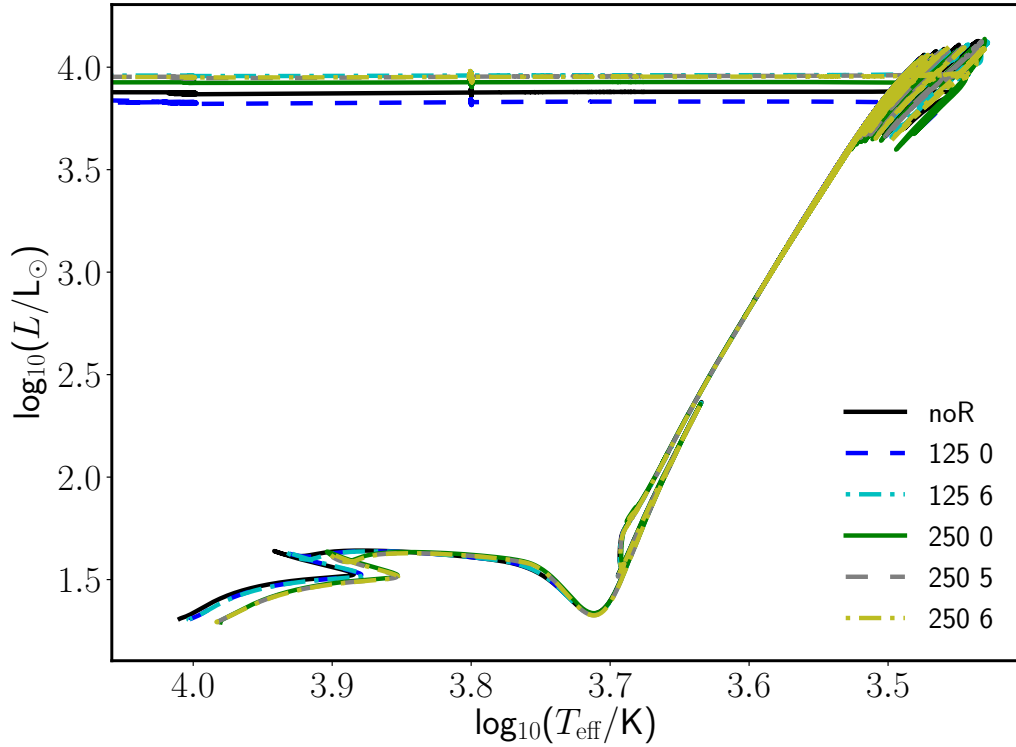
Figure 5.1: The Hertzsprurg-Russell diagrams (HRD) of the non-rotating and rotating models, see text for discussion.

The values of 10^5 and 10^6 cm^2 s^{-1} for ν_{add} were chosen to reach the observed core rotation rates, see Sect. 5.2.1 for the comparison. In all models, $\nu_{add}=0$ from the end of the core He burning phase onward. These settings follow the results of Paper I, except that the values used for ν_{add} are lower than in Paper I. This difference is caused by the different aims of the studies: in Paper I I focussed on the observations of a small data set of core He burning stars (Deheuvels et al. 2015), while in this study I am interested in obtaining a model that can serve as an upper limit of all observed core rotation rates. I also include models with $\nu_{add}=0$ for both initial rotation rates.

My rotating models only include the ES circulation and the SSI. I exclude all dynamical instabilities (DSI and SH) as these instabilities do not transport angular momentum (see

Appendix B in Chapter 4) or participate in the mixing of chemical elements. I discuss this point in more detail in Appendix 5.A. The exclusion of the GSF instability is based on Hirschi & Maeder (2010) and Caleo, Balbus & Tognelli (2016), and described in detail in Section 2.4.5.

Fig. 5.1 shows the HRDs of the models listed in Table 5.1 up to the post-AGB phase. Rotating models are located to the right of the non-rotating model on the ZAMS due to the centrifugal force expanding the star and producing a cooler surface. The core masses of the rotating models without ν_{add} at the end of the main sequence are slightly larger than those of the models including ν_{add} and of the non-rotating models because of the mixing of extra fuel into the core during the main-sequence. As a result of the larger core mass, the next core burning phase is shorter and therefore the core masses after the core He burning phase are comparable (Table 5.1). Small variations in core masses occur after the AGB phase due to differences in the number of TPs and thus core growth during the AGB phase. This mass difference, see Table 5.1 is visible as difference in luminosity in the post-AGB tracks in Fig. 5.1.

5.2.1   Rotational evolution

Figure 5.2 shows four models from Table 5.1: the two rotating models without ν_{add} and the two rotating models with $\nu_{\mathrm{add}}=10^6$ cm^2 s^{-1}. The different trends visible in the models with and without ν_{add} are explained in detail in Paper I. In short, by adding ν_{add}, coupling is provided between the core and envelope that allows for transport of angular momentum from the core to the envelope, even during the evolutionary phases where the core is contracting. As a result, the core rotation rate shows a steady decrease during the evolution, instead of an increase as in the standard rotating model without ν_{add}.

From the four models shown in this figure, those with $\nu_{\mathrm{add}} = 0$ only match the observations at the start of the main sequence, while those with $\nu_{\mathrm{add}}=10^6$ cm^2 s^{-1} represent rough upper limits of the observed core rotation rates. During the core He burning phase the comparison between these models and the observations is especially important. I therefore added markers (black dots) to the two models, indicating every 10% of the

total duration of the core He burning phase. These dots show that from 10% to 80% of the total duration of the core He burning phase, the models are in the same location as the observed rotation rates in this figure.

The core rotation rates at the first TP are given in Table 5.1. These rates show a difference of three orders of magnitude between the models with and without ν_{add}. I also calculated a model with a low initial rotation rate of 10 km/s, which has a core rotation rate of $\Omega/2\pi = 7.88 \times 10^5$ nHz at the first TP. This is still two orders of magnitude higher than the rotation rates of the models matching the observed rotation rates, showing that simply reducing the initial rotation rate cannot match the observed rotation rates. Another method to reduce the core rotation rate, for instance ν_{add}, is needed.

I also calculated the '250 5' model. The core rotation rate at the first TP is an order of magnitude higher than the '250 6' model. The core rotation rate during core He burning of this model is at least an order of magnitude higher than all observed core rotation rates for this evolutionary phase. At the first TP, the core rotation rate is an order of magnitude larger than the '250 6' model. Therefore, s-process production of this model can be considered a conservative prediction for the s-process production of stars rotating at rates matching the asteroseismically measured rotation rates. In Table 5.1 I also show the white dwarf rotation rates from the models. Most of the white dwarfs for which rotation rates are known are DAVs, which are pulsating H-rich white dwarfs. They have a T_{eff} between $10600-12600$ K, because the H on their surface has to be partially ionised for the pulsations to take place. The presented rotation rates are taken within the DAV temperature range[1]. As in Fig. 5.2, the models including $\nu_{\text{add}} = 10^6$ cm^{2}s^{-1} match the observed white dwarfs rotation rates from Kawaler (2015) and Hermes et al. (2017), while the '250 5' model is an order of magnitude too low. The models without ν_{add} are far from the observed values (confirming the results of Suijs et al. (2008) and Cantiello et al. (2014)). As mentioned previously, I remove ν_{add} after the end of the core He burning phase, therefore conserving angular momentum within the core from this point onward.

---

[1]The '250 5' model undergoes a very late thermal pulse (VLTP) whilst on the WD cooling track, before the DAV temperature range is reached. As this model runs into convergence issues before returning to the white dwarf track, I have taken the rotation rate just before the very late thermal pulse.
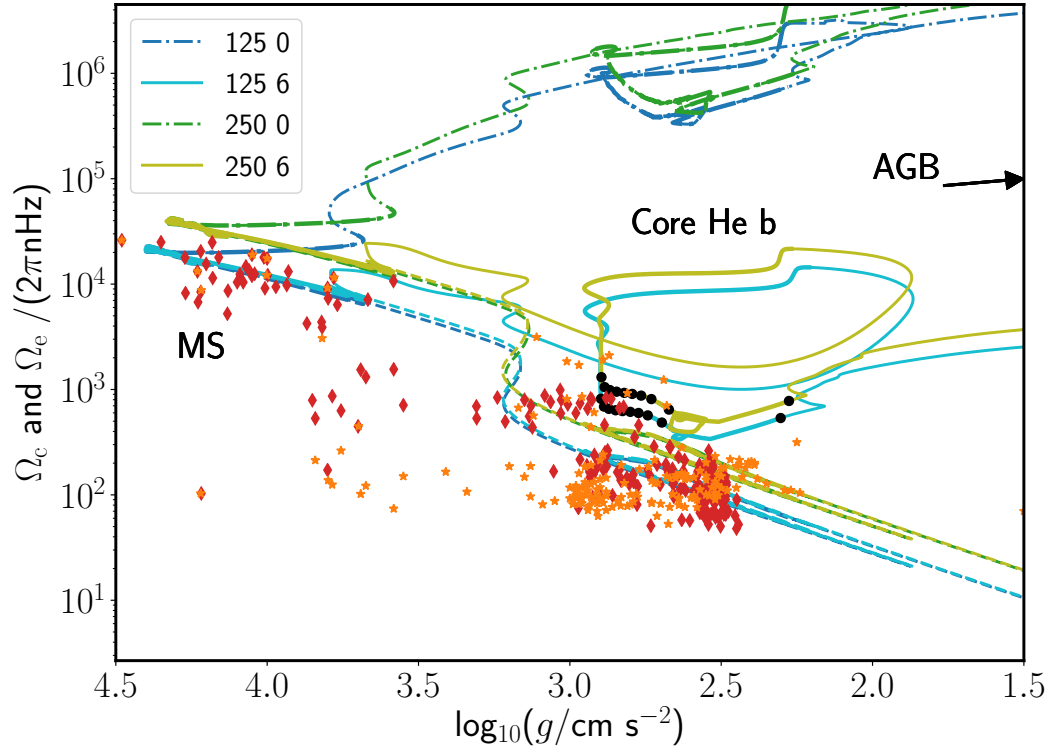
Figure 5.2: Evolution of core (Ω_c) and surface rotation (Ω_s) rates. Four of the models listed in Table 5.1 are shown here, and compared to asteroseismically obtained rotation rates. The observational data points are the core (red diamonds) and the surface (orange stars) rotation rates, taken from Mosser et al. (2012), Deheuvels et al. (2012), Deheuvels et al. (2014), Deheuvels et al. (2015), Ceillier et al. (2017), and the compilation of observed main-sequence stars from 12 other papers presented in Aerts, Reeth & Tkachenko (2017). From these observational studies, I only selected single stars in the mass range $1.4-3.0$ M$_\odot$. Typical error bars of these observations are of the order of the symbol size used. The solid and dot-dashed show the core rotation rates of the models with and without the additional viscosity respectively. The dashed lines show the envelope rotation rates of the models. The thick line segments correspond to the core burning phases, and the thin segments to the shell burning phases. The black dots indicate the time spend in the core He burning phase by the models with $\nu_{\rm add} \neq 0$, each spaced by 10% of the total duration starting at the 10% mark and ending with the 100% mark (the dots located on the most left and right, respectively). These dots show that these models spend most of their time during this evolutionary phase close to the observed rotation rates.

As in Cantiello et al. (2014); Aerts, Mathis & Rogers (2019), this approach allows to match the observed rotation rates during both the core He burning phase and the white dwarf cooling track.

5.3 s-process production in models matching asteroseismically measured rotation rates
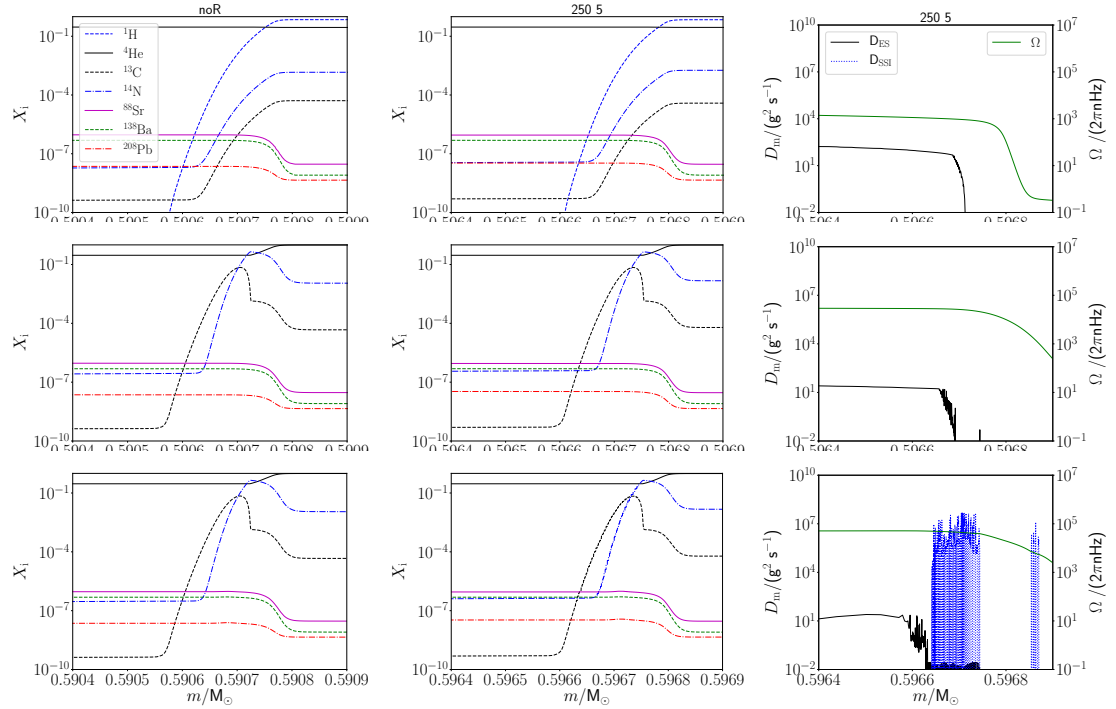
Figure 5.3: Abundance and diffusion profiles within ^{13}C-pocket regions. These regions fall within the same interpulse period as the fifth TDU (from my MPPNP results). The left panels show the abundance profiles of the non-rotating model, and the middle and right panels show the abundance and diffusion profiles of the '250 5' model. The top panels correspond to the maximum extent of the TDU, the middle panels correspond to the maximum ^{13}C-pocket size, and the bottom panels correspond to the profiles when the s-process production has started. The influence of rotation on the ^{13}C-pocket of the '250 5' is small, the only difference is that the abundance profiles are not as smooth as in the 'noR' model.

In this section I show the s-process production of two the models from Table 5.1: the '250 5' and '250 6' models. I compare the s-process production of these models to the s-process production of my non-rotating model. The other models included in Table 5.1, which do not include an additional viscosity, are discussed in Appendix 5.A together with a comparison to previously published work on s-process production in rotating AGB stars.

5.3.1 ^{13}C-pockets

As explained in the Introduction, the ^{13}C-pocket in low-mass AGB stars is where most of the neutrons for the neutron captures are produced. Therefore, I start the comparison with the abundance and diffusion profiles in the ^{13}C-pockets. Specifically, I compare the ^{13}C-pocket of the non-rotating and the '250 5' model during the interpulse period in which the fifth TDU takes place. I chose to use this model for this comparison as it will give us a conservative upper limit of the impact of rotation on the ^{13}C-pocket.

The abundance and diffusion coefficient profiles of the ^{13}C-pockets are shown in Fig. 5.3 for three different time steps. The diffusion profiles are calculated following Herwig, Langer & Lugaro (2003): I show the Lagrangian mixing coefficient (D_{m} and not the Eulerian one D_{r} which is given as MESA output) as I want to assess the effect of the mixing processes on the chemical elements:

$$D_{\mathrm{m}} = \left(\frac{dm}{dr}\right)^2 D_{\mathrm{r}} = (4\pi\rho r^2)^2 D_{\mathrm{r}} \qquad (5.1)$$

where all symbols have their usual meaning. In the same figure I also added the Ω profiles on log-scale, to better understand the behaviour of the instabilities. These Ω-profiles show that the pocket is located just below the drop in Ω, which coincides with the maximum extent of the TDU.

For all three time steps, the profiles and the size of the ^{13}C-pocket in the two models are comparable, because the diffusion coefficient of the Eddington-Sweet (ES) circulation is present with values between 10^1-10^2 g^2 s^{-1}. This is not high enough to impact the abundance profiles. Also, the ES circulation is only present in regions of constant Ω,
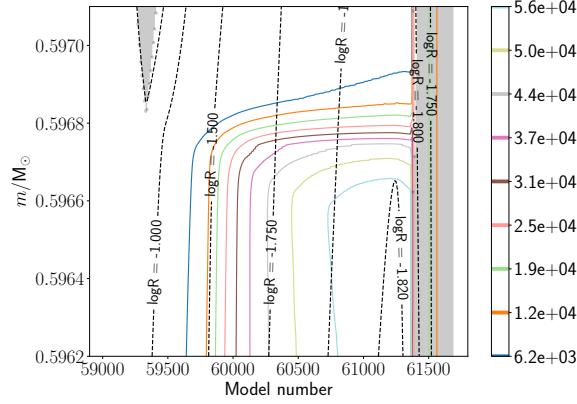
Figure 5.4: Time evolution of Ω. The Ω profile is taken from the interpulse of the '250 5' model that is shown in Fig. 5.3. Grey regions are the convective envelope during TDU (left) and the TP (right), dashed black contour lines show constant $\log_{10}(r/R_\odot)$, coloured contour lines show Ω values in linear range (the darker the contour line, the lower Ω). Model numbers 59400, 60000, and 60500 correspond to the three time steps in Fig. 5.3, and the vertical axis of this figure corresponds to the horizontal axes of the '250 5' panels in Fig. 5.3. The contraction of the region leads to a steeper Ω gradient in the ^{13}C-pocket region.

which is also where the ^{13}C abundance is low. The reason behind these characteristics can be explained by the strong dependence of D_{ES} on Ω (Heger, Langer & Woosley 2000), which is $D_{m,ES} \propto \Omega^2$. The Ω evolution during the interpulse phase of the '250 5' model is shown in Fig. 5.4. When Ω increases due to the contraction of the intershell region, $D_{m,ES}$ remains nearly constant due to the smaller radial coordinate of the ^{13}C-pocket. The ES-circulation is also dependent on the molecular weight gradient, which prevents this mixing process from being active within the ^{13}C-pocket.

The secular shear, the only other rotationally induced instability included in this model, is only present in the panels of Fig. 5.3 when the s-process production has started, in the region of the ^{13}C-pocket. The $D_{m,SSI}$ depends on $d\Omega/dr$, which is stronger in the bottom panel of Fig. 5.3, as shown in Fig. 5.4. Molecular weight gradients inhibit $D_{m,SSI}$, which is why $D_{m,SSI}$ decreases around $m/M_\odot \simeq 0.59675$. The high values of $D_{m,SSI}$ however, have little effect on the abundance profiles as $D_{m,SSI}$ is discontinuous (more details on this
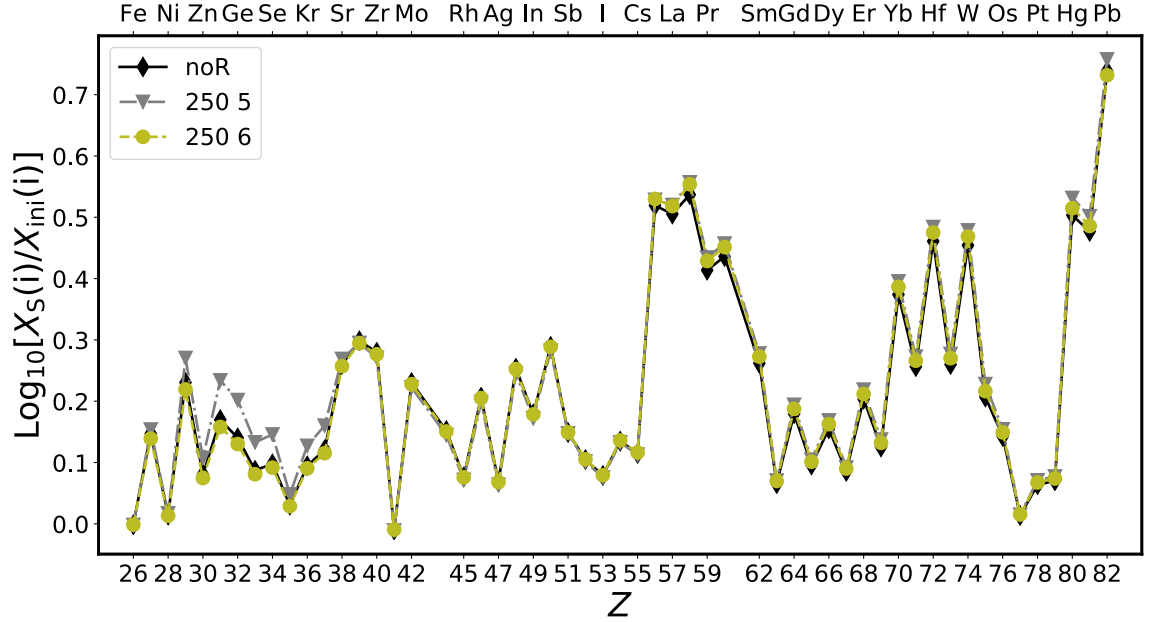
Figure 5.5: Surface enrichment of 'noR', '250 5' and '250 6'. This comparison shows that the s-process production of rotating models that match asteroseismically measured rotation rates is comparable to that of the non-rotating model.

can be found in Appendix 5.A). Continuous spatial mixing is needed to influence the abundance profiles and the resulting s-process production. It is unknown whether the discontinuous character of the SSI is physical or numerical (see also Aerts et al. 2018). Diffusion coefficients of rotationally induced instabilities have been discussed in the previous publications on rotating AGB stars (see Langer et al. 1999; Herwig, Langer & Lugaro 2003; Siess, Goriely & Langer 2004; Piersanti, Cristallo & Straniero 2013). These publications, however, discuss rotating models, that do not include a process able to decrease the core rotation rate in order to match the asteroseismically measured core rotation rates. Therefore, these models rotate too fast at the start of the AGB phase. This is clear from Column 5 in Table 5.1, where the standard rotating models '125 0' and '250 0' rotate three orders of magnitude faster than the models that match the asteroseismically measured core rotation rates ('125 6' and '250 6'). Therefore, a consistent comparison is not possible between the models of previous publications and

models described in this section. Here I only note that Fig. 2 of Piersanti, Cristallo & Straniero (2013) shows the location in the intershell where their models are unstable against the ES circulation and the GSF instability (not present in my models, as discussed in Sect. 5.2). While Piersanti, Cristallo & Straniero (2013) does not mention the strength of their diffusion coefficients, their Fig. 2 shows that they found the interpulse to be unstable for ES circulation at the same location as in my models.

5.3.2 Surface enrichment of s-process elements

In the previous subsection I found that rotation results only in small differences in the ^{13}C-pockets when the '250 5' model is compared to the non rotating model. I therefore expect the resulting s-process production of the two models to be comparable.

In Fig. 5.5 I show the surface enrichment factors for the models 'noR', '250 5', and '250 6'. The surface enrichment factors have been calculated after the final TDU and are scaled to their initial abundances. All three models largely overlap in this figure. The 'noR' model experienced one TDU more than the two rotation models, I therefore show the surface enrichment of the TDU before the last TDU for the 'noR' model to have a fair comparison.

From this I conclude that when the models rotate at a rate that matches the asteroseismically measured rotation rates or an order of magnitude faster, the s-process production is comparable to that of the non-rotating model, as suggested by Piersanti, Cristallo & Straniero (2013). A consequence of this result is that, according to my models, any spread in observed s-process production of a certain metallicity is unlikely to be caused by rotation (see e.g. Abia et al. 2002 and de Castro et al. 2016).

As the results of the rotating models described in this section match the non-rotating model, I refer the reader to Battino et al. (2016) and Battino et al. (2019) for a comparison to s-process observations, because the non-rotating models described in those papers are similar to those presented here.

5.4 Final remarks

In this paper I presented rotating AGB star models (2 M$_\odot$, Z=0.01) that are forced to match the asteroseismically measured rotation rates before and after the AGB phase. For the first time, I have presented the s-process production of such models that rotate at such rates. My main findings are described below.

- My models including additional viscosity of $\nu_{\mathrm{add}}= 10^6$ cm^2 s^{-1} follow the upper limit of the observed trend of core and envelope rotation rates inferred from Kepler observations, comparable to the results of den Hartogh, Eggenberger & Hirschi (2019).

- The models that are forced to match the asteroseismically measured core rotation rate show s-process production similar to that of the non-rotating model. Therefore the effect of rotation on s-process production is negligible in these models.

- I also calculated a model where the core rotates an order of magnitude faster than observed values, as conservative upper limit to observed rotation rates. The s-process production of this model is also comparable to the non-rotating model, strengthening my previous conclusion.

- The results above are independent of the initial rotation rate.

Several uncertainties may potentially affect these conclusions. The most important is the constant ν_{add} that is used to reduce the theoretical core rotation rates to the asteroseismically obtained rates. This constant has no physical meaning (yet) and the results presented here should therefore be interpreted as not necessarily the final answer, but as a next step towards understanding the s-process production in rotating low-mass AGB stars. In particular, different combinations of the value for ν_{add} and the values of the two f parameters in the implementation of rotation may lead to similar core rotation

rates. The range of values for these f parameters might however be limited, as more recent calibrations by Yoon, Langer & Norman (2006) and Brott et al. (2011) resulted in f_μ=0.1, f_c=0.03), similar values to the ones found by Heger, Langer & Woosley (2000). My conclusions remain the same when I tested these values in my calculations.

Another issue is that I have only investigated the effects of non-magnetic mixing processes. In Paper I, I already found that the TS-dynamo does not allow for enough transport of angular momentum in stellar evolutionary models with an initial mass of 2.5 M$_\odot$ to match the observations (confirming results of Cantiello et al. 2014, for their 1.5-M$_\odot$ models). Recently, a revised derivation of the TS-dynamo was published by Fuller, Piro & Jermyn (2019) who show that this mechanism is able to match the asteroseismically obtained core rotation rates. However, this prescription does not predict a fast rotating solar core as suggested by reported detections of gravity modes (Eggenberger, Buldgen & Salmon 2019).

Besides the uncertainties around the missing process of angular momentum transport, the current implementation of rotationally induced mixing processes remains a major challenge (Appendix 5.A). I cannot exclude the possibility that better descriptions will effect the s-process production in rotating AGB stars. Furthermore, two flavours for the implementation of rotation in stellar evolution codes exist: diffusive (see e.g. Heger, Langer & Woosley 2000) and advective (see e.g. Maeder & Meynet 2000, 2012), where the second implementation uses different prescriptions for the mixing processes and this could affect the s-process production in AGB stars.

I will investigate these uncertainties in future publications.

5.A   The s-process in models without additional viscosity

In this appendix I describe my models that rotate too fast to match asteroseismically measured core rotation rates and provide a comparison to the previously published papers (Herwig, Langer & Lugaro 2003; Siess, Goriely & Langer 2004; Piersanti, Cristallo & Straniero 2013). I stress that for all these models the core rotate orders of magnitude

Table 5.2: Set of stellar evolution models described in this Appendix. Only the rotational instabilities are listed as all other parameters are equal.

Model	ES	SSI	GSF	DSI	SH
250 0	y	y	-	-	-
250 0 +GSF	y	y	y	-	-
250 0 +all	y	y	y	y	y

faster in the evolved evolutionary phases, as compared to the observations.

Another difference between the models described in the main text and those presented here is the amount of rotationally induced mixing processes. Because in the previously published papers mentioned above all rotationally induced mixing processes as defined by Heger, Langer & Woosley (2000) were included, I provide here a model that also includes all processes. Piersanti, Cristallo & Straniero (2013) mentions that the GSF instability is the main process responsible for the pollution of the ^{13}C-pocket by ^{14}N, limiting the neutron exposure and keeping the s-process production concentrated around the Sr/Y/Zr peak. I therefore also add a model that includes only the ES circulation, the SSI, and the GSF instability. The three models described in this Appendix is listed in Table 5.2.

5.A.1 Effects on the ^{13}C-pocket of the inclusion of all rotationally induced diffusion processes

The two new models are restarted from the '250 0' model in Table 5.1 at the last TP before the first TDU and thus before the first ^{13}C-pocket. This allows for a direct comparison of s-process production in these models to the '250 0' model without the extra mixing processes, as the first TDU is the start of the s-process production.

The abundance profiles shown in the left column of Fig. 5.6 are characteristic for the models presented in this section. Compared to the abundance profiles of the '250 5' model, there are two distinct differences. The first is that the ^{13}C-pocket in Fig. 5.6 is widened compared to the ^{13}C-pocket in Fig. 5.3 . This is due to the higher rotation rate leading to the ES circulation being two orders of magnitude stronger in the '250 0'

models, see columns $2-4$ in Fig. 5.6, than in the '250 5' model. The second difference is that the abundance profiles in the '250 0' pocket are less smooth than in the '250 5' pocket. This is due to the discontinuous mixing by the SSI, as already mentioned in Sect. 5.3.1. The ES circulation is however still present in the ^{13}C-pocket region in the '250 0' model even when the s-process production has started. This results in poisoning of the '250 0' pocket by ^{14}N.

The diffusion profiles of the model including the GSF instability are shown in the third column from the left in Fig. 5.6. This instability depends on both the Ω values and on the spatial derivative of Ω, and is present almost throughout the mass range shown. It is however not dominant over the ES circulation or the SSI, and will therefore not have much effect on the s-process production, contrarily to what was concluded by Piersanti, Cristallo & Straniero (2013).

The right column in Fig. 5.6 shows the diffusion profiles of the model including all rotationally induced instabilities. Both new instabilities (DSI and SH) have diffusion profiles with a discrete character and will therefore have limited effect on the s-process production within this model.

5.A.2 Surface enrichment

Figure 5.7 shows the comparison of the surface enrichments, including the surface enrichment of the non-rotating model. All '250 0' models are comparable in this figure, confirming the findings of the previous section that the inclusion of GSF, DSI, and SH does not have an effect on the s-process production. Compared to the non-rotating model, the s-process production has greatly increased up to Sm. I thus also find that rotation could increase the s-process production. This increase can be explained by the widened ^{13}C-pocket, allowing for more Fe-group seeds to be activated by neutron captures. The pocket is widened compared to the non-rotating models because of the ES circulation being active during the creation of the pocket. The poisoning of the ^{13}C-pocket by ES circulation mixing in ^{14}N is the reason why this increased production has not continued until Pb.

The surface enrichment of the models included in Fig. 5.7 can be compared to Piersanti, Cristallo & Straniero (2013) as they present 2-$M_\odot$ models at solar metallicity albeit at much slower rotation rates. The trends these models show is that the inclusion of rotation reduces the overall s-process production, due to the contamination of the pocket by ^{14}N, which is opposite to what I find and further investigation would be needed to understand this difference. However, both sets of rotating models show core rotation rates that are several order of magnitude above the asteroseismically measured rotation rates throughout the evolution. Further studies do not seem warranted.

Comparison to Herwig, Langer & Lugaro (2003) and Siess, Goriely & Langer (2004) is less straightforward, as the first study concludes that the combination of overshoot (now renamed as convective boundary mixing) and rotation might allow for a spread in s-process production in AGB stars, while the second study does not combine the two processes.

Neither of the previously published studies on rotating AGB stars mentioned the changes in smoothness of abundance profiles as reported in the previous section.

5.A.3   Discontinuous mixing and smoothing options

The reason why I find these differences with Piersanti, Cristallo & Straniero (2013), may be related to the choice of smoothing options. The discontinuous character of several instabilities are caused by two features within the implementation of the instabilities. The first is that the implementation itself of these instabilities allows for a discontinuous behaviour, as there is of course a stability criterion present in the implementation. If the zone within a model is unstable according to the instability criterion, the instability becomes active, while in the next zone it can be stable again. The second issue is that when dynamical and secular shear appear, they should be taken into consideration immediately and not at the start of the next time step. The current implementation does include the shear at the next time step and therefore overestimates its impact. These issues reduce the practical use of these instabilities (as also concluded by Aerts et al. 2018, in a different astrophysical context).

Smoothing options are available and tested to solve the issues, however, it is impossible to decide which feature is physical and should not be smoothed, and which is numerical and should be smoothed. Therefore, in this work I have decided to avoid the use of smoothing functions. Among several different options tested, the only 'smoothing' option that seems to effectively improve stellar profiles is the inclusion of a low additional viscosity. This has the effect that the Ω-profile is smoothed, which leads to a reduced appearance of secular and dynamical shear. However, the discontinuous behaviour of the SH instability is still present. Including all instabilities in an accurate manner remains a challenge.

Figure 5.6: Abundance and diffusion plots showing the maximum extent of the TDU (top panels), the maximum ^{13}C-pocket size (middle panels), and the start of the the s-process production (bottom panels), matching the interpulse in which the fifth TDU takes place as in Fig. 5.3. I show the abundance profiles of a characteristic ^{13}C-pocket in the most left panel, followed by the diffusion profiles of the '250 0', '250 0 +GSF', and the '250 0 +all' models respectively. The ^{13}C-pockets in these models are widened when compared to the '250 5' model in Fig. 5.3 due to the ES circulation. Please note the changed range over which the diffusion coefficients are shown compared to Fig. 5.3.

Figure 5.7: Surface enrichment of the non rotating and the 250 0 models, showing that the inclusion of GSF, SH and DSI does not alter the s-process production. This is a numerical issue: there is work to be done between the derivation of the instabilities and their implementation in stellar evolutionary codes.

6 Exploratory studies

In this chapter I present some further exploratory studies. The following research questions are considered:

- The surface rotation rate of one AGB star (R Doradus) has been determined, however stellar evolution models for single stars have been unable to match this value. Can the surface rotation rates of the stellar evolution models presented in this thesis that include the additional, artificial viscosity match the surface rotation rate of R Doradus? (Section 6.1)

- What is the effect of including the additional, artificial viscosity in the mixing of chemical elements? (Section 6.2)

- What happens to the efficiency of the transport of angular momentum in the TS-dynamo model, when the dependency of the dynamo on the molecular weight profile is removed? (Section 6.3)

- A new derivation for the TS-dynamo has been presented in Fuller, Piro & Jermyn (2019). Does this process indeed transport enough angular momentum out of the stellar core? The results of this study has been included in A&A, 2019, 631 (I am second author). (Section 6.4)

6.1 Surface rotation rate of AGB star R Doradus

Vlemmings et al. (2018) determined a surface rotation rate of the nearby AGB star R Doradus of v $\sin(i) = 1\pm 0.1$ km s^{-1}, and compared this value to the surface rotation rates of stellar evolution models (García-Segura et al. 2014, 2016). Their conclusion is that the surface rotation rate of R Doradus cannot be reached by single star models. They did not, however, include any enhanced transport of angular momentum in the

single star evolutionary models. In this section I therefore test if the observed value can be reached by my models that include an additional viscosity.

The surface rotation rate for R Doradus is the first direct detection of rotation in the extended atmosphere of an AGB star has been presented, as a very high signal-to-noise ratio is needed for careful analysis of its velocity. As the star has a temperature of about 2100 K and a radius of 400 $R_\odot$, R Doradus is an oxygen-rich and far evolved along the AGB phase. Both García-Segura et al. (2014) and García-Segura et al. (2016) were performed with an initial mass of 2.5 $M_\odot$, while the initial mass of R Doradus is estimated to be 1.3-1.6 $M_\odot$. Therefore, a single star model with an initial mass of 1.5 $M_\odot$ was calculated for the comparison Vlemmings et al. (2018). The trends of the surface rotation rate during the AGB phase of this 1.5 $M_\odot$ are claimed by Vlemmings et al. (2018) to be similar to the 2.5-$M_\odot$ models, hence Vlemmings et al. (2018) inferred that the surface rotation rate of R Doradus is a strong indication that the star has a binary companion. The authors also noted that this conclusion is independent of the initial rotation rate used. Here, we test this conclusion, by comparing the trends in the 2-$M_\odot$ stellar models presented in Chapter 5 to the 2.5-$M_\odot$ models of García-Segura et al. (2014).

The surface rotation rate throughout the AGB phase for models '125 0', '125 6' and '250 0' are shown in Fig. 6.1. These models are chosen to investigate the effect on the surface rotation rate of the initial rotation rate and of the inclusion of the additional viscosity. At the start of the AGB phase, all the presented models have a surface rotation rate above 1 km s^{-1}, which decreases rapidly when mass is lost, since along with the mass also angular momentum is removed from the star. Furthermore, during the AGB phase the envelope is expanding and therefore the star rotates slower at the surface. The higher the initial rotation rate, the more angular momentum is present in the star and thus in the envelope. This is why the '250 0' model has a higher v_{surf} than the '125 0' model. When including $\nu_{\mathrm{add}}{=}10^6$ cm^2 s^{-1} ('125 6'), more angular momentum is transported from the core outwards. However, as already seen in Chapter 4 and Chapter 5, the surface rotation rate is not significantly altered by this. This is due to the large size of the envelope over which the transported angular momentum is spread out. When the three

models approach the end of the AGB phase, their surface velocity reaches values around 0.01 km s^{-1} and lower, comparable to the surface velocities of the 2.5-M$_\odot$ model from García-Segura et al. (2014). The inclusion of $\nu_{add}{=}10^6$ cm^2 s^{-1} and the increase in the initial rotation rate by a factor of two do not influence greatly the surface velocity during the AGB phase.

My test with existing models agrees with the results of Vlemmings et al. (2018) that it is not possible to match the observed surface rotation rate of R Doradus with a single star evolution. Therefore, it is likely that R Doradus has indeed experiences binary interaction in its life time. This result does not justify designing and performing a dedicated parameter study around the surface rotation rate of R Doradus.
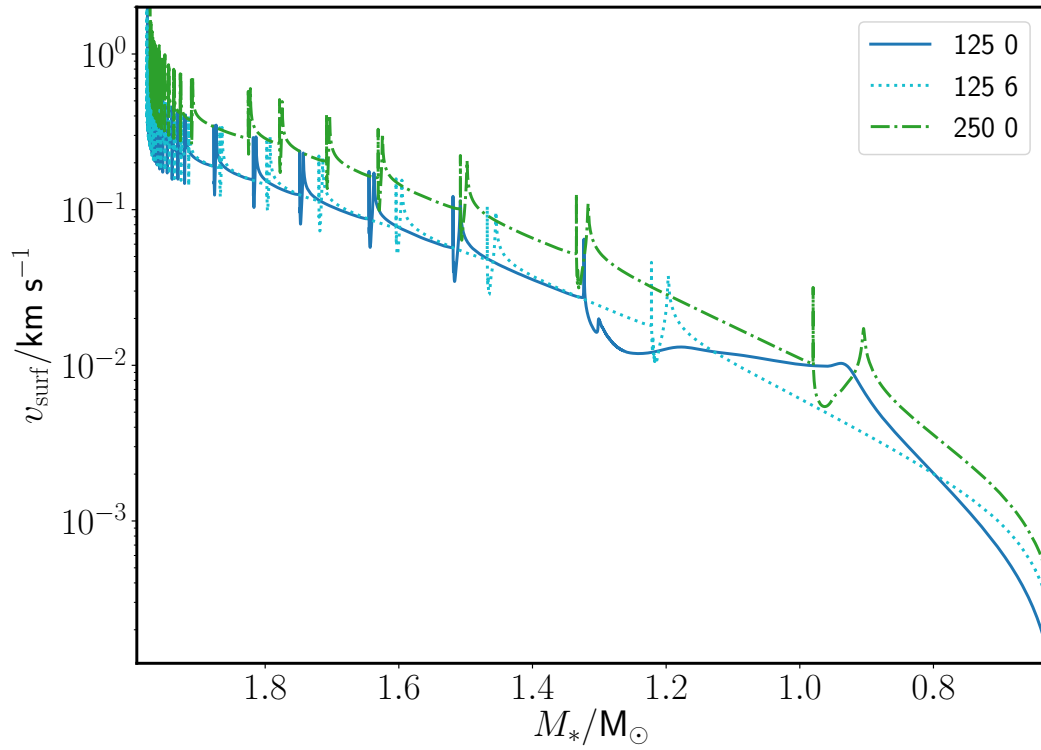
Figure 6.1: Evolution of surface rotation rate during the AGB phase. Three 2 $M_\odot$ models are presented, rotating at an initial rotation rate of 125 km s^{-1} ('125 0' and '125 6') or 250 km s^{-1} ('250 0'). One model includes the additional, artificial viscosity ('125 6'). All models are well within one order of magnitude of each other at any point in the AGB phase, showing that the inclusion of an additional viscosity ν_{add} and a change in the initial rotation rate do not alter significantly the surface rotation velocity.

## 6.2 Additional viscosity added to the chemical elements

As mentioned in Section 3.3.2, there is no observational evidence that the missing process of angular momentum transport should also strongly mix chemical elements. In this section I present some tests where I included an additional viscosity to increase the mixing of chemical elements ($\nu_{\mathrm{add,Xi}}$) to investigate what its effect would be.

This second additional viscosity $\nu_{\mathrm{add,Xi}}$ is implemented following the same method as for the additional viscosity to increase the transport of angular momentum (to avoid any confusing I rename to it in this section as $\nu_{\mathrm{add,\Omega}}$): in Eq. 2.8, $\nu_{\mathrm{add,Xi}}$ is added to D_{mix}. In Fig. 6.2 is shown the Kippenhahn diagram of the 2-M$_\odot$, Z=0.01 model that rotates with an initial rotation rate of 250 km s^{-1}, including $\nu_{\mathrm{add,\Omega}}$=10^6 cm^2 s^{-1} and $\nu_{\mathrm{add,Xi}}$=10^6 cm^2 s^{-1}. The main consequence of the inclusion of $\nu_{\mathrm{add,Xi}}$ is that the molecular weight gradients do not inhibit the mixing of chemical elements, as the enhanced mixing smooths out the molecular weight gradients faster than that they are created by nuclear fusion. Therefore, this star grows a larger He core, and later on a CO core. As a result, this 2-M$_\odot$ model will likely ignite C (the network currently does not include it), and continue its evolution through all other burning phases. This is clearly visible when comparing Fig. 6.2 to Fig. 1.2, the latter showing a non-rotating stellar evolution model of the same initial mass and metallicity as the model in Fig. 6.2. The H burning shell in the non-rotating model starts at a mass coordinate of 0.25 and ends $\simeq$ 0.35 M$_\odot$, while in the model presented in Fig. 6.2 the H burning shell starts at 0.35 M$_\odot$ and ends $\simeq$ 1.75 M$_\odot$. The corresponding HRD of the model including both ν_{add} parameters (labelled as '250 6 6') is shown in Fig. 6.3, with the model that only includes $\nu_{\mathrm{add,\Omega}}$ (labelled as '250 6 0'). A wide bifurcation in evolutionary tracks in visible. The '250 6 0' model follows the classical HRD track of a 2-M$_\odot$ star, while the '250 6 6 ' model evolves towards higher luminosities while increasing its effective temperature, and thus moves to the opposite side of the HRD.

This type of evolution is called (quasi-)chemically homogeneous (QCHE), and was first

described by Maeder (1987). In Maeder (1987), chemically homogeneous evolution was obtained in massive stars by fast rotation, where the rotationally induced instabilities were strong enough to smooth out the gradients in the molecular weight. These QCHE stars were then suggested to evolve into Wolf-Rayet stars, massive He-rich stars. The possibility of the formation of Wolf-Rayet stars via chemically homogeneous evolution in rotating massive stars has been investigated further (see e.g. Langer 1992; Yoon & Langer 2005; Schootemeijer & Langer 2018) since then. Also the formation of gamma-ray bursts (GRBs), explosions linked to supernovae, via chemically homogeneous evolution has been considered (see e.g. Yoon, Langer & Norman 2006; Woosley & Heger 2006), and merging very massive black holes (de Mink & Mandel 2016; Marchant et al. 2016; Abbott et al. 2016) might lead to QCHE as well. However, all these studies only investigated massive stars and the observational evidence of chemically homogeneous evolution is limited. For low- and intermediate-mass stars, there is no evidence of QCHE. Thus, the value of the $\nu_{\mathrm{add,Xi}}$ must be lower than of the $\nu_{\mathrm{add,\Omega}}$.

Figure 6.3 also includes tracks for models with values of $\nu_{\mathrm{add,Xi}}$ lower than 10^6 cm^2 s^{-1}. These tracks show that when $\nu_{\mathrm{add,Xi}}$ is 10^2 cm^2 s^{-1} or lower, the evolutionary tracks follow the same path as the non-rotating models, while higher values allow for the QCHE as described above. The difference of several orders of magnitude between the two ν_{add} values suggests that the missing process cannot be a diffusive process, as diffusive processes have the same efficiency for the mixing of chemical elements as for the transport of angular moment. Magnetic dynamo processes, however, transport angular momentum several orders of magnitude more efficiently than that they mix chemical elements as discussed in Section 2.5.
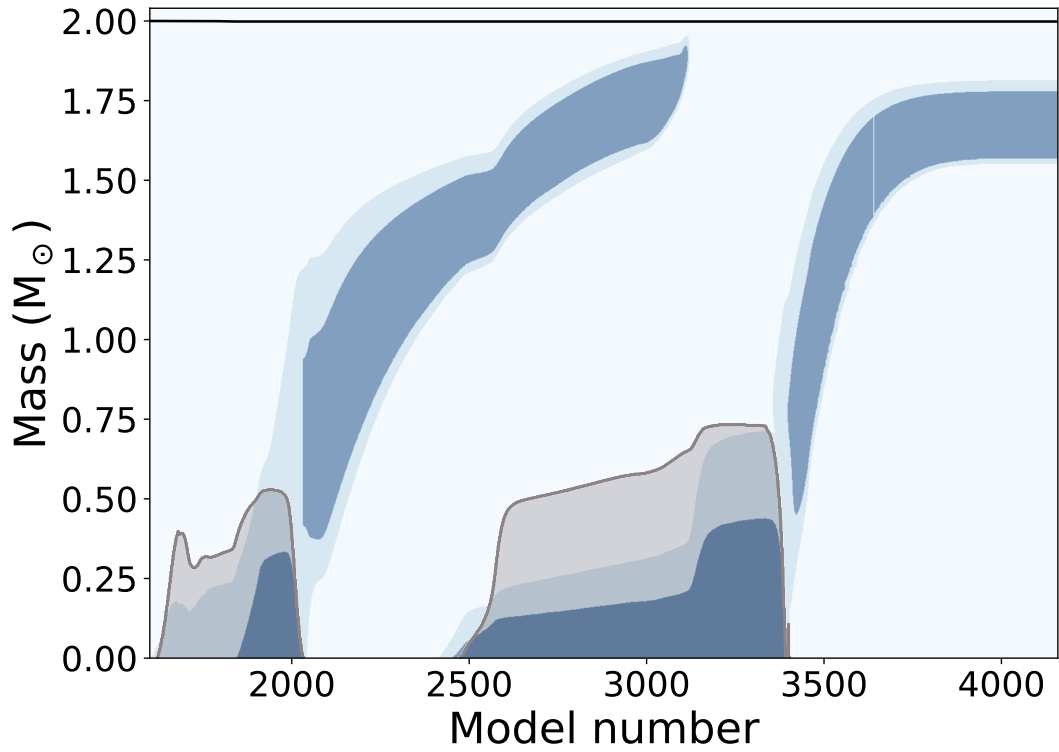
Figure 6.2: Kippenhahn diagram of the '250 6 6' model, showing that the star evolves quasi-chemically homogeneous. Convective regions are shown in grey. The H shell burning (blue shades show energy generation, the darker the higher the energy generation rate) nearly reaches the surface, indicating the stars has little H left. The same trend is visible after core He burning, as the He burning shell also moves up to near the surface. The horizontal axis shows the model numbers (non-linear in time), to ensure all evolutionary features are visible.
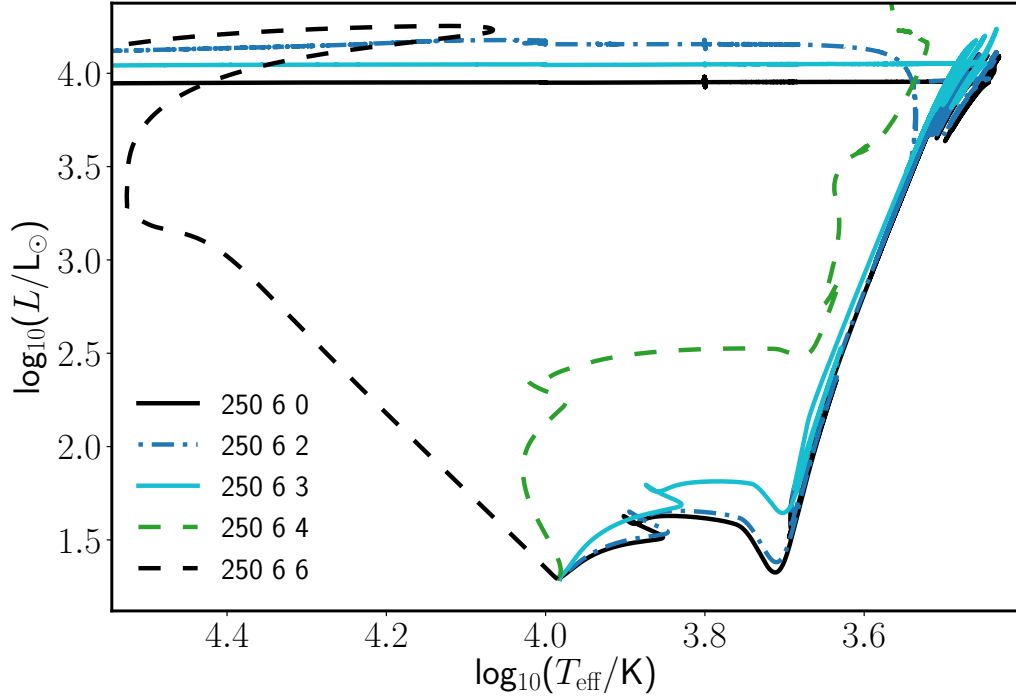
Figure 6.3: Effect on HRD tracks of adding an additional viscosity ($\nu_{\mathrm{add,Xi}}$) to mixing of chemical elements. The HRD shows the evolution of models with an initial mass of 2 $M_{\odot}$, an initial rotation rate of 250 km s^{-1}, and a $\nu_{\mathrm{add,\Omega}}$ of 10^6 cm^2 s^{-1}. The third number in the labels reflects the order of magnitude of the $\nu_{\mathrm{add,Xi}}$: here is shown 0, 10^2, 10^3, 10^4, and 10^6 cm^2 s^{-1}. See text for discussion.

6.3 Tayler-Spruit dynamo without μ dependence

A magnetic process proposed to be important for the transport of angular momentum is the azimuthal magnetorotational instability (AMRI) (see e.g. Rüdiger et al. 2007; Rüdiger et al. 2007, 2018). This instability occurs when a hydrodynamically stable medium that is differentially rotating is destabilized by an azimuthal magnetic field, where the azimuthal angle ϕ is the third spherical coordinate (with the others being r and θ) and represents the angle in the horizontal plane. It is active in regions with a (steep) radial differential rotation profile, and inactive in region with a flat rotation profile. The effect of this instability in stellar evolution models has been tested by Spada et al. (2016), and it indeed seems to be effective in the transport of angular momentum. AMRI is however still in development, and the dependency of the AMRI on molecular weight μ has not been considered yet. This is however an important variable, as a strong molecular weight gradient can stop the transport of angular momentum. The fully developed Tayler-Spruit dynamo is a much less popular instability in the asteroseismic community, because it is, in its current form, not able to provide enough transport of angular momentum to match the asteroseismically obtained core rotation rates. The current derivation, however, does include a molecular weight dependence. Therefore, as a numerical experiment, I present here a test without this dependence with the aim to investigate its importance.

The calculation of the TS-dynamo without the μ dependency is performed in two ways. The first option (labelled as 'ExMu1' in the following figures) changes how the effective diffusivity due to the TS-dynamo is calculated in the regime where both the temperature gradient and the gradient in the composition affect the diffusivity, see Eqs 2.58-2.68, by removing the effect of the gradient in composition on the effective diffusivity. The effective diffusivity is now equal to the regime where N_μ is zero. In the second option (labelled as 'ExMu2'), the effect of the gradient in composition in the calculation of the thermal buoyancy has been completely removed. Instead of $N_T^2 = N^2 - N_\mu^2$, it now is expressed as $N_T^2 = N^2$ in the MESA routine where the TS-dynamo is calculated. Both alterations affect the transport of angular momentum and the mixing of chemical elements.

This exploratory study was performed on 2.5-$M_\odot$ models with a metallicity of Z=0.014

and an initial rotational velocity of 150 km s^{-1}. Fig. 6.4 shows the evolution of the core and surface rotation rates for three models: one including the standard TS-dynamo ('TS'), and two with the altered TS-dynamo as described above. The models are compared to the same set of asteroseismically obtained core and surface rotation rates as used in Chapter 5. The two models with the altered TS-dynamo behave in a almost identical manner, showing that the both methods have the same effect, and are able to reach the asteroseismically obtained data points during the core He burning phase. The evolution during the RGB is different in the altered TS-dynamo models from the standard TS model, as the altered TS-models predict solid body rotation until $\log_{10}$=2.9 cm s^{-2} is reached, while the standard TS-dynamo model does not. This can be explained by the strong molecular weight gradient that is built up during the RGB at the edge of the core. The coupling between core and envelope is weakened by this gradient in the standard TS-dynamo. As the alterations to the TS-dynamo take away the dependence on this gradient, the model including this altered dynamo are able to transport more angular momentum out of the core during this phase than the model including the standard TS-dynamo. To summarise: the removal of the dynamo dependence on the molecular weight indeed increases the transport of angular momentum form the core outwards, to the point that the asteroseismically obtained core rotation rates can be reached.

The next step is hence to compare the final surface abundances of the models including the altered TS-dynamo to the non-rotating 2.5-M$_\odot$, Z=0.014 model. This comparison is shown in Fig. 6.5. The final abundances of the three models overlap in this figure, confirming the conclusion of Chapter 5: the s-process production of stellar evolution models that have core rotation rates that match asteroseismically obtained rates, have the same s-process production as non-rotating stellar evolution models. The conclusion is now strengthened, as in Chapter 5 the core rotation rate was reduced by ν_{add} which is constant in both time and space. Now, I have confirmed the conclusion in models which core rotation rates were reduced by a process that is constant in neither space nor time.
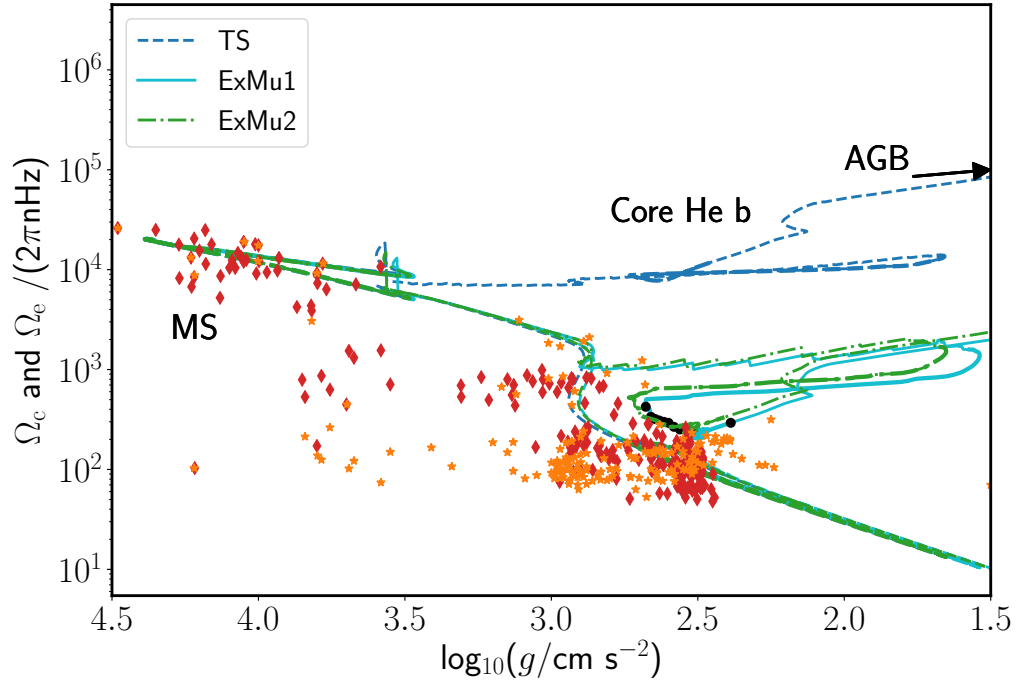
Figure 6.4: Comparison between the core and surface rotation rates of three 2.5-M$_\odot$, Z=0.014 models including the TS-dynamo, one with μ dependence ('TS'), and two without ('ExMu1' and 'ExMu2') as explained in the text. Each colour represents a different model, and both the core (Ω_c, solid and dot-dashed lines) and surface (Ω_s, dashed lines mostly overlapping each other) rotation rate are shown. The black dots indicate the time spend in the core He burning phase by the models, each spaced by 10% of the total duration starting at the 10% mark and ending with the 100% mark (the dots located on the most left and right, respectively). These dots show that these models spend most of their time during this evolutionary phase close to the observed rotation rates. The observational data points are the core (red diamonds) and the surface (orange stars) rotation rates of single stars in the mass range of 1.4−3.0 M$_\odot$, taken from Mosser et al. (2012), Deheuvels et al. (2012), Deheuvels et al. (2014), Deheuvels et al. (2015), Ceillier et al. (2017), and the compilation of observed main-sequence stars from 12 other papers presented in Aerts, Reeth & Tkachenko (2017). The two models with the altered TS-dynamo match the asteroseismically obtained values while the model with the standard TS-dynamo does not.
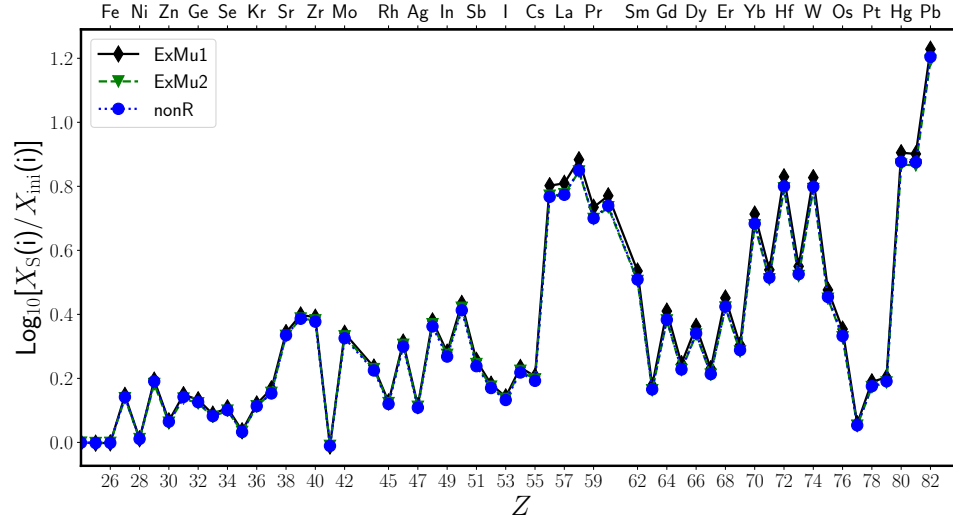
Figure 6.5: Final surface abundances of the models including the altered TS-dynamo (labelled as in Fig. 6.4), compared to the non-rotating model ('noR'). The final abundances of the three models are overlapping, confirming the conclusion of Chapter 5.

6.4   New derivation of the TS-dynamo

The results presented in this section are published in A&A, 2019, 631.

Recently a new derivation of the Tayler instability was published by Fuller, Piro & Jermyn (2019), who argue that the dynamo ('TSF-dynamo') allows transport of angular momentum during the RGB phase, despite the composition gradients. In this derivation, the saturation of the Tayler instability takes place at larger magnetic field amplitudes, and thus allows for stronger angular momentum transport. The equations for the transport of

angular momentum are:

$$\nu = \alpha_{\mathrm{TSF}}^3 r^2 \Omega \left(\frac{\Omega}{N_{\mathrm{eff}}} \right) \tag{6.1}$$

$$N_{\mathrm{eff}}^2 = \frac{\eta}{K} N_{\mathrm{T}}^2 + N_\mu^2 \tag{6.2}$$

$$q_{\mathrm{min}} = \alpha_{\mathrm{TSF}}^{-3} \left(\frac{N_{\mathrm{eff}}}{\Omega} \right)^{5/2} \left(\frac{\eta}{r^2 \Omega} \right)^{3/4} \tag{6.3}$$

with α being a dimensionless factor (discussed below), η and K the thermal and magnetic diffusivities, N_{eff} the effective Brunt-Väisälä frequency, and q_{min} the new minimum threshold for shear (q=-$\frac{\partial \ln \Omega}{\partial \ln r}$). Only when the shear is larger than q_{min} angular momentum is transported via ν.

The results are shown in Fig. 6.6, where the core rotation rates of the new and old derivation of the TS-dynamo are compared to the observed rates during the RGB, core He burning phase, and the white dwarf phase. The core rotation rates of the models presented in Fuller, Piro & Jermyn (2019) are within the range of values found via asteroseismic observations. The new derivation, however, is based on scaling relations, leading to the addition of a free parameter α which is assumed to be close to unity.

Further tests of the TSF-dynamo are prsented by Eggenberger, Buldgen & Salmon (2019) who investigated the new derivation in comparison to the solar rotation profile. The main result is that the TSF-dynamo results in transport of angular momentum too strong to be able to match the inner region of the solar rotation profile. This is no surprise, as Fuller, Piro & Jermyn (2019) already mentioned that they find near solid body rotation for the Sun.

Another test has been performed for subgiants (Eggenberger et al. 2019), including a code comparison between MESA and GENEC. I calculated the MESA models presented in this letter. In this latest paper we focussed on the rotation rates of six subgiants published by Deheuvels et al. (2014). Because these six subgiants are located at different points on the subgiant branch, we could investigate the evolution of rotation rates along this phase. Furthermore, for all six subgiants both the core and surface rotation rate has been derived from observations, therefore allowing us to also investigate whether the new derivation can reproduce the observed differential rotation within this evolutionary phase.
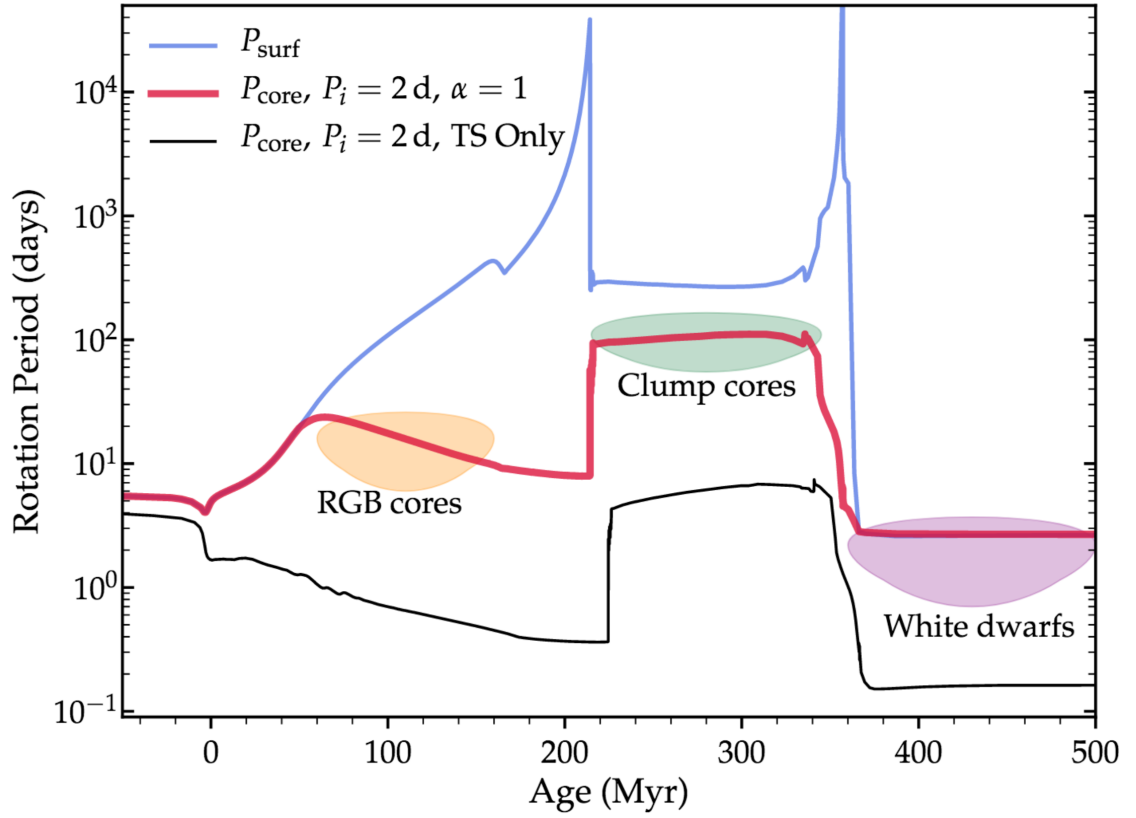
**Figure 6.6:** Comparison between the observed rotation rates (coloured areas) and rates calculated with the old (black line, labelled as 'TS only') and new derivation (thick red line, '$\alpha_{\mathrm{TSF}}=1$') of the TS-dynamo. The results calculated with the new derivation match the observed core values along the RGB, core He burning phase ('clump cores'), and the white dwarf phase. Figure from Fuller, Piro & Jermyn (2019).

We tried to match the core rotation rate of the six subgiants, and the results are shown in Fig. 6.7. The asteroseismically obtained core rotation rates can be reach by models including the TSF-dynamo. However, different values of α_{TSF} are needed to reproduce the core rotation rates of the different subgiants. The smaller α_{TSF}, the higher the value for q_{min}, and thus the higher the degree of differential rotation in the models and vice versa. A seventh data point has been added to Fig. 6.7, which is red giant KIC 4448777 (Mauro et al. 2016). This red giant has a very similar mass to the six subgiants, and they can therefore be assumed to be its progenitors. To match the values of this red giant, however, yet another α_{TSF} value of 3 is needed. Furthermore, the model with $\alpha_{\mathrm{TSF}}{=}3$ predicts a very low degree of differential rotation as the star ascends the RGB. This trend, as already mentioned in Fuller, Piro & Jermyn (2019), is in disagreement with the large sample of red giants published by Mosser et al. (2012) and Gehan et al. (2018).

We extended our the analysis by comparing these GENEC results to calculations performed with MESA and focussing on the red giant. I calculated these MESA models with the same `inlist` and `run_star_extra` files as used in Fuller, Piro & Jermyn (2019), only slightly adjusting the initial parameters like mass and chemical composition to match KIC 4448777. With this comparison, we could test if the implementation of the TSF-dynamo in GENEC is equivalent as in MESA. The results are shown in Fig. 6.8. Models of both stellar evolution codes converges to comparable ratios.

In any case the main result is that the TSF-dynamo is unable to predict the degree of differential rotation observed in consecutive evolutionary phases. This result is independent of differences in the models calculated by MESA and GENEC: in fact, Fig. 6.8 shows that the MESA and GENEC models that correctly reproduce the differential rotation in red giant KIC 4448777, cannot correctly reproduce the differential rotation in subgiants.
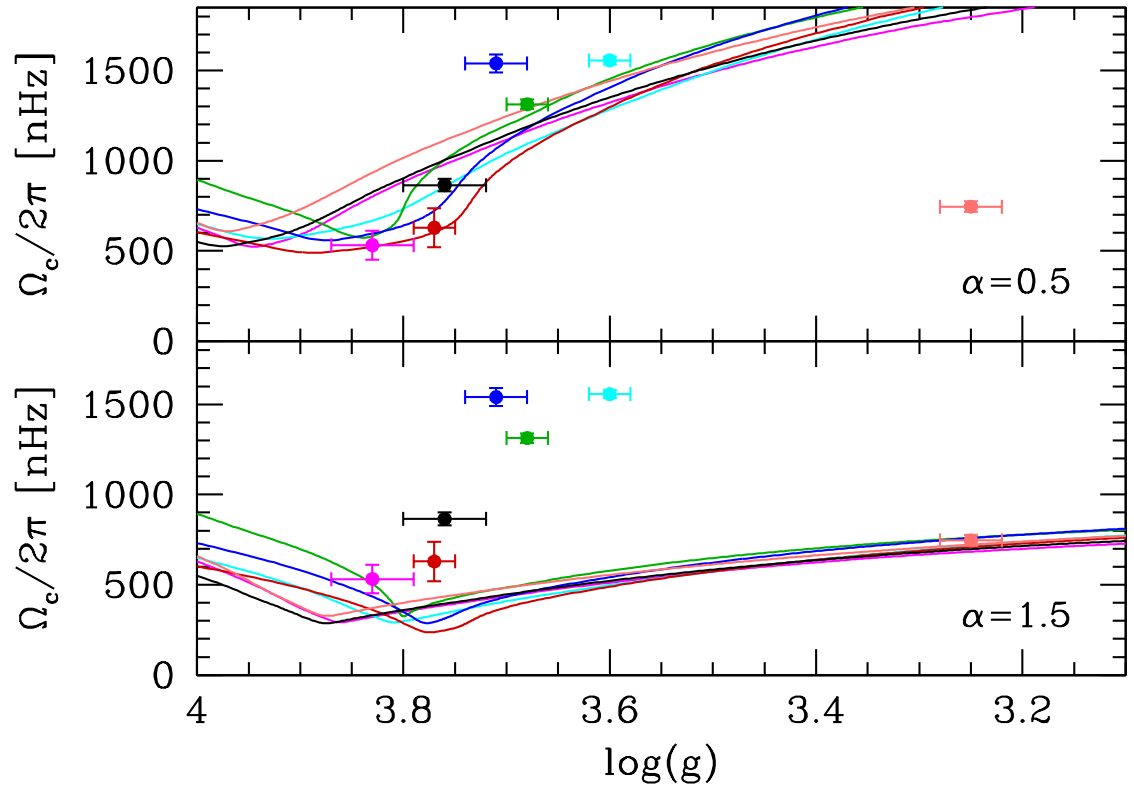
Figure 6.7: Core rotation rates as a function of surface gravity for the six subgiants. Different panels show different values for the α factor. Each subgiant and corresponding GENEC model is represented by a different colour. The seventh star, shown in orange, is a red giant with the same mass as the six subgiants. Figure from Eggenberger et al. (2019).
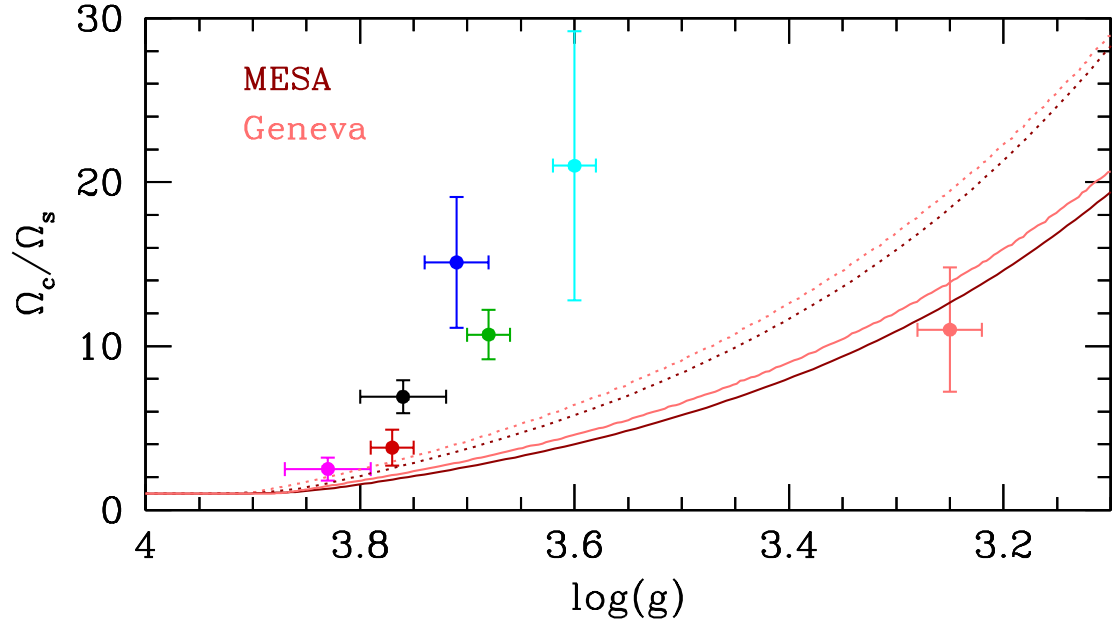
Figure 6.8: Ratio of core to surface rotation rate as function of surface gravity. The seven data points are six subgiants, and one red giant (in orange). MESA (brown lines) and GENEC (orange lines) models are shown with α_{TSF}=1 (dotted lines) and 1.5 (continuous lines). Figure from Eggenberger et al. (2019).

7 Conclusions

In this thesis, I focus on stellar evolution models including rotation and the effects of magnetic fields with an initial mass of 2.0 and 2.5 $M_\odot$ at solar metallicity. This mass range is particularly interesting, because the bulk of the s-process production in the Galaxy takes place during the AGB phase of stars with an initial mass of $\simeq$ 1.5-3 $M_\odot$. These stars thus have a large impact on galactic chemical evolution. As the s process takes place in a thin mass region ($\simeq 10^{-3}$ $M_\odot$), within a short amount of time ($\simeq 10^4$ yr), it is sensitive to rotational induced instabilities. As a result, these stars are a perfect test for the implementation of rotation in stellar evolution codes.

Another reason why this mass range is especially interesting is because asteroseismic observations are numerous for stars in this mass range, and have provided us with new information on the properties of stars. In the last half decade, researchers have been able to obtain rotational properties from asteroseismic observations of stars. When comparing these to the rotational properties resulting from stellar evolution codes, a discrepancy has been found. It is now common knowledge that a process of transport of angular momentum is missing from the current implementations of rotation in stellar evolution codes. This is another reason why these stars are a perfect test for the implementation of rotation.

This mass range thus has numerous observational constraints, both from asteroseismic and nucleosynthesis observations. As a result, I have been able to compare my models to observations, from the main sequence until their final fate as white dwarfs. The main summary points are:

- I presented 2.5-$M_\odot$, Z=0.014 models that include an artificial, additional viscosity ν_{add} which enforces the cores rotate within the observed range of core rotation rates.

- The value I had to use for such viscosity is $\nu_{\mathrm{add}} = 10^6$-$10^7$ cm^2 s^{-1}, several orders of magnitude higher than the value found to match observations for lower mass stars.

- The additional viscosity ν_{add} has to be removed from my models during or at the end of the core He burning phase to be able to match the white dwarf rotation rates.

- I presented for the first time the s-process nucleosynthesis of stellar evolution models with cores that are made to rotate within the observed range of core rotation rates.

- Based on the final surface abundances in these models, I concluded that the effect of rotation on the s-process production of low mass AGB stars is negligible.

- I also calculated the s process production of a model that is enforced to rotate one order of magnitude faster than the observed core rotation rates. Also the final surface enrichment of this model is comparable to that of the corresponding non-rotating model.

- These results are in agreement with the recent works by Lugaro et al. (2018) on stardust grains and Cseh et al. (2018) on Ba stars, showing that non-rotating models can match the s-process observations.

Furthermore, from my exploratory studies I conclude that:

- R Doradus has likely experienced binary interaction during its evolution.

- The efficiency for the mixing of chemical elements by the missing process of angular momentum transport has to be several orders of magnitude lower than the efficiency for the transport of angular momentum. If the efficiencies were similar, the stellar models would predict (quasi-)chemically homogeneous evolution for which there is no observational evidence.

- The dependence of the TS-dynamo on the molecular weight profile strongly reduces its efficiency to transport angular momentum.

- Models including the newly derived TSF-dynamo (Fuller, Piro & Jermyn 2019), which is able to reduce the core rotation rate to match the asteroseismically

obtained core rotation rates of subgiants, struggle to also correctly predict the core rotation rate in the subsequent stellar evolutionary phase.

As summarised above, I presented for the first time detailed s-process nucleosynthesis within stellar evolutionary models that match the asteroseismically obtained core rotation rates. I showed that the s-process production in these models is similar to that of corresponding non-rotating models. This result is in agreement with the most recent observations of s-process in stardust grains and Ba stars, which show limited spread in the s-process efficiency.

I also showed that the missing process of angular momentum transport cannot be as efficient in the mixing of chemical elements as it has to be in the transport of angular momentum. This puts extra constraints on the missing process of angular momentum: magnetic processes are more likely to be the solution than diffusive processes. The exact origin of this missing process of angular momentum transport is still unknown, and requires further investigation.

Besides the missing process of angular momentum transport, there are several uncertainties in the implementation of rotation in stellar evolutionary codes. One way to move forward with the implementation of rotation in MESA and other stellar evolution codes would be to investigate the different instabilities individually, as is done for the GSF-instability by Hirschi & Maeder (2010) and Caleo, Balbus & Tognelli (2016) and for the DSI by Edelmann et al. (2017). The impact of the investigations into the GSF-instability is that I have not included this instability in any of my models presented in this thesis. The investigation into the DSI showed that dynamical shear calculated with a 2D code is present where the 1D GENEC model predicted it to be, however, the instability lasted longer in the 1D than in the 2D models, due to the limitations in the 1D code related to the length of time steps, as already discussed in Section 2.4.2. Similar detailed studies are urgently needed for all the other rotationally induced instabilities, to check whether their effects in stellar evolution codes are correctly implemented.

Such investigations could also reveal whether all instabilities are significant in stellar evolution models, or if some dominate over others. In the latter case, the inclusion of

some instabilities could be redundant. For instance in Fuller, Piro & Jermyn (2019), only the new dynamo is considered, as they assume that the transport of angular momentum by the dynamo is dominant over all other instabilities. The next step could then be to investigate the combined effects of the dominant processes. Possibly the behaviour of this sum would be easier to implement into stellar evolutionary codes than the individual instabilities.

Furthermore, the implementation of rotationally induced instabilities all include an on/off criterion, which is one of the reasons why the diffusion coefficients sometimes show sharp discontinuities instead of being continuous. Whether these criteria are all needed, and whether we can reduce their influence on stellar models is an urgent question.

The models presented in the result chapters occupy a small but important part of the possible parameter space. Therefore, performing a study over a bigger parameter space including an additional, artificial viscosity to study the effect of rotation on all (low-mass) AGB stars could be the next step. As each mass and metallicity regime has its own set of computational challenges and observational constraints, calculating a large set of models will require extensive literature review and code testing. Furthermore, the missing process is also active in massive stars (see e.g. Suijs et al. 2008) and tests are required to understand the mass dependence of the missing process of angular momentum transport. Within this landscape there are many open questions left to investigate on the topic of rotation models. For example:

- How does the extra transport of angular momentum in combination with thermohaline mixing influence the results of Charbonnel & Lagarde (2010); Lagarde et al. (2011) on surface abundances pre-AGB?

- What is the effect of the extra transport of angular momentum on the large discrepancy between rotating and non-rotating models in the HRD tracks of the GENEC as presented by Ekström et al. (2012)?

- Several of the rotating models presented in Chapter 4 and 5 undergo a (very) late thermal pulses, which have never been studied in rotating stellar evolution

models. Do these pulses mix chemical elements and do they transport angular momentum?

Some open questions concerning the non-rotating stellar evolution models are:

- Can we use 3D-hydrodynamical simulations to determine the dominant process responsible for creating the ^{13}C-pocket?

- Some of the input physics can be updated (mass-loss, initial abundances, α_{MLT}). How will the comparison change between the s-process models and the s-process observations after these updates have been included?

Other possible studies concerning different mass regimes include:

- Is the effect on the s-process production of slowing down the core rotation rates the same at all metallicities?

- What is the effect of the extra transport of angular momentum on the detailed nucleosynthesis in higher mass AGBs and massive stars?

- In particular what is the effect of the extra transport of angular momentum on the s-process in low Z, high mass stars (Frischknecht et al. 2016; Limongi & Chieffi 2018; Choplin et al. 2018)? Will it still take place?

Finding a physical mechanism to slow down the core rotation rate that matches all the defined constraints should be the priority, as using a physical process would allow for more detailed analysis of surface abundances and s-process production. For example, I could then check if the outliers in the data set of stardust grains and Ba stars could be reached with rotating AGB models.

Therefore, in the near future I plan to focus on understanding and testing the TSF-dynamo as introduced in Section 6.4, as continuation of the study presented in Chapter 4. The first results are shown in Fig. 7.1, where I show the core and surface rotation rates of three models: one with the TS-dynamo (labelled as 'TS'), and two with the TSF-dynamo with α_{TSF}=1 ('TSF') and 4 ('TSF $\alpha_{\mathrm{TSF}} = 4$') respectively. The top panel

shows the individual rotation rates, and the bottom panel shows their ratio. The figure includes the core and surface rotation rates of the seven core He burning stars determined by Deheuvels et al. (2015). As already shown in Chapter 4, the TS-dynamo is unable to reach the asteroseismically obtained rotation rates. The TSF-dynamo with α_{TSF}=4 however is able to reach the observed values in both panels in Fig. 7.1. The lack of differential rotation in the earlier evolutionary phases will likely cause problems when comparing this model to those asteroseismically obtained data points, as discussed in Section 6.4.

These results were preliminary results of this study. In the time between the submission of this thesis and the acceptance of it, I finished the study and published the results in A&A 634, L16. The publication includes the comparison between the predicted and observed white dwarf rotation rates, which show that the models including the TSF-dynamo that match the rotation rates of core He burning stars from Deheuvels et al. (2015) do not match the white dwarfs rotation rates of Hermes et al. (2017) and vice versa. Therefore, the final conclusion of my publication is that the TSF-dynamo is also not the sole solution for the missing process in the transport of angular momentum in stars.
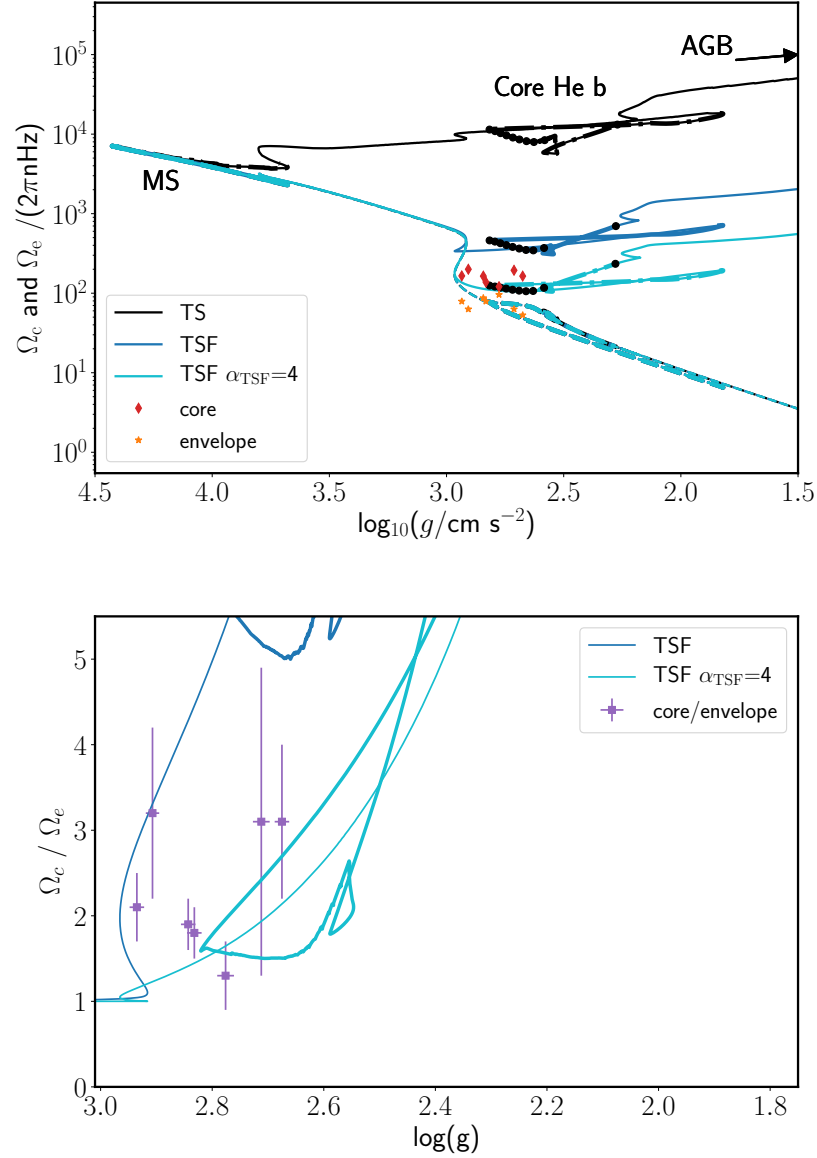
Figure 7.1: Comparison between core and surface rotation rate of models including the TS- or TSF-dynamo, as continuation of the models shown in Chapter 4. The data points are the seven core He burning stars as determined in Deheuvels et al. (2015). As discussed in Chapter 4, the model including the TS-dynamo ('TS') is unable to reach the data points, but the model including the TSF-dynamo with $\alpha_{\mathrm{TSF}}=4$ ('TSF $\alpha_{\mathrm{TSF}}=4$') is able to do so. The black dots indicate the time spend in the core He burning phase by the models, each spaced by 10% of the total duration starting at the 10% mark and ending with the 100% mark (the dots located on the most left and right, respectively). These dots show that these models spend most of their time during this evolutionary phase close to the observed rotation rates. Figures from den Hartogh (in prep).

Publications

Refereed

- **den Hartogh J.W.**; Eggenberger, P.; Deheuvels, S., 2020, A&A, 634, *Asteroseismology of evolved stars to constrain the internal transport of angular momentum. III. Using the rotation rates of intermediate-mass stars to test the Fuller-formalism*

- Eggenberger, P.; **den Hartogh, J.W.**; Bundgen, G.; Meynet, G.; Salmon, S.; Deheuvels, S., 2019, A&A, 631, *Asteroseismology of evolved stars to constrain the internal transport of angular momentum. II Test of a revised prescription for the transport by the Tayler instability*

- **den Hartogh, J.W.**; Hirschi, R.; Lugaro, M.; Doherty, C.L.; Battino, U.; Herwig, F.; Pignatari, M.; Eggenberger, P., 2019, A&A, 629, *The s process in rotating low-mass AGB stars: Nucleosynthesis calculations in models matching asteroseismic constraints*

- Battino, U.; Tattersall, A.; Lederer-Woods, C.; Herwig, F.; Denissenkov, P.; Hirschi, R.; **den Hartogh, J.W.**; Pignatari, M., 2019, MNRAS, 489, *NuGrid Stellar Data Set. II: updated low-mass AGB models and s-process nucleosynthesis*

- **den Hartogh, J.W.**; Eggenberger, P.; Hirschi, R., 2019, A&A, 622, *Constraining transport of angular momentum in stars: Combining asteroseismic observations of core helium burning stars and white dwarfs*

- Eggenberger, P.; Lagarde, N.; Miglio, A.; Montalbán, J.; Ekström, S.; Georgy, C.; Meynet, G.; Salmon, S.; Ceillier, T.; García, R. A.; Mathis, S.; Deheuvels, S.; Maeder, A.; **den Hartogh, J. W.**; Hirschi, R., 2017, A& A, 599, *Constraining the efficiency of angular momentum transport with asteroseismology of red giants: the effect of stellar mass*

- **den Hartogh, Jacqueline**; Battino, Umberto; Hirschi, Raphael; Pignatari, Marco; Herwig, Falk;, 2017, Proceedings of the 14th International Symposium on Nuclei in the Cosmos (NIC2016), id.020904, *Impact of Rotation and Convective Boundary Mixing in Low Mass AGB Stars*

- Nishimura, N.; Cescutti, G.; Hirschi, R.; Rauscher, T.; **Den Hartogh, J**.; Murphy, A. St. J.;, 2017, Proceedings of the 14th International Symposium on Nuclei in the Cosmos (NIC2016), id.020903, *Impacts of Nuclear-Physics Uncertainty in Stellar Temperatures on the s-Process Nucleosynthesis*

- Cescutti, G.; Nishimura, N.; Hirschi, R.; Rauscher, T.; **den Hartogh, J. W.**; Murphy, A. St. J.; 2017, MNRAS, 478, *The s-process nucleosynthesis: impact of the uncertainties in the nuclear physics determined by Monte Carlo variations*

- Battino, U.; Pignatari, M.; Ritter, C.; Herwig, F.; Denisenkov, P.; **Den Hartogh, J. W**.; Trappitsch, R.; Hirschi, R.; Freytag, B.; Thielemann, F.; Paxton, B.; 2016, ApJ, 827,1, *Application of a Theory and Simulation-based Convective Boundary Mixing Model for AGB Star Evolution and Nucleosynthesis*

- Kozyreva, Alexandra; Hirschi, Raphael; Blinnikov, Sergey; **den Hartogh, Jacqueline**, 2016, MNRAS Letters, 459, 1, *How much radioactive nickel does ASASSN-15lh require?*

- Hirschi, R.; **den Hartogh, J.W.**; Cristini, A.; Georgy, C.; Pignatari, M., 2014, conf. proc. XIII Nuclei in the Cosmos (NIC XIII), *Stellar structure, evolution and nucleosynthesis*

In review

- Deheuvels, S.; Ballot, J.; Eggenberger, P.; Spada, F.; Noll, A.; **den Hartogh, J. W.**, submitted to A&A, *Seismic evidence for near solid-body rotation in two Kepler subgiants and implications for angular momentum transport*

Soon to be submitted

- Yagüe, A.; García-Hernández, D.A.; Ventura, P.; Doherty, C.L.; den Hartogh, J.W.; Lugaro, M., to be submitted to MNRAS, *New models of s process in AGB stars of solar metallicity for the stellar evolutionary code ATON. I. Advective overshoot scheme.*

Bibliography

Abate C., Pols O. R., Karakas A. I., Izzard R. G., 2015, A&A, 576, A118

Abbott B. et al., 2016, Phys. Rev. L., 116

Abia C., Cristallo S., Cunha K., de Laverny P., Smith V. V., 2019, A&A, 625, A40

Abia C. et al., 2002, ApJ, 579, 817

Abolfathi B. et al., 2018, ApJS, 235, 42

Aerts C., Christensen-Dalsgaard J., Kurtz D. W., 2010, Asteroseismology. Springer Netherlands

Aerts C., Mathis S., Rogers T. M., 2019, ARAA, 57

Aerts C. et al., 2018, ApJS, 237, 15

Aerts C., Reeth T. V., Tkachenko A., 2017, ApJ, 847, L7

Aguirre V. S., Ballot J., Serenelli A. M., Weiss A., 2011, A&A, 529, A63

Aikawa M., Arnould M., Goriely S., Jorissen A., Takahashi K., 2005, A&A, 441, 1195

Amdahl G. M., 1967, in Proceedings of the April 18-20, 1967, AFIPS, ACM Press

Angelou G. C., 2014, PhD thesis, Monash centre for Astrophysics, School of Mathematical Sciences, Monash University, Australia

Angelou G. C., Stancliffe R. J., Church R. P., Lattanzio J. C., Smith G. H., 2012, ApJ, 749, 128

Angulo C. et al., 1999, Nucl. Phys. A, 656, 3

Aoki W., Norris J. E., Ryan S. G., Beers T. C., Ando H., 2000, ApJ, 536, L97

Arlandini C., Kappeler F., Wisshak K., Gallino R., Lugaro M., Busso M., Straniero O., 1999, ApJ, 525, 886

Arnett W. D., Meakin C., Hirschi R., Cristini A., Georgy C., Campbell S., Scott L. J. A., Kaiser E. A., 2019

Arnett W. D. et al., 2019, ApJ, 882, 18

Arnould M., Goriely S., Jorissen A., 1999, A&A, 347, 572

Balmforth N. J., 1992, MNRAS, 255, 603

Battino U. et al., 2016, ApJ, 827, 30

Battino U. et al., 2019, MNRAS

Beck P. G. et al., 2011, Science, 332, 205

Beck P. G. et al., 2014, A&A, 564, A36

Beck P. G. et al., 2018, A&A, 612, A22

Beck P. G. et al., 2012, Nature, 481, 55

Belkacem K. et al., 2015, A&A, 579, A31

Bennett M. E. et al., 2012, MNRAS, 420, 3047

Bernatowicz T., Fraundorf G., Ming T., Anders E., Wopenka B., Zinner E., Fraundorf P., 1987, Nature, 330, 728

Bidelman W. P., Keenan P. C., 1951, ApJ, 114, 473

Biermann L., 1932, Zeitschrift für Astrophysik, 5, 117

Bisterzo S., 2017, ApJ

Bisterzo S., Gallino R., Straniero O., Cristallo S., Käppeler F., 2010, MNRAS

Bitzaraki O. M., Rovithis-Livaniou H., Tout C. A., van den Heuvel E. P. J., 2004, A&A, 416, 263

Black D. C., Bodenheimer P., 1975, ApJ, 199, 619

Blöcker T., 1995, A&A, 297, 727

Böhm-Vitense E., 1958, Zeitschrift für Astrophysik, 46, 108

Bonačić Marinović A., Izzard R., Lugaro M., Pols O., 2007, A&A, 469, 1013

Boothroyd A. I., Sackmann I.-J., 1988, ApJ, 328, 671

Boothroyd A. I., Sackmann I.-J., 1999, ApJ, 510, 232

Borucki W. J. et al., 2010, Science, 327, 977

Bowen G. H., 1988, ApJ, 329, 299

Braithwaite J., 2006, A&A, 449, 451

Braithwaite J., Spruit H. C., 2004, Nature, 431, 819

Brandenburg A., 2001, ApJ, 550, 824

Brott I. et al., 2011, A&A, 530, A115

Brown T. M., Christensen-Dalsgaard J., Dziembowski W. A., Goode P., Gough D. O., Morrow C. A., 1989, ApJ, 343, 526

Browning M. K., Brun A. S., Toomre J., 2004, ApJ, 601, 512

Brun A. S., Palacios A., 2009, ApJ, 702, 1078

Brun A. S. et al., 2017, ApJ, 836, 192

Buntain J. F., Doherty C. L., Lugaro M., Lattanzio J. C., Stancliffe R. J., Karakas A. I., 2017, MNRAS, 471, 824

Burbidge E. M., Burbidge G. R., Fowler W. A., Hoyle F., 1957, Rev. Mod. Phys., 29, 547

Busso M., Gallino R., Lambert D. L., Travaglio C., Smith V. V., 2001, ApJ, 557, 802

Busso M., Gallino R., Wasserburg G. J., 1999, ARAA, 37, 239

Busso M., Lambert D. L., Beglio L., Gallino R., Raiteri C. M., Smith V. V., 1995, ApJ, 446, 775

Caleo A., Balbus S. A., Tognelli E., 2016, MNRAS, 460, 338

Cameron A. G. W., 1957, AJ, 62, 9

Cantiello M., Mankovich C., Bildsten L., Christensen-Dalsgaard J., Paxton B., 2014, ApJ, 788, 93

Caputo F., Chieffi A., Tornambe A., Castellani V., Pulone L., 1989, ApJ, 340, 241

Cassisi S., Salaris M., Irwin A. W., 2003, ApJ, 588, 862

Ceillier T. et al., 2017, A&A, 605, A111

Chaboyer B., Demarque P., Pinsonneault M. H., 1995, ApJ, 441, 865

Chaboyer B., Zahn J.-P., 1992, A&A, 253, 173

Chandrasekhar S., 1961, Hydrodynamic and hydromagnetic stability

Chaplin W. J., Miglio A., 2013, ARAA, 51, 353

Charbonnel C., Lagarde N., 2010, A&A, 522, A10

Chieffi A., Limongi M., 2013, ApJ, 764, 21

Chieffi A., Limongi M., 2017, ApJ, 836, 79

Choi J., Dotter A., Conroy C., Cantiello M., Paxton B., Johnson B. D., 2016, ApJ, 823, 102

Choplin A., Hirschi R., Meynet G., Ekström S., Chiappini C., Laird A., 2018, A&A, 618, A133

Constantino T., Campbell S., Gil-Pons P., Lattanzio J., 2014, ApJ, 784, 56

Cosner K., Truran J. W., 1981, Astrophysics and Space Science, 78, 85

Cowen R., 2012, Nature, 481, 18

Cowling T. G., 1945, MNRAS, 105, 166

Cox J. P., Giuli R. T., 1968, Principles of stellar structure. New York: Gordon and Breach

Cristallo S. et al., 2011, ApJS, 197, 17

Cristallo S., Straniero O., Gallino R., Piersanti L., Domínguez I., Lederer M. T., 2009, ApJ, 696, 797

Cristallo S., Straniero O., Piersanti L., Gobrecht D., 2015, ApJS, 219, 40

Cseh B. et al., 2018, A&A, 620, A146

Cyburt R. H. et al., 2010, ApJS, 189, 240

de Castro D. B., Pereira C. B., Roig F., Jilinski E., Drake N. A., Chavero C., Silva J. V. S., 2016, MNRAS, 459, 4299

De Marco O., Izzard R. G., 2017, PASA, 34, e001

de Mink S. E., Mandel I., 2016, MNRAS, 460, 3545

De Smedt K., Van Winckel H., Kamath D., Karakas A. I., Siess L., Goriely S., Wood P., 2014, A&A, 563, L5

Deheuvels S., Ballot J., Beck P., Mosser B., 2015, A&A, 580

Deheuvels S. et al., 2014, A&A, 564, A27

Deheuvels S. et al., 2012, ApJ, 756, 19

Delgado-Inglada G., Rodríguez M., Peimbert M., Stasińska G., Morisset C., 2015, MNRAS, 449, 1797

den Hartogh J. W., Eggenberger P., Hirschi R., 2019, Astronomy & Astrophysics, 622, A187

Denissenkov P. A., Pinsonneault M., 2007, ApJ, 655, 1157

Denissenkov P. A., Pinsonneault M., Terndrup D. M., Newsham G., 2010, ApJ, 716, 1269

Denissenkov P. A., Tout C. A., 2003, MNRAS, 340, 722

Deupree R. G., 1984, ApJ, 287, 268

Deupree R. G., 2004, in IAU Symposium, Vol. 215, Stellar Rotation, Maeder A., Eenens P., eds., p. 378

Deupree R. G., Wallace R. K., 1987, ApJ, 317, 724

Dillmann I., Szücs T., Plag R., Fülöp Z., Käppeler F., Mengoni A., Rauscher T., 2014, Nuclear Data Sheets, 120, 171

Dupret M.-A. et al., 2009, A&A, 506, 57

Eddington A. S., 1917, The Observatory, 40, 290

Eddington A. S., 1925, The Observatory, 48, 73

Edelmann P. V. F., Röpke F. K., Hirschi R., Georgy C., Jones S., 2017, A&A

Eggenberger P., 2015, in IAU Symposium, Vol. 307, New Windows on Massive Stars, Meynet G., Georgy C., Groh J., Stee P., eds., pp. 165–170

Eggenberger P., Buldgen G., Salmon S. J. A. J., 2019, A&A, 626, L1

Eggenberger P. et al., 2019, A&A, 621, A66

Eggenberger P., den Hartogh J. W., Buldgen G., Meynet G., Salmon S. J. A. J., Deheuvels S., 2019, A&A, 631, L6

Eggenberger P. et al., 2017, A&A, 599, A18

Eggenberger P., Maeder A., Meynet G., 2005, A&A, 440, L9

Eggenberger P., Meynet G., Maeder A., Hirschi R., Charbonnel C., Talon S., Ekström S., 2008, ApSS, 316, 43

Eggenberger P., Montalbán J., Miglio A., 2012, A&A, 544, L4

Eggleton P. P., 1972, MNRAS, 156, 361

Eggleton P. P., Dearborn D. S. P., Lattanzio J. C., 2006, Science, 314, 1580

Ekström S. et al., 2012, A&A, 537, A146

Elsworth Y., Howe R., Isaak G. R., McLeod C. P., Miller B. A., New R., Wheeler S. J., Gough D. O., 1995, Nature, 376, 669

Endal A. S., Sofia S., 1976, ApJ, 210, 184

Endal A. S., Sofia S., 1978, ApJ, 220, 279

Ferguson J. W., Alexander D. R., Allard F., Barman T., Bodnarik J. G., Hauschildt P. H., Heffner-Wong A., Tamanai A., 2005, ApJ, 623, 585

Fields C. E., Farmer R., Petermann I., Iliadis C., Timmes F. X., 2016, ApJ, 823, 46

Fishlock C. K., Karakas A. I., Stancliffe R. J., 2014, MNRAS, 438, 1741

Fletcher A., 2006, Instabilities, lecture notes, University of Newcastle upon Tyne, UK

Fossat E. et al., 2017, A&A

Freytag B., Ludwig H.-G., Steffen M., 1996, A&A, 313, 497

Fricke K., 1968, Zeitschrift für Astrophysik, 68, 317

Frischknecht U. et al., 2016, MNRAS, 456, 1803

Frost C. A., Lattanzio J. C., 1996, ApJ, 473, 383

Fuller G. M., Fowler W. A., Newman M. J., 1985, ApJ, 293, 1

Fuller J., Lecoanet D., Cantiello M., Brown B., 2014, ApJ, 796, 17

Fuller J., Piro A. L., Jermyn A. S., 2019, MNRAS

Fynbo H. O. U. et al., 2005, Nature, 433, 136

Gallino R., Arlandini C., Busso M., Lugaro M., Travaglio C., Straniero O., Chieffi A., Limongi M., 1998, ApJ, 497, 388

García R. et al., 2004, Solar Physics, 220, 269

García R. A., Turck-Chieze S., Jimenez-Reyes S. J., Ballot J., Palle P. L., Eff-Darwich A., Mathur S., Provost J., 2007, Science, 316, 1591

García-Segura G., Villaver E., Langer N., Yoon S.-C., Manchado A., 2014, ApJ, 783, 74

García-Segura G., Villaver E., Manchado A., Langer N., Yoon S.-C., 2016, ApJ, 823, 142

Gathier R., Lamers H. J. G. L. M., Snow T. P., 1981, ApJ, 247, 173

Gehan C., Mosser B., Michel E., Samadi R., Kallinger T., 2018, A&A, 616, A24

Georgy C., Meynet G., Maeder A., 2011, A&A, 527, A52

Gizon L., Birch A. C., Spruit H. C., 2010, ARAA, 48, 289

Goldreich P., Schubert G., 1967, ApJ, 150, 571

Goriely S., Jorissen A., Arnould M., 1989, in Nuclear Astrophysics, Lozano M., Gallardo M. I., Arias J. M., eds.

Goriely S., Mowlavi N., 2000, A&A, 362, 599

Gossage S., Conroy C., Dotter A., Choi J., Rosenfield P., Cargile P., Dolphin A., 2018, ApJ, 863, 67

Grevesse N., Noels A., 1993, in Perfectionnement de l'Association Vaudoise des Chercheurs en Physique, Hauck B., Paltani S., Raboud D., eds., pp. 205–257

Hansen T. T., Andersen J., Nordström B., Beers T. C., Placco V. M., Yoon J., Buchhave L. A., 2016, A&A, 588, A3

Heger A., Fryer C. L., Woosley S. E., Langer N., Hartmann D. H., 2003, ApJ, 591, 288

Heger A., Langer N., Woosley S. E., 2000, ApJ, 528, 368

Heil M. et al., 2014, Phys. Rev. C, 90

Heisenberg W., 1927, Zeitschrift für Physik, 43, 172

Hermes J. J. et al., 2015, MNRAS, 451, 1701

Hermes J. J. et al., 2017, ApJS, 232, 23

Herwig F., 2000, A&A, 360, 952

Herwig F., 2005, ARAA, 43, 435

Herwig F., Bloecker T., Schoenberner D., 1999, in IAU Symposium, Vol. 191, Asymptotic Giant Branch Stars, Le Bertre T., Lebre A., Waelkens C., eds., p. 41

Herwig F., Bloecker T., Schoenberner D., El Eid M., 1997, A&A, 324, L81

Herwig F., Freytag B., Fuchs T., Hansen J. P., Hueckstaedt R. M., Porter D. H., Timmes F. X., Woodward P. R., 2007, in Astronomical Society of the Pacific Conference Series, Vol. 378, Why Galaxies Care About AGB Stars: Their Importance as Actors and Probes, Kerschbaum F., Charbonnel C., Wing R. F., eds., p. 43

Herwig F., Langer N., Lugaro M., 2003, ApJ, 593, 1056

Hirschi R., Maeder A., 2010, A&A, 519, A16

Hirschi R., Meynet G., Maeder A., 2004, A&A, 425, 649

Hirschi R., Meynet G., Maeder A., 2005, A&A, 443, 581

Höfner S., Olofsson H., 2018, ARAA, 26

Hollowell D., Icko J. I., 1988, ApJ, 333, L25

Hoppe P., Ott U., 1997, in Astrophysical implications of the laboratory study of presolar materials, ASCE

Houdek G., 2006, in ESA Special Publication, Vol. 624, Proceedings of SOHO 18/GONG 2006/HELAS I, Beyond the spherical Sun, p. 28

Huang W., Gies D. R., McSwain M. V., 2010, ApJ, 722, 605

Hunter I. et al., 2009, A&A, 496, 841

Iben I., 1975, ApJ, 196, 525

Iben I., Renzini A., 1982a, ApJ, 263, L23

Iben I., Renzini A., 1982b, ApJ, 259, L79

Iben, Jr. I., 1976, ApJ, 208, 165

Iliadis C., D'Auria J. M., Starrfield S., Thompson W. J., Wiescher M., 2001, ApJS, 134, 151

Imbriani G. et al., 2004, A&A, 420, 625

Izzard R. G., Glebbeek E., Stancliffe R. J., Pols O. R., 2009, A&A, 508, 1359

Jaeger M., Kunz R., Mayer A., Hammer J. W., Staudt G., Kratz K. L., Pfeiffer B., 2001, Phys. Rev. L., 87

James H., Kahn F., 1970, A&A

James R., Kahn F., 1971, A&A

Jorissen A., Smith V., Lambert D., 1992, A&A, 261, 164

Jönsson H. et al., 2014a, A&A, 564, A122

Jönsson H., Ryde N., Harper G. M., Richter M. J., Hinkle K. H., 2014b, ApJ, 789, L41

Jönsson H., Ryde N., Spitoni E., Matteucci F., Cunha K., Smith V., Hinkle K., Schultheis M., 2017, ApJ, 835, 50

Käppeler F., Gallino R., Bisterzo S., Aoki W., 2011, Rev. Mod. Phys., 83, 157

Karakas A., Lattanzio J. C., 2007, PASA, 24, 103

Karakas A., Lugaro M., Carlos M., Cseh B., Kamath D., García-Hernández D. A., 2018, MNRAS, 477, 421

Karakas A. I., Lattanzio J. C., 2014, PASA, 31, e030

Karakas A. I., Lattanzio J. C., Pols O. R., 2002, PASA, 19, 515

Karakas A. I., Lugaro M., 2016, ApJ, 825, 26

Kato S., 1966, PASJ, 18, 201

Kawaler S. D., 2015, in Astronomical Society of the Pacific Conference Series, Vol. 493, 19th European Workshop on White Dwarfs, Dufour P., Bergeron P., Fontaine G., eds., p. 65

Kawaler S. D., Hostler S. R., 2005, ApJ, 621, 432

Kippenhahn R., 1974, in IAU Symposium, Vol. 66, Late Stages of Stellar Evolution, Tayler R. J., Hesser J. E., eds., p. 20

Kippenhahn R., Thomas H.-C., 1970, in IAU Colloq. 4: Stellar Rotation, Slettebak A.,

ed., p. 20

Kippenhahn R., Weigert A., Weiss A., 2013, Stellar Structure and Evolution. Springer-Verlag Berlin Heidelberg

Knobloch E., Spruit H. C., 1983, A&A, 125, 59

Kobayashi C., Izutani N., Karakas A. I., Yoshida T., Yong D., Umeda H., 2011, ApJ, 739, L57

Kobayashi C., Karakas A. I., Umeda H., 2011, MNRAS, 414, 3231

Korzennik S. G., 2005, ApJ, 626, 585

Kosovichev A. G., 1988, Soviet Astronomy Letters, 14, 145

Kunz R., Fey M., Jaeger M., Mayer A., Hammer J. W., Staudt G., Harissopulos S., Paradellis T., 2002, ApJ, 567, 643

Kurtz D. W., Saio H., Takata M., Shibahashi H., Murphy S. J., Sekii T., 2014, MNRAS, 444, 102

Kwok S., 2000, The Origin and Evolution of Planetary Nebulae (Cambridge Astrophysics). Cambridge University Press

Lagarde N., Charbonnel C., Decressin T., Hagelberg J., 2011, A&A, 536, A28

Lagarde N., Decressin T., Charbonnel C., Eggenberger P., Ekström S., Palacios A., 2012, A&A, 543, A108

Lambert D., 1985, Cool Stars with Excesses of Heavy Elements, Proceedings of the Strasbourg Observatory Colloquium, Universite de Strasbourg, 114, 191

Lambert D. L., Smith V. V., Busso M., Gallino R., Straniero O., 1995, ApJ, 450, 302

Langanke K., Martínez-Pinedo G., 2000, Nucl. Phys. A, 673, 481

Langer N., 1992, A&A, 265, 17

Langer N., 1998, A&A, 329

Langer N., Fricker K., Sugimoto D., 1983, A&A, 126

Langer N., Heger A., Wellstein S., Herwig F., 1999, A&A

Langer N., Maeder A., 1995, A&A, 295, 685

Lau H. H. B., Gil-Pons P., Doherty C., Lattanzio J., 2012, A&A, 542, A1

Lau H. H. B., Izzard R. G., Schneider F. R. N., 2014, A&A, 570, A125

Leighton R. B., Noyes R. W., Simon G. W., 1962, ApJ, 135, 474

Lewis R. S., Amari S., Anders E., 1990, Nature, 348, 293

Limongi M., Chieffi A., 2018, ApJS, 237, 13

Little S. J., Little-Marenin I. R., Bauer W. H., 1987, AJ, 94, 981

Liu N., Gallino R., Bisterzo S., Davis A. M., Savina M. R., Pellin M. J., 2014, ApJ, 788, 163

Lucatello S., Masseron T., Johnson J. A., Pignatari M., Herwig F., 2011, ApJ, 729, 40

Lucy L. B., 1974, AJ, 79, 745

Lugaro M., Herwig F., Lattanzio J. C., Gallino R., Straniero O., 2003, ApJ, 586, 1305

Lugaro M., Karakas A. I., Pető M., Plachy E., 2018, Geochimica et Cosmochimica Acta, 221, 6

Lugaro M., Karakas A. I., Stancliffe R. J., Rijs C., 2012, ApJ, 747, 2

Lugaro M., Tagliente G., Karakas A. I., Milazzo P. M., Käppeler F., Davis A. M., Savina M. R., 2014, ApJ, 780, 95

Lugaro M., Zinner E., Gallino R., Amari S., 1999, ApJ, 527, 369

Maeder A., 1987, A&A, 178, 159

Maeder A., 1997, A&A, 321, 134

Maeder A., 2009, Physics, Formation and Evolution of Rotating Stars. Springer Berlin Heidelberg

Maeder A., Meynet G., 2000, ARAA, 38, 143

Maeder A., Meynet G., 2004, A&A, 422, 225

Maeder A., Meynet G., 2012, Rev. Mod. Phys., 84, 25

Maeder A., Meynet G., 2012, Rev. Mod. Phys., 84, 25

Maeder A., Meynet G., Lagarde N., Charbonnel C., 2013, A&A, 553, A1

Maeder A., Zahn J.-P., 1998, A&A, 334, 1000

Marchant P., Langer N., Podsiadlowski P., Tauris T. M., Moriya T. J., 2016, A&A, 588, A50

Marigo P., Aringer B., 2009, A&A, 508, 1539

Marigo P., Bressan A., Chiosi C., 1996, A&A, 313, 545

Marigo P., Girardi L., 2007, A&A, 469, 239

Marigo P., Girardi L., Bressan A., 1999, A&A

Markey P., Tayler R. J., 1973, MNRAS, 163, 77

Marks P. B., Sarna M. J., 1998, MNRAS, 301, 699

Marques J. P. et al., 2013, A&A, 549, A74

Martin D., José J., Longland R., 2018, Computational Astrophysics and Cosmology, 5

Massarotti A., Latham D. W., Stefanik R. P., Fogel J., 2007, ApJ, 135, 209

Mattsson L., Höfner S., 2011, A&A, 533, A42

Mattsson L., Wahlin R., Höfner S., 2010, A&A, 509, A14

Mauro M. P. D. et al., 2016, ApJ, 817, 65

McCarthy M. F., 1994, in Astronomical Society of the Pacific Conference Series, Vol. 60, The MK Process at 50 Years: A Powerful Tool for Astrophysical Insight, Corbally C. J., Gray R. O., Garrison R. F., eds., p. 224

Merrill S. P. W., 1952, ApJ, 116, 21

Mestel L., 1953, MNRAS, 113, 716

Meynet G., Maeder A., 1997, A&A, 321, 465

Mosser B. et al., 2012, A&A, 548, A10

Mowlavi N., 1999, A&A, 344

Nanni A., Marigo P., Girardi L., Rubele S., Bressan A., Groenewegen M. A. T., Pastorelli G., Aringer B., 2017, MNRAS, 473, 5492

Nieuwenhuijzen H., de Jager C., 1988, A&A, 203

Nucci M. C., Busso M., 2014, ApJ, 787, 141

Oda T., Hino M., Muto K., Takahara M., Sato K., 1994, Atomic Data and Nuclear Data Tables, 56, 231

Otsuka M., Tajitsu A., 2013, ApJ, 778, 146

Ott U., Begemann F., 1990, ApJ, 353, L57

Pauli W., 1925, Zeitschrift fur Physik, 31, 765

Paxton B., Bildsten L., Dotter A., Herwig F., Lesaffre P., Timmes F., 2011, ApJS, 192, 3

Paxton B. et al., 2013, ApJS, 208, 4

Paxton B. et al., 2015, ApJS, 220, 15

Paxton B. et al., 2018, ApJS, 234, 34

Paxton B. et al., 2019, ApJS

Pearson K., 1900, The London, Edinburgh, and Dublin Philosophical Magazine and Journal of Science, 50, 157

Péquignot D., Walsh J. R., Zijlstra A. A., Dudziak G., 2000, A&A, 361, L1

Pettini M., 2014, Structure and evolution of stars, lecture notes, Cambridge University

Piersanti L., Cristallo S., Straniero O., 2013, ApJ, 774, 98

Pignatari M., Gallino R., Heil M., Wiescher M., Käppeler F., Herwig F., Bisterzo S., 2010, ApJ, 710, 1557

Pignatari M. et al., 2016, ApJS, 225, 24

Pinçon C., Belkacem K., Goupil M. J., Marques J. P., 2017, A&A, 605, A31

Pinsonneault M. H., Kawaler S. D., Sofia S., Demarque P., 1989, ApJ, 338, 424

Plez B., Smith V. V., Lambert D. L., 1993, ApJ, 418, 812

Pols O., 2009, Stellar structure and evolution. University Lecture. University of Utrecht

Pols O. R., Tout C. A., 2001, Mem. S.A.It., 72, 299

Potter A. T., Chitre S. M., Tout C. A., 2012, MNRAS, 424, 2358

Potter A. T., Tout C. A., Brott I., 2012, MNRAS, 423, 1221

Potter A. T., Tout C. A., Eldridge J. J., 2012, MNRAS, 419, 748

Prantzos N., Abia C., Limongi M., Chieffi A., Cristallo S., 2018, MNRAS, 476, 3432

Reddy B. E., Lambert D. L., Gonzalez G., Yong D., 2002, ApJ, 564, 482

Reimers D., 1975, Memoires of the Societe Royale des Sciences de Liege, 8, 369

Reyniers M., van de Steene G. C., van Hoof P. A. M., van Winckel H., 2007, A&A, 471, 247

Reyniers M., Van Winckel H., Gallino R., Straniero O., 2004, A&A, 417, 269

Richard, D. ; Zahn J.-P., 1999, A&A, 347, 734

Ritter C., Herwig F., Jones S., Pignatari M., Fryer C., Hirschi R., 2018, MNRAS, 480, 538

Robertson J. W., Faulkner D. J., 1972, ApJ, 171, 309

Rodríguez M., Delgado-Inglada G., 2011, in Revista Mexicana de Astronomia y Astrofisica, vol. 27, Vol. 40, Revista Mexicana de Astronomia y Astrofisica Conference Series, pp. 179–180

Rogers F. J., Nayfonov A., 2002, ApJ, 576, 1064

Rogers F. J., Swenson F. J., Iglesias C. A., 1996, ApJ, 456, 902

Rogers T. M., 2015, ApJ, 815, L30

Rogers T. M., McElwaine J. N., 2017, ApJ, 848, L1

Rüdiger G., Gellert M., Hollerbach R., Schultz M., Stefani F., 2018, Physics Reports, 741, 1

Rüdiger G., Hollerbach R., Gellert M., Schultz M., 2007, Astronomische Nachrichten, 328, 1158

Rüdiger G., Hollerbach R., Schultz M., Elstner D., 2007, MNRAS, 377, 1481

Salaris M., Cassisi S., 2017, Royal Society Open Science, 4, 170192

Salpeter E. E., 1955, ApJ, 121, 161

Sandage A., Tammann G. A., 2006, ARAA, 44, 93

Schootemeijer A., Langer N., 2018, A&A, 611, A75

Schönberg M., Chandrasekhar S., 1942, ApJ, 96, 161

Sharpee B., Zhang Y., Williams R., Pellegrini E., Cavagnolo K., Baldwin J. A., Phillips M., Liu X.-W., 2007, ApJ, 659, 1265

Siess L., 2009, A&A, 497, 463

Siess L., Goriely S., Langer N., 2004, A&A, 415, 1089

Smith V. V., Lambert D. L., 1990, ApJS, 72, 387

Sneden C., 2003, Science, 299, 70

Sneden C., Cowan J. J., Gallino R., 2008, ARAA, 46, 241

Spada F., Gellert M., Arlt R., Deheuvels S., 2016, A&A, 589, A23

Spruit H. C., 1999, A&A, 349, 189

Spruit H. C., 2002, A&A, 381, 923

Spruit H. C., Knobloch E., Roxburgh I. W., 1983, Nature, 304, 520

Stancliffe R. J., Glebbeek E., 2008, MNRAS, 389, 1828

Stancliffe R. J., Izzard R. G., Tout C. A., 2004, MNRAS, 356, L1

Stancliffe R. J., Jeffery C. S., 2007, MNRAS, 375, 1280

Stancliffe R. J., Lugaro M., Ugalde C., Tout C. A., Görres J., Wiescher M., 2005, MNRAS, 360, 375

Stancliffe R. J., Tout C. A., Pols O. R., 2005, MNRAS, 352, L1

Steenbeck M., Krause F., Rädler K.-H., 1966, Zeitschrift für Naturforschung A, 21

Sterling N. C., Dinerstein H. L., Bowers C. W., 2002, ApJL, 578, L55

Sterling N. C. et al., 2009, PASA, 26, 339

Straniero O., Chieffi A., Limongi M., Busso M., Gallino R., Arlandini C., 1997, ApJ, 478, 332

Straniero O., Gallino R., Busso M., Chiefei A., Raiteri C. M., Limongi M., Salaris M., 1995, ApJ, 440, L85

Suijs M. P. L., Langer N., Poelarends A.-J., Yoon S.-C., Heger A., Herwig F., 2008, A&A, 481, L87

Sweet P. A., 1950, MNRAS, 110, 548

Sweigart A. V., 1999, in IAU Symposium, Vol. 190, New Views of the Magellanic Clouds, Chu Y.-H., Suntzeff N., Hesser J., Bohlender D., eds., p. 370

Talon S., Zahn J.-P., 1997, A&A, 317, 749

Talon S., Zahn J.-P., Maeder A., Meynet G., 1997, A&A

Tayar J. et al., 2015, ApJ, 807, 82

Tayar J., Pinsonneault M. H., 2013, ApJL, 775, L1

Tayar J., Pinsonneault M. H., 2018, ApJ, 868, 150

Tayler R. J., 1973, MNRAS, 161, 365

Terebey S., Shu F. H., Cassen P., 1984, ApJ, 286, 529

Thielemann F.-K. et al., 2011, Progress in Particle and Nuclear Physics, 66, 346

Thomas H.-C., 1967, Zeitschrift für Astrophysik, 67, 420

Thompson M. J. et al., 1996, Science, 272, 1300

Toomre A., 1964, ApJ, 139, 1217

Toomre J., Brun A. S., 2004, in IAU Symposium, Vol. 215, Stellar Rotation, Maeder A.,
Eenens P., eds., p. 326

Travaglio C., Gallino R., Arnone E., Cowan J., Jordan F., Sneden C., 2004, ApJ, 601, 864

Trippella O., Busso M., Palmerini S., Maiorca E., Nucci M. C., 2016, ApJ, 818, 125

Urpin V., Shalybkov D., Spruit H., 1996, A&A, 306, 455

van Aarle E., Van Winckel H., De Smedt K., Kamath D., Wood P. R., 2013, A&A, 554,
A106

Vardya M. S., 1985, ApJ, 299, 255

Vassiliadis E., Wood P. R., 1993, ApJ, 413, 641

Vauclair S., 2004, ApJ, 605, 874

Ventura P., Marigo P., 2010, MNRAS, 408, 2476

Vlemmings W. H. T. et al., 2018, A&A, 613, L4

Walder R., Folini D., Meynet G., 2012, SSRv, 166, 145

Wallerstein G. et al., 1997, Rev. Mod. Phys., 69, 995

Wallner A. et al., 2016, Phys. Rev. C, 93

Wasiutynski J., 1946, Astrophysica Norvegica, 4, 1

Weaver T. A., Zimmerman G. B., Woosley S. E., 1978, ApJ, 225, 1021

Wellstein S., Langer N., Braun H., 2001, A&A, 369, 939

Werner K., Herwig F., 2006, PASP, 118, 183

Werner K., Rauch T., Kepler S. O., 2014, A&A, 564, A53

Westbrook W. E., Willner S. P., Merrill K. M., Schmidt M., Becklin E. E., Neugebauer G., Wynn-Williams C. G., 1975, ApJ, 202, 407

Winget D., Kepler S., 2008, ARAA, 46, 157

Wood P. R., Faulkner D. J., 1986, ApJ, 307, 659

Woosley S. E., Heger A., 2006, ApJ, 637, 914

Wright G. A. E., 1973, Monthly Notices of the Royal Astronomical Society, 162, 339

Yoon S.-C., Langer N., 2005, A&A, 443, 643

Yoon S.-C., Langer N., Norman C., 2006, A&A, 460, 199

Yoon S.-C., Langer N., van der Sluys M., 2004, A&A, 425, 207

Yorke H. W., Bodenheimer P., 1999, ApJ, 525, 330

Zahn J.-P., 1974, in IAU Symposium, Vol. 59, Stellar Instability and Evolution, Ledoux P., Noels A., Rodgers A. W., eds., pp. 185–194

Zahn J.-P., 1992, A&A, 265, 115

Zahn J.-P., Brun A. S., Mathis S., 2007, A&A, 474, 145

Zeipel H. V., 1924, MNRAS, 84, 665

Zinner E., Amari S., Lewis R. S., 1991, ApJ, 382, L47

A Derivation of the differential equations for the mixing of chemical elements and transport of angular momentum

A.1 Mixing of chemical elements

The derivation of the equation for mixing of chemical elements starts with the continuity equation of a conserved quantity:

$$\frac{\partial \rho}{\partial t} + \nabla \cdot \mathbf{j} = 0 \tag{A.1}$$

where t is time, ρ the density of quantity q, and j the flux of quantity q, which can also be written as $\mathbf{j} = \rho \mathbf{u}$ where $\mathbf{u}$ is the velocity of the flow of q. In this instance, I am interested in a diffusive flow and I can write the relation between relative velocity V_i of a particle i and diffusion coefficient D as:

$$V_i = -\frac{D}{X_i} \nabla X_i \tag{A.2}$$

where X_i is the mass fraction of particle i. The minus sign enters the equation as the mass fraction and velocity increase in opposite directions. As I am deriving an expression for in a 1 dimensional code, I can consider this as a 1 dimensional problem and replace the ∇ by $\frac{1}{r^2}\frac{\partial}{\partial r}(r^2)$. Here I am considering mixing of chemical elements, for which I use a number density n_i.

Putting Eqs.A.1 and A.2 together with the expression for the number density gives:

$$\frac{\partial n_i}{\partial t} = -\nabla(n_i V_i) \tag{A.3}$$

$$= -\frac{1}{r^2}\frac{\partial}{\partial r}\left[-r^2 n_i \frac{D}{X_i}\frac{\partial X_i}{\partial r}\right] \tag{A.4}$$

As n_i can be written as $n_i = \frac{\rho X_i}{A_i} m_H$, where n_i is the number density of particle i, A_i the atomic weight expressed in unit of proton mass m_H, I obtain:

$$\frac{\partial}{\partial t}(\rho X_i) = \frac{1}{r^2}\frac{\partial}{\partial r}\left(\rho r^2 D \frac{\partial X_i}{\partial r}\right) \tag{A.5}$$

Which is almost Eq.2.8, except that the ρ is still in the time derivative. However, I can move it outwards as when I sum over all elements $\Sigma_i X_i = 1$, then Eq.A.5 is:

$$\frac{\partial}{\partial t}(\rho * 1) = \frac{1}{r^2}\frac{\partial}{\partial r}\left(\rho r^2 D\frac{\partial}{\partial r}(1)\right) = 0 \tag{A.6}$$

When using:

$$\frac{\partial}{\partial r} = 4\pi r^2 \rho\frac{\partial}{\partial m}, \tag{A.7}$$

Eq. A.5 can be rewritten as:

$$\rho\frac{\partial}{\partial t}(X_i) = \frac{4\pi r^2 \rho}{r^2}\frac{\partial}{\partial m}\left(4\pi r^2 \rho^2 r^2 D\frac{\partial X_i}{\partial m}\right) \tag{A.8}$$

$$\text{and thus: } \frac{\partial}{\partial t}(X_i) = \frac{\partial}{\partial m}\left((4\pi r^2 \rho)^2 D\frac{\partial X_i}{\partial m}\right) \tag{A.9}$$

$$\tag{A.10}$$

Which is Eq.2.8, as the second term at the right side of the equal side in Eq.2.8 simply account for the nuclear burning by reactions creating and destroying particle i.

A.2 Transport of angular momentum

The derivation of the equation for transport of angular momentum stars with finding a relation between torque $\mathcal{M}$ and the time derivative of angular momentum $\mathcal{L}$. Torque is the product of a force $\mathbf{F}$ and the distance $\mathbf{s}$ between the axis of rotation and the line of action of the force $\mathbf{F}$:

$$\mathbf{F} = \frac{d}{dt}(m\mathbf{v}) \tag{A.11}$$

working on an object with the mass m that is moving at velocity $\mathbf{v}$. The torque $\mathcal{L}$ then is:

$$\mathcal{M} = \mathbf{s} \times \mathbf{F}$$
$$= \mathbf{s} \times \frac{d}{dt}(m\mathbf{v}) \tag{A.12}$$

The angular momentum $\mathcal{L}$ is defined as:

$$\mathcal{L} = \mathbf{s} \times m\mathbf{v} \tag{A.13}$$

The absolute time derivative of $\mathcal{L}$ is:

$$
\begin{aligned}
\frac{d}{dt}\mathcal{L} &= \frac{d}{dt}\left(\mathbf{s} \times m\mathbf{v}\right) \\
&= \frac{d}{dt}\mathbf{s} \times m\mathbf{v} + \mathbf{s} \times \frac{d}{dt}(m\mathbf{v}) \\
&= m\underbrace{(\mathbf{v} \times \mathbf{v})}_{=0} + \mathbf{s} \times \frac{d}{dt}(m\mathbf{v}) \\
&= \mathbf{s} \times \frac{d}{dt}(m\mathbf{v})
\end{aligned}
\tag{A.14}
$$

And thus:

$$
\mathcal{M} = \frac{d}{dt}\mathcal{L}
\tag{A.15}
$$

Now that the relation is defined, I continue with deriving expressions for both sides. I start with the time derivative of $\mathcal{L}$.

In spherical coordinates the distance $\mathbf{s}$ can be expressed as $\mathbf{s} = \mathbf{r}\sin(\theta)$. Also, the orbital angular velocity $\mathbf{\Omega}$ is defined as:

$$
\mathbf{\Omega} = \frac{\mathbf{r} \times \mathbf{v}}{r^2}
\tag{A.16}
$$

Therefore, I can rewrite Eq. A.14:

$$
\begin{aligned}
\frac{d}{dt}\mathcal{L} &= \frac{d}{dt}\left(\mathbf{s} \times m\mathbf{v}\right) \\
&= m\frac{d}{dt}\left(r^2\sin^2(\theta)\mathbf{\Omega}\right)
\end{aligned}
\tag{A.17}
$$

$$
\text{and thus: } \mathcal{L} = \left(r^2\sin^2(\theta)\mathbf{\Omega}\right)
\tag{A.18}
$$

The mass derivative of $\mathcal{L}$ then is (using $dm = \rho \cdot dV$):

$$
\begin{aligned}
\frac{d\mathcal{L}}{dm} &= r^2\sin^2(\theta)\mathbf{\Omega} \\
d\mathcal{L} &= \rho r^2\sin^2(\theta)\mathbf{\Omega} \cdot dV \\
&= \rho r^2\sin^2(\theta)\mathbf{\Omega} \cdot r^2\sin(\theta)d\theta d\varphi dr
\end{aligned}
\tag{A.19}
$$

With Eq.A.17 the time derivative of the angular momentum in Lagrangian coordinates can then be written as [1]

$$\rho \frac{d}{dt}(\mathcal{L}) = \rho \frac{d}{dt}\left(r^2 \sin^2(\theta)\mathbf{\Omega}\right)_{M_r} \cdot r^2 \sin(\theta) d\theta d\varphi dr \tag{A.20}$$

This equation expresses the temporal changes of angular momentum of a volume element in an Eulerian coordinate system.

Now I move to deriving the left hand side of Eq.A.15. In stars torque results in shear between different layers. The shear stress is given:

$$\tau(\mathbf{u}) = \nu \nabla \cdot \mathbf{v} \tag{A.21}$$

$$\text{and } \tau(\mathbf{u}) = \frac{\mathbf{F}}{\mathbf{A}} \tag{A.22}$$

where ν is the viscosity. This gives a force per unit area of

$$d\mathbf{F} = d\mathbf{A}\nu\nabla \cdot \mathbf{u} \tag{A.23}$$

The change of force of a volume element over a distance $d\ell = (dr, rd\theta, r\sin(\theta)d\varphi)$ is

$$\left(\frac{\partial}{\partial r}dF_r + \frac{\partial}{r\partial\theta}dF_\theta + \frac{\partial}{r\sin(\theta)\partial\varphi}dF_\varphi\right)d\ell$$
$$\equiv \nabla \cdot d\mathbf{F}d\ell$$
$$= \nabla \cdot (d\mathbf{A}\nu\nabla \cdot \mathbf{u})\,d\ell \tag{A.24}$$

which is equal to the torque due to shear. In spherical coordinates Eq.A.24 can be written as:

$$\nabla \cdot d\mathbf{F}d\ell = \frac{1}{r^2}\frac{\partial}{\partial r}\left(r^2\sin(\theta)d\theta d\varphi\nu\frac{1}{r^2}\frac{\partial}{\partial r}u_r\right)dr \cdot \hat{e}_r$$
$$+ \frac{1}{r\sin(\theta)}\frac{\partial}{\partial\theta}\left(r\sin(\theta)drd\varphi \cdot \nu\frac{1}{r\sin(\theta)}\frac{\partial}{\partial\theta}u_\theta\right) \cdot rd\theta \cdot \hat{e}_\theta \tag{A.25}$$

---

[1]The volume can be considered continuous and steady and can therefore be moved out of the time derivative.

where symmetry in $\hat{e}_\varphi$ is assumed.

Combining Eqs.A.20 and A.24 in Eq.A.15, an equation for the change of angular momentum is recovered:

$$\frac{d}{dt}\mathcal{L} = \mathcal{M} \tag{A.26}$$

$$\frac{d}{dt}\mathcal{L} = \rho\frac{d}{dt}\left(r^2\sin^2(\theta)\boldsymbol{\Omega}\right)_{M_r} \cdot r^2\sin(\theta)d\theta d\varphi dr \tag{A.27}$$

$$\mathcal{M} = \frac{1}{r^2}\frac{\partial}{\partial r}\left(r^2\sin(\theta)d\theta d\varphi \nu\frac{1}{r^2}\frac{\partial}{\partial r}v_r\right)dr\cdot\hat{e}_r$$
$$+\frac{1}{r\sin(\theta)}\frac{\partial}{\partial\theta}\left(r\sin(\theta)drd\varphi\cdot\nu\frac{1}{r\sin(\theta)}\frac{\partial}{\partial\theta}v_\theta\right)\cdot rd\theta\cdot\hat{e}_\theta \tag{A.28}$$

This can be simplified to

$$\rho\frac{d}{dt}\left(r^2\sin^2(\theta)\boldsymbol{\Omega}\right)_{M_r} \cdot r^2\sin(\theta)$$
$$= \frac{1}{r^2}\frac{\partial}{\partial r}\left(\sin(\theta)\nu\frac{\partial}{\partial r}\cdot u_r\right)\cdot\hat{e}_r + \frac{1}{r\sin(\theta)}\frac{\partial}{\partial\theta}\left(\nu\frac{\partial}{\partial\theta}\cdot u_\theta\right)\cdot\hat{e}_\theta \tag{A.29}$$

If in Eq.A.29 only the radial transport is considered one can further simplify:

$$\frac{d}{dt}\left(r^2\sin^2(\theta)\boldsymbol{\Omega}\right)_{M_r} = \frac{1}{\rho r^4\sin(\theta)}\frac{\partial}{\partial r}\left(\sin(\theta)\nu\frac{\partial}{\partial r}\cdot v_r\right)\cdot\hat{e}_r$$
$$= \frac{1}{\rho r^4}\frac{\partial}{\partial r}\left(\nu\frac{\partial}{\partial r}v_r\right)\cdot\hat{e}_r \tag{A.30}$$

The left hand side of Eq.A.30 can be rewritten as:

$$\frac{d}{dt}\left(r^2\sin^2(\theta)\boldsymbol{\Omega}\right)_{M_r} = \frac{d}{dt}(r^2\sin^2(\theta))_{M_r}\Omega + r^2\sin^2(\theta)\frac{d}{dt}(\Omega)_{M_r} \tag{A.31}$$

When again using:

$$\frac{\partial}{\partial r} = 4\pi r^2\rho\frac{\partial}{\partial m} \tag{A.32}$$

The right hand side of Eq.A.30 can be rewritten:

$$\frac{1}{\rho r^4}\frac{\partial}{\partial r}\left(\nu\frac{\partial}{\partial r}v_r\right) = \frac{4\pi r^2\rho}{\rho r^4}\frac{\partial}{\partial m}\left(4\pi r^2\rho\nu\frac{\partial}{\partial m}v_r\right) \tag{A.33}$$

When combining the rewritten left and right side of Eq.A.30, I get:

$$\frac{d\Omega}{dt}\bigg|_{M_r} = \frac{1}{r^2\sin^2(\theta)}\frac{\partial}{\partial m}\left((4\pi)^2 r^2\rho\nu\frac{\partial}{\partial m}v_r\right) - \frac{\Omega}{r^2\sin^2(\theta)}\frac{d}{dt}(r^2\sin^2(\theta))_{M_r} \qquad (A.34)$$

by substituting $i = \frac{2}{3}r^2$ and multiplying the first term on the right side with $\frac{\rho}{\rho} = \frac{\rho 4/3\pi r^3}{m}$ (=1), I obtain Eq.2.33

A.3   Derivation GENEC implementation

In the GENEC code, an advective term is also included in the equation for the transport of angular momentum. Here I show where this term originates from, but the complete derivation of Eq.A.38 is not given.

The time derivative in Eq. A.20 can be rewritten to:

$$\rho\frac{d}{dt}\left(r^2\sin^2(\theta)\mathbf{\Omega}\right)_{M_r}$$
$$= \frac{d}{dt}\left(\rho r^2\sin^2(\theta)\mathbf{\Omega}\right)_{M_r} - r^2\sin^2(\theta)\mathbf{\Omega}\frac{d}{dt}\left(\rho\right)_{M_r}$$
$$= \frac{\partial}{\partial t}\left(\rho r^2\sin^2(\theta)\mathbf{\Omega}\right)_r + \mathbf{u}\nabla\cdot\left(\rho r^2\sin^2(\theta)\mathbf{\Omega}\right)$$
$$- r^2\sin^2(\theta)\mathbf{\Omega}\frac{\partial}{\partial t}\left(\rho\right)_r - r^2\sin^2(\theta)\mathbf{\Omega}\cdot\mathbf{u}\cdot\nabla\rho \qquad (A.35)$$

Using the continuity equation,

$$\frac{\partial}{\partial t}\rho = -\nabla\cdot(\mathbf{v}\rho) \qquad (A.36)$$

one can write

$$-\frac{\partial}{\partial t}\rho - \mathbf{v}\cdot\nabla\rho = \nabla\cdot(\mathbf{v}\rho) - \mathbf{v}\cdot\nabla\rho$$
$$= \rho\nabla\cdot\mathbf{v}. \qquad (A.37)$$

With this, the two last terms of the right hand side of Eq.A.35 can be further simplified,

$$\rho \frac{d}{dt} \left(r^2 \sin^2(\theta) \mathbf{\Omega} \right)_{M_r}$$

$$= \frac{\partial}{\partial t} \left(\rho r^2 \sin^2(\theta) \mathbf{\Omega} \right)_r + \mathbf{v} \nabla \cdot \left(\rho r^2 \sin^2(\theta) \mathbf{\Omega} \right)$$

$$+ \rho r^2 \sin^2(\theta) \mathbf{\Omega} \nabla \mathbf{v}$$

$$= \frac{\partial}{\partial t} \left(\rho r^2 \sin^2(\theta) \mathbf{\Omega} \right)_r + \nabla \left(\rho r^2 \sin^2(\theta) \mathbf{\Omega} \cdot \mathbf{v} \right) \qquad (A.38)$$

Combining Eqs.(A.15), (A.38) and (A.24), an equation for the change of angular momentum is recovered, but now also including an advective term (the second term on the right side of the equal sign in Eq. A.38).

This term could be added to this equation and not to Eq. 2.8, as Ω is a vector and n_i is not.

B   Input files

B.1   Inlist

```
&star_job

create_pre_main_sequence_model = .true.


change_net = .true.
new_net_name = 'agb.net'


set_uniform_initial_xa_from_file = .true.
file_for_uniform_xa = 'falk_xa.list.agb'


set_rates_preference = .true. ! for use by net + rates modules
new_rates_preference = 1
! 1 = NACRE rates -- this is the default
! 2 = jina reaclib rates -- to match jina where possible

set_rate_c12ag = 'Kunz' ! empty string means ignore this control
! one of 'NACRE', 'jina reaclib', 'Kunz', or 'CF88'
! note: original CF88 rate is actually multiplied by 1.7 as in Timmes' rates
set_rate_n14pg = 'jina reaclib' ! empty string means ignore this control
! one of 'NACRE', 'jina reaclib', or 'CF88'
set_rate_3a = 'jina reaclib' ! empty string means ignore this control
! one of 'NACRE', 'jina reaclib', or 'CF88

use_se_output = .true.
```

```
change_rotation_flag = .false.
new_rotation_flag = .false.

!change_D_omega_flag = .true.
!new_D_omega_flag = .true.

new_surface_rotation_v = 250.0 ! km/s
set_near_zams_surface_rotation_v_steps = 10


/ ! end of star_job namelist

&controls
initial_mass = 2.0
initial_z = 0.01d0

mixing_length_alpha = 1.73

!operator_coupling_choice = 0
 0 -- fully coupled


! some logistics
!max_model_number = 5001 ! negative means no maximum
!stop_at_TP = True

photo_interval = 500
profile_interval = 10
max_num_profile_models = 100000 ! maximum number of saved profiles
```

```
history_interval = 1
terminal_interval = 10
write_header_frequency = 10


! mesh
max_allowed_nz = 10000 ! maximum number of grid points allowed
! resolve the C13 pockets
xa_function_species(1) = 'h1'  ! name of nuclide as defined in chem_def
xa_function_weight(1) = 20
xa_function_param(1) = 1d-9
xa_function_species(2) = 'he4'  ! name of nuclide as defined in chem_def
xa_function_weight(2) = 10
xa_function_param(2)  = 1d-4
xa_function_species(3) = 'c13'  ! name of nuclide as defined in chem_def
xa_function_weight(3) = 25
xa_function_param(3) = 3d-10
xa_function_species(4) = 'n14'  ! name of nuclide as defined in chem_def
xa_function_weight(4) = 25
xa_function_param(4) = 5d-9


omega_function_weight = 50



! timesteps
! general
varcontrol_target = 5d-5
! this is the target value for relative variation in the structure from one
! model to the next. The default timestep adjustment is to increase or
! reduce the timestep depending on whether the actual variation was
```

```
! smaller or greater than this value.

delta_lgRho_cntr_limit = 0.05
delta_lgRho_cntr_hard_limit = 0.1


delta_lgT_cntr_limit = 0.01
delta_lgT_cntr_hard_limit = 0.02


delta_lgTeff_limit = 0.01
delta_lgTeff_hard_limit = 0.02


delta_lgL_limit = 0.1
delta_lgL_hard_limit = 0.2


! TP
delta_lgL_He_limit = 0.01 ! for TP resolution
!delta_lgL_He_hard_limit = 0.05
lgL_He_drop_factor = 0.5
lgL_He_burn_min = 2.0 ! ignore changes in lgL_He if value
! is less than this



dH_limit_min_H = 1.e-2
dH_limit = 0.1


dH_div_H_limit_min_H = 1d-5
dH_div_H_limit = 0.5


dHe_limit_min_He = 1.e-2
dHe_limit = 0.1
```

```
dHe_div_He_limit_min_He = 1d-5
dHe_div_He_limit = 0.5


! Overshooting
mass_for_overshoot_full_on = 1.8 ! Msun units
mass_for_overshoot_full_off = 1.1 ! Msun units
!mass_for_overshoot_full_off = 0.9 ! Msun units


overshoot_f_above_burn_h_core   = 0.014
overshoot_f_above_burn_h_shell  = 0.014
overshoot_f_below_burn_h_shell  = 0.014
overshoot_f0_above_burn_h_core   = 0.014
overshoot_f0_above_burn_h_shell  = 0.014
overshoot_f0_below_burn_h_shell  = 0.014


! C13 pocket
overshoot_below_noburn_shell_factor = 1
! He-shell flash convection zone
!ovr_below_burn_he_shell_factor = 0.5714


! atmosphere option
which_atm_option = 'simple_photosphere'


! mass loss
cool_wind_RGB_scheme = 'Reimers'
cool_wind_AGB_scheme = 'Blocker'
RGB_to_AGB_wind_switch = 1d-4
Reimers_scaling_factor = 0.5d0
Blocker_scaling_factor = 0.01d0
```

```
! rotation
skip_rotation_in_convection_zones =.true.
am_D_mix_factor = 0.03333333333333333d00

am_nu_addition_omega = 1d6

D_DSI_factor = 0.0
D_SH_factor  = 0.0
D_SSI_factor = 1.0
D_ES_factor  = 1.0
D_GSF_factor = 0.0
D_ST_factor  = 0.0

smooth_D_DSI = 0
smooth_D_SH  = 0
smooth_D_SSI = 0
smooth_D_ES  = 0
smooth_D_GSF = 0
smooth_D_ST  = 0
smooth_nu_ST = 0

angsmt_D_DSI = 0.0d0
angsmt_D_SH  = 0.0d0
angsmt_D_SSI = 0.0d0
angsmt_D_ES  = 0.0d0
angsmt_D_GSF = 0.0d0
angsmt_D_ST  = 0.0d0
angsmt_nu_ST = 0.0d0
angsml       = 1d-3
```

```
! opacities
use_Type2_opacities = .true.
Zbase = 0.010

kap_Type2_full_off_dZ = 0.00d0
kap_Type2_full_on_dZ = 0.00d0
kap_Type2_full_off_X = 0.749
kap_Type2_full_on_X = 0.748
/ ! end of controls namelist
```

B.2 Run_ star_ extra

Only the subroutines that are different from the default file are shown here.

```
subroutine data_for_extra_history_columns(id, id_extra, n, names, vals, ierr)
integer, intent(in) :: id, id_extra, n
character (len=maxlen_history_column_name) :: names(n)
real(dp) :: vals(n), ratio
integer, intent(out) :: ierr
type (star_info), pointer :: s
ierr = 0
call star_ptr(id, s, ierr)
if (ierr /= 0) return
```

```
if (s% c_core_mass .ge. 0.01) then
    s% xa_function_weight(1) = 20
    s% am_nu_addition_omega = 0
    write(*, *) 'artvisc=0'
endif


if (s% center_omega .ge. 0.0001) then
    s% angsmt_D_ST  = 0.2d0
    s% angsmt_nu_ST = 0.2d0
    s% angsml       = 1d-3
endif


if (s% he_core_mass .ge. 0.00001) then
    s% overshoot_f_above_nonburn_core  = 0.014
    s% overshoot_f_above_nonburn_shell = 0.014
    s% overshoot_f_below_nonburn_shell = 0.014
    s% overshoot_f_above_burn_he_core  = 0.014
    s% overshoot_f_above_burn_he_shell = 0.014
    s% overshoot_f_below_burn_he_shell = 0.014
    s% overshoot_f_above_burn_z_core   = 0.014
    s% overshoot_f_above_burn_z_shell  = 0.014
    s% overshoot_f_below_burn_z_shell  = 0.014
    s% overshoot_f0_above_nonburn_core  = 0.014
    s% overshoot_f0_above_nonburn_shell = 0.014
    s% overshoot_f0_below_nonburn_shell = 0.014
    s% overshoot_f0_above_burn_he_core  = 0.014
    s% overshoot_f0_above_burn_he_shell = 0.014
    s% overshoot_f0_below_burn_he_shell = 0.014
    s% overshoot_f0_above_burn_z_core   = 0.014
    s% overshoot_f0_above_burn_z_shell  = 0.014
```

```
    s% overshoot_f0_below_burn_z_shell   = 0.014

    s% overshoot_D2_below_nonburn = 100000000000

    s% overshoot_D2_below_burn_h = 100000000000

    s% overshoot_D2_below_burn_he = 100000

    s% overshoot_D2_below_burn_z = -0.0001

    s% overshoot_f2_below_nonburn = 0.25

    s% overshoot_f2_below_burn_h = 0.25

    s% overshoot_f2_below_burn_he = 0.14

    s% overshoot_f2_below_burn_z = -0.00001

    s% dH_div_H_limit_min_H =1d-6


end if



ierr = 0
ratio=(s% surface_c12*4d0)/(s% surface_o16*3d0)
if ((ratio .ge. 1.15 ) .and. ( abs(s% Blocker_scaling_factor - 0.04 ) > 1d-4))...
 ...then
    s% Blocker_scaling_factor=0.04
    write(*, *) 'Change blocker massloss eta to',s% Blocker_scaling_factor,'...
    ...at model ',s% model_number,' (if needed)'
end if
if ((ratio .le. 1.15 ) .and. (abs(s% Blocker_scaling_factor - 0.01 ) >  1d-4 ))..
 ...then
    s% Blocker_scaling_factor=0.01
    write(*, *) 'Change blocker massloss eta to',s% Blocker_scaling_factor,'...
    ...at model ',s% model_number,' (if needed)'
end if


end subroutine data_for_extra_history_columns
```